

**Cordierite and its retrograde breakdown products as
monitors of fluid-rock interaction during retrograde
path metamorphism: case studies in the
Schwarzwald and the Bayerische Wald
(Variscan belt, Germany)**

Dissertation
submitted to the
Combined Faculties for the Natural Sciences and for Mathematics
of the Ruperto-Carola University of Heidelberg, Germany
for the degree of
Doctor of Natural Sciences

presented by

Diplom-Geol.: Jörn Christian Ogiermann
born in: Offenbach/Main

Oral examination: 13. December, 2002

Cordierite and its retrograde breakdown products as monitors of fluid-rock
interaction during retrograde path metamorphism: case studies in the
Schwarzwald and the Bayerische Wald
(Variscan belt, Germany)

Referees: Prof. Dr. Angelika Kalt
Prof. Dr. Rainer Altherr

Abstract

Retrograde breakdown products of cordierite are commonly termed pinite, but their modes, compositions and formation conditions are only poorly known. The author carried out a systematic study on pinitised cordierite from Variscan high-temperature metamorphic pelites of the Schwarzwald and the Bayerische Wald using electron microprobe (EM), transmission electron microscope (TEM), scanning electron microscope (SEM), x-ray diffraction (XRD), petrographic microscope and Fourier Transformation Infrared Spectroscopy (FTIR) investigations. On the basis of composition, phase assemblage, textural position and grain size four pinite types (border, mat, fissure, isotropic type) were distinguished that formed by distinct allochemical processes under different pressure-temperature conditions at different times. They probably represent general features of cordierite breakdown.

Border-type (b-type) pinite consists of muscovite and biotite, formed at 350 - 550 °C from a K⁺-bearing fluid, most likely derived from the breakdown of K-feldspar to muscovite and quartz. B-type pinitisation may be related to granite intrusion in the Carboniferous.

Mat-type (m-type) pinite encompasses chlorite-muscovite pinite and complex m-type pinite, bearing clay minerals, and is in general considered to represent the alteration of cordierite by an alkali-bearing fluid. Petrogenetic grids define an upper P-T limit muscovite of around 500 °C. TEM revealed that complex clay mineral-bearing m-type pinite of this study has the principal constituents chlorite, berthierine, I/S R₁ and I/S R₀ mixed-layers, Na/K-illite and random chlorite/berthierine mixed-layers. The observed features are similar to those of non-equilibrium assemblages from early to late diagenetic parts of burial metamorphic sequences as complex m-type pinite lacks stable equilibrium and should have been formed much below 200 °C. In this case, its genesis is a complex two-stage process, with chlorite and I/S R₁ representing the primary product of m-type pinitisation. Secondary berthierine and I/S R₀ are formed by the replacement of chlorite and I/S R₁ via a dissolution/precipitation process driven by the infiltration of an additional very low-grade fluid. M-type pinitisation could be related to low-temperature meteoric alteration of granites.

F-type pinites form alteration veins penetrating intact cordierite. They are filled with tiny (< 20 - 250 Å in thickness), randomly oriented and randomly related, highly imperfect crystals, floating in an amorphous matrix. The principal crystals or packets of layers detected by TEM are berthierine, illite and/or I/S R₁, smectite and chlorite, mixed-layers including 7/14 Å, 10/14 Å, I/S and complex mixed-layering of 7 Å, 10 Å and 14 Å layers. Randomness in orientation of f-type pinite crystallites points to *in situ* crystallisation of packets of layers

directly either from a solution present in alteration veins or from a pre-existing gel-like material as more stable secondary phases. The occurrence of corresponding optical and chemical zonation pattern as further characteristics of f-type pinite let the author assume that corresponding processes of leaching and repolymerisation acting in discrete band-like zones are the principle mechanism of f-type pinitisation. Lack of perfect and homogeneous structures and enhanced thickness of individual packets of layers indicate f-type pinitisation to result from cordierite alteration at very low-grade conditions (weathering), perhaps at surface conditions, with Permian-Mesozoic sediments as possible Ca source.

I-type pinite is in most cases in direct contact to intact cordierite, is fairly homogenous in BSE images, isotropic under crossed polars, lacks optical zonation patterns and occurs sporadically. I-type pinite shows similarities to hydrated glassy layers described from feldspar alteration. Compared to cordierite, i-type pinite is depleted in most elements but networkforming species (Si and Al) and potential interlayer cations with K and Ca being most abundant ($Ca > K$). A dramatic fall in Si counting rates occurred during electron beam exposure at standard conditions, suggesting that i-type pinites may represent amorphous gel-like highly hydrated material with a high portion of low-energy H-H bonds. This assumption is confirmed by the occurrence of fissures penetrating i-type pinite, which are strongly suspected to represent dehydration shrinkage fissures as they do not continue into adjacent material and do not show a preferred orientation. Unfortunately, TEM could not give further evidence. Therefore, the phase inventory and structural state of i-type pinite remain unclear. I-type pinitisation is probably a leaching process at very low temperatures (weathering) with network-modifying species being preferentially dissolved.

H₂O and CO₂ contents of partly pinitised cordierite were determined by *in situ* FTIR measurements in order to detect possible late-stage modifications of the cordierite channel compositions, possibly related to pinitisation. Despite the fact that all samples record infiltration of several hydrothermal aqueous fluids by the alteration of cordierite to various types of pinite, a post-peak re-equilibration with hydrous fluids can be ruled out. The volatile contents of all investigated samples were found to be consistent with equilibration with a H₂O undersaturated melt, during high-grade metamorphism. Therefore, a systematic change of cordierite channel volatile contents as a key step within the process of pinitisation is not indicated. Nevertheless, the crystallographic control of f-type pinitisation implies that the channel structure determines the c axis to be the preferred direction of cordierite dissolution/leaching.

Contents

1. INTRODUCTION	7
1.1 Cordierite and pinitite	7
1.2 Role of the structural channels in pinitisation	9
1.3 Aims and concept of this study	11
2. GEOLOGICAL SETTING AND SAMPLES	13
2.1 The Schwarzwald	13
2.2 The Bayerische Wald	16
2.3 Samples	18
3. ANALYTICAL TECHNIQUES	19
3.1 Transmission electron microscopy	19
3.1.1 The electron source and the electron-optical system	20
3.1.2 Image contrast	20
3.1.3 Resolution and lens aberrations	20
3.1.4 Electron diffraction	21
3.1.5 Analytical electron microscopy	23
3.1.6 Sample preparation and beam damage	23
3.2 Electron microprobe	24
3.2.1 The electron source and the electron-optical system	25
3.2.2 Electron microprobe analysis	26
3.2.3 Destruction of material	27
3.2.4 Sample preparation	27
3.3 Scanning electron microscope	27
3.3.1 Secondary electrons	28
3.3.2 Backscattered electrons	28
3.4 X-ray diffraction	29
3.4.1 Oriented powdered samples	30
3.4.2 Intensity of a reflection	30
3.5 Fourier-Transform infrared spectroscopy (FTIR)	31
3.5.1 Theory	31
3.5.2 FTIR spectrometer	32

4. EM, SEM AND PETROGRAPHIC MICROSCOPY: PETROGRAPHY, CLASSIFICATION AND CHEMICAL CHARACTERISATION OF RETROGRADE CORDIERITE BREAKDOWN PRODUCTS IN GNEISSES AND MIGMATITES OF THE SCHWARZWALD AND THE BAYERISCHE WALD, GERMANY	35
4.1 Abstract	35
4.2 Introduction	35
4.3 Sample selection and geological setting	38
4.4 Analytical techniques	40
4.5 Microscopic characterisation and BSE imaging of cordierite breakdown products	41
4.5.1 Border-type pinite (b-type)	41
4.5.2 Fissure-type (f-type) and isotropic-type pinite (i-type)	41
4.5.3 Mat-type pinite (m-type)	42
4.5.4 Samples Al-20 and To-2	43
4.5.5 Textural relationship between the pinite types	43
4.6 Composition of retrograde breakdown products	47
4.6.1 Primary and secondary biotite	47
4.6.2 Muscovite and muscovite-rich domains	48
4.6.3 Na-rich domains	50
4.6.4 Chlorite	51
4.6.5 F-type pinite	52
4.6.6 I-type pinite and fi-type	56
4.6.7 M-type pinite	56
4.7 Pinitisation processes	58
4.7.1 B-type pinitisation	59
4.7.2 M-type pinitisation	60
4.7.3 F-type and i-type pinitisation	61
4.8 Pinitisation processes in the regional context	63
4.9 Summary and conclusions	65
5. TEM & XRD: CHARACTERISATION OF VERY FINE-GRAINED PINITE FROM THE SCHWARZWALD, GERMANY	67
5.1 Abstract	67
5.2 Introduction	67
5.3 Samples and pinite types	69
5.4 Methods	71
5.5 X-ray diffraction	72

5.6 TEM observations	74
5.6.1 M-type pinite	74
5.6.2 F-type pinite	80
5.6.3 I-type pinite	87
5.7 AEM data	88
5.7.1 M-type pinite	88
5.7.2 F-type pinite	92
5.8 Discussion	93
5.8.1 Genesis of m-type pinite	94
5.8.2 Genesis of f-type pinite	95
5.8.3 Relationship between f-type and m-type pinite	97
5.9 Summary and conclusions	97
6. FTIR: THE ROLE OF THE STRUCTURAL CHANNELS IN THE PROCESS OF PINITISATION	99
6.1 Abstract	99
6.2 Introduction	99
6.3 Samples, geological settings and pinite types	101
6.4 Analytical techniques	103
6.5 Cordierite compositions	105
6.5.1 Major element concentrations	105
6.5.2 Cordierite intra-grain FTIR spectra	105
6.5.3 Pinite FTIR spectra	106
6.5.4 FTIR spectra of outermost cordierite rims	107
6.6 Discussion	108
6.6.1 Incorporation of volatiles in cordierite	108
6.6.2 Behaviour of volatile contents at low temperatures	112
6.6.3 Volatile contents of cordierite from granulitic and migmatitic terranes	112
6.6.4 Significance of the cordierite volatile contents determined in this study	112
6.7 Conclusions	118
7. RESÜMEE	119
REFERENCES	123
DATA APPENDIX	137

1. Introduction

1.1 Cordierite and pinitite

Cordierite $(\text{Mg,Fe})_2\text{Al}_4\text{Si}_5\text{O}_{18}(n\text{H}_2\text{O},m\text{CO}_2)$ is a common Fe-Mg-Al silicate in aluminous medium to high-grade metamorphic rocks. The cordierite structure contains six-membered rings of $(\text{Si,Al})\text{O}_4$ tetrahedra, which form structural channels aligned parallel to the crystallographic c-axis (Fig. 1.1) (e.g. Aines & Rossman, 1984). These channel-forming tetrahedra are linked laterally and vertically by additional $(\text{Si,Al})\text{O}_4$ tetrahedra (Fig. 1.1), making cordierite strictly a framework and not a ring silicate. Octahedrally coordinated sites for (Mg,Fe) are placed within this framework (Fig. 1.1).

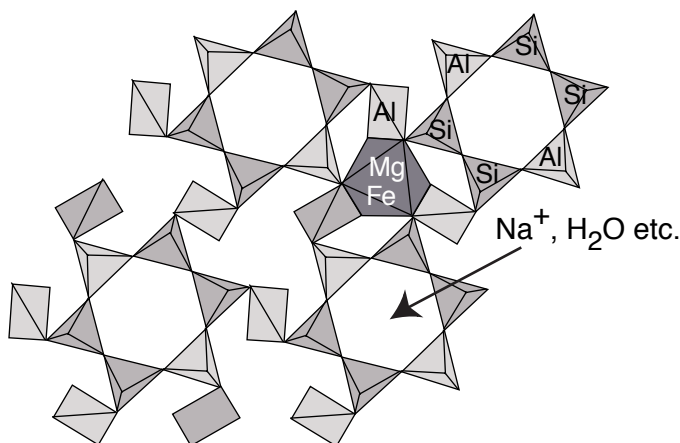


Fig. 1.1. Structure of a fully ordered cordierite projected on (001) (after Cohen *et al.*, 1977). Parallel to crystallographic c, six-membered rings of $(\text{Si,Al})\text{O}_4$ tetrahedra form structural channels, which can incorporate volatiles (H_2O , CO_2 etc.) and alkalis (Na^+ , K^+). The fully ordered high-temperature polymorph of cordierite is hexagonal and called indialite. Natural cordierite is usually of the orthorhombic pseudo-hexagonal low-temperature polymorph, the transition from hexagonal to orthorhombic cordierite occurs at about 1450 °C (e.g. Deer *et al.*, 1992).

The channels narrow to ‘bottle necks’ in the plane of the rings (Fig. 1.2; $\text{Ø} \approx 2.5\text{Å}$), widen to ‘cages’ in the plane between two rings (Fig. 1.2; $\text{Ø} 5.4\text{Å}$ and 6.0Å along crystallographic b and a, respectively) and are large enough to allow accommodation of alkalis ($\text{Na} \gg \text{K}$) at the ‘bottle necks’ and of volatiles species such as H_2O , CO_2 , N and Ar ($\text{H}_2\text{O} > \text{CO}_2 \gg \text{N}$, Ar, etc.) at the ‘cages’ (e.g. Aines & Rossman 1984; Vry *et al.*, 1990).

In contrast to other Fe-Mg silicates such as garnet and biotite, which show retrograde breakdown mainly at the grain boundaries or along fissures and cleavage plains, cordierite is often altered penetratively during retrogression. Hence, cordierite seems to be extremely reactive along the retrograde path of metamorphism and its breakdown is a potential monitor of retrogression and hydrothermal activity, including the composition of fluids. For fine-grained retrograde

decomposition products of natural cordierite the term pinitite was introduced (Lacroix, 1962; Deer *et al.*, 1962). Unfortunately, pinitite is in most cases of such a fine-grained nature that recognition by optical methods and electron microprobe (EM) point analysis is hampered. Consequently, the complete phase inventory of pinitite as well as mechanisms of pinitisation are still unclear.

Experimentally, the isochemical breakdown of Mg-cordierite has been extensively studied (e.g. Schreyer & Yoder, 1964; Seifert & Schreyer, 1970; Newton, 1972; Mirwald & Schreyer, 1977; Massonne & Schreyer, 1983). At pressures below 0.6 GPa, which is the pressure range relevant for this study, and at temperatures between 520 - 600 °C, Mg-cordierite breaks down to Al-silicate + chlorite + quartz ($P_{\text{H}_2\text{O}} = P_{\text{tot}}$; Seifert & Schreyer, 1970; Fig. 1.2). The experimental isochemical breakdown of the low-pressure phase Fe-cordierite (Fig. 1.2) is less well studied and the experimentally observed low-temperature counterpart of Fe-cordierite, chloritoid + quartz, is suspected to represent a metastable intermediate assemblage (Schreyer, 1965b; Boberski & Schreyer, 1990; Schreyer *et al.*, 1993).

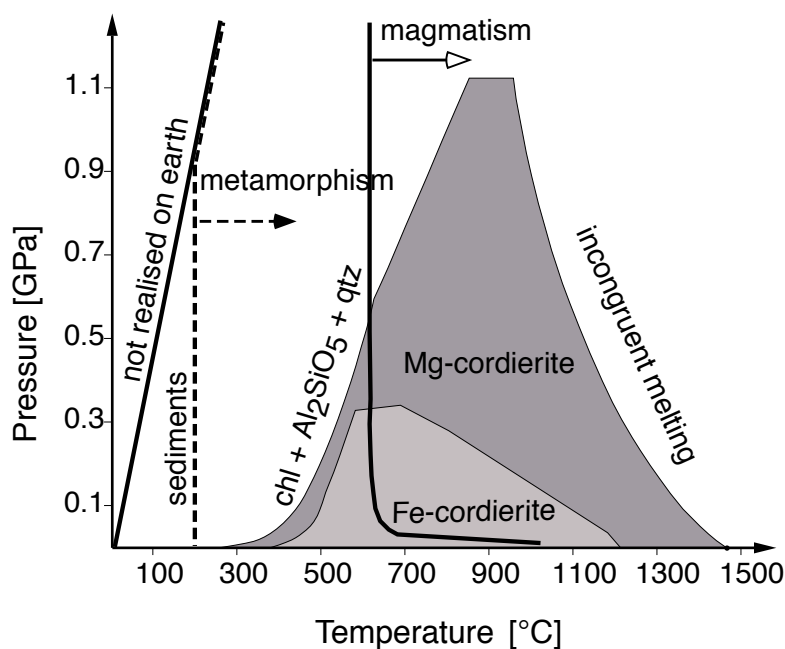


Fig. 1.2. P-T stability diagram of Mg and Fe cordierite modified after Schreyer (1986). The existence of Fe cordierite is restricted to low pressures; with increasing X_{Mg} the stability limit of cordierite is shifted to higher pressures and also to higher temperatures. The channel volatile content of cordierite also affects its stability (e.g. Schreyer, 1986). Compared to H_2O -free cordierite, the stability limit of H_2O -bearing cordierite is shifted to higher pressures.

In contrast, the products of natural cordierite alteration (pinitisation) commonly include hydrous alkali-bearing phyllosilicates (Chapter 4.2; e.g. McKenzie, 1981; Mathias, 1952; Chandler, 1975; Haslam, 1983; Nédélec & Paquet, 1981; Clemens & McMillan, 1982), which do not coincide with the experimentally observed isochemical breakdown products of both cordierite endmembers.

Therefore, pinites are clearly the product of an allochemical transformation process. Besides chlorite-muscovite pinite, which is considered as the most abundant pinite type (Chapter 4.2; e.g. Seifert & Schreyer, 1970; Deer *et al.*, 1992) and clay mineral-bearing assemblages (Chapter 4.2; e.g. Černý & Povondra, 1967; Schenk & Armbruster, 1985), isotropic alteration products were described in several studies (Chapter 4.2; e.g. Mathias, 1952; Haslam, 1983). In most cases, a satisfactory characterisation of these isotropic pinites was not given. Only a limited number of different pinite types have been described in the literature (Chapter 4.2), and it has hardly been attempted to link pinitisation of cordierite to known geological events of fluid infiltration in regional studies.

To sum up, it is not known whether pinitisation is a general and systematic process of cordierite breakdown at specific pressure-temperature-composition (P-T-X) conditions and fairly independent from the local environment, or whether it encompasses a variety of processes taking place under fluid-controlled, open-system, locally varying conditions. Moreover, it is not known whether pinitisation is a one-step process or a complex process, for example including isochemical breakdown as a first step and the alteration of the primary breakdown assemblage to alkali-bearing minerals as a second step (Chapter 4; Seifert & Schreyer, 1970).

1.2 Role of the structural channels in pinitisation

Infrared (IR) spectroscopy (e.g. Goldman *et al.*, 1977) revealed channel H₂O to occur in two principle orientations, I and II, and the long axis of CO₂ molecules to be oriented parallel to the crystallographic a direction (Fig. 1.3). The H-H vector of H₂O I is parallel to the channels long axis (parallel to crystallographic c) whereas the H-H vector of H₂O II is parallel to crystallographic b (Goldman *et al.*, 1977) (Fig. 1.3). H₂O II is assumed to interact with alkalis trapped in the 'bottle necks', which does not seem to be the case for H₂O I (Fig. 1.3). Additionally, recent IR and Raman spectroscopic studies of Kolesov & Geiger (2000) identified H₂O with its H-H vector parallel to crystallographic a, showing no interaction with alkalis.

By quantifying the volatile contents of natural cordierites and comparing them to experimentally obtained values, conclusions can be drawn on the equilibration environment. In particular, experiments on the hydration/dehydration of cordierite under fluid-present conditions (e.g. Johannes & Schreyer, 1981; Jochum, 1986) and on the partitioning of volatiles between cordierite and coexisting melt (e.g. Carrington & Harley, 1996; Harley *et al.*, 2002) allow to decide whether the channel composition equilibrated with a melt or with a fluid (Chapter 6). Nevertheless, there are several examples of natural cordierite whose low volatile contents can be explained by equilibration neither with a fluid nor with a melt (Chapter 6; e.g. Vry *et al.*, 1990; Harley *et al.*,

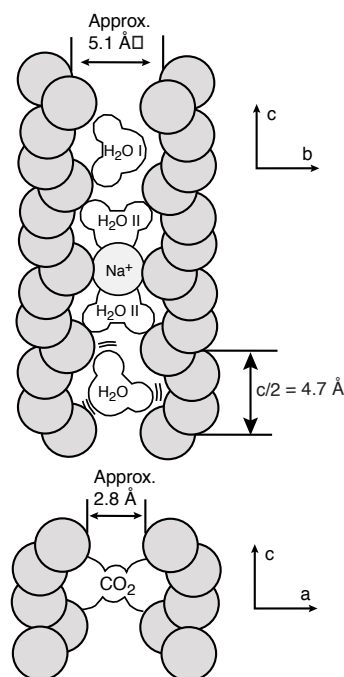


Fig. 1.3. Schematic cross section of cordierite along the channel axis, modified after Aines & Rossman (1984). Alkalis are located in the plane of the six-membered rings ('bottle necks') with Na^+ being much more abundant than K^+ in the channel structure of natural cordierite. At least two types of water are distinguished: H_2O I does not interact with alkalis, whereas the orientation of H_2O II is controlled by the presence of alkali cations. Unbonded water is assumed to occur at high temperatures (Aines & Rossman, 1984). CO_2 is also located in the 'cages' of the channel structure in the plane between two six-membered rings with its long axis parallel to crystallographic a .

2002). In consequence, it was suggested that the release of 'excess' H_2O during uplift and retrogression, as cordierite passes the volatile saturation surface, may provide a principle mechanism for hydrous alteration of cordierite (pinitisation; Harley *et al.*, 2002). To be more general, it is possible that systematic changes of the channel composition by hydration or dehydration are a key step within the process of pinitisation. Several observations imply that this may be the case:

- (1) Some authors report pinitite veins to be oriented parallel to the crystallographic c axis (e.g. Schreyer *et al.*, 1993) or to the c and a axis (Chapters 4, 5).
- (2) Hydration experiments in the P - T range below the stability of cordierite (200 - 400 °C, $P_{\text{tot}} = P_{\text{H}_2\text{O}} = 0.15 - 0.44$ GPa) by Jochum (1986) resulted in rapid breakdown of natural Na-bearing and synthetic Na-free Mg-cordierite along veins oriented parallel to crystallographic c .
- (3) Casey & Bunker (1990) argued on a theoretical basis that the structural channels of beryl, which is quasi isostructural to cordierite, control the leaching behaviour as the channel diameter is large enough to accelerate H_2O diffusion significantly.
- (4) In a recent *in situ* Fourier Transform Infrared Spectroscopy (FTIR) study, Kalt (2000) reported a systematic difference in H_2O content between cordierite cores and rims for one sample of the Bayerische Wald (BW), with the rims being higher in H_2O . This could be due to retrograde modification of the channel composition, possibly in the context of pinitisation.

However, it is still unclear if and in which way the structural channels of cordierite provide a mechanism for pinitisation.

1.3 Aims and concept of this study

A systematic study on natural retrograde cordierite breakdown products (pinites) in metapelitic migmatites and gneisses of the Bayerische Wald (BW) and the Schwarzwald (SW) was carried out to contribute to our knowledge on the modes, compositions, formation conditions and formation mechanisms of pinite. In consequence, the aims in focus of this study were:

- (1) to give a detailed characterisation of pinite in each of the samples on the basis of petrography, chemical composition and phase inventory
- (2) to find out whether different types of pinite can be distinguished systematically and if / how they vary regionally and locally
- (3) to specify the mechanisms of pinitisation and the formation conditions of the studied pinites
- (4) to clarify the role of the structural channels in pinitisation of the studied cordierite
- (5) to discuss the implications of the results for general models of pinite formation

The samples chosen for this study have comparable bulk and mineralogical compositions and peak-metamorphic equilibration conditions, but come from different regions and localities. This selection allows for conclusions on the general or regional / local character of pinitisation. Chapter 2 gives an overview of the geological setting and the samples investigated. Several analytical techniques were applied to achieve the above aims. Most of the applied techniques are *in-situ* methods, because the nature of the problem required chemical / structural analysis in the textural context. The methods are briefly described in Chapter 3.

Petrography was based on scanning electron microscopy (SEM) and petrographic microscopy. The major element compositions were determined by electron microprobe (EM) investigations. The results obtained by these three analytical techniques allowed the introduction of a detailed pinite classification. This work is presented in Chapter 4. Some of the investigated pinite types were too fine-grained for a complete characterisation by EM, SEM and petrographic microscopy. X-ray diffraction (XRD) and transmission electron microscopy (TEM) were applied to give a full characterisation of these very fine-grained types of pinite. In addition, useful information on the formation conditions and formation mechanisms of these types of pinite could be obtained. The results and implications of the TEM and XRD investigations are presented in Chapter 5.

For drawing conclusions on the role of the structural channels in pinitisation, *in situ* Fourier Transform infrared spectroscopy (FTIR) was carried out. This allows to determine potential late-

stage modifications of cordierite channel compositions and may provide useful information on the mechanisms of pinitisation. The results and implications of FTIR are given Chapter 6. The major results, implications and conclusions of this study are compiled in Chapter 7.

2. Geological setting and samples

The nine samples investigated were carefully selected from existing sample suites of the BW (Kalt *et al.*, 1999) and the SW (Kalt *et al.*, 2000a and unpublished data). Both crystalline complexes are part of the internal zone of the Variscan orogenic belt in central Europe, which resulted from collision of Laurasia and Gondwana and several microplates in between during Devonian to Carboniferous times (Matte, 1986). Due to post-Variscan uplift and erosion of the Mesozoic and younger sedimentary cover, several isolated fragments of the Variscan basement were exposed to the earth surface in central and western Europe (Fig. 2.1). The BW and the SW are two of these exposed basement areas. The SW is located at the eastern flank of the Rheingraben (Fig. 2.2) and the BW forms the southwestern margin of the Bohemian Massif (Fig. 2.3). In both crystalline complexes, low-pressure high-temperature (LP-HT) metamorphic gneisses and migmatites and granites are the most abundant rocks.

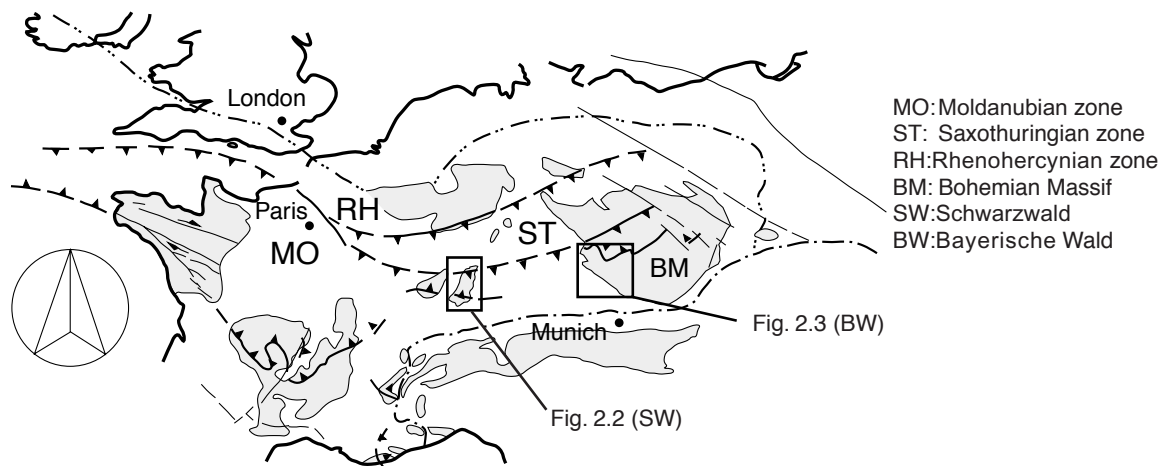


Fig. 2.1. Schematic sketch map of the Variscan massifs in central Europe (after Franke, 1989) that are not covered by Mesozoic or younger sediments, and their subdivision into the three zones (RH, ST, MO) according to Kosmat (1927). The two quadrangles encompass the areas shown in Fig. 2.2 (Schwarzwald) and Fig. 2.3 (Bayerische Wald).

2.1 The Schwarzwald

The SW basement can be divided into three different metamorphic units (Hanel *et al.*, 1999), which occur within two crystalline blocks, the Central Schwarzwald Gneiss Complex (CSGC) and the Southern Schwarzwald Gneiss Complex (SSGC) (Fig. 2.2). Common to all units is a final equilibration at $\sim 730 - 780^\circ \text{C} / 0.40 - 0.45 \text{ GPa}$ at approximately 330 Ma (Kalt *et al.*, 1994; Lippolt

et al., 1994; Kalt *et al.*, 2000a and references therein). Besides granites, metapsammitic and metapelitic gneisses and migmatites are the dominant lithologies.

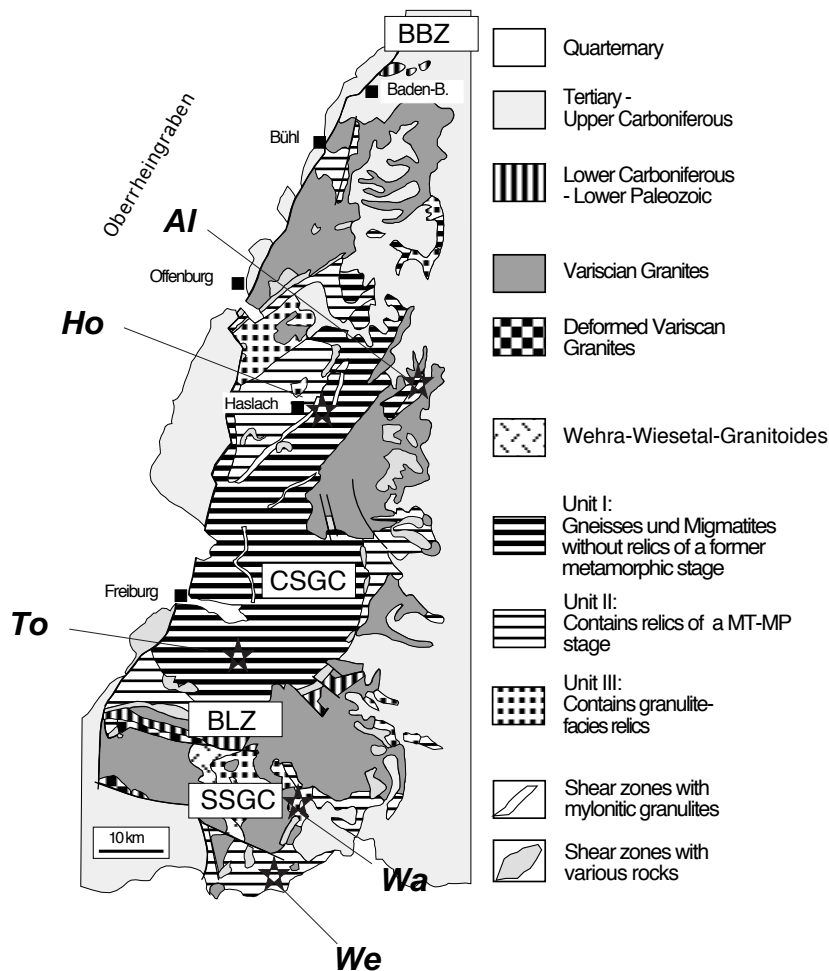


Fig. 2.2. Simplified geological map of the Schwarzwald, modified after Marschall *et al.* (2001). The Variscan basement of the SW is subdivided into three tectonometamorphic units, which occur in the two principle crystalline complexes of the SW: the Central Schwarzwald Gneiss Complex (CGSC) and the Southern Schwarzwald Gneiss Complex (SSGC). The Badenweiler-Lenzkirch zone (BLZ) is a fault zone that separates the CSGC and SSGC. The Baden-Baden zone in the northernmost part of the Schwarzwald is assigned to the Saxothuringian. Ho, To, Wa and We mark the sample locations.

Unit I contains mainly migmatites and gneisses, that show no evidence for an earlier metamorphic stage and bear the phase assemblage biotite + plagioclase + quartz \pm alkali feldspar \pm garnet \pm sillimanite \pm cordierite (e.g. Wimmenauer, 1984). Evidence for the formation and crystallisation of partial melts is widespread in rocks of unit I (Kalt *et al.*, 2000a and references therein). Besides biotite-plagioclase gneisses **unit II** comprises graphite-bearing gneisses, amphibolites, quartzites, calc-silicate rocks and marbles and in places relictic mineral assemblages (staurolite + garnet + kyanite) recording a medium-temperature medium-pressure (MT-MP) stage of 550 - 650 °C and a minimum pressure of 0.5 GPa (Rehfeld, 1983). More recent P-T calculations

suggest pressures between 0.7 - 1.5 GPa and temperatures between 690 - 720 °C (Kalt *et al.*, 2000a). In contrast to unit I, evidence for partial melting is not very widespread. In fact, Kalt *et al.* (1994) concluded that not all migmatites were formed by partial melting and favoured stromatitic migmatites to have rather formed by metamorphic segregation at subsolidus conditions with, if at all, only small amounts of melt present. Metapelitic gneisses of **unit III** record a granulitic HP stage at approximately 1015 °C and 1.5 GPa by relictic mineral equilibria (Kalt *et al.*, 2000a and references therein; Marschall *et al.*, 2002). In places, metapelitic gneisses bear the granulitic-facies assemblage garnet + kyanite + rutile + ternary feldspar + quartz ± biotite whereas psammitic gneisses are mainly quartzo-feldspathic with relics of ternary feldspar and garnet (Kalt *et al.*, 2000a and references therein; Marschall *et al.*, 2002). In unit III, melt formed prograde at high pressures via breakdown of biotite. Back reaction textures indicate that melt was not entirely segregated from the rocks during decompression but partly remained *in situ* and crystallised at low pressures (Marschall *et al.*, 2002). In unit I and III, high pressure relics of retrogressed eclogite lenses, spinel peridotite and garnet-spinel peridotite occur (Klein & Wimmenauer, 1984; Hanel *et al.*, 1993; Kalt *et al.*, 1995; Kalt & Altherr, 1996).

The two major crystalline blocks of the SW the CSGC and the SSGC are separated by a east-west trending fault zone, the Badenweiler-Lenzkirch zone (BLZ, Fig. 2.2). It consists of tectonic slivers of non- to high-grade metamorphic Paleozoic rocks. The Baden-Baden zone (BBZ, Fig.2.2) is located in the northernmost part of the Schwarzwald (Fig.2.2) and is assigned to the Saxothuringian zone of Kosmat (1927) (Fig. 1.1; Kalt *et al.*, 2000a). It consists of isolated outcrops of metamorphic rocks of variable metamorphic grade from the greenschist to the upper amphibolite facies and a Permo-Carboniferous cover of undeformed sedimentary and volcanic rocks.

The vast majority of the SW basement was affected by regional to local-scale post-peak-metamorphic hydrothermal activity (e.g. Simon, 1990; Hagedorn & Lippolt, 1994; Lippolt *et al.*, 1994; Lüders, 1994; Wernicke & Lippolt, 1997; Markl, 1999) that produced most of the ore and mineral deposits in the Schwarzwald (e.g. von Gehlen, 1989). A reconnaissance study of fluid inclusions in Variscan basement rocks and Mesozoic sediments (Behr & Gerler, 1987; Behr *et al.*, 1987; von Gehlen, 1989) was conducted in order to characterise the fluids to be expected during drilling in the course of the German Deep Drilling Program. H₂O-rich fluids related to granite emplacement (late and post-magmatic) were found to be relatively uniform in composition. They were of medium to low salinity and had predominantly K as the major cation. Analyses of oxygen isotopes of granites showed most of the H₂O responsible for the alteration of granites, which is especially recorded by the breakdown of feldspar to sericite, in the temperature range between 400 - 200 °C to be of meteoric origin (Simon & Hoefs, 1987). Predominately K and Na were found to be the major cations of these fluids. Fluids extremely enriched in CaCl₂ and to a lesser degree in NaCl are associated with post-Variscan hydrothermal activity and the formation of Pb-Zn and fluorite-barite deposits at temperatures between 150-180 °C (Behr *et al.*, 1987; von Gehlen, 1989). They are

interpreted as saline basinal brines, most likely originating from the Permian Zechstein, that may have been mixed with formation fluids from Mesozoic marine carbonate (Behr *et al.*, 1987; von Gehlen, 1989). Dating of hydrothermal hematite deposits by (U+Th)-He ages (Wernicke & Lippolt, 1997) showed continuous hydrothermal activity throughout the Jurassic at temperatures of the zeolite facies in the Schwarzwald. Regional and local scale geological events of fluid infiltration are of special interest here, as these fluids may be responsible for hydrous alteration of cordierite (pinitisation).

2.2 The Bayerische Wald

The Bohemian Massif comprises several tectonometamorphic zones (Fig. 2.3; Matte, 1986; Franke, 1989). The Teplá-Barrandium unit represents a polyorogenic basement, which was metamorphosed during the Cadomian and the Variscan orogeny. In contrast, the Moldanubicum *sensu stricto* suffered only the Variscan orogeny. It comprises the Drosendorf unit, which includes the Monotonous series (Fig. 2.3) and the Varied series, and the Gföhl unit. The Monotonous series consists of pelitic to psammitic HT-LP gneisses and migmatites, the Varied series (Zoubek, 1965) is a more variegated gneiss complex with calc-silicates, marbles, and amphibolites, and the Gföhl unit comprises high-temperature-high-pressure (HT-HP) granulites, peridotites and eclogites. In places, the Monotonous series contains isolated relics of eclogite lenses, documenting collision prior to the final LP-HT event (e.g. Medaris *et al.*, 1995).

The BW consists mainly of metapelitic to metapsammitic gneisses and migmatites of the Monotonous series, which equilibrated at low pressures and high temperatures and were intruded by granitoids (Fig. 2.3). Evidence for the formation and crystallisation of partial melts is widespread in the BW (Kalt *et al.*, 1999). The highest grade metapelitic gneisses and migmatites bear quartz + K-feldspar (perthitic) + plagioclase + cordierite + biotite ± sillimanite ± garnet ± ilmenite. Differentiation into layered quartzo-feldspathic leucosomes and biotite-rich melanosomes is common in these rocks (Kalt *et al.*, 1999). Psammitic gneisses are mainly cordierite-free (Kalt *et al.*, 1999). Kalt *et al.* (1999) distinguished several types of migmatites according to their degree of melt segregation. Schreyer & Blümel (1974) and Blümel & Schreyer (1976, 1977) described a sequence of six metamorphic zones situated between the Teplá-Barandium and the Pfahl, showing increasing metamorphic grade from NW to the SE from the greenschist facies to the higher amphibolite facies (650 - 730 °C, 0.2 - 0.4 GPa).

Petrological studies (Kalt *et al.*, 1999) showed that the migmatites of the BW followed a clockwise P-T path and suffered biotite-dehydration melting in the absence of an aqueous fluid during prograde P-T evolution. Peak metamorphic conditions of ~ 800 - 900° C / 0.5 - 0.7 GPa

were estimated for the migmatites of the BW. Maximum conditions of 770 - 846 °C and 0.44 - 0.51 GPa, calculated by mineral equilibria were interpreted to reflect near-peak re-equilibration along the retrograde path (Kalt *et al.*, 1999; Kalt, 2000b). The thermal peak for the BW migmatites was dated at 326 - 323 Ma by U-Pb single zircon and monazite dating and cooling of the migmatites below 300 °C was dated by single K-Ar biotite ages of 312 - 315 Ma (Kalt *et al.*, 1999).

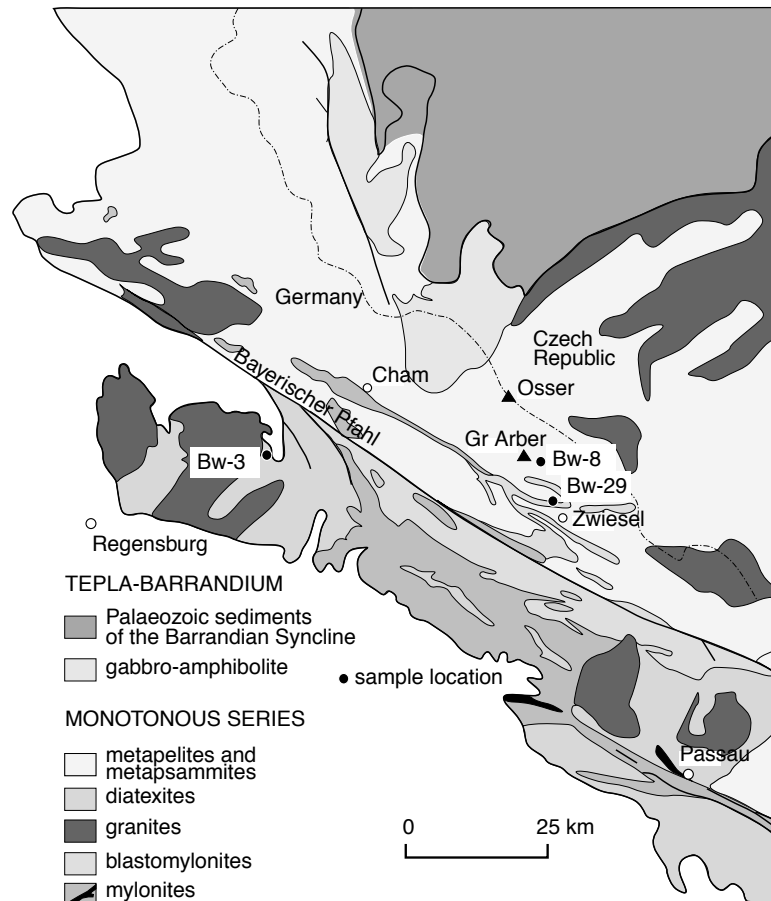


Fig. 2.3. Simplified geological sketch map of the Bayerischer Wald, modified after Troll (1967, 1968) and the Geological Map of Bavaria. The BW consists mainly of LP-HT gneisses and migmatites of the Monotonous series. The Bayerische Pfahl is a late mylonitic fault zone, crosscutting the BW from NW to the SE. The black circles mark the sample locations; Bw-3, Bw-8 and Bw-29 are the sample abbreviations. For further explanation see section 2.2.

A late NW-SE trending fault zone, the Bayerische Pfahl, cuts the BW in its central part. Along the Bayerische Pfahl, metamorphic rocks and granitoids suffered a mylonitic re-equilibration under greenschist-facies to amphibolite-facies conditions during retrogression from the LP-HT event (Beer, 1981; Masch & Cetin, 1991). Post-peak-metamorphic large scale hydrothermal activity seems to be mainly limited to the Bayerische Pfahl (Beer, 1981), although rocks with retrogression features like pinitised cordierite or chloritised biotite are common in the BW. Moreover, hydrous

alteration features (e.g. pinitisation) are also known from the Donaurandbruch, a fault zone of brittle to ductile deformation (Schreyer, 2002 personal communication).

2.3 Samples

Six of the investigated samples come from the SW (Al-20, Ho-10, Ho12, To-2, Wa-4, We9) and three from the BW (Bw-3, Bw-8, Bw-29). The exact sample locations can be depicted from Fig. 2.2 and Fig. 2.3. All samples investigated here are cordierite-bearing migmatites of metapelitic bulk compositions. All investigated rocks bear quartz, plagioclase, biotite and K-feldspar. Garnet, sillimanite and ilmenite may also be present (Chapter 4, Table 4.2). All samples have in common that primary muscovite does not occur. Hence all samples had similar starting conditions in terms of phase assemblage, bulk compositions and final prograde metamorphic evolution before they underwent pinitisation. In addition, the compositions of primary cordierite are similar. All investigated cordierite grains are fairly homogenous. Mean X_{Mg} values range from 0.42 to 0.58. Mean Na contents scatter between 0.03 and 0.07 cations per formula unit (c.p.f.u.) and Mn contents are always between 0.02 - 0.04 c.p.f.u. Fourier Transformation infrared spectroscopy (FTIR) showed H₂O and CO₂ contents of cordierite from the samples of the BW of 0.38 to 0.74 and 0.04 to 0.10 wt%, respectively (Kalt, 2000). Cordierite in the samples from the SW contains 0.56 to 1.00 wt% H₂O and 0.02 to 0.06 wt% CO₂ (Kalt, unpubl. data).

The rationale behind the sample selection was twofold. The first aim was to investigate samples from different localities in order to detect regional variations in pinitisation. As bulk composition, mode and prograde metamorphic evolution for all samples are similar, pinitisation should reflect the specific retrograde and/or postmetamorphic hydrothermal history of the areas the samples come from. The second aim was to investigate samples with different degrees of retrogression/alteration in order to gain information on the process of pinitisation. The selected samples reflect various stages from beginning pinitisation to complete replacement of primary cordierite (Chapter 4, Table 4.2). The degree of pinitisation can vary to the extremes even between adjacent grains. Other retrogression features display sericite formed at the expense of plagioclase and K-feldspar, medium- to fine-grained muscovite-quartz aggregates formed at the expense of K-feldspar and chlorite formed at the expense of biotite. In analogy to pinitisation, the degree of these retrogression features is variable.

3. Analytical techniques

3.1 Transmission electron microscopy

Transmission electron microscopy (TEM) is a powerful tool for studying very fine-grained materials and very small-scaled structures as details on the unit cell level of most minerals can be imaged directly. TEM uses an accelerated electron beam that interacts with a thin sample (Fig. 3.1). Among other reactions, this produces characteristic x-rays, secondary electrons, backscattered electrons, etc. TEM images use those electrons which traverse the sample, unscattered or scattered. Analytical electron microscopy (AEM) with a TEM uses the x-rays for chemical analysis. The material investigated in this study is extremely fine-grained and beyond resolution of SEM and EM point analysis and the petrographic microscope in most cases. Clay minerals with thicknesses of a few tens of Å to some thousands of Å were studied as well as amorphous material. TEM is particularly useful for studying clay minerals, as structure, texture, size, shape and relations between individual layers and packets of layers, including mixed layering, layer stacking and structural imperfection, can be viewed and imaged directly. Moreover AEM allows chemical analysis with a spatial resolution of a few tens of Å. These features make the TEM one of the key instruments of this study. A serious problem of this study was the extreme sensitivity of the investigated material to electron beam exposure.

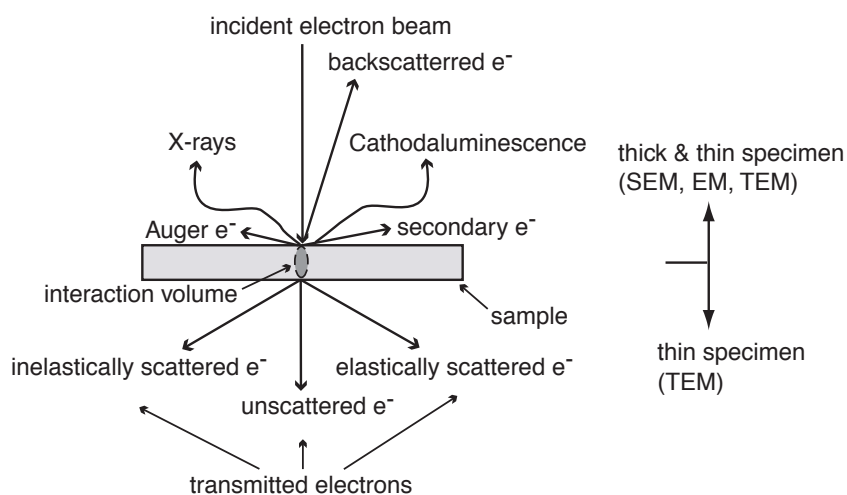


Fig. 3.1. Schematic diagram showing the interaction of an incident electron beam with a sample, modified after Buseck (1992).

Instrumentation running and samples preparation techniques for TEM used in this study see are explained in Chapter 5.

3.1.1 The electron source and the electron-optical system

The electron source (filament) is commonly a LaB₆ or W-cathode, located in a Wehnelt cap, that emits monochromatic electrons by thermionic, Schottky or field emission. The Wehnelt cylinder impedes emission from the filament except at its tip and focuses the electrons like a convergent lens. The anode, which is positively charged and placed just below the filament, accelerates the electrons and forces them to form a beam as they pass a tiny hole in the anode. The electrons are accelerated at some tens to several hundred keV. Electron-magnetic lenses are placed down a high-vacuum column to focus the electrons. The condenser lens assembly is located between the anode and the specimen and focuses the electron beam onto the specimen. The specimen itself is fixed on a movable and turnable stage. Then the electron beam passes through the specimen and is finally focused by the objective lens, some intermediates lenses and the projector lens either onto a phosphorescent screen or a photographic film to form a highly magnified image.

3.1.2 Image contrast

Formation of TEM contrast can be achieved in two different ways:

(1) Amplitude contrast. In the bright field (BF) or in the dark field (DF) modus only focused electrons are allowed to hit the fluorescent screen. Unfocussed electrons are blocked out by the objective aperture. This enhances the image contrast. In the BF modus only the primary electron beam is directed to the screen, while in the DF modus only one or a few scattered beams are used to form an image.

(2) Phase contrast. As the electrons pass the specimen they change their phase in relation to the mass of the atoms they interact with. When the electrons are re-combined for image formation, interference between the primary and scattered electrons occurs. This also results in enhancement of the image contrast as electrons which are out of phase compensate or weaken each other and electrons which are in phase produce resultant waves with higher amplitudes.

3.1.3 Resolution and lens aberrations

High spatial resolution is one of the major advantages of TEM. Most useful is point to point resolution, which is the ability to optically separate two objects in the process of reproducing the structure of the sample in the direction of the incident electron beam. The resolution **R** of light microscopes is described by the expression

$$R = \lambda / 2 NA,$$

where λ is the wavelength and NA the numerical aperture of the objective lens. From the equation for the resolution r of TEM at bright-field point-to-point imaging

$$r = 0.67 \lambda^{3/4} C_s^{1/4},$$

where λ is the electron wavelength and C_s the coefficient of spherical aberration, it is evident that the limiting factor of TEM resolution is the lens aberration, which allows only for a much poorer resolution than implied by the short wavelength of electrons. Therefore, the basic drawback of TEM is that magnetic fields can not be manipulated, shaped and grouped the way optical glass lenses are to manipulate visible light.

3.1.4 Electron diffraction

Electron diffraction patterns are used to specify lattice parameters and polytypes; they can provide key information on orientation relationships, the nature of defects in solids and on order-disorder effects. In a first approximation, the principles of electron diffraction are identical to those of x-ray diffraction. The geometry of x-ray and electron diffraction follows the Bragg equation

$$n\lambda = 2d \sin \Theta$$

and the Ewald sphere (Fig. 3.2). The Ewald sphere describes the geometry of diffraction in the reciprocal space. It is constructed in the way that reciprocal vectors coincide with directions of normals to the real space planes. There are prominent differences between diffraction of electrons and x-rays. Electrons interact with the electron sphere and the nuclei of atoms and electron diffraction is by a factor of 10^2 to 10^3 stronger than the interaction of x-rays with atoms, which is restricted to the electron cloud. In consequence, electrons can be focused into a narrow and highly intense beam and can be used to produce an image, which is not possible with x-rays.

Electrons accelerated by some hundred keV have much shorter wavelengths than x-rays, e.g. $\lambda = 2.5 \times 10^{-3}$ nm for 200 KeV electrons and $\lambda = 1.54 \times 10^{-1}$ nm for $\text{CuK}\alpha$ radiation. It follows that the Bragg angles are much smaller for electrons than for x-rays, which allows simplification of the Bragg equation to

$$\lambda = 2d \Theta,$$

and that the Ewald sphere is far larger for electrons than for x-rays (Fig. 3.2). In consequence, with a TEM, many diffraction spots can be viewed without any motion of the detector as the image is tangent over a relatively large region in reciprocal space (Fig. 3.2). In contrast, x-rays require complex motions of the camera to maintain the film tangent to the x-ray sphere of reflection.

Another consequence of the strong interaction of electrons with atoms is multiple scattering. Multiple scattering diffraction is characteristic for TEM, of importance for all but the thinnest specimen and also called dynamical. The kinematical theory comprises the Bragg equation and the Ewald sphere and is typically used for x-ray diffraction. It is also useful as a first approximation for describing electron diffraction, particularly the electron diffraction of very thin

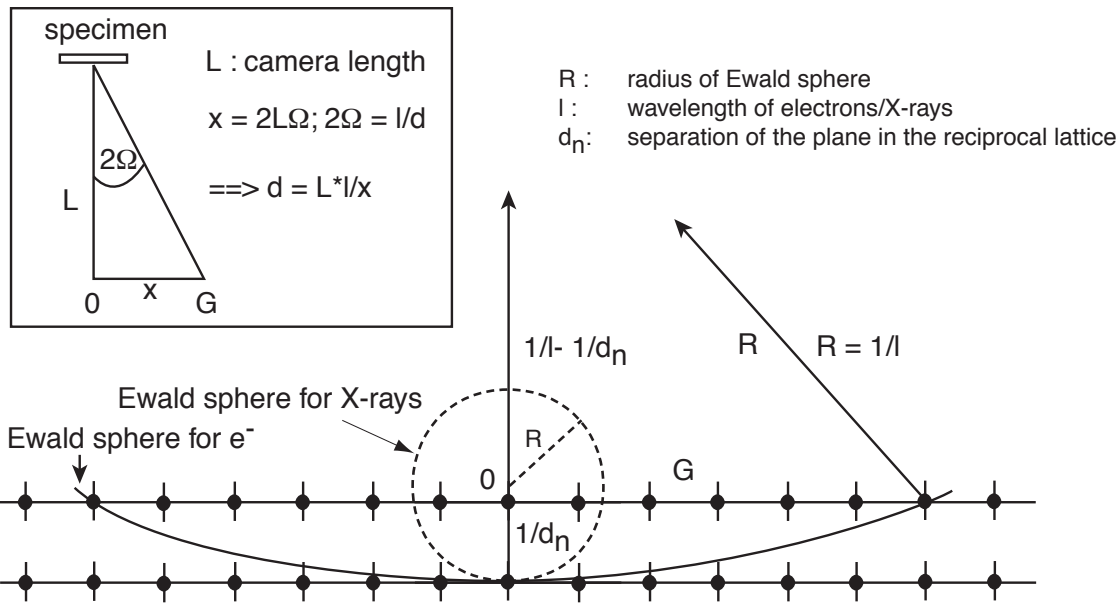


Fig. 3.2. Schematic diagram of the Ewald sphere of radius $R = 1/\lambda$, modified after Steeds & Morniroli (1992). The short wavelengths of electrons cause the Ewald sphere to intersect many reciprocal-lattice points (spots with lines) simultaneously at one given orientation. The lines in the centre of the spots represent the excitation error. Due to the strong interaction of electrons the spots need not exactly intersect the Ewald sphere to generate a reflection. In contrast, the Ewald sphere for x-rays (dashed circle) is much smaller. Therefore, x-ray diffraction requires complex motions of the camera to maintain the film tangent to the x-ray sphere of reflection. The inset illustrates the relationship between distance x of a diffracted beam (G) from the direct beam (0) and the camera length.

specimen. Multiple scattering produces intensities and reflections which can not be explained by the kinematical theory and which are difficult to interpret, e.g. reflections forbidden by the kinematical theory may be produced by dynamical effects or scattered beams may have the same intensity as the incident beam. For calculation of intensities of dynamically diffracted beams, in addition to the structure factor and the atomic factor, the thickness of the crystal, the effective excitation error and the extinction path have to be considered:

$$I_g = \pi^2 / \xi_g^2 \sin^2(\pi t s_{\text{eff}}) / (\pi s_{\text{eff}})^2$$

I_g : intensity of scattered beam

ξ_g : extinction path; $\xi_g = \pi V_c \cos \nu / \lambda F_{\text{unit-cell}}$ with $V_c =$ Volume of the unit cell and

$F_{\text{unit-cell}}$ = amplitude of the unit cell

t : thickness

s_{eff} : effective excitation error; $s_{\text{eff}} = (s^2 + 1/\xi_g^2)^{1/2}$

The electron diffraction pattern is formed in the back focal plane of the objective lens. To project it onto the fluorescent screen, the projector lens has to be focused onto the back focal plane of the objective lens. Regions are selected for electron diffraction by inserting the selected area aperture, which is located below the objective lens and the objective aperture, into the electron

stream. The resulting diffraction images are called selected area electron diffraction (SAED) pattern.

3.1.5 Analytical electron microscopy

AEM allows chemical analysis with accuracies close to those of EM analyses, but with a much higher spatial resolution of up to a few hundred Å. AEM uses energy-dispersive detectors (EDS), that detect characteristic x-ray spectra resulting from inelastic scattering (inner sphere ionisation) of the incident electron beam by the specimen (Fig. 3.1). The EDS technique collects all x-ray photon energies simultaneously. A relatively poor spectral resolution resulting in overlap and interference of peaks is the limiting factor of EDS sensitivity. Usually, the detection limit for AEM is around 0.1 wt% for elements with $Z > 10$, but is much higher for elements with $Z < 10$ and depends strongly on the composition and structure of the matrix.

Quantification of x-rays grounds on the equation of Castaing (1951):

$$C_i / C_{(i)} = K I_i / I_{(i)},$$

where C_i is the concentration of an element in the specimen, $C_{(i)}$ the concentration of an element in a standard, K a sensitivity factor, I_i the measured intensity emerging from the specimen and $I_{(i)}$ the measured intensity from the standard. Three components contribute to the sensitivity factor K , the atomic number (Z), the absorption of x-ray within the specimen (A) and the fluorescence of x-rays within the specimen (F). K factors vary with the x-ray detector, the microscope and the microanalysis conditions. They are hence sensitivity factors and not element specific constants. Consequently, K is most accurately determined experimentally by using standards. Theoretical K values have also been calculated by several workers and TEM manufacturers.

Several effects, which are related to the sample compositions and therefore are called 'matrix effects', have an influence on the x-ray spectrum. Corrections of these matrix effects have to be carried out in order to perform accurate analysis. In reference to the three major components atomic number (Z), absorption (A) and fluorescence (F) these matrix corrections are called ZAF corrections. Several workers have developed routines to correct for the ZAF effects (e.g. Pouchou & Pichoir, 1985). With a TEM, thin electron-transparent specimen are investigated. As a consequence, the ZAF correction is in a first approximation mainly a Z correction in TEM-EDS analysis.

3.1.6 Sample preparation and beam damage

Sample preparation is a critical part of electron transmission microscopy. There is only little tolerance in crystal thickness as the specimen must be transparent for electrons. In addition, optimum high-resolution imaging requires multiple scattering to be minimised. As electrons interact strongly with the specimen, sample thickness must be less than ~10 nm.

TEM samples can be made from petrographic thin section prepared with a removable adhesive. By microdrilling, areas of interest can be cut and placed onto a small metal plate. These slices, which usually have diameters of a ~ 3 mm and are thinned to perforation by bombardment with ions or atoms typically at an angle of $10^\circ - 17^\circ$ and for 5 to 24 hours in a mil. Finally, they may be coated with carbon.

Beam damage is a serious problem in TEM. Several techniques have been developed to avoid or reduce beam damage. Beam damage may arise directly from the electrons which travel close to the speed of light when hitting the sample. 'Knock-on damage' is the direct displacement of atoms from the crystal lattice that creates point defects within the specimen. It is called 'sputtering' if it occurs at the specimen surface. Temperature rise in TEM high vacuum may induce alkali migration or dehydration of hydrous material. Clay minerals, which were mainly investigated by TEM in this study, are particularly sensitive to beam damage. Chemical diffusion and dehydration may result in structural damage of clay minerals, and collapse of expandable clay mineral layers as a result of dehydration usually occurs. Mottled contrast caused by heterogeneity induced by diffusion of cations and/or dehydration is typical for regions which are affected by beam damage. Much work has focused on finding a method to preserve expandable layers of clay minerals expanded in the TEM high vacuum (e.g. Vali & Hesse, 1990; Kim *et al.*, 1995), e.g. treatment of clay separates with long organic molecules (n-alkylammonium) embedded in Spur resin (e.g. Vali & Hesse, 1990). The drawback of most of these methods is that the original textures are destroyed as they can only be used on clay separates and that most of these techniques require extensive treatment of the samples. Viewing with the weakest beam possible that still allows images to be seen and focusing in structurally contiguous areas are still the key techniques for imaging clay minerals in their textural context and avoiding beam damage at the same time.

References

- Buseck, P.R. (Ed) (1992). *Minerals and reactions on the atomic scale: Transmission electron microscopy: Reviews in Mineralogy*, **27**, Mineralogical Society of America, Washington D.C., 516 pp.
- Williams D.B. & Carter, C.B. (1996). *Transmission electron microscopy: a textbook for material science*. Plenum Press, New York, 729 pp.

3.2 Electron microprobe

The electron microprobe (EM) is an instrument for non-destructive chemical analysis of solid-state materials at the μm scale. In analogy to TEM, the electron-optical system of the EM generates a focused electron beam, which in this case has a minimum spot size of $\sim 1 \mu\text{m}$ and is typically accelerated by 15 - 20 keV. In consequence, small compositional variations within and

between individual mineral grains with a spatial resolution of a few microns or less can be detected. EM deals with analysis of relatively thick specimen. Therefore, the interaction volume is much larger than with TEM and EM in general deals with the effects of electron interaction noted on the top side of Fig. 3.1. Therefore, contrary to AEM, the ZAF correction cannot be reduced to Z corrections. Another difference to AEM is the additional use of wavelength dispersive spectrometers (WDS). This technique allows a much higher spectral resolution than the EDS technique and significantly lowers detection limits to about 0.01 - 0.1 wt%. Quantitative analysis of elements with $Z = 11$ (Na) to $Z = 92$ (U) is routine in EM investigations. In this study, the chemical characterisation by EM was one of the key criteria to establish the pinite classification presented Chapter 4. The instrumentation and exact conditions of EM investigations of this study are given there. In analogy to TEM, the extreme sensitivity of the investigated material to electron beam exposure was a major problem. In consequence, EM standard conditions (increase of the beam size to 8 - 15 μm) were modified to enable analysis accurate as possible, for further explanation see Chapter 4.

3.2.1 The electron source and the electron-optical system

In principle, the electron-optical system of EM is similar to those of TEMs and consists of an electron gun, a high vacuum electron column with a system of electron-magnetic lenses and apertures and the spectrometer assembly (Fig. 3.3), but there are also some differences. The

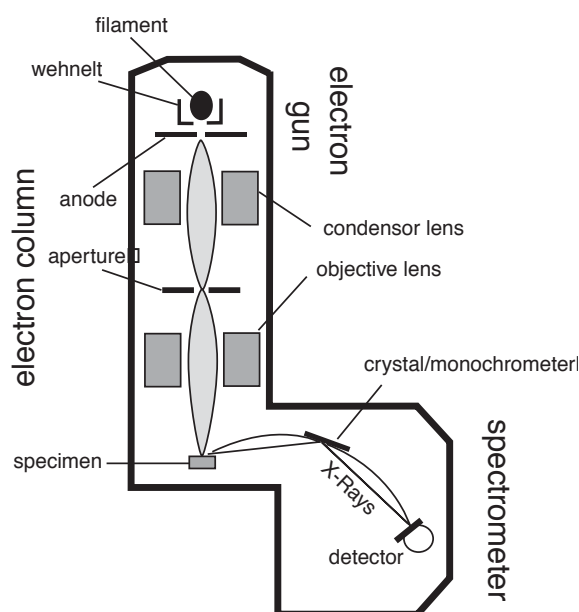


Fig. 3.3. Schematic diagram showing the electron-optical system of an EM, modified after Potts *et al.* (1995).

accelerating voltage (15 - 20 keV) is one magnitude of order smaller than for TEM, the objective lens is placed before the specimen and focuses the beam onto the specimen and controls its final

size and position. In the WDS mode the electron beam is deflected by a crystal (monochromator) before it is collected by the detector (Fig. 3.3).

Electrons are produced by thermionic emission of a filament, which usually is a tungsten wire cathode. As in TEM, the cathode is heated until the emission current and the sample current reach the edge of a saturation plateau. The stability, alignment and shape of the electron beam is of major importance for quality of EM analysis. One of the major sources of beam instability is movement or displacement of the filament tip. Therefore, the position of the filament relative to the anode and column beneath it has to be controlled (alignment of the electron gun). A further source of error are variations in the emission from the filament, e.g. a W filament can vary up to 1% within a period of time of 10 minutes. This is compensated by the beam regulator, an additional lens and aperture system located between the condensor and the objective lenses. The stigmators, a set of 8 additional radially oriented lenses, are housed inside of the objective lens and control the final beam shape and correct especially for astigmatism.

3.2.2 Electron microprobe analysis

The electron beam is used to bombard the sample and to produce x-rays from a very small volume (about 4 to 9 μm^3). When the electrons enter the sample, they interact with the atoms in the interaction volume and cause x-rays by ionisation in the inner electron sphere. Each element present in the sample produces x-rays with characteristic energies. These x-rays can then be analysed by WDS or EDS.

The WDS assembly consists of a monochromator and a detector (Fig. 3.3). The monochromator is a crystal which disperses x-rays by Bragg reflection. The angle formed by the three components x-ray source, monochromator and detector is changed by repositioning the monochromator and the detector in order to collect x-ray of different wavelength. Most electron microprobes are equipped with several crystals of differing *d*-spacing to allow analysis of a wider range of x-ray wavelengths. The most common crystals are lithium fluoride (LIF), pentaerythritol (PET) and thallium acid phthalate (TAP). This technique allows a high spectral resolution with detection limits in the order of 100 ppm. The chemical composition of the area excited by electron beam is determined by counting the x-rays generated by each element in the area and comparing that number to the number of x-ray generated by a standard of known composition (see above, 'TEM').

The EDS assembly consists of a solid-state detector which, in contrast to the WDS technique, collects all x-ray photon energies simultaneously. In case of some applications, e.g. compositional mapping, this is advantageous as mapping with the WDS method would require much more time. The primary disadvantage of EDS is the poorer spectral resolution, which results in a significantly higher detection limit in the range of 1000 ppm.

3.2.3 Destruction of material

Although in general electron microprobe analysis is described as a non-destructive method, this holds only partly true. Compared to TEM, the EM electrons have a much lower kinematic energy. Consequently, 'knock-on damage' and 'sputtering' are only minor problems. But temperature in combination with the high vacuum EM environment give rise to dehydration and migration of certain chemical species. Diffusion of loosely bond network-modifying chemical species, e.g. alkalis in clay minerals and zeolites, away from the beam is a well-known phenomenon. As a consequence the counting rates of alkalis fall and those of non-migrating chemical species, e.g. Si, rise. Highly hydrous materials of poor crystallinity may even be destroyed structurally. Here, dehydration may result in shrinkage, leaving less and less material in the excited areas. Consequently, even the counting rates of network-forming species, e.g. Si and Al, may decrease significantly. This phenomenon was also a serious problem in this study (Fig. 4.1). To achieve as constant counting rates as possible the spot size, the sample current and the acceleration voltage have to be optimised to the material of interest. This was also done in this study as highly hydrous materials extremely sensitive to the electron beam were investigated.

3.2.4 Sample preparation

Specimens for EM analysis have to be highly polished, otherwise x-ray quantitative analysis will not be possible, and artefacts may be introduced into x-ray maps and electron images. Finally, specimen must be coated with carbon.

References

Potts P.J., Bowles J.F.W., Reed, S.J.B. & Cave M.R. (1995). *Microprobe Techniques in the Earth Sciences*. Chapman & Hall, 419 pp.

3.3 Scanning electron microscope

The scanning electron microscope (SEM) is used for imaging and chemical analysis of thick specimen. An electron-optical system generates a focused electron beam and the SEM deals especially with backscattered and secondary electrons, which provide useful information of the specimen surface. The electron-optical system is similar to that of the EM and produces a highly magnified image or rather an electronic map of the specimen. As a main difference, the beam is rastered (scanned) across the sample by varying the current through the two sets of scanning coils. The objective lens focuses the scanning beam onto the area of interest and the secondary/backscattered electrons or x-rays are detected. The beam dwells for a few

microseconds at one point and before it moves to the next, the detector counts the number of reactions and displays a pixel on a cathode ray tube (CRT). The intensity of the point is determined by this number: the more reactions the brighter the pixel. The acceleration voltage is typically in the range of 15 - 20 KeV and the maximum resolution of an SEM is in the range of a few microns.

The SEM is especially useful for electronic mapping of polished specimen. This technique helped significantly to develop the below presented pinite classification (see Chapter 4) and provided also key information for the models genesis of pinite genesis. The instrumental specifications relevant for this study are given in Chapter 4 'EM, SEM & Petrographic Microscopy'.

3.3.1 Secondary electrons

The production of secondary electrons is strongly related to the topography of the sample. If the incident electrons pass close to atoms of the specimen very low energy electrons (5 eV) may be ionised from the electron shell of these atoms, these are called secondary electrons. Due to their low energy, only secondary electrons near the surface (<10 nm, Fig. 3.4) can exit the sample and be examined. Any changes in topography in the sample that are larger than the sampling depth will change the number of electrons collected in the detector due to variations in the collection efficiency. Therefore, secondary electrons are suited to image the specimens topography.

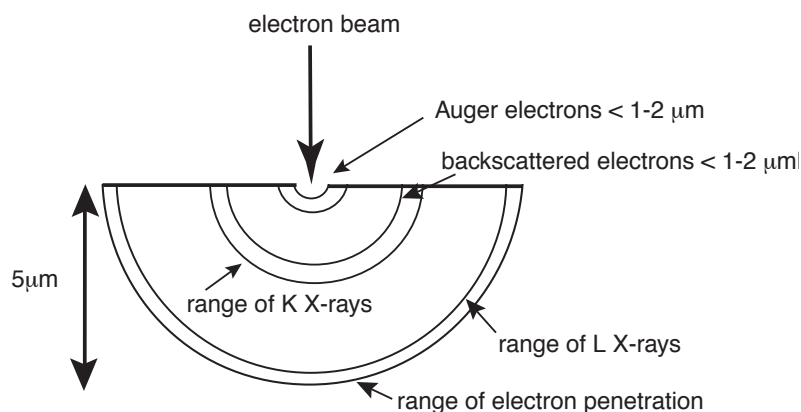


Fig. 3.4. Schematic diagram showing the specimen volume that interacts with an electron beam of 20 kV acceleration voltage, modified after Potts *et al.* (1995). This depth depends on the atomic number of the material, the accelerating voltage and the angle of incidence for the electron beam. K and L reference x-rays produced from different shells in the electron cloud of the atoms examined by electron diffraction.

3.3.2 Backscattered electrons

If the incident beam collides with an atom in the specimen, which is about normal to the path of the incident electron, electrons are scattered backwards in the opposite direction (Fig. 3.4). The

number of backscattered electrons per unit time depends strongly on the atomic number Z of the element they interact with. In SEM images regions with higher Z atoms usually appear brighter than regions with lower Z atoms. Therefore, backscattered electrons are suited to produce electronic maps showing compositional variations of the average atomic number of the specimen.

References

Potts P.J., Bowles J.F.W., Reed, S.J.B. & Cave M.R. (1995). *Microprobe Techniques in the Earth Sciences*. Chapman & Hall, 419 pp.

3.4 X-ray diffraction

X-ray diffraction is used for identification of mineral phases by their structures. It includes various techniques, e.g. the Laue method for determining large single crystals or the powder

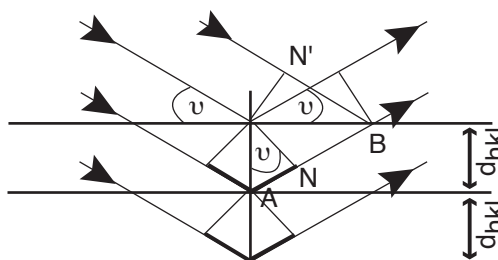


Fig. 3.5. Schematic diagram showing the geometry of Bragg reflection in real space, modified after Kleber *et al.* (1990). Reflections can only be produced if the extra distance $2xAN$ (thick line), which has to be travelled by a beam reflected at the next lower plane, is an integral multiple of the wavelength. If this is given, the recombined beams are in phase after reflection and this is expressed by the Bragg equation. The angle ν is the half angle of diffraction of the incident beam, d_{hkl} is the distance between adjacent planes. The distance BN is equal to the distance BN' .

method for investigating powdered samples with hundreds to thousands of randomly oriented crystals. The powder method uses monochromatic x-rays, e.g. Cu K_α radiation, to irradiate the sample. The random orientation ensures that some of the investigated crystallites are always in the appropriate orientation to produce reflections, which is described by the Bragg equation (Fig. 3.5).

$$n\lambda = 2d_{hkl} \sin \Theta,$$

where n is a whole number, λ the wavelength, d_{hkl} the distance of the (hkl) plane and Θ the half angle between the incident and the diffracted x-ray beam. Additional rotation of the sample ensures that planes of different hkl pass the appropriate orientation to produce reflections. The

powder method was applied in this study as it allows phase identification of a bulk sample with a detection limit of approximately 5 wt%. The oriented powder method (see below) is especially useful for identification of clay minerals and mixed layers, therefore it was also used in this study. The instrumental specifications and conditions of XRD analysis are given in Chapter 5.

3.4.1 Oriented powdered samples

X-ray diffraction using powdered, oriented specimen is particularly useful for studying phyllosilicates. The latter are forced to settle onto a glass plate with their 001 planes oriented parallel to the surface by a pipette method. This is especially useful to investigate d_{001} of phyllosilicates. Due to the fact that many phyllosilicates have similar d_{001} values, but behave differently upon heating or treatment with organic molecules (e.g. glycol), the samples are heated or saturated with organic liquids before they are examined by x-ray diffraction. Expansion of expandable layers by saturation with these organic liquids and differences in stability upon heating allows identification even of mixed-layers (interstratification of phyllosilicates with different d_{001}), which are common in low-grade metamorphic environments. Investigation of oriented specimen was also carried out in this study.

3.4.2 Intensity of a reflection

The intensity of a reflection is positively correlated to the second of the structure factor

$$I_{hkl} \sim |F_{hkl}|^2.$$

The structure factor is given by the equation

$$F_{hkl} = \sum_j f_j e^{2\pi i(-hx-ky-lz)} = |F_{hkl}| e^{-2\pi i\alpha},$$

where (x, y, z) refer to the position of element j in the unit cell, (hkl) to a specific atomic layer (plane) in the crystal and f_j is the atomic factor of the element j . If $F_{hkl} = 0$, the reflection does not occur. It follows from the symmetry of unit-cells that certain reflections are always forbidden, e.g. diffractions from body-centred cubic packing planes where $h + k + l$ is odd are always of zero intensity. In contrast to x-ray diffraction, these reflections may occur in electron diffraction due to dynamical effects.

References

- Kleber, Kleber, I., Bausch, H.-J. & Bohn, J. (1990). *Einführung in die Kristallographie*. Berlin : Verlag Technik GmbH, 416 pp.
 Moore, D.M. & Reynolds, R.C. Jr (1997). *X-ray Diffraction and the Identification and Analysis of Clay Minerals*. Oxford : Oxford University Press, 378 pp.

3.5 Fourier-Transform infrared spectroscopy (FTIR)

FTIR uses changes of the dipole moment of chemical bonds as these interact with infrared light (IR). The frequencies of molecule vibrations coincide with IR wavelengths. Therefore, absorption of characteristic IR wavelengths occurs in these molecules and can be used to identify and quantify chemical-structural fragments (functional groups) in minerals. In principle, IR spectra are collected by measuring the intensity I_0 of the incident IR beam and comparing it with the intensity I of the beam transmitted/reflected by the sample. Quantification of IR spectra follows the Lambert-Beer equation

$$E = \epsilon cd,$$

where E is the linear extinction, ϵ is a linear extinction coefficient, d the thickness of the specimen and c the concentration of a specific chemical fragment in mol^{-1} .

In this study, *in situ* FTIR on 200 μm thick sections was carried out to determine the H_2O and CO_2 contents in the channels of cordierite. *In situ* FTIR allows determination of compositional variations within and between grains in the textural context. The aim was especially to detect potential late stage modifications of the channel compositions of cordierite, because this may provide information on the mechanism of pinitisation and on the possible role of the structural channels in the processes of pinitisation. The instrumentation and conditions of FTIR measurements of this study are given in Chapter 6.

3.5.1 Theory

IR light covers the electromagnetic spectrum between 0.78 and 1000 μm . Usually, the wavelength is measured in ‘wavenumbers’, which have units of cm^{-1} .

$$\text{wavenumber} = 1 / \text{wavelength in cm}$$

The infrared region is divided into three regions for *near*, *mid* and *far* infrared. The IR wavenumbers most useful for FTIR lie between 4000 - 670 cm^{-1} .

Region	Wavelength range (μm)	Wavenumber range (cm^{-1})
Near	0.78 - 2.5	12800 - 4000
Middle	2.5 - 50	4000 - 200
Far	50 - 1000	200 - 10

In contrast to light and x-rays, IR does not have enough energy to induce ionisation in the electron sphere of atoms. Therefore, absorption of IR is restricted to processes which require much smaller amounts of energy, namely vibrations within a molecule. Absorption of IR by a molecule is only possible if the vibrations and rotations induce a net change in the dipole moment. A dipole occurs when there is a difference of charge across a bond in a molecule. The dipole moment will change, if the two oppositely charged atoms get closer or further apart as their bond bends or stretches. Light is composed of an oscillating electrical field and an oscillating magnetic field. The electric and magnetic waves are perpendicular to each other and both are perpendicular to the propagation direction of light. It is the alternating electrical field that interacts with fluctuations in the dipole moments of molecules. In case that the wavelength of the electrical wave matches the vibrational frequency of the molecule, the latter will absorb the energy, which causes a change in the amplitude of the molecular vibration. In other words, IR of appropriate wavenumber moves a molecule bond from one vibrational state to the next highest. Two types of molecular vibrations are distinguished, stretching and bending. Stretching changes the distance between atoms along the bond axis, and upon bending the angle between two atomic bonds is changed.

Chemical structural fragments within molecules, known as functional groups, tend to absorb infrared radiation of the same wavenumber range regardless of the structure of the surrounding molecule. This is what makes infrared spectroscopy a useful tool for chemical analyses. Calibration curves even allow for quantification. It should be noted that the exact absorption wavenumber of a specific molecule or structural fragment does vary slightly with their position in the sample and with neighbouring molecules. As a consequence, even differently positioned molecules of the same species can be distinguished. This was used in several studies and also in this study to distinguish different orientations of H₂O molecules in the structural channels of cordierite (see Chapter 6). An IR spectrum is generally displayed as a plot of the energy of the infrared radiation (wavenumbers with unit cm⁻¹) versus the percent of light transmitted (absorption units).

3.5.2 FTIR spectrometer

An FTIR spectrometer consists of an IR source, an interferometer, a beamsplitter, a stationary and a moveable mirror and a detector (Fig. 3.6) The source generates the IR waves of interest. All the source energy is sent through the interferometer and onto the sample. The light passes the beamsplitter, which separates the incident beam in two directions at right angles (Fig. 3.6).

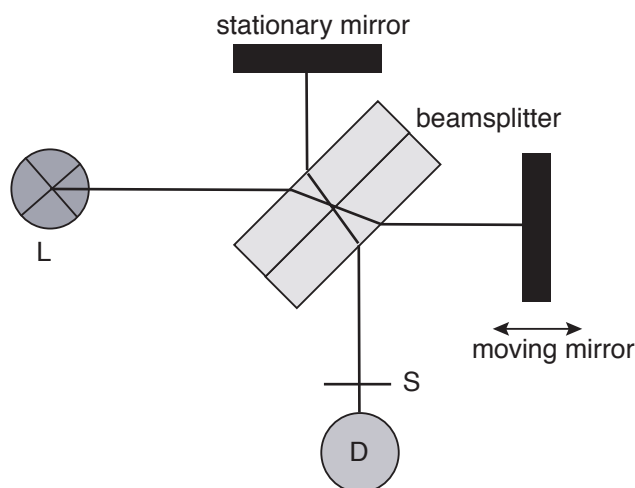


Fig. 3.6. Schematic diagram showing an FTIR instrument, modified after Amthauer & Pavicevic (Eds.) (2001). L ist the light source, D the detector and S the sample.

One beam goes to the stationary mirror and then back to the beamsplitter. The other goes to the moving mirror. The motion of the mirror makes the total path length variable compared to that taken by the stationary-mirror beam. Upon meeting again at the beamsplitter, both beams recombine and the difference in path lengths induced by the moving mirror creates constructive and destructive interference: an interferogram. Now the recombined beam passes through the sample which absorbs all the different wavelengths characteristic of its spectrum and consequently subtracts specific wavelengths from the interferogram. Finally, the beam goes to the detector, which reports variation in energy versus time for all wavelengths simultaneously. A mathematical function called a Fourier transform converts the initial intensity vs. time spectrum into an intensity vs. frequency spectrum.

References

Amthauer; G. & Pavicevic, M.K. (Eds.) (2001). *Physikalisch-chemische Untersuchungsmethoden in den Geowissenschaften*. E. Schweizerbartsche Verlagsbuchhandlung (Nägele u. Obermiller), Stuttgart, 262 pp.

4. EM, SEM and Petrographic Microscopy: Petrography, Classification and Chemical Characterisation of Retrograde Cordierite Breakdown Products in Gneisses and Migmatites of the Schwarzwald and the Bayerische Wald, Germany

4.1 Abstract

Retrograde breakdown products of cordierite are commonly termed pinite, but their modes, compositions and formation conditions are only poorly known. The author carried out a systematic study on pinitised cordierite from Variscan high-temperature metamorphic pelites of the Schwarzwald and the Bayerische Wald using electron microprobe and scanning electron microscope analyses. On the basis of composition, phase assemblage (as far as possible), textural position and grain size, four pinite types (b, m, f, i) were distinguished that formed by distinct allochemical processes under different pressure-temperature conditions at different times. They probably represent general features of cordierite breakdown. B-type pinite consists of muscovite and biotite, formed at 350 - 550 °C from a K⁺-bearing fluid, most likely derived from the breakdown of K-feldspar to muscovite and quartz. B-type pinitisation may be related to granite intrusion in the Carboniferous. M-type pinite encompasses chlorite-muscovite pinite and complex m-type pinite, most likely with illite, smectite and chlorite. M-type pinitisation by a K/Na-bearing hydrous fluid could be related to low-temperature meteoric alteration of granites. F-type and i-type pinite are enriched in Ca and partly contain amorphous material. They probably formed by leaching and/or precipitation/repolymerisation at very low temperatures, perhaps at surface conditions, with Permian-Mesozoic sediments as possible Ca source.

4.2 Introduction

Cordierite is a common Fe-Mg-Al framework silicate in aluminous medium- to high-grade metamorphic rocks. In contrast to other Fe-Mg silicates such as garnet and biotite, cordierite is often altered penetratively during retrogression. Its breakdown is thus a potential monitor of retrograde metamorphism, including fluid composition. For fine-grained retrograde decomposition products of natural cordierite the term pinite was introduced (Lacroix, 1962; Deer *et al.*, 1962). Pinite is in most cases of such a fine-grained nature that recognition by optical methods and electron microprobe (EM) point analysis is hampered. Consequently, the complete phase inventory of pinite is still unclear.

Breakdown products of cordierite are known from experimental studies, particularly on the stability of Mg-cordierite (e.g. Schreyer & Yoder, 1964; Seifert & Schreyer, 1970; Newton, 1972; Mirwald & Schreyer, 1977; Massonne & Schreyer, 1983). At pressures relevant for this study (< 0.6 GPa), Mg-cordierite breaks down to Al-silicate + chlorite + quartz ($P_{\text{H}_2\text{O}} = P_{\text{tot}}$; Seifert &

Table 4.1: Natural breakdown products of cordierite

Author	Locality and context	Breakdown products
Mathias (1952)	crd rock, Cape Province, Canada	brownish-yellow isotropic alteration products
Schreyer & Yoder (1961)	crd from cordierite gneiss Schwarzwald, Germany	1M muscovite + 7 Å phase (septechlorite)
Schreyer & Yoder** (1964)	experimental work lower temperature stability of Mg-cordierite	chlorite + pyrophyllite + Al ₂ SiO ₅ ; pyrophyllite + chlorite/7Å phase; montmorillonite + chlorite ± quartz
Schreyer** (1965b)	experimental work stability of Fe-cordierite	7Å phyllosilicate ± pyrophyllite ± kaolinite; chloritoid + quartz
Layman (1963)	various localities in Europe and New England	muscovite + chlorite + paragonite + quartz + 7Å phyllosilicate + hydrous iron oxides
Černý & Povondra (1967)	pegmatitic Na-Be crd, western Moravia	phlogopite; secondary Be-containing vermiculite + muscovite; sericite + chlorite ± smectite + Be-milarite + celadonite
Lal (1969)	crd-grt-ged gneisses, Fishal Lake, Canada	chlorite + andalusite ± kyanite
Černý (1970)	review of crd alteration	muscovite and/or biotite; andalusite + quartz; dioctahedral mica + chlorite; secondary vermiculite + muscovite; montmorillonite ± chlorite
Chevalier & Dejou (1972)	granitic crd from Provence cristalline, France	muscovite + chlorite with illite; vermiculite; secondary kaolinite after chlorite
Chandler (1975)	crd-sil-bt gneiss, Wollaston Lake, Canada	green and yellow pinite
Vrána (1979)	pegmatite crd, southern Bohemia, Czech Republic	Mg-containing beryl + muscovite + chlorite
Clemens & Mc-Millan (1982)	migmatitic crd from the Haut-Allier Massif, France	gels and clays (kaolinite)
Haslam (1983)	migmatitic crd from Campira Dome, Malawi	yellow isotropic alteration products + (secondary?) kaolinite
Povondra et al. (1984)	pegmatitic Na-Be-crd from Kemiö Island, Finland	paragonite + muscovite + chlorite + quartz + beryl
Schenk & Armbruster (1985)	rhyolitic crd from Torniella, Tuscany, Italy	ferric beidellite-nontronite
Schreyer et al. (1993)	pegmatitic Fe-crd (X _{Fe} ~ 0.8) from Dolni Bory, Moravia	ferrogredite + siderophyllite; septechlorite + andalusite + quartz
Abdad-Ortega & Mieto (1994)	pegmatitic crd, Sierra Albarana, Iberian Massif, Spain	14Å chlorite + 7Å berthierine

Mineral abbreviations after Kretz (1983). **Experimental study.

Schreyer, 1970) at temperatures between 520 and 600 °C. Fe-cordierite is only stable up to pressures of $\sim 0.2 - 0.35$ GPa (Richardson, 1968; Mukhopadhyay & Holdaway, 1994). The experimental low-temperature breakdown of Fe-cordierite to chloritoid + quartz is sluggish (Schreyer, 1965b; Boberski & Schreyer, 1990; Schreyer *et al.*, 1993). Schreyer *et al.* (1993) found the first field evidence that its low-temperature counterpart might not be chloritoid + quartz, but in analogy to Mg-cordierite, chlorite + andalusite + quartz and at very low temperatures a 7Å chamosite \pm kaolinite.

The natural retrograde breakdown of cordierite was treated in the course of several studies (Table 4.1). The first pinitisation model based on experimental and natural observations (Seifert & Schreyer, 1970) focused on the genesis of chlorite-muscovite pinite which was considered as the most abundant pinite type (e.g. Deer *et al.* 1992). The authors distinguished between the isochemical breakdown of cordierite below its stability conditions, followed by subsequent sericitisation by a K⁺-bearing fluid on the one hand:

(1a) cordierite \Rightarrow Al₂SiO₅ + chlorite + quartz

(1b) cordierite \Rightarrow pyrophyllite + chlorite + andalusite (at very low water pressures)

and the decomposition of cordierite within its stability field by a K⁺-bearing fluid on the other:

(2) cordierite + K⁺ + OH⁻ + H₂O \Rightarrow muscovite + chlorite.

However, the postulated first isochemical step of pinitisation (1a, b), was never described from natural samples in the context of pinitisation. Other retrograde alteration products of cordierite were reported (Table 4.1), among them manifold hydrous phyllosilicates, including clay minerals and a 7Å phyllosilicate (berthierine; e.g. Schreyer & Yoder, 1961), as well as undifferentiated isotropic to slightly birefringent alteration products (e.g. McKenzie, 1981; Mathias, 1952; Schreyer & Yoder, 1961; Chandler, 1975; Haslam, 1983; Nédélec & Paquet, 1981; Clemens & McMillan, 1982).

However, no satisfactory characterisation of the phase inventory of these pinites was given in most cases. Therefore, it is not known whether pinitisation is a general process of cordierite breakdown at specific P-T-X conditions or whether it encompasses a variety of processes taking place under fluid-controlled, open-system, locally varying conditions.

This chapter focuses on the description, classification and preliminary chemical characterisation of the cordierite breakdown products in migmatites and gneisses from the BW and the SW. We will show that the investigated pinites display systematic features of cordierite breakdown that seem to be independent of the local conditions of retrogression. This study is exclusively based on electron microprobe (EM) data, on back scattered electron (BSE) imaging with a scanning electron microscope (SEM) and on element mappings. None of these methods are suited for a complete

identification of the pinitic phase inventory, but represent only a first step towards the understanding of natural cordierite breakdown. Transmission electron microscope (TEM) and X-ray diffraction (XRD) studies are also being carried out. The results are presented in Chapter 5.

4.3 Sample selection and geological setting

The nine samples investigated were carefully selected from existing sample suites (Table 4.2) of the BW (Kalt *et al.*, 1999) and the SW (Kalt *et al.*, 2000b, Kalt, *et al.* 2000c and unpublished data). The two crystalline complexes are part of the Variscan orogenic belt in central Europe. The SW is located at the eastern flank of the Oberrheingraben while the BW forms the southwestern margin of the Bohemian Massif. Both complexes are dominated by granites and low-pressure high-temperature (LP-HT) metamorphic gneisses and migmatites.

The gneisses and migmatites of the SW investigated here equilibrated at conditions of $\approx 730 - 780$ °C / 0.40 - 0.45 GPa at approximately 330 Ma (Kalt *et al.*, 1994; Lippolt *et al.*, 1994; Kalt *et al.*, 2000a). There is textural evidence for the formation and crystallisation of partial melts during the LP-HT overprint. The migmatites from the BW underwent prograde biotite dehydration melting at peak metamorphic conditions of $\approx 800 - 850$ °C / 0.5 - 0.7 GPa in the absence of aqueous fluids (Kalt, 2000). They followed a clockwise P-T path (Kalt *et al.*, 1999). The thermal peak was dated at 326 - 323 Ma (Kalt *et al.*, 2000b).

All samples investigated here are cordierite-bearing migmatites of metapelitic bulk compositions. Besides cordierite, all rocks bear quartz, plagioclase, biotite and K-feldspar. Garnet, sillimanite and ilmenite may also be present (Table 4.2). Primary muscovite does not occur in any of the samples. Hence all samples had similar starting conditions in terms of phase assemblage, bulk compositions and final prograde metamorphic evolution before they underwent pinitisation. Also, the compositions of primary cordierite are similar. All investigated cordierite grains are fairly homogenous. Mean X_{Mg} values range from 0.42 to 0.58. Mn contents are always between 0.02 - 0.04 cations per formula unit (c.p.f.u.) and mean Na contents scatter between 0.03 - 0.07 c.p.f.u. H₂O and CO₂ contents of cordierite from the samples of the BW, measured by Fourier Transformation Infrared Spectroscopy (FTIR), are 0.38 - 0.74 and 0.04 - 0.10 wt%, respectively (Kalt, 2000). Cordierite in the samples from the SW contains 0.56 to 1.00 wt% H₂O and 0.02 - 0.06 wt% CO₂ (Kalt, unpubl. data). For cordierite composition see Tables I - 68 - 71 in the data appendix.

The rationale behind the sample selection was twofold. The first aim was to investigate samples from different localities in order to detect regional variations in pinitisation. As bulk composition, modes and prograde metamorphic evolution for all samples are similar, pinitisation should reflect

the specific retrograde and/or postmetamorphic hydrothermal history of the areas the samples come from. The second aim was to investigate samples with different degrees of retrogression/alteration in

Table 4.2: *Sample Characteristics*

Sample	provenience	primary phase assemblage	degree of pinitisation of individual crd grains	types of pinite
Al-20	Southern Schwarzwald	grt-bt-crd-qtz-pl-gr-ilm	complete	m-type ; f-type
Bw-3	Bayerischer Wald	pl-qtz-ms-crd-Kfs-sil-ilm	slight to complete	b-type; fi-type
Bw-8	Bayerischer Wald	pl-qtz-ms-crd-Kfs-sil-ilm	slight to medium	b -type; f-type; i-type
Bw-29	Bayerischer Wald	grt-pl-qtz-ms-crd-Kfs-sil-ilm	slight	b-type; f-type; i-type
Ho-10	Central Schwarzwald	crd-bt-qtz-pl-ilm-Kfs	medium to complete	b-type; m-type; i-type; f-type
Ho-12	Central Schwarzwald	crd-bt-qtz-pl-ilm-Kfs	medium to complete	b-type; m-type; i-type; f-type
To-2	Central Schwarzwald	qtz-pl-bt-crd-ilm-Kfs-gr	complete	m-type
Wa-4	Southern Schwarzwald	crd-bt-pl -Kfs-sil-ilm-qtz	medium to complete	m-type; f-type; fi-type
We-9	Southern Schwarzwald	crd-bt-pl -Kfs-sil-ilm-qtz	medium to complete	m-type; f-type

Mineral abbreviations after Kretz (1983). For pinite types see Chapter 4.5.

order to gain information on the process of pinitisation. The selected samples reflect various stages from beginning pinitisation to complete replacement of primary cordierite (Table 4.2). In some samples, even between adjacent grains, the degree of pinitisation can vary to the extremes. In addition, all samples display sericite formed at the expense of plagioclase and K-feldspar, medium to fine-grained muscovite-quartz aggregates formed at the expense of K-feldspar and chlorite

formed at the expense of biotite. As for pinitisation, the degree of these retrogression features is variable.

4.4 Analytical techniques

All analytical work was carried out at the Mineralogical Institute of Ruprecht-Karl-University in Heidelberg. The samples were investigated with a LEO 440 SEM, equipped with an Oxford semiconductor detector. The SEM was used with an accelerating voltage of 20 kV and a beam current of 0.5 - 1.8 nA. Besides BSE imaging, several energy-dispersive (EDX) element mappings were carried out with the SEM. The major element concentrations of the minerals were determined with a Camebax SX 51 microprobe using the wavelength-dispersive (WDX) spectrometric technique. For single phase analyses, the EM was run with a 15 kV accelerating voltage, a sample current of 20 nA, a beam diameter of 1 μm and natural and synthetic silicate and oxide standards. Na and K were analysed first to minimise a loss of alkalis. Matrix corrections were done by PAP (Pouchou & Pichoir, 1985). One of the samples (We-9) was mapped with the EMS using the WDX technique.

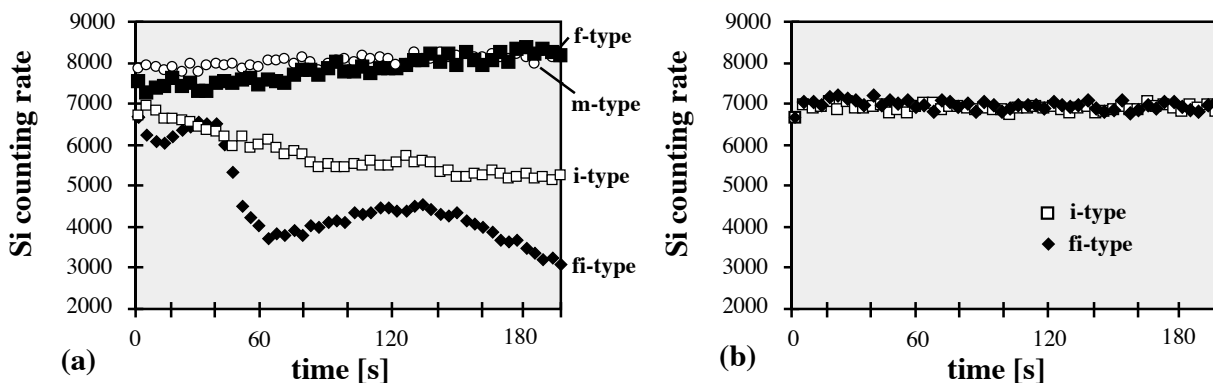


Fig. 4.1. EM counting rate tests on different pinite types. (a) with standard beam size (approximately 1 μm), 15 kV acceleration voltage and a sample current of 20 nA, (b) with 10 μm beam size, 15 kV acceleration voltage and a sample current of 20 nA.

Among the different pinite types observed in this study (b-, f-, i- and m-type pinite, see section 4.5), only b-type pinite and in cases m-type pinite were sufficiently coarse-grained to permit single phase analyses under standard conditions (see above). Hence, many of the EM analyses of m-type (and b-type) pinite represent mixtures of phases. In f and i-type pinite, single phase analyses were in general impossible. Therefore, EM analyses were performed with an extended beam diameter (8-15 μm), also because i-type and f-type pinite turned out to be sensitive to the electron beam. Besides a loss of alkalis, Al_2O_3 , SiO_2 and oxide totals varied during measurements at standard conditions (Fig.

4.1a). Therefore, counting rate tests of 200 s duration were carried out in order to find a suitable analysis mode. The most constant counting rates were obtained with a sample current of 20 nA, large beam sizes (8-15 μm) and 15 kV accelerating voltage (Fig. 4.1b). The behaviour of i- and f-type pinite under the electron beam gives clues to their crystalline state and will be discussed in the section on pinitisation processes. As phyllosilicates are major constituents of most of the pinite types, pinite analyses, including those that represent mixtures, were generally normalised to 22 oxygens for the sake of comparability.

4.5 Microscopic characterisation and BSE imaging of cordierite breakdown products

Investigations with the petrographic microscope and BSE imaging reveal that four types of cordierite breakdown products can be distinguished (Table 4.2). The different types of pinite vary systematically in terms of textural position, grain size and phase assemblage. In most of the samples, at least two pinite types are present.

4.5.1 Border-type pinite (b-type)

The term 'b-type pinite' describes unfoliated medium- to predominantly fine-grained aggregates of white muscovite and greenish biotite that have grown inwards at the primary grain boundaries of cordierite (Fig. 4.2a, b, c). Texturally, b-type pinites always represent the outermost breakdown products of cordierite (Fig. 4.2a, b, c). The degree of b-type pinitisation differs, but b-type pinite : cordierite ratios are in general comparatively low and a complete replacement of cordierite by b-type pinite was never observed.

The greenish colour of biotite within b-type pinite differs significantly from the reddish brown colour of primary biotite. The occurrence of greenish biotite is restricted to the direct surroundings of cordierite. Often, primary biotite grains in close vicinity to b-type pinite show a continuous change of colour from reddish brown to green, the latter intensifying towards the pinite. In contrast, former inclusions of primary biotite in cordierite, which are now enclosed in other pinite types (see below) still show their original reddish brown colour.

4.5.2 Fissure-type (f-type) and isotropic-type pinite (i-type)

F-type pinites form alteration veins penetrating cordierite and being filled with an extremely fine-grained material far beyond the resolution of EM single phase analyses and high-resolution BSE imaging. The veins cross sections are of a few to some tens of μm (Fig. 4.2c-k). BSE imaging, element mapping (EDX and WDX) and petrographic microscope investigations reveal

corresponding compositional and optical zoning, showing a symmetric pattern of bright to dark grey bands and corresponding isotropic and slightly birefringent bands (Fig. 4.2d-e, g-h, i). In accordance with their colouring in BSE images, bright and dark f-type pinites are distinguished. The orientation of f-type pinites seems to be controlled crystallographically, with directions parallel and perpendicular to [001]. However, it cannot be ruled out that also pre-existing fractures and fissures served as pathways for f-type pinitisation. The degree of f-type pinitisation is variable. All stages from initial to complete alteration of cordierite were observed. In all cases, contacts of f-type pinite with cordierite or m-type pinite (see below) are extraordinarily sharp (Fig. 4.2e, i). Under the microscope, most f-type pinites are yellowish to brownish. In places they can be reddish or have red patches.

Some samples show tiny domains that are as dark as or even darker than f-type pinite and fairly homogeneous in BSE images (Fig 2b, f, l-m). They are in most cases in direct contact to intact cordierite, lack optical zonation patterns, occur sporadically, are isotropic under crossed polars and are hence termed i-type (isotropic type) pinite. I-type pinite always represents the most interior pinite type at the contact with intact cordierite (Fig 2b, f, l-m). It is always penetrated by fissures. The latter are strongly suspected to represent dehydration shrinkage fissures as they do not continue into adjacent material and do not show a preferred orientation (Fig 2b f, l-m).

In samples BW-3a and Wa-4, pinites intermediate between f- and i-type pinite occur. Similar to f-type pinite, they display compositional zoning and are not penetrated by fissures. Similar to i-type pinite, they do not form veins (Fig. 4.2n) and are isotropic under crossed polars. These pinites are termed fi-type.

4.5.3 Mat-type pinite (m-type)

‘M-type pinite’ is used here as a general term for mats of very fine-grained aggregates that replace cordierite pseudomorphically (Fig. 4.2a, d-e). The degree of m-type pinitisation is variable. All stages from beginning m-type pinitisation to complete replacement of cordierite have been found. Even with adjacent cordierite grains, the degree of m-type pinitisation can vary to the extremes. M-type pinitisation is particularly intense in the samples of the southern Schwarzwald where cordierite can be completely replaced by fine-grained mats of phyllosilicates (Fig. 4.2e, g, o-p). In general, m-type pinite : cordierite ratios are the highest observed among all the pinite types.

Under the polar microscope, the interference colours of m-type pinite vary from grey to the typical first order blue of muscovite. However, their greenish or brownish colours in plain light clearly indicate that white mica can not be the only phase being present. In fact, the most prominent m-type pinites are muscovite-chlorite pinites (Fig. 4.2g, i, o-p). They occur exclusively in samples from the SW. Other m-type pinites of extremely fine grain sizes (complex m-type pinite) occur in samples from both sample sites and are suspected to contain clay minerals (Fig. 4.2f, j, o-p). A clear distinction of the two types under the polar microscope cannot be made, but chlorite-muscovite

pinites tend to be of coarser grain-size and higher birefringence. M-type pinites can display homogenous extinction, giving them a single grain-like appearance, or diffuse inhomogenous extinction. Isotropic behaviour is restricted to complex m-type pinite. Both m-type pinites may occur within one sample (Fig. 4.2j, o-p), the complex type always being the more interior pinite.

4.5.4 Samples Al-20 and To-2

Al-20 and To-2 are specific in terms of pinitisation, because cordierite is completely replaced by isotropic pseudomorphs. These pseudomorphs show a pronounced yellow colour and consist of isotropic to slightly birefringent mats of extremely fine-grained phyllosilicates. They correspond to complex m-type pinite. The pseudomorphs are penetrated by green chlorite-rich veins and flanked by chlorite-rich phyllosilicate mats that consist of chlorite-muscovite (Fig. 4.2o). M-type pinites in sample Al-20 may contain relics of strongly overprinted f-type pinite (Fig. 4.2p).

4.5.5 Textural relationship between the pinite types

Given that different combinations of pinite types can be found in the samples, the pinite types most likely formed independently. Moreover, textures do not indicate that any of the pinite types grew at the expense of another and all types of pinite have been observed in direct contact with intact cordierite. In addition, there are systematic differences in textural position, grain size, phase assemblage and composition (see subsequent section) between the four pinite types. All of these observations strongly argue for distinct and independent pinitisation processes.

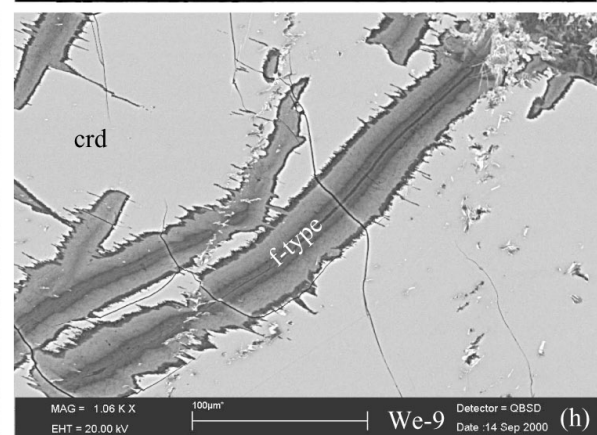
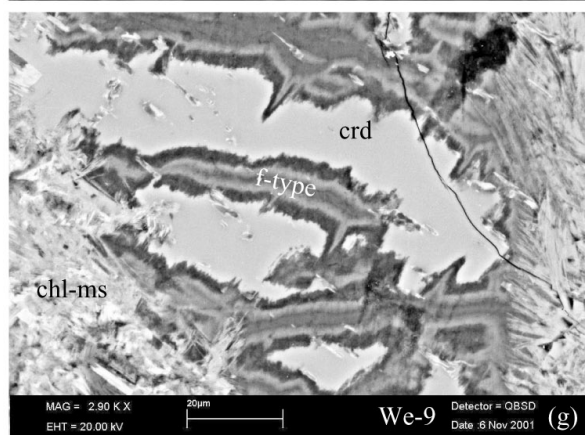
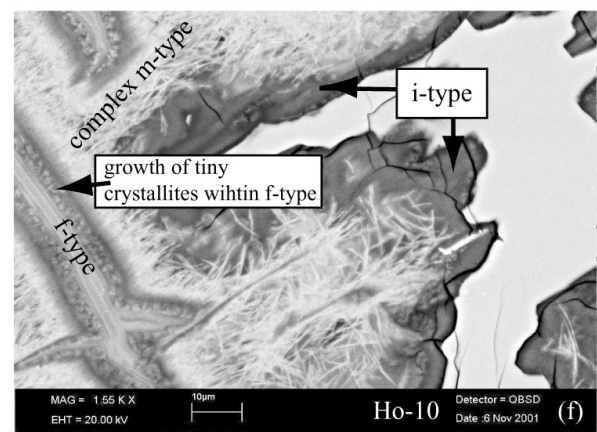
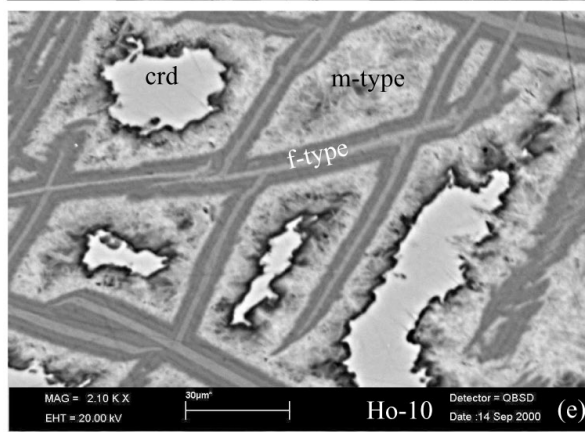
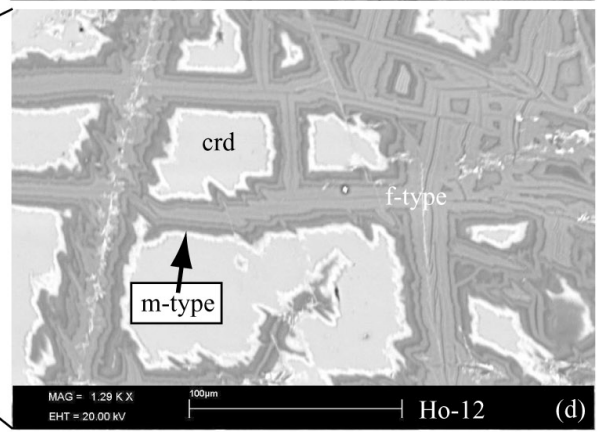
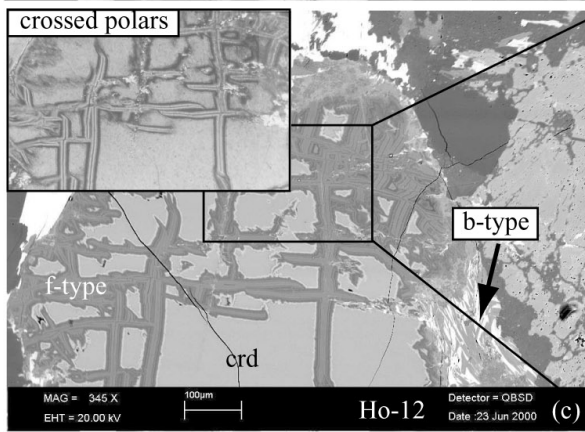
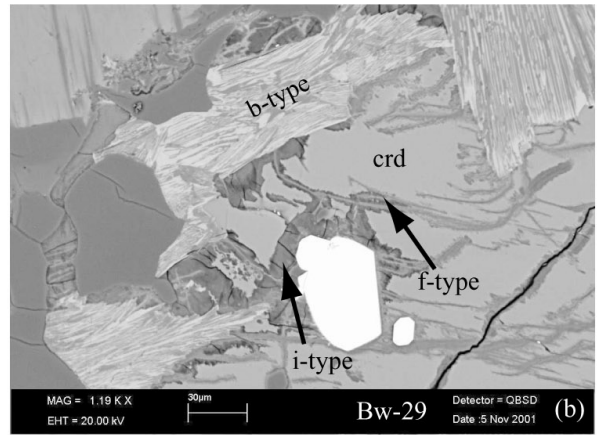
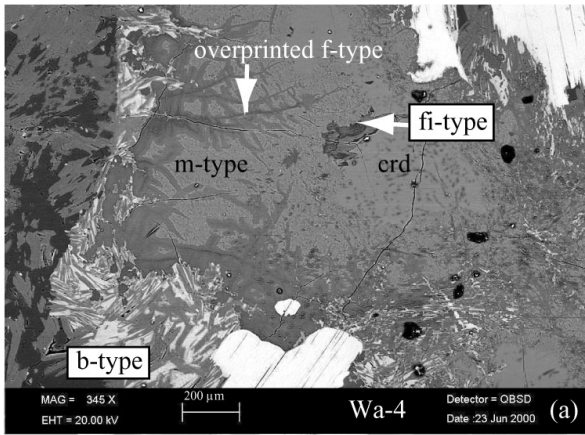
The pinitisation processes could have acted simultaneously or subsequently. Several observations suggest b-type pinite to be the earliest type. B-type pinite texturally always represents the most exterior pinite type. Primary matrix biotite in contact with b-type pinite is affected by b-type pinitisation as indicated by the continuous change in colour from reddish brown to green. The preservation of reddish brown colour in former inclusions of biotite, now embedded in f- or m-type pinite, indicates that b-type pinitisation affected only the rims of cordierite and suggests that cordierite grains were still intact. Moreover, growth of large crystals should require higher temperatures than growth of small crystals. As temperatures decreased during the retrograde evolution of the cordierite-bearing rocks of the BW and the SW, coarse-grained b-type pinite should have formed earlier than the extremely fine-grained m- and f-type pinite.

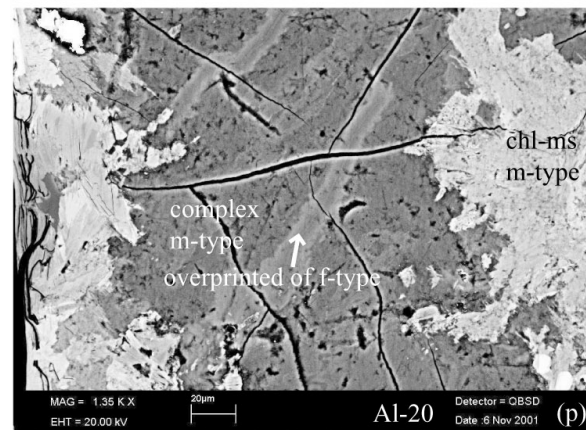
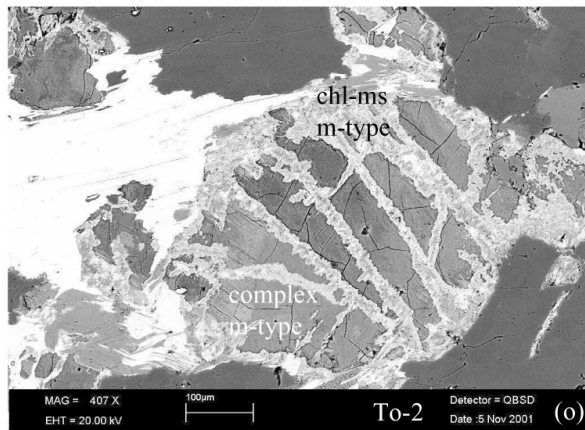
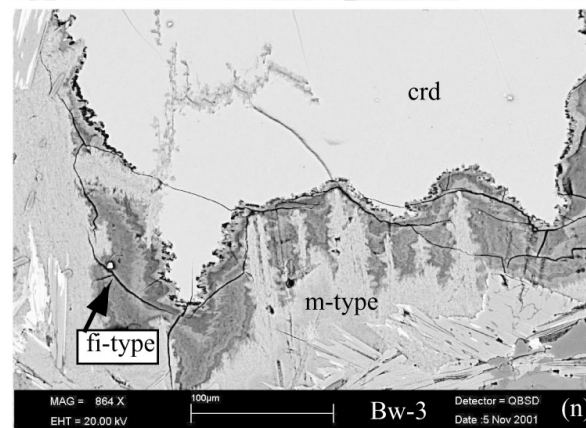
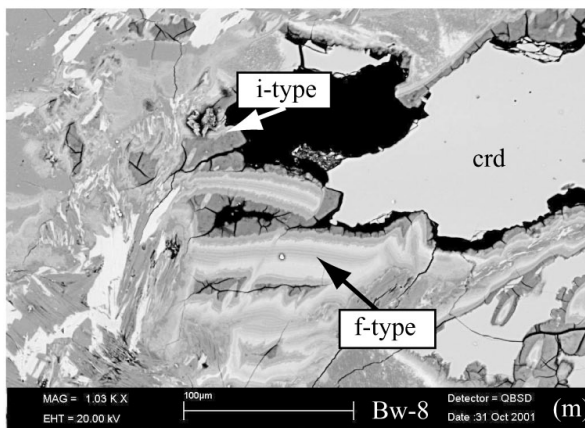
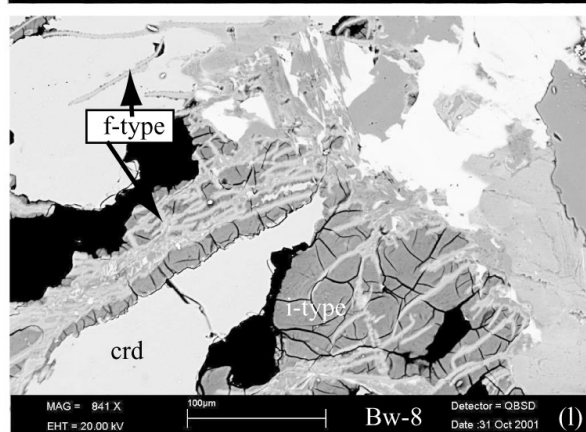
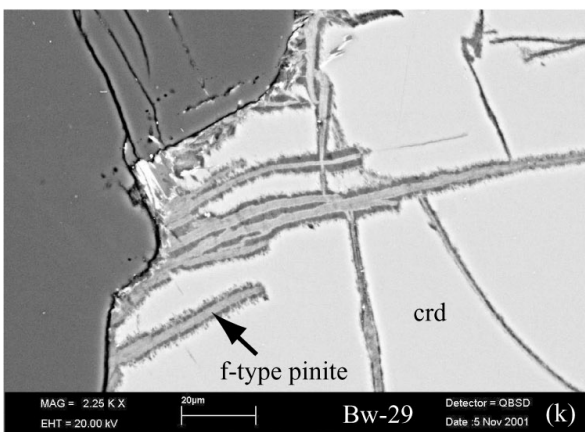
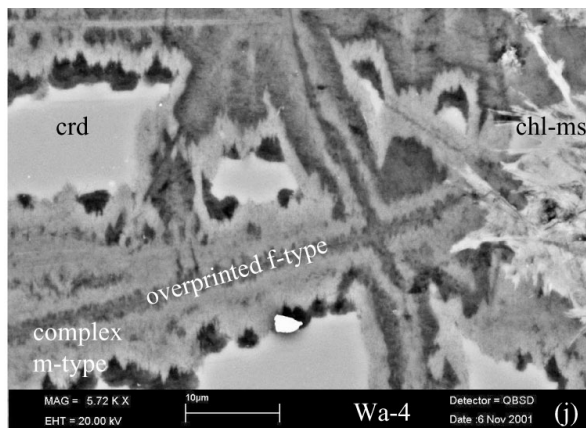
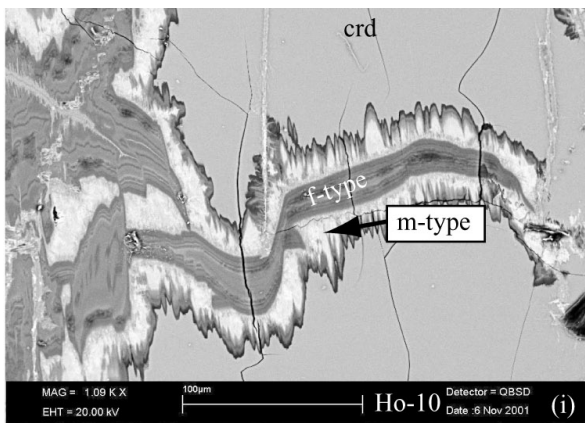
The relative chronology of f- and m-type pinitisation is ambiguous. Texturally, both types can be in contact with intact cordierite and either of them can be the more exterior pinite type, suggesting that the relative chronology of both types can vary. There are examples for f-type pinite being earlier than m-type pinite (Fig. 4.2a, d-f) and vice versa (Fig. 4.2g, j, o). Moreover, the strongly contrasting internal structures of both and the sharp contacts between them render unlikely that one is the product of secondary alteration of the other (Fig. 4.2e, g, i). Only in a few samples does the growth

of tiny crystallites within f-type pinite in the course of later m-type pinitisation (Fig. 4.2f, j) indicate a temporal sequence. These pinites were termed overprinted f-type pinite (Fig. 4.2 a, j).

I-type pinite and fi-type pinite occur exclusively in contact with intact cordierite and are always the most interior type of pinite. They should therefore represent the youngest pinitisation process.

Fig. 4.2 (pp. 45 - 46). BSE images of the different pinite types. For further information see section 4.4.1 – 4.4.6. Mineral abbreviations according to Kretz (1983).





4.6 Composition of retrograde breakdown products

The number of the relevant mineral composition tables of the data appendix are given in the headings or in the text and have the form: Table I - 'number'.

4.6.1 Primary and secondary biotite (Table I - 48 - 62)

Primary reddish brown matrix biotites are usually fairly large and homogenous, with X_{Mg} varying between 0.27 - 0.44 and Si ranging from 5.31 to 5.64 c.p.f.u. Octahedral site totals range from 5.58 to 5.51 c.p.f.u. for core compositions. Ti variations are from 0.20 to 0.75 c.p.f.u. and correlate with octahedral Al (0.71 to 1.50 c.p.f.u., Fig. 4.3a; see below). X site totals range from 1.78 to 1.92

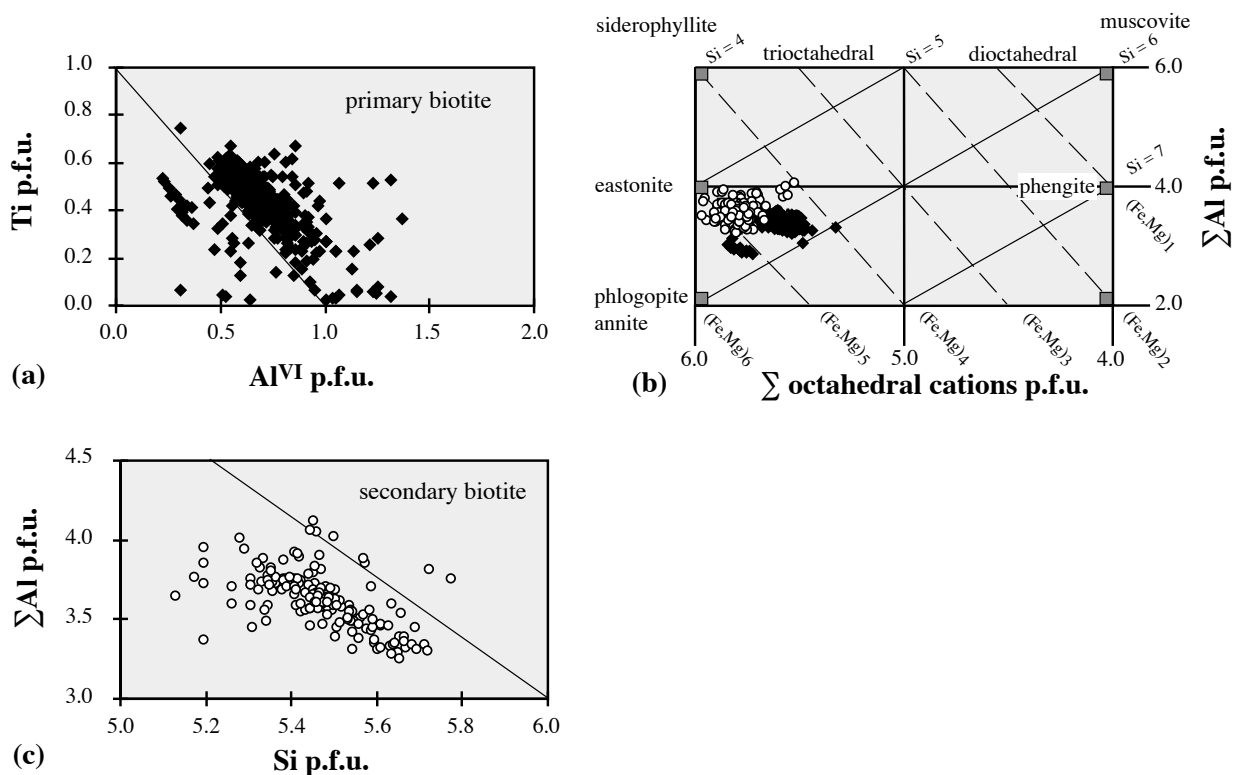


Fig. 4.3. Composition of biotite. **(a)** Diagram Ti versus octahedral Al for primary biotite, (core and rim compositions). **(b)** Diagram ΣAl versus total number of octahedral cations (after Deer *et al.*, 1992), showing the compositions of primary (black rhombs) and secondary biotite (white circles). For primary biotite, only core compositions are considered. **(c)** Diagram ΣAl versus Si, showing the composition of secondary biotite. Variations mainly involve the Tschermak's substitution. Mineral abbreviations according to Kretz (1983).

c.p.f.u. F contents range from 0.11 - 0.16 c.p.f.u. and Cl contents from 0.01 - 0.04 c.p.f.u. The rims of primary matrix biotite are usually only slightly chloritised (low X-site totals, octahedral site totals in excess of 6 c.p.f.u., oxide totals lower than 94 wt%, decrease in Si and Ti contents; Fig. 4.3a). Chloritised primary biotite is always accompanied by Ti-bearing phases such as rutile or ilmenite.

The compositions of the reddish brown biotite inclusions in cordierite correspond to those of primary matrix biotite, unless the grains are in contact with b-type pinite.

Green, secondary biotite shows larger intra-sample variations in nearly all compositional parameters than primary biotite. Compared to the latter, it has lower Ti (≤ 0.02 c.p.f.u.) and Cl, but higher X_{Mg} (0.36 - 0.56), Al (Fig. 4.3b) and F contents (0.14 - 0.26 c.p.f.u.) and a higher occupation of octahedral sites (Fig. 4.3b). Compositional variations occur mainly along the Tschermaks exchange vector (Fig. 4.3c). Often, secondary biotite shows the same chloritisation effects at its rims as primary biotite.

Zoned biotite grains are reddish brown and become green towards b-type pinite. They display a pronounced decrease of Ti and octahedral site vacancies towards the pinite contacts as well as increasing octahedral Al and Mg (Fig 4.4a, b). At the outermost rims of zoned biotite in contact with pinite, enrichment in Ti may be observed. A Ti-bearing phase was never observed. Besides the described modifications, some compositional trends related to chloritisation (see above) can be observed.

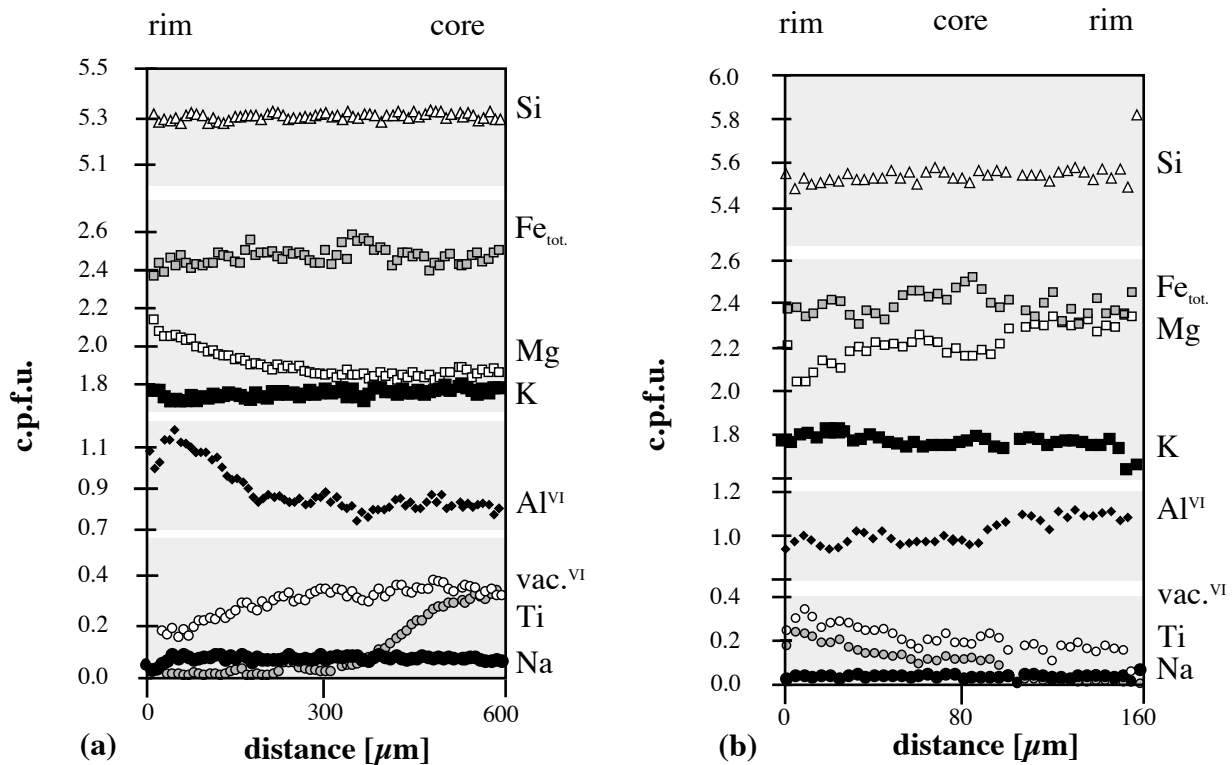


Fig. 4.4. Zoning patterns of biotite grains adjacent to b-type pinite (sample To-2). (a) The contact with pinite is on the left-hand side. (b) The contact with pinite is on the right-hand side.

4.6.2 Muscovite and muscovite-rich domains (Table I - 29 - 36 and Table I - 63 - 67)

Muscovite is a major constituent of b-type pinite and also occurs within m-type pinite. Besides pinites, decomposing plagioclase or K-feldspar and altered primary biotite are the main sites of retrograde muscovite formation.

Muscovite in m-type and b-type pinite deviates from ideal muscovite mainly along the Tschermak's substitution towards phengitic compositions (Fig. 4.5a). $Fe_{tot} + Mg$ contents range from 0.10 to 0.54 c.p.f.u., Si contents from 6.05 to 6.35 c.p.f.u.; higher contents were rarely found (Fig. 4.5a). $Na/(Na+K)$ values range from 0.05 to 0.14 with a maximum at 0.07. Ti is in most cases lower than 0.01 c.p.f.u. X_{Mg} values are intermediate (0.35 to 0.64). F contents range from 0.04 - 0.12 c.p.f.u. and Cl contents are not detectable.

Within very fine-grained b-type pinite, many analyses display K contents (1.55 to 1.85 c.p.f.u.)

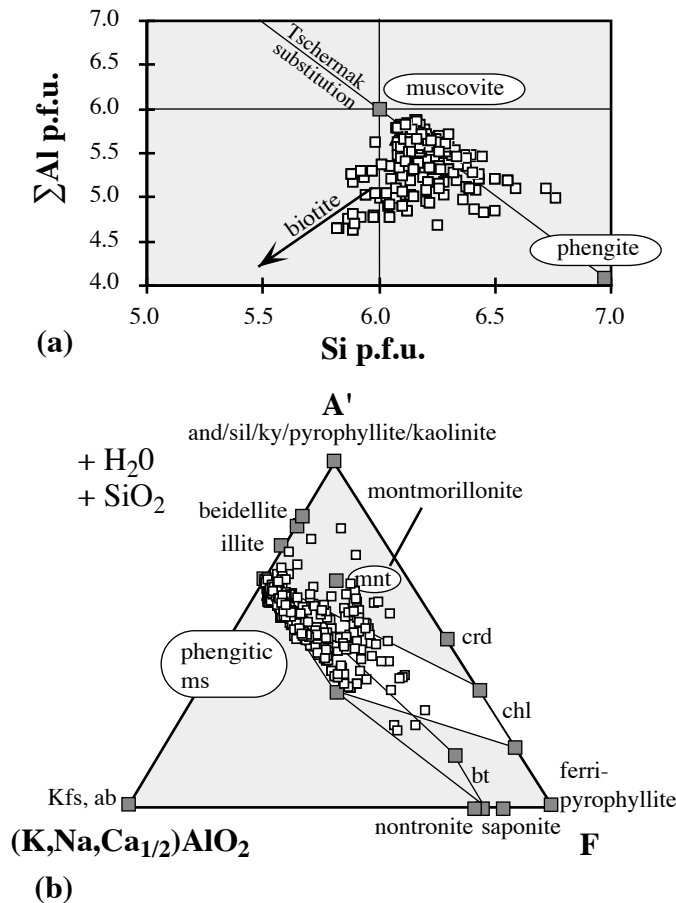


Fig. 4.5. Composition of muscovite and muscovite-rich domains. (a) Diagram ΣAl versus Si. Compositional variations mainly involve the Tschermak's exchange vector. (b) Diagram $A' - (K,Na,Ca_{1/2})AlO_2 - F$ ($F = FeO + MgO + MnO$; $A' = Al_2O_3 - (K,Na,Ca_{1/2})AlO_2$) showing the compositions of muscovite and muscovite-rich domains. Three types of phase mixtures can be distinguished: muscovite-biotite, muscovite-chlorite and complex mixtures plotting above the chlorite-muscovite join shown as white field. Mineral abbreviations according to Kretz (1983).

and oxide totals (~ 94 wt%) typical for micas, but with octahedral site occupancies (4.40 to 5.06 c.p.f.u.) intermediate between dioctahedral and trioctahedral values. As muscovite is known to show only minor deviations from being purely dioctahedral (Radoslovich, 1963; Green, 1981; Guidotti, 1984), the analyses must represent mixtures of secondary biotite and muscovite (Fig. 4.5 a, b). Similarly, within m-type pinite, many analyses represent mixtures of muscovite and chlorite that

deviate from the ideal muscovite-phengite join towards chloritic compositions (Fig. 4.5b). They are characterised by oxide totals lower than 93 wt% and X site totals lower than 1.3 c.p.f.u.. Additionally, some analyses plot above the chlorite-muscovite join (Fig. 4.5b), indicating X site deficiencies. These analyses may represent a more complex mixture of phases, including clay minerals (smectite). Sericite replacing plagioclase or K-feldspar does not differ much in composition from muscovite in b-type pinite. On the average, it is slightly less phengitic, lower in $Fe_{tot} + Mg$ values and closer to the ideal octahedral site total of 4.00 c.p.f.u.

4.6.3 Na-rich domains (Table I - 38 - 40)

Na-rich domains were found as constituents of b-type and m-type pinite. Two compositional groups of Na-rich domains can be distinguished (Fig. 4.6).

The Si contents of group I range mostly from 6.10 to 6.50 c.p.f.u. $Fe_{tot} + Mg$ is lower than 0.20 c.p.f.u., Na contents vary between 0.38 and 1.52 c.p.f.u. and K contents between 0.25 and 1.28 c.p.f.u. Na/(Na+K) values range mainly from 0.50 to 0.98. Octahedral site totals are close to ideal dioctahedral values (Fig. 4.6a). X site totals range from 0.25 to 2.00 c.p.f.u. and oxide totals scatter between 95 and 93 wt%.

Ternary diagrams (Fig. 4.6b-d) reveal that the analyses represent different mixtures of phases. In the diagram $Al_2O_3 - KAlO_2 - NaAlO_2$ (Fig. 4.6b), some analyses plot within the muscovite-paragonite miscibility gap (e.g. Blencoe *et al.*, 1994) and may thus represent muscovite-paragonite mixtures. Most of the analyses deviate from ideal paragonite/muscovite towards higher Al contents (Fig. 4.6b-c) and lower X-site totals (Fig. 4.6d). This points to the involvement of an Al_2O_3 -rich phase with balanced tetrahedral to octahedral charges (e.g. pyrophyllite) and/or the occurrence of illite and Na-illite. Other analyses plot close to the chlorite-mica join (Fig. 4.6b), possibly representing mixtures of chlorite and white mica. Finally, some analyses come close to the montmorillonite composition (Fig. 4.6c-d). However, the occurrence of metastable low-grade Na-K 2:1 phyllosilicates must be discussed as well (Jiang & Peacor, 1993; Li *et al.*, 1994; Livi *et al.*, 1997).

In contrast to group I analyses, Si contents of group II domains as low as 4.97 - 5.81 c.p.f.u., octahedral site totals are within the trioctahedral range and even higher (5.58 to 6.68 c.p.f.u., Fig. 4.6a) and $Fe_{tot} + Mg$ is 3.58 to 5.27 c.p.f.u. K contents are lower and Na/(Na+K) ratios higher than those of group I domains. The data points plot close to the white mica-chlorite join in Fig. 4.6c, and interlayer charges intermediate between white mica and chlorite are indicated (Fig. 4.6d). Therefore, group II domains most likely represent chlorite-rich mixtures of chlorite and white mica, but the involvement of biotite cannot be excluded (Fig. 4.6d).

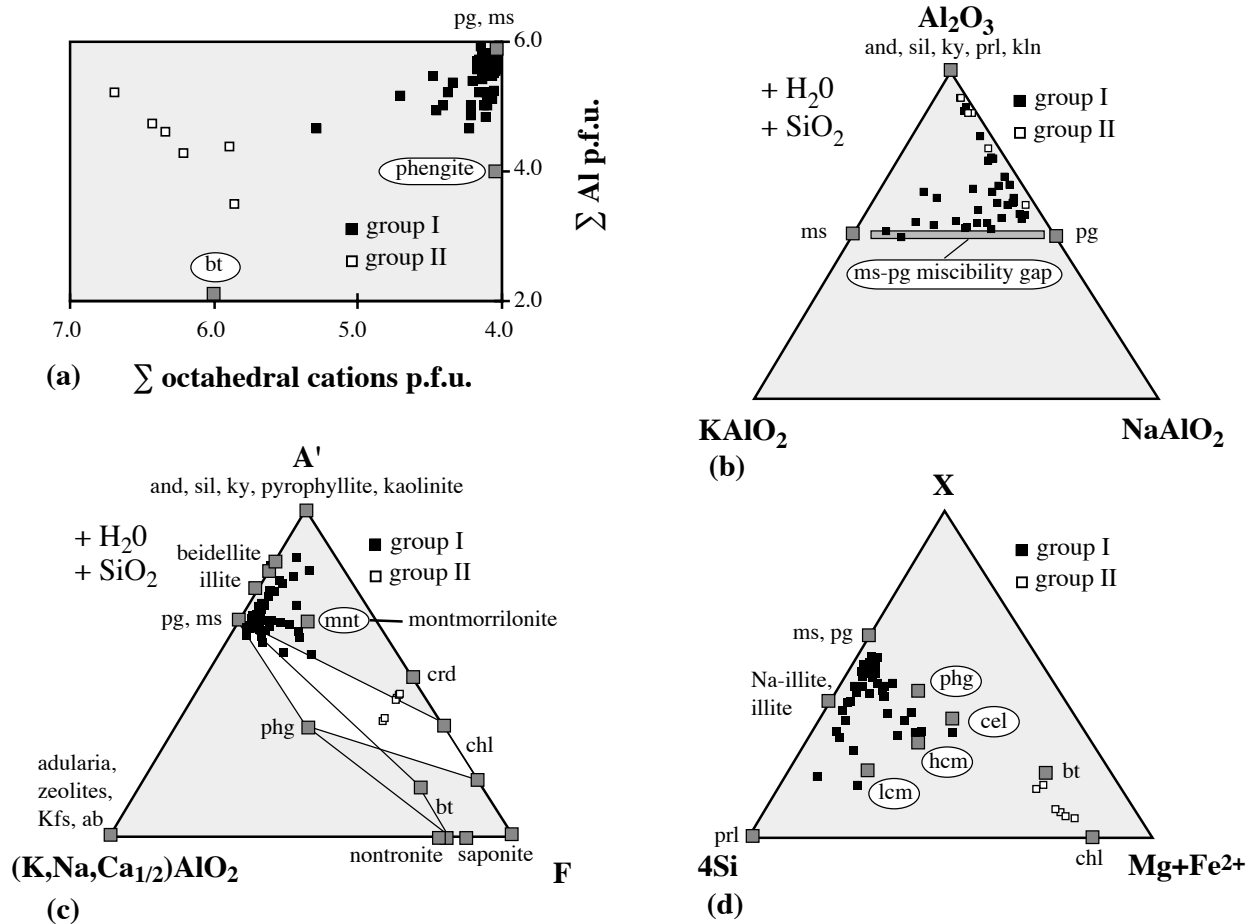


Fig. 4.6. Composition of Na-rich domains. **(a)** Diagram Σ octahedral cations versus ΣAl (after Deer *et al.*, 1992). **(b)** Ternary diagram Al_2O_3 - $KAlO_2$ - $NaAlO_2$. **(c)** Ternary diagram A' - $(K,Na,Ca_{1/2})AlO_2$ - F ($F = FeO + MgO + MnO$; $A' = Al_2O_3 - (K,Na,Ca_{1/2})AlO_2$). The chlorite-muscovite join is shown as a white field. **(d)** Ternary diagram X - $4Si$ - $Mg + Fe^{2+}$ (X : X site totals), modified after Livi *et al.* (1997). Mineral abbreviations according to Kretz (1983); lcm, low charge montmorillonite; hcm, high charge montmorillonite; cel, celadonite; phg, phengite.

4.6.4 Chlorite (Table I - 41 - 47)

Chlorite is a major phase of m-type pinite and it forms at the expense of biotite.

Most chlorite of m-type pinite has K contents lower than 0.02 c.p.f.u. and Si values from 5.17 to 5.65 c.p.f.u. Contents of tetrahedral Al range from 2.34 to 2.75 c.p.f.u. and of octahedral Al from 2.63 to 3.32 c.p.f.u. Octahedral site totals are close to the ideal trioctahedral 12 c.p.f.u. (11.66 - 11.89 c.p.f.u.) and X_{Mg} values vary from 0.49 to 0.59. These analyses represent members of the trioctahedral clinocllore-chamosite solid solution series (Bayliss, 1975; Bailey, 1980). Other analyses in m-type pinite show $Ca + K + Na > 0.01$ c.p.f.u. (Fig. 4.7a), with $K \gg Ca, Na$. These contents are clearly beyond the concentrations compatible with the chlorite structure (e.g. Foster, 1962; Bettison & Schiffmann, 1988). The increasing $Ca + K + Na$ values correlate with octahedral vacancies (Fig. 4.7a) and with Si. The totals of non-interlayer cations for these analyses are lower

than the ideal 20.00 (Fig. 4.7b), suggesting chlorite interlayered with smectite or white mica (Schiffmann & Fridleifsson, 1991). Octahedral vacancies in excess of 1 c.p.f.u. and interlayer cation totals up to 1.7 c.p.f.u. imply mixtures with a high percentage of dioctahedral K-bearing phyllosilicates. Mixed layers of chlorite with illite, kaolinite, biotite, white mica and expandable 2:1 minerals (smectite, vermiculite) are well known (e.g. Banos & Amouric, 1984; Francescellini *et al.*, 1986; White *et al.*, 1985; Ahn *et al.*, 1988; Jiang *et al.*, 1994; Merriman & Peacor, 1999 and references therein).

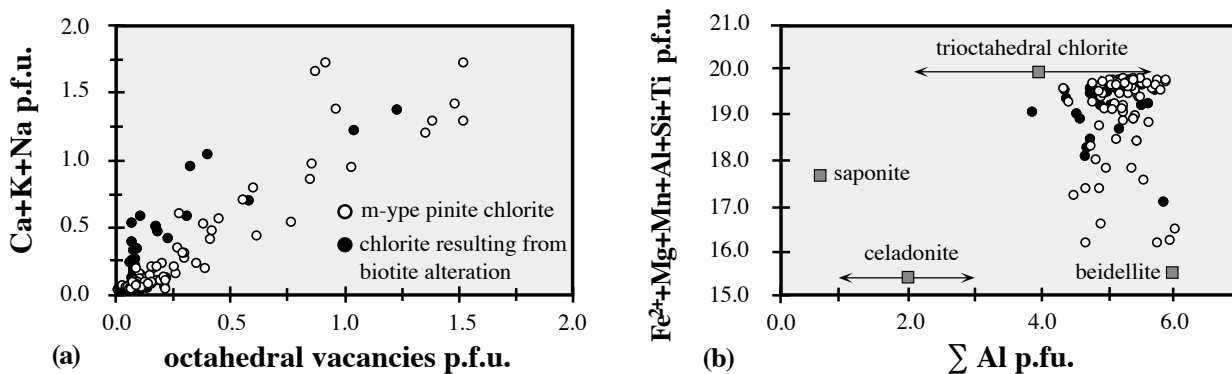


Fig. 4.7. Composition of chlorite. (a) Diagram Ca + K + Na versus octahedral vacancies. (b) Diagram non-interlayer cation total versus total Al vacancies (modified after Schiffman & Fridleifsson, 1991).

Chlorite formed at the expense of primary biotite has Si, Al and K contents as well as octahedral site totals similar to chlorite in m-type pinite (Figs. 7a, b). X_{Mg} values are usually slightly lower (0.38 - 0.56), but chamositic chlorites with X_{Mg} values as low as 0.15 have been found as well. As with chlorite from m-type pinite, increasing Ca + K + Na values and octahedral vacancies (Fig. 4.7a) for some analyses point to the involvement of dioctahedral K-bearing phyllosilicates.

4.6.5 F-type pinite (Table I - 1 - 4, I - 7 - 13, I - 15 - 17)

F-type pinite compositions (Table 4.3) show moderate to strong intra- and inter-sample variations. The dominant feature are high Ca contents compared to m-type pinite (Fig. 4.8). Ca contents (0.06 - 0.36 c.p.f.u.) and average Ca/(Ca+K) ratios (> 0.5) of dark f-type pinite tend to be higher than the respective values for bright f-type pinite (0.05 - 0.24 c.p.f.u. and < 0.5). In bright f-type pinite, the potential occupancy of octahedral sites and the oxide totals are systematically higher than in dark f-type pinite (Table 4.3). However, the size of the bands was often smaller than the beam diameter, so that many analyses represent mixtures. F-type pinite contains no Cl, but F (0.01 - 0.06 c.p.f.u.). Compared to cordierite, dark f-type pinite is deficient in Fe and Mg (Fig. 4.9) and enriched in Al, Si, K and Ca (Fig. 4.8b). Bright f-type pinite shows similar compositional trends, but may also be enriched in Fe. If Ca, Na and K were to act as interlayer cations, f-type pinite should be illite or smectite. However, the Ca, Na and K contents (Table 4.3) are clearly below interlayer cation total

Table 4.3: Representative compositions of pinnite types and their statistical standard deviations.

	Ho-12* dark f-type N = 54	Ho-12* bright f-type N = 41	Bw-3* dark fi-type N = 51	Bw-3* bright fi-type N = 119	Ho-10/12* i-type N = 17	Wa-4 m-type (ch-lms) N = 44	Ho-10* m-type (complex) N = 39	Wa-4* f-type overprinted N = 71
SiO ₂	40.38±0.80	40.61±1.50	42.40±2.79	42.42±2.58	42.40±2.66	44.70±1.87	39.80±3.45	41.12±2.00
TiO ₂	0.01±0.01	0.01±0.01	0.01±0.01	0.01±0.01	0.01±0.01	0.01±0.01	0.00±0.00	0.01±0.01
Al ₂ O ₃	31.96±1.15	31.47±1.79	32.16±2.56	31.94±2.44	37.43±3.47	30.15±0.70	29.61±2.98	29.68±1.29
FeO*	8.35±1.62	9.54±2.33	5.33±1.05	6.04±1.46	1.87±1.52	6.93±1.24	11.74±5.38	9.82±1.92
MnO	0.10±0.04	0.13±0.04	0.12±0.06	0.13±0.05	0.04±0.04	0.12±0.05	0.10±0.06	0.17±0.05
MgO	2.34±0.70	3.40±0.72	3.02±0.71	3.56±1.13	0.52±0.44	3.15±0.53	3.33±1.54	4.90±1.22
CaO	1.21±0.28	0.69±0.29	1.90±0.38	1.73±0.48	1.26±0.45	0.09±0.08	0.45±0.21	0.51±0.25
Na ₂ O	0.08±0.03	0.10±0.03	0.31±0.11	0.29±0.12	0.14±0.07	0.19±0.10	0.11±0.08	0.13±0.11
K ₂ O	0.54±0.28	1.53±0.54	0.79±0.20	0.85±0.48	0.69±0.40	7.39±1.388	2.91±1.84	2.53±1.12
Cl**	b. d.	b. d.	b. d.	b. d.	b. d.	b. d.	b. d.	b. d.
F**	0.06±0.02	0.05±0.01	0.04±0.02	0.05±0.03	0.04±0.02	0.09±0.07	0.06±0.03	0.04±0.01
Total	84.99±1.75	87.51±1.73	86.12±4.18	86.97±3.70	84.31±3.32	92.76±1.51	88.09±1.74	88.86±1.58
<i>Formula based on 22 O</i>								
Si	5.85±0.11	5.77±0.12	6.06±0.25	6.04±0.20	5.99±0.22	6.18±0.10	5.72±0.32	5.82±0.20
Al ^{IV}	2.15±0.11	2.23±0.12	1.94±0.25	1.96±0.20	2.01±0.22	1.82±0.10	2.28±0.32	2.18±0.20
Σ ^{VI}	8.00	8.00	8.00	8.00	8.00	8.00	8.00	8.00
Al ^{VI}	3.30±0.12	3.05±0.28	3.14±0.18	3.40±0.24	4.21±0.33	3.15±0.11	2.74±0.61	2.76±0.30
Ti	0.00±0.00	0.00±0.00	0.00±0.00	0.00±0.00	0.00±0.00	0.00±0.00	0.00±0.00	0.00±0.00
Fe*	0.91±0.07	1.03±0.27	0.32±0.13	0.72±0.19	0.20±0.20	0.80±0.15	1.29±0.64	1.05±0.21
Mn	0.01±0.01	0.02±0.01	0.02±0.01	0.01±0.01	0.02±0.01	0.01±0.00	0.01±0.01	0.02±0.01
Mg	0.50±0.12	0.72±0.15	0.15±0.62	0.76±0.25	0.12±0.07	0.65±0.18	0.71±0.32	1.04±0.27
Σ ^{VI}	4.72±0.10	4.82±0.10	4.79±0.16	4.89±0.10	4.55±0.09	4.61±0.18	4.75±0.22	4.86±0.20
Ca	0.19±0.05	0.11±0.04	0.29±0.05	0.26±0.07	0.20±0.07	0.01±0.01	0.07±0.03	0.08±0.04
Na	0.02±0.01	0.03±0.01	0.09±0.03	0.08±0.03	0.04±0.02	0.05±0.01	0.03±0.02	0.03±0.01
K	0.10±0.04	0.26±0.12	0.14±0.04	0.15±0.10	0.12±0.07	1.31±0.24	0.53±0.33	0.46±0.20
ΣX	0.31±0.16	0.40±0.09	0.52±0.09	0.50±0.10	0.36±0.16	1.37±0.08	0.63±0.32	0.57±0.21
Cl**	b. d.	b. d.	b. d.	b. d.	b. d.	b. d.	b. d.	b. d.
F**	0.03±0.01	0.02±0.01	0.02±0.01	0.02±0.01	0.02±0.01	0.03±0.02	0.02±0.01	0.02±0.01

* Fe: all Fe was calculated as Fe³⁺ as reddish colors dominate. ** Cl and F values base on lower N. Analyses were performed with a beam size of 8-15 μm. B.d.: below detection limit.

for illite (≈ 1.10 to 1.50 c.p.f.u.) or smectite (≈ 0.60 to 0.80 c.p.f.u.) or mixtures of both (e.g. Srodon *et al.*, 1986; Nadeau & Bain, 1986; Ransom & Helgeson, 1993). If these low values were due to mixtures of 2:1 interlayer-bearing phyllosilicates with non-interlayer-bearing phyllosilicates, correlations among Ca, Na and K and with Si and Al should be expected. Weak to moderate correlations can be observed in most cases, so that at least a part of Ca, Na and K should represent interlayer cations of 2:1 phyllosilicates, probably mixed with chlorite. However, the data arrangement in Fig. 4.9 requires the involvement of a phyllosilicate with balanced octahedral to tetrahedral charges (e.g. pyrophyllite, kaolinite). The involvement of adularia, feldspar, zeolites or epidote is not indicated (Fig. 4.9).

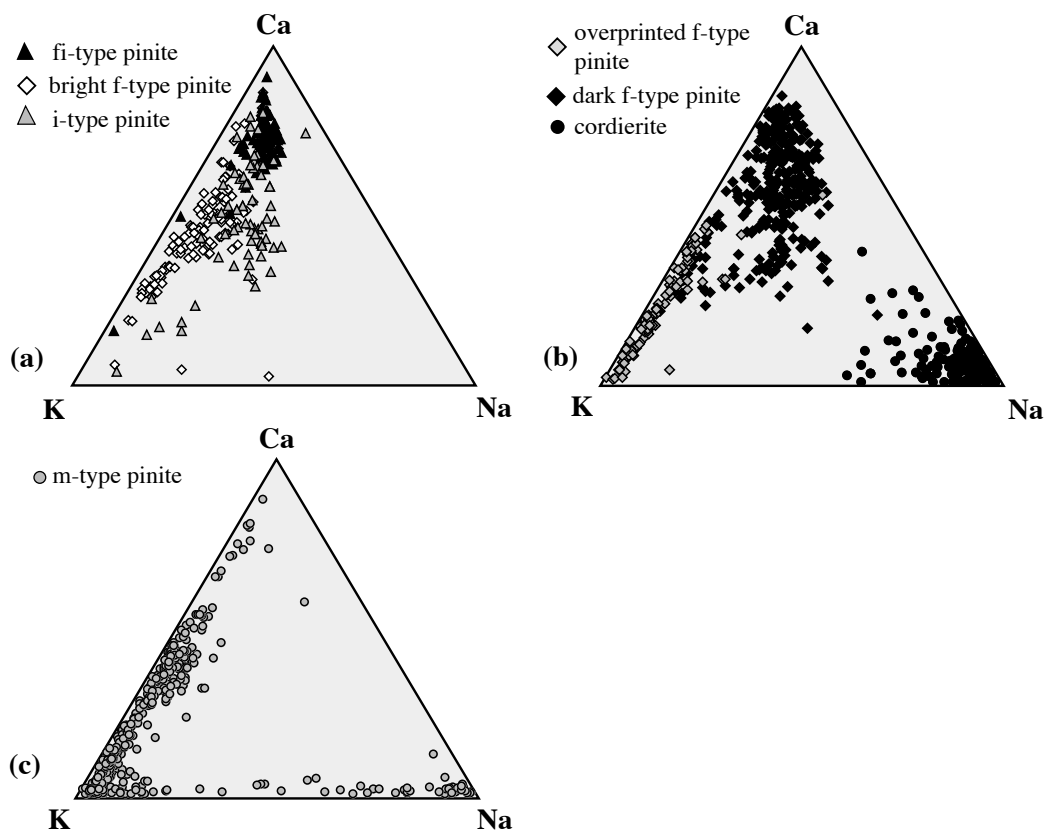


Fig. 4.8. Ternary diagram Ca-K-Na with compositions (a) of bright f-type pinite, i-type pinite, fi-type pinite; (b) of cordierite, dark f-type pinite, overprinted f-type pinite; (c) of m-type pinite, including Na-rich domains within m-type pinite.

The microprobe analyses confirm that f-type pinites of samples Wa-4 and Al-20 were overprinted by later m-type pinitisation (Tab. 3). For samples Wa-4 and Al-20, compositional trends typical of f-type pinite (Ca as the major interlayer cation, varying Ca:K ratios) and of m-type pinite (K as the major interlayer cation, strong correlations between Si and K; see below) are observable (Figs. 8b, 9a, g).

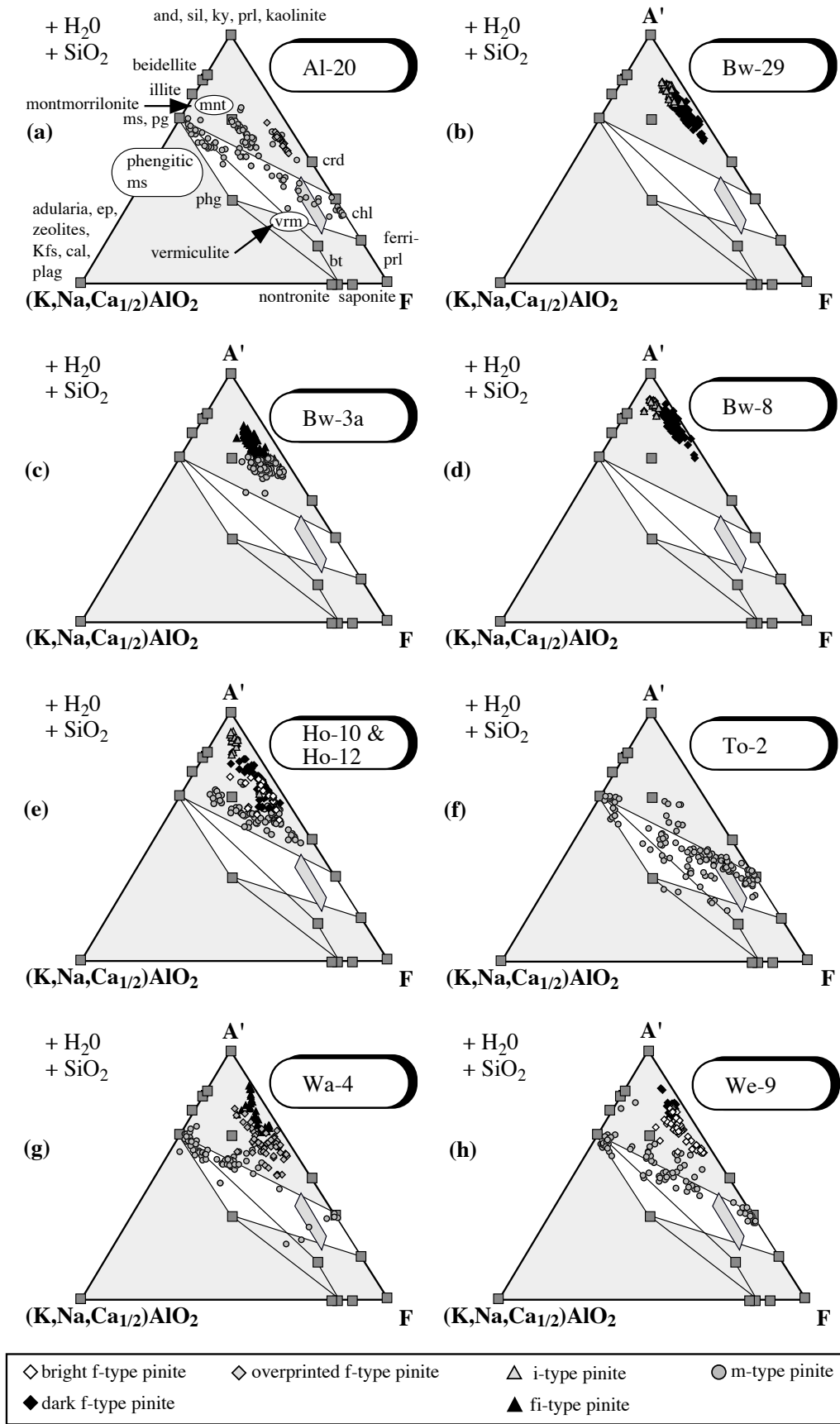
4.6.6 I-type pinite and fi-type pinite (Table I - 25 - 28 and Table I - 5 - 6, 14)

I-type pinite and fi-type consist mainly of SiO_2 (43 - 46 wt%) and Al_2O_3 (33 - 39 wt%). Other oxides rarely exceed 5 wt% (Table 4.3). Cl contents are below the detection limit and F contents scatter between 0.00 - 0.03 c.p.f.u. In fi-type pinite, Ca is dominant over Na and K, but i-type pinites display a wide range in Ca:K ratios and are more enriched in Na (Fig. 4.8a). Correlations among Ca, Na and K with Si and Al were not found for i-type pinite, indicating that these cations are not bound on phyllosilicate interlayer sites, but may be incorporated in non-silicate minerals. In contrast, fi-type pinite in Bw-3 and Wa-4 shows weakly defined Si-Ca and Si-K correlations, respectively. In both cases, Si:Al ratios (1:1) are close to those of kaolinite and do not match those of pyrophyllite (2:1). Oxide totals suggest H_2O contents of 15 - 18 wt% (Tab. 3). The arrangement of analysis in Fig. 4.9 does not point to the involvement of zeolites.

4.6.7 M-type pinite (Table I - 18 - 24)

Both groups of m-type pinite mainly have high, but variable K contents and usually lower Ca and Na contents (Fig. 4.8c). Analyses with K : Ca ratios close to 1 : 1 originate from complex m-type pinite. For all m-type pinites, well-defined correlations between K and Si emphasise the role of K as the dominating interlayer cation, and octahedral site totals range from values close to the ideal dioctahedral 4.00 c.p.f.u. to values in excess of those for 2:1 phyllosilicates (up to 7.23 c.p.f.u.). Complex m-type pinite does not contain detectable Cl and F values scatter from 0.01 - 0.04 c.p.f.u. It has lower oxide totals and lower potential occupancies of interlayer sites. Chlorite-muscovite pinites have F contents up to 0.05 p.f.u. and no Cl. Chlorite-muscovite pinites plot close to and along the muscovite-chlorite join, while complex m-type pinites generally plot above the join (Fig. 4.9). The arrangement of data points subparallel to and above the chlorite-muscovite join suggests the presence of smectite-chlorite mixtures (corrensite), of illite-smectite mixtures or even a combination of all three (Fig. 4.9a, c, e, h). The involvement of vermiculite and beidellite and of phases with balanced tetrahedral to octahedral charges cannot be excluded (Fig. 4.9 a, f, g).

Fig. 4.9 (on p. 57). Compositions of f-, i-, fi- and m-type pinite in ternary diagrams $\text{A}'(\text{KNaCa}_{1/2})\text{AlO}_2 - \text{F}$ ($\text{A}' = \text{Al}_2\text{O}_3 - (\text{KNaCa}_{1/2})\text{AlO}_2$; $\text{F} = \text{FeO} + \text{MgO} + \text{MnO}$).



4.7 Pinitisation processes

The compositions of all pinite types deviate considerably from those of primary cordierite and clearly indicate that pinitisation is an allochemical process. The systematic relationships between textural position, grain size, chemical composition and, as far as they can be deciphered, also phase assemblages in the different pinite types confirm the hypothesis of independent pinitisation processes. The fact that samples coming from different areas show largely the same pinitisation features, suggests that b-, m-, f- and i-type pinite represent systematic and general features of cordierite breakdown that are at least to a certain degree independent of local late- to post-metamorphic conditions. This hypothesis is corroborated by the fact that most of the described pinite types have already been reported in literature. The occurrence of chlorite-muscovite pinite is a generally accepted fact (e.g. Seifert & Schreyer, 1970; Deer *et al.* 1992), and the involvement of clay minerals, biotite and muscovite was also reported earlier (Černý & Povondra, 1967; Černý, 1970).

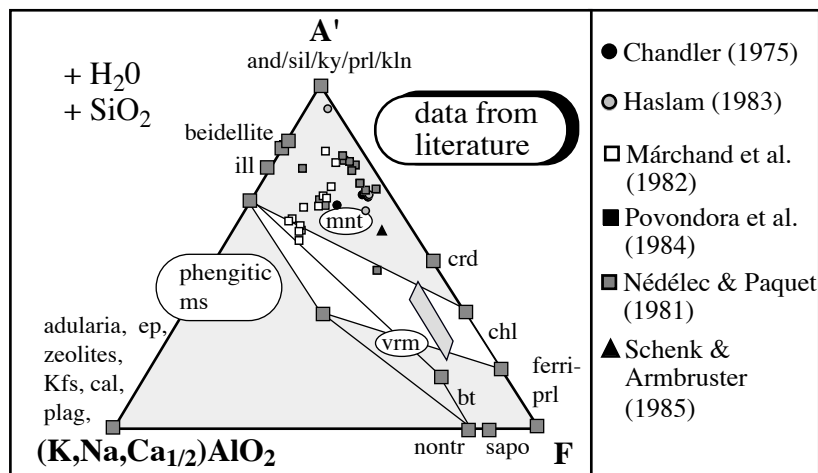


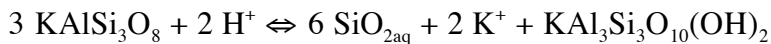
Fig. 4.10. Compositions of pinite data from literature in ternary diagrams A'(KNaCa_{1/2}) AlO₂-F (A' = Al₂O₃ - (KNaCa_{1/2}) AlO₂; F = FeO+MgO+MnO).

Descriptions, figures and analyses resembling f-type pinite can be found in literature as well (e.g. McKenzie & Guilford, 1981; Mathias, 1952; Chandler, 1975; Haslam, 1983; Nédélec & Paquet, 1981; Clemens & McMillan, 1982, Schenk & Armbruster, 1985; Fig. 4.10). In contrast, it is unclear whether i-type and fi-type pinite have been described earlier. The nature of pinitisation and its petrological significance is yet unclear. EM and SEM studies are insufficient to identify the complete phase inventory of pinite. Detailed models can only be presented on the base of TEM and XRD studies that allow for phase identification. Therefore, only a preliminary model is given below that will be substantiated by TEM and XRD data (Chapter 5).

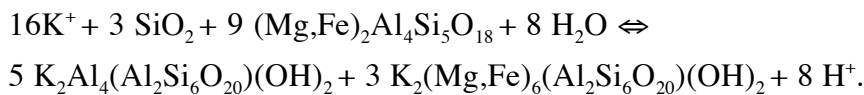
4.7.1 B-type pinitisation

The formation of biotite and muscovite indicates that b-type pinitisation takes place within the stability field of the two phases as a fluid-induced allochemical process. Coexisting muscovite and biotite occur over a wide range of metamorphic conditions from the lower greenschist to the upper amphibolite facies. Minimum temperatures can be estimated from petrogenetic grids at around 300-400 °C (e.g. Spear & Cheney, 1989; Spear, 1992).

Besides cordierite, K-feldspar has been affected by various hydrous breakdown reactions, leading to the formation of muscovite + quartz as the earliest retrograde breakdown products. There is always a good agreement between the degree of K-feldspar breakdown and b-type pinitisation. Moreover, the grain sizes of the quartz + muscovite assemblages and of the b-type pinites are similar. This strongly suggests a coupled process. In fact, hydrolysis of K-feldspar



liberates K^+ and SiO_2 for the b-type pinitisation of cordierite



The acidity of the solution increases through the hydrolysis of cordierite, which further drives the breakdown of K-feldspar. The muscovite + quartz assemblage gives an upper temperature limit of 550 - 650 °C for b-type pinitisation (e.g. Spear & Cheney, 1989; Spear, 1992; Deer *et al.*, 1992). The exact position of the quartz-saturated ms-out reaction in P-T space is strongly dependent on the composition (e.g. a_{H^+} , a_{SiO_2} , a_{K^+}) and activity ($a_{\text{H}_2\text{O}}$) of coexisting solutions (e.g. Bucher & Frey, 1994). These parameters are not determinable. However, as the approximate lower stability of muscovite + biotite is very close to the lower stability of (Fe,Mg) cordierite (Spear & Cheney, 1989; Schreyer, 1986) it is very likely that b-type pinitisation represents the breakdown of cordierite within its stability field, driven by a fluid with high K^+ activity.

An important feature obviously related to b-type pinitisation is the occurrence of strongly zoned primary biotite in close vicinity to b-type pinitised cordierite. The grains are not zoned symmetrically, but show a decrease in Ti (and Fe) and an increase in Mg and octahedral Al towards b-type pinitite. High Ti contents and X_{Mg} values are characteristic of biotite stable at high temperatures in pelitic systems (e.g. Patiño-Douce & Johnston, 1991; Patiño-Douce *et al.*, 1993). The high Ti contents and X_{Mg} values of primary biotite cores studied here still record the peak temperatures of 730 - 780 °C for migmatites from the SW and of 800 - 850 °C for migmatites from the BW. In samples that contains fresh, nearly non-pinitised cordierite, biotite is fairly homogenous. There are some intra-grain variations in X_{Mg} and at rims in contact to cordierite, minor depletions in

TiO₂ occur. Therefore, the strong decrease in Ti and the increase in Mg and Al observed in primary biotite towards pinite cannot reflect simple cooling, but must be due to an exchange with a fluid. Most likely, primary biotite located between cordierite and K-feldspar was probably affected by fluids from both sides during the formation of b-type pinite (see above). Fluids coming from the cordierite side were most likely enriched in Mg and Al and depleted in Ti, due to the anisochemical decomposition of cordierite to biotite and muscovite. This may explain the zoning patterns of primary biotite (Fig. 4.4).

The equations for the coupled breakdown of K-feldspar and cordierite require a supply of H₂O. The H₂O channel contents of cordierite are rather low (see Chapter 6). Moreover, from infrared spectroscopy, there are no indications of significant H₂O having left the channels (Chapter 6). A potential source of H₂O are the partial melts that were present in the gneisses and migmatites at peak metamorphic conditions. The H₂O contents of these melts can be estimated at 2 - 5 wt% on the basis of experiments with cordierite and H₂O-undersaturated melts (Carrington & Harley, 1996) and on the basis of the measured channel H₂O contents of the cordierites (Kalt, 2000). Partial melts in metapelitic rocks crystallise down to their solidus temperatures of approximately 750 °C (e.g. Le Breton *et al.*, 1988) in the absence of an external H₂O-rich fluid. If no or only little crystallisation or growth of OH-bearing minerals takes place, the remaining melts become increasingly saturated in H₂O and may release H₂O-dominated fluids. However, in samples with only fresh cordierite, there is no evidence for the release of significant amounts of fluids during cooling. Moreover, fluids released from the melts would have formed at temperatures 100 - 200 °C higher than the upper stability limit of b-type pinite (see above). Therefore, it is more likely that the H₂O and perhaps also some of the K necessary for b-type pinite was derived from an exterior source.

4.7.2 M-type pinite

M-type pinites are dominated by mixtures of hydrous phyllosilicates, including 2:1 phyllosilicates with unbalanced tetrahedral to octahedral charges bearing K as the main potential interlayer cation. Besides chlorite-muscovite pinite, complex m-type pinites were distinguished with illite, smectite and chlorite as the major potential phases. Therefore, it is reasonable to consider m-type pinite as the product of hydrothermal alteration by an alkali-bearing fluid with K ≫ Na. An upper P-T limit for chlorite-muscovite pinite is given by the upper stability of muscovite plus chlorite (plus quartz) at around 500 - 550 °C (Spear & Cheney, 1989; Bucher & Frey, 1994). This is in line with the fact that it formed later than b-type pinite (see section 4.5.5).

The possible presence of illite in complex m-type pinite may indicate that it formed at lower temperatures than chlorite-muscovite pinite (Merriman & Peacor, 1999 and references therein). However, the fact that the majority of complex m-type pinite is red or reddish brown, whereas chlorite-muscovite pinite shows greenish colours, suggests that also f_{O_2} was one of the major factors controlling the formation of m-type pinites. Other factors are a_{K^+} , a_{SiO_2} , a_{H^+} etc. in the fluid. At fixed

P and T, small differences in a_{SiO_2} can determine whether illite or muscovite is precipitated (Garrels, 1984). The possible presence of smectite or chlorite-smectite mixed layers would point to formation conditions of < 200 °C (Frey & Robinson, 1999) that are incompatible with the stability of muscovite. Therefore, most likely, complex m-type pinite formed at lower temperatures than chlorite-muscovite pinite. There is no evidence for the former forming at the expense of the latter as the contacts between both – when present – are always very sharp.

In contrast to b-type pinite, m-type pinite : cordierite ratios are usually high and often a complete replacement of cordierite by m-type pinite can be observed. This suggests high fluid : rock ratios. A potential K source could be the chloritisation of biotite. This process is later than the formation of b-type pinite as it affects also secondary biotite. However, the degree of biotite chloritisation is on the average minor and can vary strongly within one sample. Therefore, a contribution of K released by the chloritisation of biotite cannot be excluded, but is certainly not generally the case. Another K source is the late-stage sericitisation of K-feldspar. There is a good agreement between the grain size of late-stage K-feldspar alteration products (sericite) and m-type pinite phyllosilicates. As for b-type pinite, an external source of H_2O and perhaps also of K must be assumed. Na-rich domains also require an Na source. As possible internal Na source, hydrolysis of plagioclase has to be mentioned, as sericitisation of plagioclase was observed in all investigated samples.

4.7.3 F-type and i-type pinitisation

The outstanding compositional characteristic of f-type, i-type and fi-type pinites is their enrichment in Ca. Their phase inventory is unclear, especially the Ca-bearing phases have not been identified yet. The absence of Ca-Si correlations in i-type pinite suggests incorporation of Ca in a non-phyllosilicate phase. In f-type pinite, weak to moderate correlations are observable, so that an incorporation of Ca in phyllosilicate interlayer sites is likely. In marginal f-type pinite both features were found.

The behaviour of the three pinite types during electron beam exposure gives some clues to their nature. Beam damage is a well-known phenomenon for hydrous silicates (e.g. Jiang & Peacor, 1991; Peacor, 1992; Essene, 2000, personal communication; Schiffmann & Day, 1992; Ferrell & Carpenter, 1990). Whereas loosely bound alkalis are strongest affected and tend to migrate away from the beam site, Si-O or Si-O-Al networks even of minerals that are very sensitive to electron beam exposure, such as zeolites and clay minerals, are known to stay intact when exposed to e^- -rays (Ferrell & Carpenter, 1990). Therefore, zeolites and clay minerals are usually characterised by an increase in the counting rates of non-migrating ions such as Si (e.g. Schiffmann & Day, 1992; Ferrell & Carpenter, 1990).

F-type pinite shows the increase in Si counting rates expected for hydrous silicates bearing loosely bound alkalis and H_2O (Fig. 4.1a). The stepwise increase of the counting rates (not visible on the scale of Fig. 4.1) may point to the release of water in different states of bonding, e.g.

interlayer water as well as colloidal water. Taking into account the high volatile contents of f-type pinite (15 - 18 wt%, Table 4.3) as well as its partly isotropic behaviour under crossed polars, the involvement of amorphous material (see below) is likely. However, Ca and K-bearing 2:1 phyllosilicates (illite, smectite) and phyllosilicates free of interlayer cations (pyrophyllite or kaolinite) should be principal constituents of f-type pinite.

Contrary, a dramatic loss in Si counting rates is observed with i- and fi-type pinite (Fig. 4.1a), questioning the crystalline state of both pinites. Probably, i-type and fi-type pinites are highly hydrated, possibly amorphous, material. The very high volatile contents of both (up to 14-19 wt% H₂O; Table 4.3) support this assumption as well as their isotropic behaviour under the polar microscope and the characteristic occurrence of fissures within i-type pinite that most likely represent dehydration shrinkage fissures. The holes left behind at the beam sites clearly indicate the destruction of the sample. Most likely, a rapid H₂O loss leading to shrinkage and leaving less and less material in the excited area causes the dramatic decrease of the Si counting rate curve (Essene, 2000; personal communication). Temperature has to be considered as the main cause of beam damage (Schiffmann & Day, 1992). Whereas the bonding energy of covalent Si-O bonds (368 kJ/mol at 25 °C; Cotton *et al.*, 1990) in intact silicate networks is too high to be affected at temperatures of EM high vacuum, highly hydrated hydrosilicate gel-like materials with a high portion of polar low-energy H-H bonds (20 - 30 kJ/mole; Cotton *et al.*, 1990) are easily affected.

As indicated by their extremely poor crystallinity, high water contents and low thermal stability, f, i and fi-type pinites are most likely produced by very low-temperature processes, even weathering. F-type pinitisation probably is a leaching-precipitation process with dark and bright f-type pinite representing discrete zones of leaching and repolymerisation/precipitation, respectively. Most likely, the process of f-type pinitisation is controlled by chemical gradient acting between the vein centres and cordierite rims. Dark f-type pinite is in contact to intact cordierite and relatively depleted in network-modifying cations compared to the network-forming species Si and Al. Bright f-type pinite has higher oxide totals and higher concentrations of network-modifying cations and never occurs in contact to intact cordierite. The formation of amorphous and repolymerised layers or sequences of amorphous and polymerising stages during weathering of aluminosilicates have been described earlier (e.g. Kawano & Tomita, 1994, 2001; Mazer *et al.*, 1992; Eggleton, 1980). The crystallographic control of f-type pinite orientation suggests the channel-like structures oriented parallel to c to play a major role during f-type pinitisation. In analogy, Casey and Bunker (1990) argued that the structural channels of beryl, which is quasi isostructural with cordierite, control the leaching as the channel diameter (up to 5 Å) is large enough to accelerate H₂O diffusion. It is questionable whether the observed f-type pinites really represent primary features as material of such poor crystallinity should be extremely sensitive to secondary overprint.

I-type pinitisation probably represents a pure leaching process with network-modifying species being preferentially dissolved. Compared to cordierite, all major elements but networkformers (Al

and Si) are strongly depleted in i-type pinites (Table 4.3). It is well-known from experiments and nature that uniform stoichiometric dissolution of minerals (hydrolysis) competes with selective, non-stoichiometric leaching of network-modifying cations, resulting in the formation of leached layers (e.g. Casey & Bunker, 1990; Kawano & Tomita, 2001). Which of both is the dominant process is controlled by reaction rates and strongly depends on pH (Casey & Bunker, 1990). Leaching is generally followed by hydration of the network-forming cations. As the removal of hydrated species is slower than hydration, a depolymerised hydrated surface layer is produced (Kawano & Tomita, 2001). This glassy, highly hydrated material is known to develop dehydration fissures on drying (Casey & Bunker, 1990) and should be very sensitive to electron beam exposure. In analogy, air-dried i-type pinites are always penetrated by fissures (Fig. 4.2d, f, g). However, the thickest hydrated glassy layer reported from a natural samples is a 500 Å thick layer on oligoclase (Nesbitt & Muir, 1988) and experiments report maximum thicknesses of labradorite leached layers of 2000 Å at pH = 1 (e.g. Casey *et al.*, 1989), whereas the observed i-type pinites have cross sections of several tens of µm (Fig. 4.2d, f, g). Although the dissolution behaviour of cordierite and feldspar is only partly comparable, it is clear that i-type pinites exceed known values for hydrated mineral surface layers by far. Therefore, the nature of i-type pinites remains unclear.

Given that cordierite contains no Ca, the question for the Ca source remains. The major Ca-bearing phase in the migmatites and gneisses is plagioclase. A Ca depletion of plagioclase by marginal albitisation or by sericitisation has never been observed in contact or close vicinity to i-type and f-type or marginal f-type pinitised cordierite. Therefore, an external Ca-source has to be invoked.

4.8 Pinitisation processes in the regional context

As set out in the previous chapters, the four pinitisation processes found in the studied rocks show an age sequence which is from oldest to youngest b-type, m-type, f-type, i-type (Fig. 4.11). The four processes are most likely due to different episodes of fluid infiltration. However, the lack of compositional differences between pinites formed in rocks of the BW and in those of the SW implies that these fluid infiltrations must be related to geological events active in both areas. It is generally recognised that the vast majority of the SW basement was affected by regional to local-scale post-peak-metamorphic hydrothermal activity (e.g. Simon, 1990; Hagedorn & Lippolt, 1994; Lippolt *et al.*, 1994; Lüders, 1994; Wernicke & Lippolt, 1997; Markl, 1999) that produced most of the ore and mineral deposits (e.g. von Gehlen, 1989). In the BW, post-peak-metamorphic hydrothermal activity seems to be limited to the Bayerische Pfahl, a quartz lode of km size related to ductile-brittle deformation (Beer, 1981).

In the course of the German Deep Drilling Program, a reconnaissance study of fluid inclusions in Variscan basement rocks and Mesozoic sediments was conducted in order to characterise the fluids to be expected during drilling (Behr & Gerler, 1987; Behr *et al.*, 1987; von Gehlen, 1989). While older metamorphic fluids trapped in gneisses, migmatites and granulites showed varying compositions, fluids related to granite emplacement (late and post-magmatic) were relatively uniform in composition. They were H₂O-rich with medium to low salinity and predominantly K as the major cation. These fluids may well be responsible for the formation of b-type pinite in the temperature range below 550 - 650 °C. Oxygen isotope analyses of granites from the SW show most H₂O to be of meteoric origin (Simon & Hoefs, 1987). The temperature range for the alteration of granites by

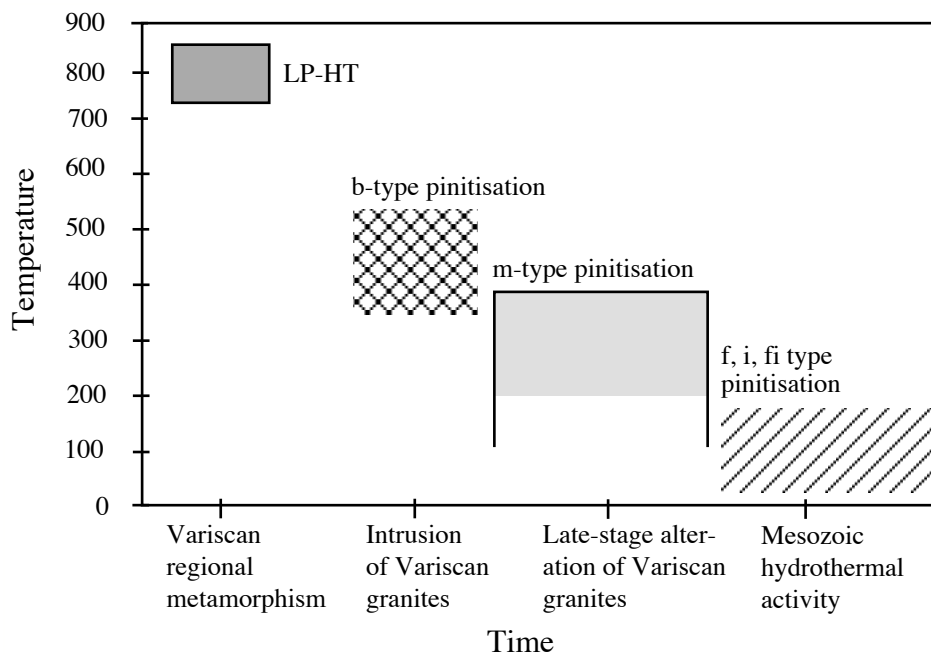


Fig. 4.11. Temperature-time diagram (qualitative for time) showing the approximate formation temperatures of the observed pinite types and their proposed geological context. As the relative age sequence of the different types of pinite especially of m and f-type pinite varies between samples, Fig. 4.11 offers only a possible age sequence that is not valid for all samples. For further explanation see section on pinitisation in the regional context.

these fluids is 400 - 200 °C (Simon & Hoefs, 1987). These mainly K- and Na-bearing fluids could thus have also been the source of H₂O and K for m-type pinite that formed later and at lower temperatures than b-type pinite. Fluids that are associated with post-Variscan hydrothermal activity and most of the Pb-Zn and fluorite-barite deposits are highly saline, formed at low temperatures (150-180 °C) and are extremely enriched in CaCl₂ and to a lesser degree in NaCl. These fluids are also encountered in boreholes in Northern Switzerland that penetrate Variscan basement (Mullis & Stalder, 1987). They are interpreted as saline basinal brines, most likely originating from the Permian Zechstein, that may have been mixed with formation fluids from Mesozoic marine carbonate (Behr *et al.*, 1987; von Gehlen, 1989). (U+Th)-He dating of hydrothermal hematite

deposits in the Schwarzwald (Wernicke & Lippolt, 1997) showed continuous hydrothermal activity throughout the Jurassic at temperatures of the zeolite facies. The Permian to Mesozoic Ca-rich fluids may have well been the Ca source of f-, i- and fi-type pinite at a time when the crystalline basement had already been exhumed. Nevertheless, local very low-grade fluids of meteoric origin (weathering fluids) should not be unconsidered to be responsible for the formation of f-, i- and fi-type of pinite.

4.9 Summary and conclusions

(1) On the basis of major element composition, phase assemblage (as far as possible), textural position and grain size four types of pinite could be distinguished in cordierite-bearing migmatites and gneisses from the BW and the SW. The four pinite types were formed by distinct pinitisation processes taking place under different P-T conditions and at different times.

(2) B-type pinite as the earliest type consists of muscovite and biotite, which were formed under medium-grade conditions (350 - 550 °C) from a K⁺-bearing fluid, most likely derived from the concurrent initial breakdown of K-feldspar to muscovite and chlorite. The water and some of the potassium required for this coupled reaction may be derived from external fluids related to the intrusion of granites in the Carboniferous.

(3) M-type pinite formed later. It encompasses chlorite-muscovite pinite which is considered as the product of hydrothermal alteration by an alkali-bearing fluid with K⁺>>Na at temperatures lower than 500 - 550 °C. M-type pinite can also be complex, most likely with illite, smectite and chlorite as the most likely major phases and with lower formation temperatures. M-type pinitisation is perhaps related to late-stage, low-temperature alteration of granites by meteoric waters.

(4) F-type and i-type pinite are enriched in Ca and partly contain amorphous material. F-type pinrites were most likely formed by leaching and precipitation/repolymerisation. I-type pinite shows similarities to hydrated glassy layers described from feldspar alteration and was probably formed by selective leaching of network-modifying cations from cordierite. F-type and i-type pinite were produced by very low-temperature processes, perhaps at surface-conditions, with Permian-Mesozoic sediments as possible source of Ca.

(5) Due to the fact that samples from two different Variscan massifs were studied, the different processes of pinitisation observed here could represent general features of the breakdown of metapelitic cordierite, at least in the Variscan belt.

5. TEM & XRD: Characterisation of very fine-grained Pinite from the Schwarzwald, Germany

5.1 Abstract

Concerning fine-grained retrograde breakdown products of cordierite (pinite), the modes, compositions and formation conditions are only poorly known. In a study on pinitised cordierite from Variscan high-temperature metamorphic pelites of the Schwarzwald and the Bayerische Wald, a four-fold pinite classification was established (Chapter 4) using etrography, electron microprobe analysis and scanning electron microprobe imaging: b (border), m (mat), f (fissure) and i (isotropic) type pinite. Except for b-type, the phase assemblages and in part also the structural state of the pinite types could not be satisfactorily determined. Therefore, in this study, transmission electron microscope investigations, supported by analytical electron microscopy and X ray diffraction were carried out on samples from the Schwarzwald. The results are the following: F-type pinite consists of randomly related phyllosilicates (berthierine, chlorite, smectite, I/S, I/S R₁/illite, chlorite/berthierine mixed-layering) with thicknesses of 20 - 250 Å parallel to c and < 100 - 1000 Å perpendicular to it, floating in an amorphous-like low-contrast matrix. Randomness in orientation points to *in situ* crystallisation either from a low-grade solution present in the f-type pinite alteration veins or from pre-existing amorphous material, representing the primary metastable product of cordierite f-type breakdown. M-type pinite is the product of a complex two-stage process. The primary assemblage of m-type pinitisation is I/S R₁ + chlorite formed by the infiltration of an alkali-rich fluid. Secondary berthierine and I/S R₀ are formed by the replacement of chlorite and I/S R₁ via a dissolution/precipitation process driven by the infiltration of an additional very low-grade fluid. The complex m-type pinite studied here may be regarded as the low-temperature equivalent of chlorite-muscovite pinite. F-type pinitisation clearly has to be understood in terms of weathering. The phase and structural state of i-type pinite could not be determined.

5.2 Introduction

Cordierite, $(\text{Mg,Fe})_2\text{Al}_4\text{Si}_5\text{O}_{18}x(\text{H}_2\text{O,CO}_2)$, is well known to be extremely reactive on the retrograde path of metamorphism and during hydrothermal processes, including low to very low-grade conditions (e.g. Abada-Ortega & Mieto, 1995; Haslam, 1983; Marchand *et al.*, 1982; Ogiermann & Kalt, 2002; Povondra *et al.*, 1984; Schenk & Armbruster, 1985; Schreyer *et al.*, 1993; Schreyer & Seifert, 1970). For very fine-grained products of retrograde cordierite breakdown the term 'pinite' was established (Lacroix, 1962; Deer *et al.*, 1962). Usually, pinite is of a such fine-grained nature that recognition by electron microprobe (EM) or petrographic microscope investigations is hampered. Therefore, 'pinite' is used in a purely descriptive sense and may encompass a variety of breakdown products.

The most common pinite composition is thought to be a mixture of chlorite and muscovite (e.g. Seifert & Schreyer, 1970; Deer *et al.*, 1992), but manifold other hydrous phyllosilicates, including clay minerals and especially a 7Å phase, as well as Fe-oxyhydroxides and undifferentiated isotropic to slightly birefringent pinites were also reported (e.g. Mathias, 1952; Layman, 1963; Schreyer & Seifert, 1970; Chevalier & Dejou, 1972; Chandler, 1975; Vraná, 1979; Paquet, 1981; Clemens & McMillan, 1982; Haslam, 1983; Povondra *et al.*, 1984; Schenk & Armbruster, 1985; Schreyer *et al.*, 1993; Abada-Ortega & Mieto, 1995). These studies also revealed that pinites usually contain alkali-ion bearing hydrous silicates. This finding contrasts with the experimentally obtained isochemical breakdown products of Mg cordierite (Al-silicate + chlorite + quartz; Seifert & Schreyer, 1970) and Fe cordierite (chloritoid + quartz; Schreyer, 1965a, b) and implies that pinitisation is commonly a fluid-induced allochemical process.

Despite the allochemical nature of cordierite breakdown, it is not clear whether pinitisation is exclusively controlled by local conditions such as fluid and mineral composition, temperature, cooling rate and fluid flux. As there is only a limited number of phases identified in natural pinites (Chapter 4.2), pinitisation could as well be a process proceeding in a very systematic way. However, in many studies, especially in those dealing with metapelitic assemblages, there has been no satisfactory characterisation of the pinitic phase inventory. Also, no synthesis of the results of these studies was made. The only existing pinitisation model focuses on the genesis of chlorite-muscovite pinite (Seifert & Schreyer, 1970).

In Chapter 4, a preliminary pinite classification was presented: b-type (border type), m-type (mat type), f-type (fissure type) and i-type (isotropic type) pinite. The systematic phenomenology, major element chemistry and, as far as could be deciphered, phase inventory strongly suggest that each of the pinite types records a distinct process of cordierite breakdown. None of the pinite types was restricted to one sample or locality, and microphotographs, compositions and descriptions matching these types of pinite can be found in literature (e.g. Mathias, 1952; Layman, 1963; Schreyer & Seifert, 1970; Chevalier & Dejou, 1972; Chandler, 1975; Vraná, 1979; Paquet, 1981; Clemens & McMillan, 1982; Haslam, 1983; Povondra *et al.*, 1984; Schenk & Armbruster, 1985; Schreyer *et al.*, 1993; Abada-Ortega & Mieto, 1995). These facts suggest that cordierite should generally break down to the four pinite types mentioned above - at least in the Variscan basement. However, the pinite phases could not be determined in this combined EM-SEM petrographic study (Chapter 4), except in b-type pinite, which consists of fine-grained aggregates of muscovite and biotite. Nevertheless, the results suggest that m-type pinite should mainly consist of

hydrous phyllosilicates (e.g. clay minerals). In contrast, due to their extremely fine grain size, the phase inventory of f-type and i-type pinite and even their structural state are still unclear. Only indirect evidence was found that f-type pinite may contain clay minerals.

Transmission electron microscopy (TEM) is particularly useful for studying very small particles, including clay minerals, as individual layers, packets of layers and structure of packets, including mixed layering, layer stacking and structural imperfection, can be directly imaged. As a consequence, TEM studies, supported by XRD and analytical electron microscopy (AEM) were carried out, and the results are presented in this chapter. The issues in focus are: (1) the phase inventories of m, f and i-type pinite, (2) the grain texture and crystal structure of m-type pinite, (3) the long-range order of f and i-type pinite and (4) the preliminary pinitisation model presented in Chapter 4.

5.3 Samples and pinite types

The two samples studied (Ho-10 and Ho-12) are metapelitic migmatites from the southern Schwarzwald and were selected from the existing sample suite of Chapter 4 for combined XRD and TEM studies. Both samples were extensively studied by SEM, EM and with a petrographic microscope (Chapter 4). They were selected as they display the whole span of very fine-grained pinite types (f-, i- and m-type pinite). Before these migmatites underwent pinitisation, they experienced Variscan HT-LP metamorphism, including partial melting (Kalt et al., 1999 and reference therein). The following description of pinite types is based on Chapter 4, where more details are available. Representative compositions of the pinite types described below, based on EM data, are given in Table 5.1.

'M-type pinite' was introduced as a general term for fine-grained phyllosilicate aggregates that replace cordierite pseudomorphically (Fig. 5.1), encompassing chlorite-muscovite pinite as well as clay mineral-bearing assemblages (complex m-type pinite). The m-type pinite in focus of this study is of the clay mineral-bearing variety. The largest grain size observed by BSE imaging is in the range of 5 μm along the a-b plane. K and Ca with $\text{K} > \text{Ca}$ are the most abundant principal interlayer cations. Average potential interlayer charges of these mixtures scatter around 0.63, oxide totals are around 88 wt% and the average potential total occupancy of octahedral sites is intermediate to ideal dioctahedral and trioctahedral values (4.75 cations per formula unit (c.p.f.u.); Table 5.1). Thus, the obtained compositions suggest complex

mixtures of dioctahedral (illite, smectite, I/S) and trioctahedral (chlorite) phases that are only poorly characterised by EM, petrographic and BSE data.

F-type pinites form alteration veins penetrating intact cordierite (Fig. 5.1a, b). These veins are filled with an extremely fine-grained phase mixture far beyond the resolution of EM single phase analyses. Orientation of alteration veins seems to be controlled crystallographically, with directions parallel and perpendicular to the crystallographic c-axis

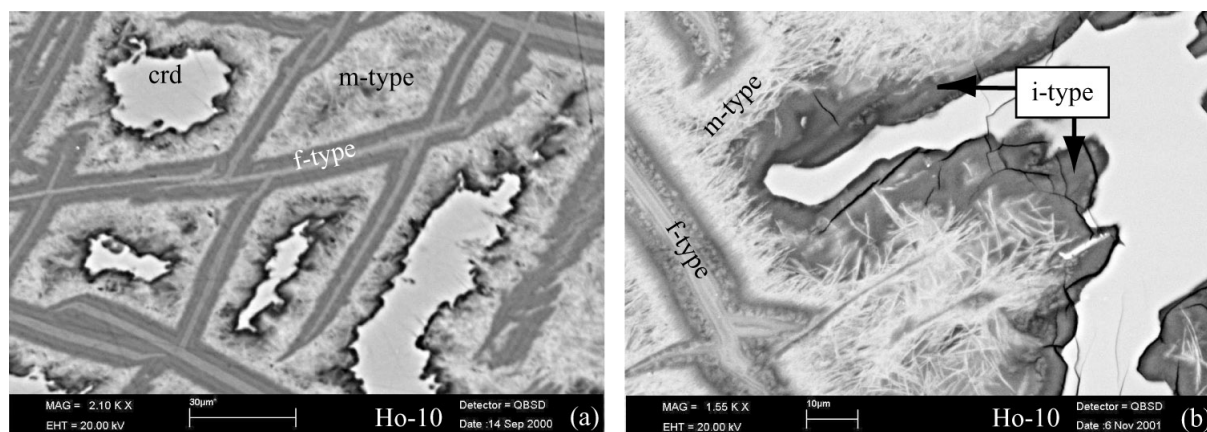


Fig. 5.1. BSE images, showing f, m and i-type pinite.

of cordierite occurring. F-type pinites show corresponding chemical and optical zonation patterns (Fig. 5.1a). According to colouring in BSE images, dark and bright f-type were distinguished. Ca and K occur as the most abundant potential interlayer cations with Ca/(Ca + K) ratios > 0.5 in dark and < 0.5 in bright f-type pinite. Average potential interlayer charges are 0.31 in dark and 0.40 in bright f-type pinite. Average potential total octahedral site occupancies are higher in bright (4.86 c.p.f.u.) than in dark f-type (4.79 c.p.f.u.) and intermediate to dioctahedral and trioctahedral values in both. However, the zonation bands were too narrow for effective distinction between both types.

EM data suggest mixtures of illite/smectite and chlorite plus aluminous 2:1 or 1:1 phyllosilicates with balanced octahedral to tetrahedral charges (e.g. pyrophyllite or kaolinite). However, only indirect evidence for phyllosilicates was found. Firstly, during EM counting rate tests at standard condition (15 kV acceleration voltage, 20 nA sample current, 1 μm beam diameter), f-type pinites showed a moderate stepwise-like increase in Si counting rates (Fig. 4.1a), a behaviour well-known for hydrous silicates with loosely bond alkalis, such as interlayer cation-bearing 2:1 phyllosilicates or zeolites (e.g. Schiffmann & Day, 1992; Ferrell & Carpenter, 1990). Secondly, a weak to moderate correlation between Si and potential interlayer cations (Ca and K) was found. In summary, the phase inventory and even structural

state of f-type pinite is still unclear as crystallites could not be directly imaged by SEM and petrographic microscope investigations.

I-type pinite occurs sporadically, is in most cases in direct contact with intact cordierite, fairly homogenous in BSE images, isotropic under crossed polars and lacks optical zonation patterns (Fig. 5.1b). Ca and K occur as the major principal interlayer cations with $Ca > K$. Compared to cordierite, i-type pinite is strongly depleted in Fe and Mg. Calculated potential X site occupancies scatter around 0.36 c.p.f.u. No direct or indirect evidence for hydrous phyllosilicates was found. At standard conditions, i-type pinites showed a dramatic decrease in Si counting rates during electron beam exposure (Fig 3.1a). Such a behaviour is not even known from beam-sensitive hydrous silicates (clay minerals and zeolites) as the Si-O-Si or Si-O-Al networks of these minerals are known to stay intact during electron beam exposure. This results in an increase in the counting rates of non-migrating cations (Si; e.g. Schiffmann & Day, 1992; Ferrell & Carpenter, 1990). Consequently, the crystalline nature of i-type pinites was questioned and it was suggested that i-type pinites may represent amorphous gel-like highly hydrated material with a high portion of low-energy H-H bonds. This assumption is confirmed by the occurrence of fissures penetrating i-type pinite, which are strongly suspected to represent dehydration shrinkage fissures as they do not continue into adjacent material and do not show a preferred orientation (Fig. 5.1b, Fig. 4.2). Correlations between Si and principal interlayer cations were not found for i-type pinite. Therefore, the phase inventory and even structural state of i-type pinite is also still unclear.

5.4 Methods

For TEM investigations, carbon-coated ion-milled specimen were prepared. From carefully selected areas, slices of 3 mm diameter were cut from unpolished thin sections with an Ultrasonic Disc Cutter (Gatan). These slices were supported with Cu grids, thinned to perforation by Ar-ion bombardement at an angle of $15^\circ - 17^\circ$ and 4.0 kV using a Gatan Duomil 600 DIF and finally carbon-coated. The samples were studied using a PHILIPS CM 12 STEM of the Institut für Mineralogie, Darmstadt, operating at 120 kV. Lattice fringe images were obtained at conditions close to Scherzer focus conditions (focusing to minimum contrast at observed thin edges) and at slight overfocus conditions, following the reference of Guthrie and Veblen (1989, 1990), and at magnifications of 60,000 - 430,000. To minimise beam damage, samples were viewed with minimum brightness that still allowed images to be

seen. Before lattice fringes were obtained, focusing was achieved in structurally contiguous areas. Usually, electron diffraction patterns were obtained using a selected-area aperture of 10 μm and a camera length of 1.10 m. The CM 12 STEM was fitted with a EDAX 9900 system for energy dispersive X-ray (EDX) microanalysis. EDX analyses were carried out by tilting the specimen holder about 20° to the detector; spectrum acquisition time was 100 s. Experimental 'k' factors were not established. Quantification of AEM data was performed using the method of Zaluzec *et al.* (1981) under the use of theoretical 'k' factors. There was no compensation for alkali loss during condensed-beam analyses of ion-milled specimen. Therefore, K and Na analyses are considered to be unreliable. Detection of Na and K loss was difficult as no phase with well-defined K or Na contents was analysed. Selected area diffraction (SAED) was also carried out. SAED pattern give evidence on lattice parameters, structural defects, order/disorder effects and the polytype. Lattice fringe imaging in combination with AEM and SAED is essential for a complete characterisation of phyllosilicates.

For XRD investigations, selected areas were cut by the microdrilling technique developed by O. Medenbach or carefully handpicked to minimise contamination by non-pinitic minerals. The samples were studied using a SIEMENS D 500 of the Geologisch-Paläontologisches Institut, Heidelberg, operating with Cu K α radiation at 40 kV and 30 mA. Disaggregated samples were studied as oriented specimen prepared with a pipette method on the one hand and as powdered samples on the other. XRD patterns in both cases were obtained under air-dried and ethylene glycol-saturated conditions. Powdered samples were scanned from 0 to 70°2 Θ and oriented and aggregated specimen from 0 to 50°2 Θ with counting times of 1 and 2 seconds per 0.01° interval. Quartz was used as an internal standard.

5.5 X-ray diffraction

X-ray diffraction measures bulk properties averaged over many grains with textural information being lost. It is therefore not possible to assign identified peaks to a certain type of pinite. Difficulties in phase identification are even enhanced by the fact that different pinite types should contain phases that show an overlap of (001) peaks, as suggested by EM data (Chapter 4). Both features clearly limit the potential of XRD studies.

XRD patterns of oriented specimen are presented in Fig. 5.2. Patterns obtained at air-dried conditions (pattern a in Fig. 5.2) are simple and mainly display reflections at approximately

14 Å, 10 Å, 8.54 Å and 7 Å in the 2-14 2θ CuK α region. The very weak 14 Å and the 7 Å reflections are compatible with the presence of high-Fe chlorite (e.g. Reynolds, 1989) and the peak at 8.54 Å corresponds to (020) of cordierite. The occurrence of a 7 Å phase (e.g. berthierine) cannot be excluded, but peak overlap with 14 Å chlorite hampers distinction. The 10.05 Å reflection is relatively sharp, shows only minor broadening at the base and should represent muscovite rather than illite. However, as suggested by EM and SEM data (Chapter 4), (001) of biotite is also likely to interfere with the 10 Å muscovite/illite peak, because b-type pinite (aggregates of biotite and muscovite) is too fine-grained and too intimately intergrown with cordierite and other types of pinite to allow effective separation by microdrilling. XRD patterns of powdered specimen display a peak at $d = 1.54$ Å (not shown), which may correspond to (006) of trioctahedral species, but interference with (211) peak of quartz has to be considered and hampers identification. XRD pattern from glycol-saturated specimen do not display any well-defined shift in 2θ position (pattern b, Fig. 2). The 7 Å peak becomes slightly more asymmetric with the shoulder skewed to the low 2θ side,

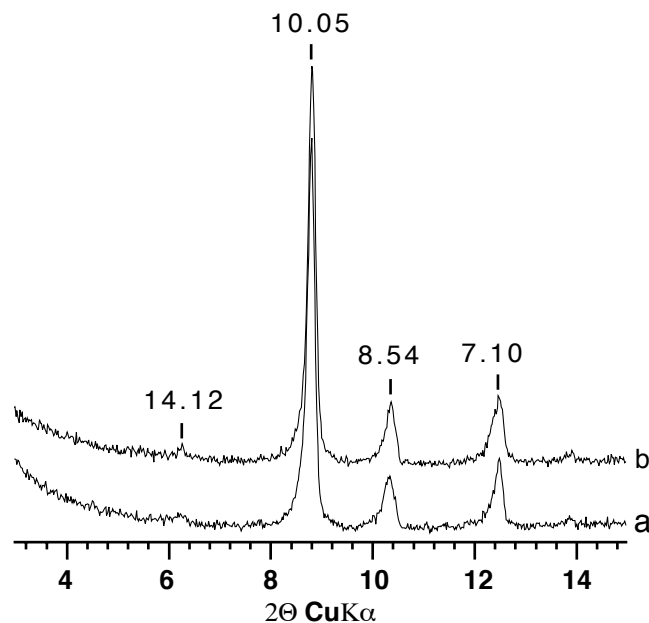


Fig. 5.2. XRD pattern of oriented specimen under (a) air-dried and (b) ethylen glycol-saturated conditions (sample Ho-10). For further see section on X-ray diffraction.

which may indicate minor involvement of expandable layers (smectite). A significant change in position or morphology of the 10 Å peak is not introduced by ethylen glycol-saturation. In summary, chlorite (and a 7 Å phase ?) and mica/illite are the principal phyllosilicates detected by XRD. Considerable smectite or chlorite-smectite and illite-smectite mixed layers, compatible with the EM data (Chapter 4), were not detected.

5.6 TEM observations

5.6.1 M-type pinite

From SEM, EM and petrographic microscope investigations m-type pinite of the sample Ho-10 and Ho-12 was known to represent a comparatively coarse-grained mixture of dioctahedral (smectite, illite, I/S) and trioctahedral (chlorite) phyllosilicates (see section on samples and pinite types). In good agreement with these findings, TEM showed m-type pinite to consist of phyllosilicate aggregates with thickness of individual packet layers from 100 - 1500 Å along *c* and of some thousand Å in the cross section. In analogy to SEM and petrography, these aggregates were found to occur in contact to cordierite or as isolated packages surrounded by f-type pinite, with or without preferred orientation. Chlorite, berthierine and mixed-layering, including random I/S and ordered I/S R_1 and random chlorite/berthierine mixed-layering, were identified as the principal constituents of m-type pinite by lattice fringe imaging (see below). The structure of packets was found to be heterogeneous. 'I/S R_1 ' refers to ordered 1:1 illite-smectite mixed-layering and 'I/S R_0 ' to random illite-smectite mixed-layering with smectite \gg illite. Highly imperfect as well as relatively well-ordered, continuous and regular packets of layers or domains were observed. Rapid beam damage was also a serious problem for m-type pinite. Especially packets of layers with irregular 10 Å layer stacking showed fading of lattice fringes and diffraction patterns within seconds at focused beam. Additionally, certain crystals with a 20 Å superperiodicity pulsed vigorously at focused beam (see 'Na-K intermediate').

I/S R_0

Fig. 5.3 presents a packet of layers in contact to cordierite. In the left part, TEM contrast defines a domain with a relatively defect-free and regular 10 Å periodicity with relatively constant and continuous interlayer spacing and pronounced mottled contrast. Interstratification with a small packet of 7 Å layers, showing mixed-layering with 14 Å layers over limited range is observable. Locally, variations in thickness of individual layers (black circle) can be observed. Layer terminations are relatively rare (Fig. 5.3, black arrow, black circle) and superposition of a 20 Å periodicity on the 10 Å substructure over a limited range is also rare and only poorly defined. These features are characteristic for ordered illite-smectite mixed-layering with $R = 1$ (e.g. Gutherie & Veblen, 1989, 1990; Ahn & Peacor, 1986, 1989; Peacor, 1992). Absence of long-range 20 Å superperiodicity may be due to non-appropriate imaging conditions. To the upper right hand corner of Fig. 5.3, the crystal structure changes

significantly. Lattice fringes are wavy, show pronounced variation in thickness (e.g. white circles) and layer terminations are abundant (Fig. 5.3, e.g. thick white arrows). 20 Å superperiodicity imposed on the 10 Å substructure over limited distances occurs frequently and implies local illite-smectite mixed layering (e.g. Gutherie and Veblen, 1989, 1990; Ahn & Peacor, 1986, 1989). This domain most likely represents smectite-rich random I/S ($R = 0$)

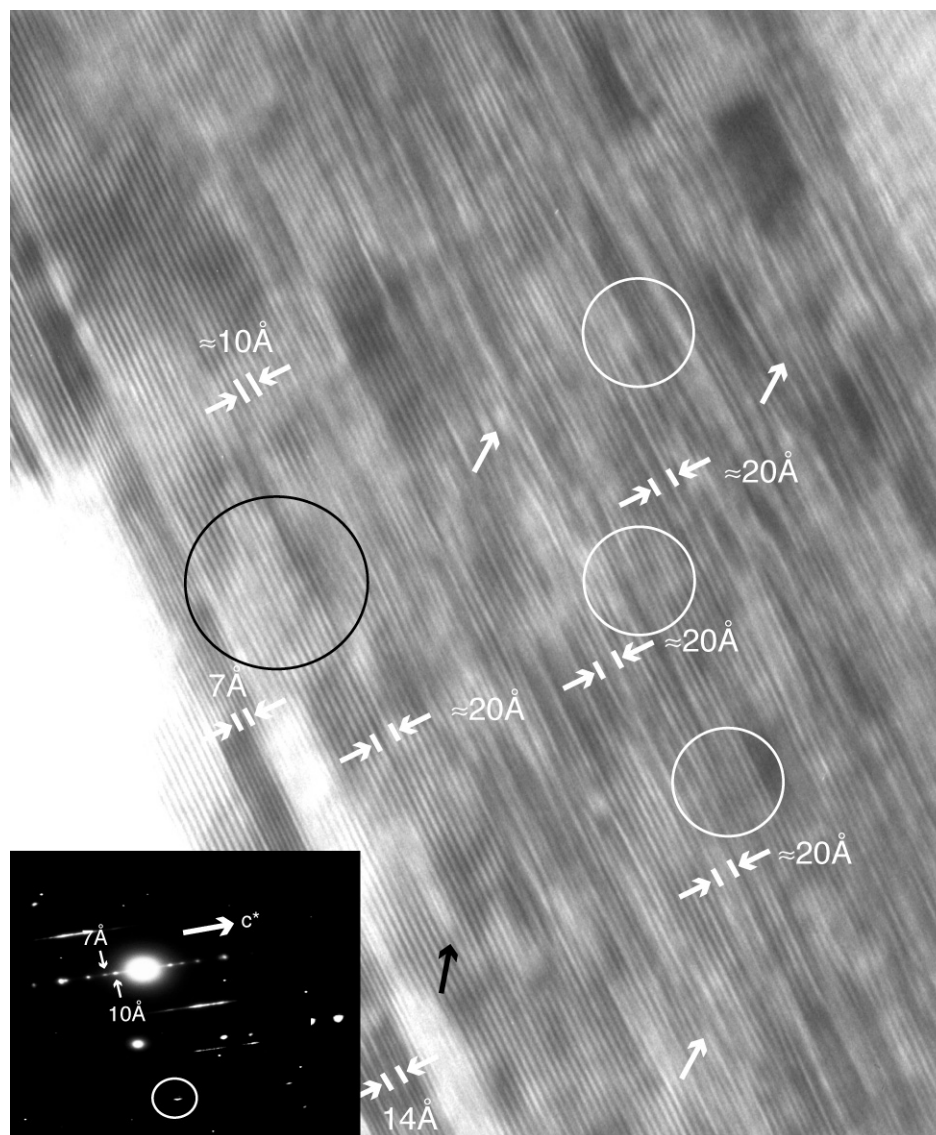


Fig. 5.3. Lattice fringe image (m-type pinite), showing a packet of layers in contact to cordierite with domains of ordered I/S R_1 and random smectite-rich I/S R_0 mixed-layering. Circles and single thick arrows mark variation in layer thickness and occurrence of layer termination. Corresponding SAED pattern displays 7 Å and 10 Å sequences. Streaking parallel to c^* can be observed in rows with $k \neq 3$ and $k = 3$. In the 00l row, weak streaking perpendicular to c^* can be seen. For further see section on TEM observations.

with ordered I/S occurring locally. The corresponding diffraction pattern displays 7 Å and 10 Å sequences with poor streaking perpendicular to c^* in the (00l) row (inset Fig. 5.11). Streaking parallel to c^* in non-00l reflections can be observed in rows with $k \neq 3n$ and $k = 3$

(white circle, inset, Fig. 5.3), which is in line with the observed domains of highly disordered stacking sequence and variable interlayer spacing and domains of ordered I/S.

I/S R₁

Much more homogeneous packets of layers with illite/smectite 1:1 ordering were found to be the major dioctahedral phase within m-type pinite. Fig. 5.4a was obtained at slightly overfocused conditions, following the reference of Gutherie & Veblen (1989, 1990) that alternating contrast giving rise to 20 Å superperiodicity on 10 Å R₁ I/S ordering may be observed at these conditions. Fig. 5.4a presents a relatively defect-free and well-ordered sequence of 10 Å layers with constant interlayer spacing and pronounced mottled contrast. Indeed, a relatively regular and continuous 20 Å periodicity is superimposed on the 10 Å substructure over large parts, indicating ordered I/S R₁ mixed-layering to be present (Gutherie & Veblen, 1989, 1990; Ahn & Peacor, 1986, 1989; Peacor, 1992). I/S ordering may be detectable only locally even though it is present throughout the whole packet of layers (e.g. Jiang & Peacor, 1990; Dong *et al.*, 1997). As most 10 Å sequences showed 20 Å superperiodicities over short or large distances I/S R₁ is thought to be the dominant dioctahedral phase within m-type pinite.

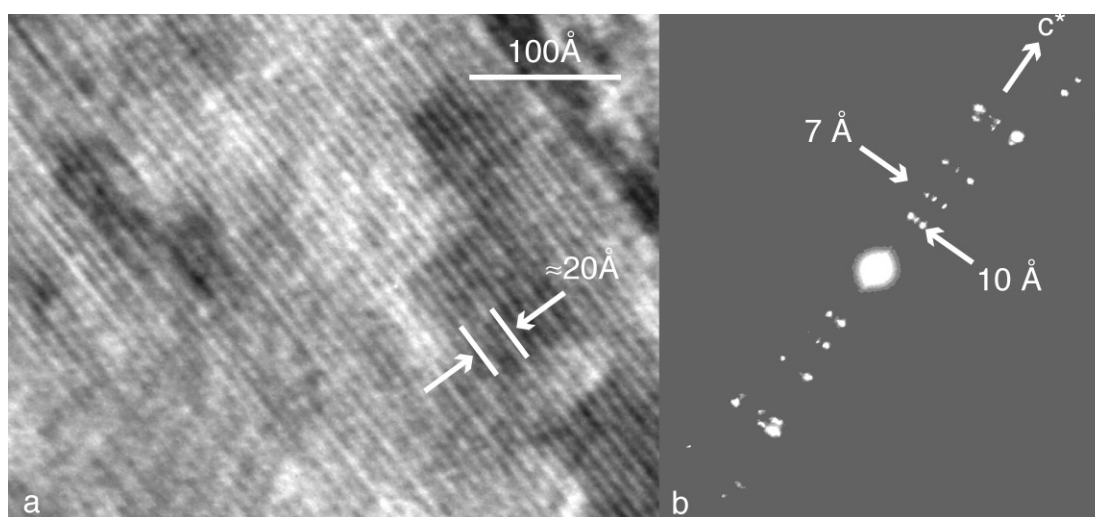


Fig. 5.4. (a) Lattice fringe image (m-type pinite). The image was obtained at slightly overfocused conditions and presents a relatively defect-free and regular 10 Å layer stacking with a ~20 Å superperiodicity occurring over large distances. For further see section on TEM observations. (b) SAED pattern corresponding showing several sets of a relatively well-defined 10 Å sequence with minor streaking parallel c^* . In addition, sets of 7 Å with strong streaking parallel c^* are observable.

Electron diffraction pattern indicating presence of 2M polytype were not found, implying that the observed 20 Å periodicities indeed are an effect of I/S mixed-layering and

not of two-layer polytypism. This is also consistent with AEM and EM data as no analyses compatible with K-illite, but compatible with I/S R_1 was obtained (see below and Chapter 4). Usually observed SAED pattern corresponding to I/S R_1 mixed-layering are presented in Fig. 5.4b, showing relatively well-defined 10 Å sequences with minor streaking parallel c^* .

Relationship between I/S R_1 and I/S R_0

The coexistence of two dioctahedral phases, namely ordered 1:1 I/S and random I/S with $R < 1$, begs the question whether both have formed simultaneously or whether one of both is the alteration product of the other. In the upper left of Fig. 5.5, lattice fringe contrast defines a regular 10 Å sequence with constant interlayerspacing and pronounced mottled contrast, representing I/S R_1 . Due to the loss of image contrast during the digitising and the printing

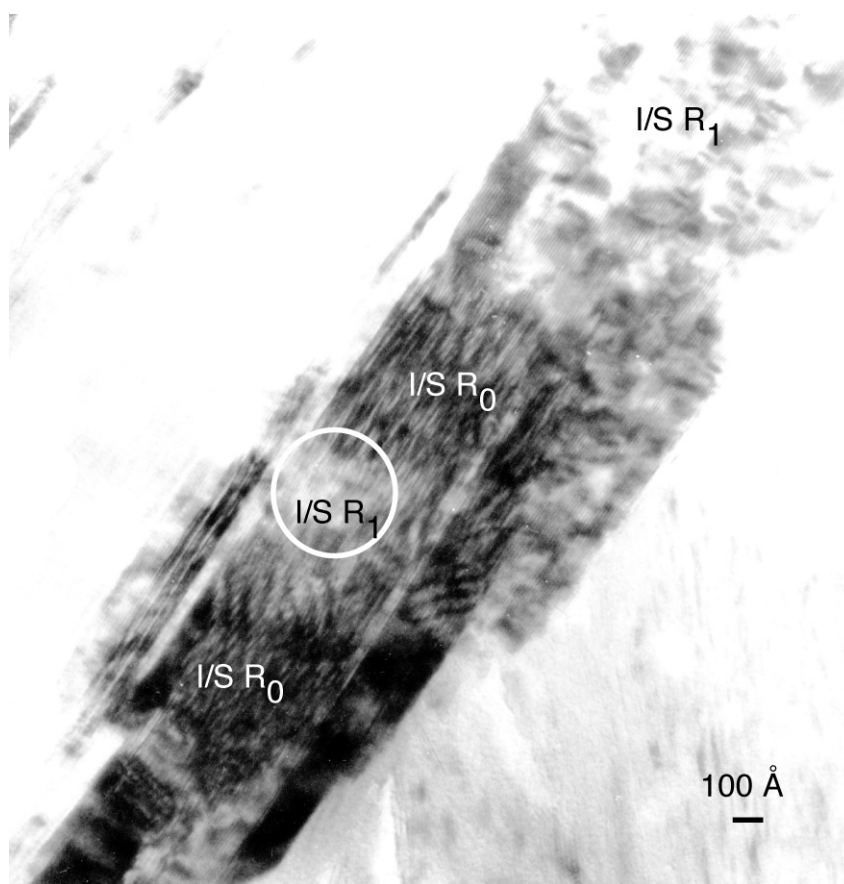


Fig. 5.5. Lattice fringe image. In the upper left, lattice fringe contrast defines a regular 10 Å sequence. Over limited distances, 20 Å superperiodicities are observable. Along layers, this sequence is continuously transformed into I/S R_0 , indicating formation of random I/S at the expense of ordered I/S. For further see section 5.6.1. The white circle encompasses a relict of I/S R_1 .

process the 10 Å periodicity is only poorly defined. Over limited distances, 20 Å superperiodicities are superimposed on the 10 Å substructure, which is also not well observable at this magnification. Along layers, this sequence is continuously transformed into I/S R₀, showing variable interlayer spacing of 10 - 13 Å and being of a general wavy appearance. Layers in both domains appear parallel and continuous and mottled contrast is also lost along layers. The white circle highlights a relict of I/S R₁. These textural features are interpreted to represent alteration of ordered I/S to smectite-rich random I/S.

Chlorite and random chlorite/berthierine mixed-layering

Fig. 5.6a and b exhibit at least three different regions with distinct contrast. Region A shows stacking of highly strained 14 Å layers. 001 fringes in region B display complex and random mixed-layering of 7 Å and 14 Å layers parallel and mainly continuous to fringes in region A. The contact between region A and B is clearly not a low-angle boundary, because the majority of layers in both regions are parallel and continuous and because the contact is not associated with layer termination or dislocations. The boundary between both regions cuts across the basal plane and strain contrast is different on both sides. Strain contrast in region B

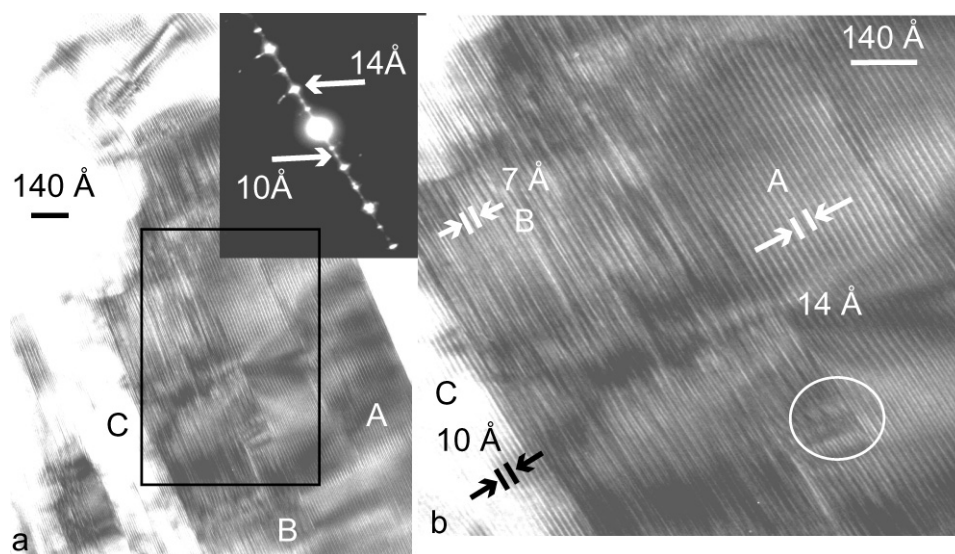


Fig. 5.6. (a) 'A' is a region of chlorite with pronounced strain contrast, which is partly replaced by random chlorite/berthierine mixed-layering (B). 'C' marks a region of 10 Å layering, probably representing I/S R₁ mixed-layering. The black frame indicates the region shown in (b). The inset shows the corresponding SAED pattern. (b) Detail of (a). The white circle highlights a layer termination at the boundary between 'B' and 'A'. For further see section 5.6.1.

is less pronounced and at least partly associated with layer termination located sporadically at the contact to region A (e.g. white circle, Fig. 5.6b). In contrast, strain contrast in region A was induced by deformation, which is confirmed by strongly bent layers with high strain contrast in the upper part of Fig. 5.6a. Difference in strain contrast and in origin of strain

contrast and continuity and parallelism of fringes of both regions favours region B to be the result of overgrowth of chlorite by berthierine. Obviously, the chlorite crystal was deformed prior to overgrowth. Region C displays a packet of 10 Å layers with pronounced mottled contrast and a wavy appearance, possibly representing I/S R₁ mixed-layering. The corresponding SAED pattern (inset in Fig. 5.6b) shows a 14 Å sequence with strong even-order and weak odd-order reflections, which is consistent with SAED patterns of chlorite/berthierine random mixed-layering (Ahn & Peacor, 1985; Jiang *et al.*, 1992, Abdad-Ortega & Mieto, 1995), but also with diffraction patterns of Fe-rich chlorite (e.g. Baileys, 1980). A poorly-defined 10 Å sequence with strong streaking in 00l reflections parallel to c* is also present. Parallelism of c* of both sequences hampers recognition of origin of streaking parallel c*, which may partly also be attributed to the 14 Å sequence. Relatively sharp spots of the 14 Å sequence are rather unusual for chlorite/berthierine mixed-layering (e.g. Jiang *et al.*, 1992, Abdad-Ortega & Mieto, 1995), but may arise from domain 'C'. Curved streaking perpendicular to c* in the 14 Å sequence corresponds well to bending of layers in the upper region of Fig. 5.6a.

Berthierine

Fig. 5.7a presents a part of a large area (> 1500 Å parallel c*) consisting of several lath-like 'subpackets' of 7 Å layers, each ≈ 50 - 250 Å thick, showing relatively strong strain contrast, which is in most cases associated to layer terminations. Individual 'subpackets' are parallel to subparallel to each other and separated by layers with distinct and complex contrast including 14 Å spacing. 7 Å layers within 'subpackets' may be subparallel and wavy and there are layer terminations within subpackets (Fig. 5.7b, single thick arrows). Black arrows in Fig. 5.7a highlight layers with distinct 14 Å contrast holding out over relatively long distances and being continuous and parallel to 7 Å layers, most likely these layers represent chlorite. The loss of 14 Å contrast is either induced by the change of one 14 Å layer in two 7 Å layers or occurs in association with a layer termination. Domains of random chlorite/berthierine mixed-layering (not shown), resembling domain B of Fig. 5.6, also occur within this area and are continuously transformed to 7 Å berthierine layers. A packet of 10 - 12 Å layers is interlayered and marked by the black arrows (Fig. 5.7a) and possibly represents partially collapsed expandable smectite and I/S layers. The corresponding electron diffraction pattern (inset in Fig. 5.7b) is that of a 7 Å phase and shows several sets of 7 Å sequences slightly rotated to each other. A less well-defined 10 Å sequence with streaking parallel and perpendicular to c* is also observable.

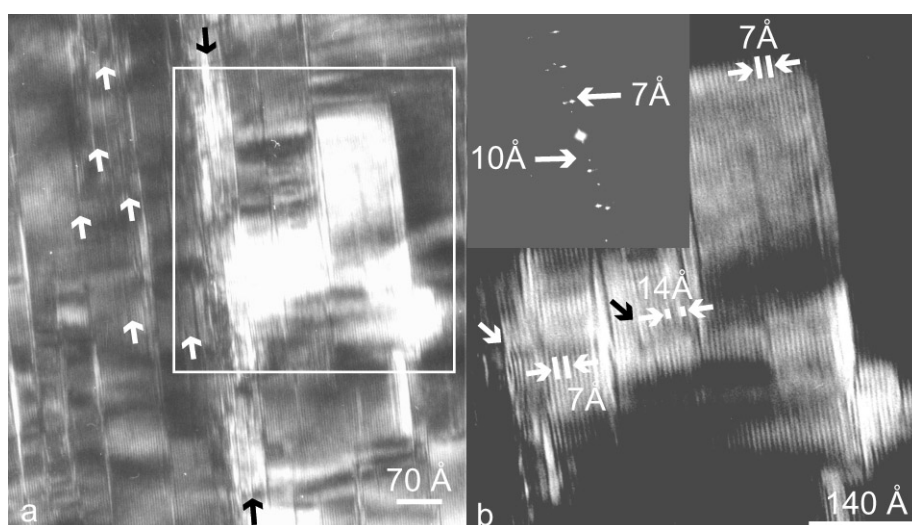


Fig. 5.7. Lattice fringe images. **(a)** Part of an area of lath-like ‘subpackets’ of berthierine with 7 Å layers, each of which is $\approx 50 - 250$ Å thick. Single thick arrows marks 14 Å chlorite layers continuing over relatively large distances. The white frame encloses the region presented in **(b)**. **(b)** Detail of **(a)**. 7 Å layers within ‘subpackets’ may be subparallel and wavy and there are layer terminations (single thick arrow) within subpackets. The inset shows the corresponding SAED pattern with several sets of 7 Å and a 10 Å sequence. For further see section 5.6.1.

The textural features are interpreted to represent alteration of chlorite to berthierine. The 14 Å layers are regarded as relictic chlorite layers and the domain of random chlorite/berthierine mixed-layering as a possible intermediate stage of chlorite alteration. In summary, the alteration sequence chlorite \rightarrow chlorite/berthierine mixed layering \rightarrow berthierine is deduced from the observed reaction textures in Fig. 5.6 and Fig. 5.7.

5.6.2 F-type pinite

Results of EM, SEM and microscopy suggested that f-type pinite may contain a mixture of dioctahedral (illite, smectite, I/S) and trioctahedral (chlorite) clay minerals plus an aluminous phase of balanced tetrahedral to octahedral charges (e.g. kaolinite or pyrophyllite; see section on samples and pinite types). The assumption that phyllosilicates occur within f-type pinite could be verified by TEM as tiny packets of layers could be directly detected by lattice fringe imaging.

The principal crystals or packets of layers detected by TEM are 7 Å (berthierine), 10 Å (illite or I/S R_1 , smectite) and 14 Å (chlorite) phases and complex mixed-layering including 7/14 Å, 10/14 Å, I/S and complex mixed-layering of 7 Å, 10 Å and 14 Å layers. Most packets of layers were found to be highly imperfect and heterogeneous in structure. At low magnification, f-type pinites appear as low-contrast areas, which lack thickness contours and

were very rapidly damaged by electron beam. Within seconds, a pock-marked texture occurring as small rounded areas of light contrast could be observed. The size of these areas increased with time of continuous beam exposure, and lattice fringes and electron diffraction

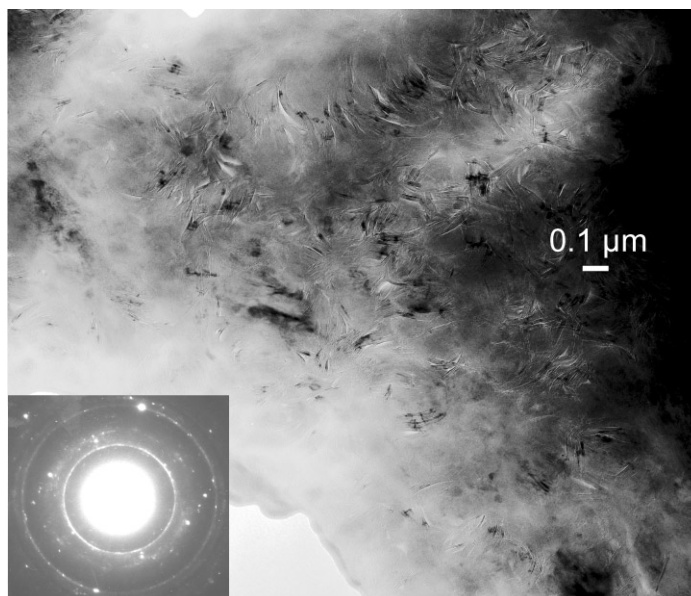


Fig. 5.8. Low-magnification (35000x) bright field image of an area within f-type pinite. Randomly oriented tiny phyllosilicate crystallites float in a low-contrast amorphous-like matrix. The ratio of crystallites : amorphous-like matrix is relatively high. The corresponding SAED pattern is powder-like (inset). For further see section 5.6.2.

patterns were often lost in a few seconds at focused beam. By tilting the specimen, individual crystals or packets of layers, that seemed to float in an amorphous low-contrast matrix, passed through the appropriate orientation for contrast and lattice fringe imaging, respectively (Fig. 5.8). Obviously, randomly related and randomly oriented crystals with thicknesses rarely exceeding 150 - 200 Å along *c* and ca. 100 - 1000 Å in cross section are the major constituents of f-type pinite (Fig. 5.8 - 11).

SAED patterns correspond to random orientation as they are powder-like by showing a ring-like patterns (inset in Fig. 5.8), but may also yield a broad diffraction halo. The lack of crystallinity may be an effect of electron beam damage or a true feature of cordierite alteration. Randomness in orientation of crystals also contributes to lack of TEM contrast as individual crystals only produce contrast at appropriate orientation.

In summary, the involvement of amorphous material *sensu stricto* can not be excluded. Observed ratios of contrast-producing crystals to low-contrast amorphous-like areas vary strongly. Completely 'amorphous' areas as well as completely crystalline areas were found. Sporadically, larger packets of layers with thicknesses $\gg 200$ Å along *c* occur within f-type pinite areas. The packets of layers observed within f-type pinite are described in detail below.

Unfortunately, distinction of dark and bright f-type pinite (see section on samples and pinite types) was not successful. The nature of the zonation pattern remains unclear. Zones with ordered crystallite textures were not observed within f-type pinite. Crystallographic control of f-type pinite orientation could be verified by TEM (see below).

7Å phase and 7/14 Å mixed layering

In Fig. 5.9a and b, TEM contrast defines lattice fringes of constant 7Å spacing, forming packets of less than 20 layers thickness. TEM contrast varies along layers, which corresponds to changes in the orientation of lattice fringes, and a slight curvature is imposed on the packets (Fig. 5.9a, b). Such 7Å crystals occur frequently within f-type pinite and as they are relatively stable in TEM high vacuum, they should represent rather 1:1 berthierine than a kaolinite family mineral (e.g. Jiang & Peacor, 1991), which is confirmed by AEM data (see below). Layer termination within 7 Å layer stacks was rarely observed and the thickness of 7 Å crystals is below 150 - 200 Å in most cases. Random intergrowth of 7 Å and 14 Å layers was also found within f-type pinite (Fig. 5.9c) and presents some problems of interpretation (Amouric *et al.*, 1988; Gutherie & Veblen, 1990, Jiang *et al.*, 1992). 7Å berthierine is known to give rise to four-, three-, two- and mainly one-layer polytypes, displaying 28 Å, 21 Å, 14 Å and 7 Å spacing, and often shows randomness in the layer stacking (Bailey, 1980; Abdad-Ortega & Mieto, 1995, Amouric *et al.*, 1988). Chlorite can give rise to 7 Å periodicity resembling spacing of 1:1 phyllosilicates at certain conditions (e.g. Amouric *et al.*, 1988; Gutherie & Veblen, 1990). Therefore, depending on image conditions (focus, thickness, orientation) the appearance of 7 Å and 14 Å layer intergrowth can be interpreted as the true occurrence of a mixed-layered sequence of 7 Å and 14 Å layers as well as the exclusive existence of a 7 Å phase or a 14 Å phase, respectively (Amouric *et al.*, 1988, Gutherie & Veblen, 1990). In Fig. 5.9c, TEM contrast presents a tiny packet of layers with complex 7/14 Å mixed-layering of less than 100 Å thickness parallel c and of less than 200 Å thickness in cross section. Layers are straight and lattice fringe contrast is relatively constant and does not change from 7 Å to 14 Å or vice versa along layers. This argues in favour of true 7 Å and 14 Å layer intergrowth. Complex stacking of 7 Å and 14 Å layers is well-known from the non-equilibrium low-grade diagenetic parts of burial metamorphism and from low-grade hydrothermal environments. There, the 7Å phase (berthierine) was described as either the metastable precursor of 14 Å chlorite or as a retrograde replacement product of chlorite (e.g. Nelson & Roy, 1958; Ahn & Peacor, 1985; Amouric *et al.*, 1988; Abdad-Ortega & Mieto, 1995; Jiang *et al.*, 1992).

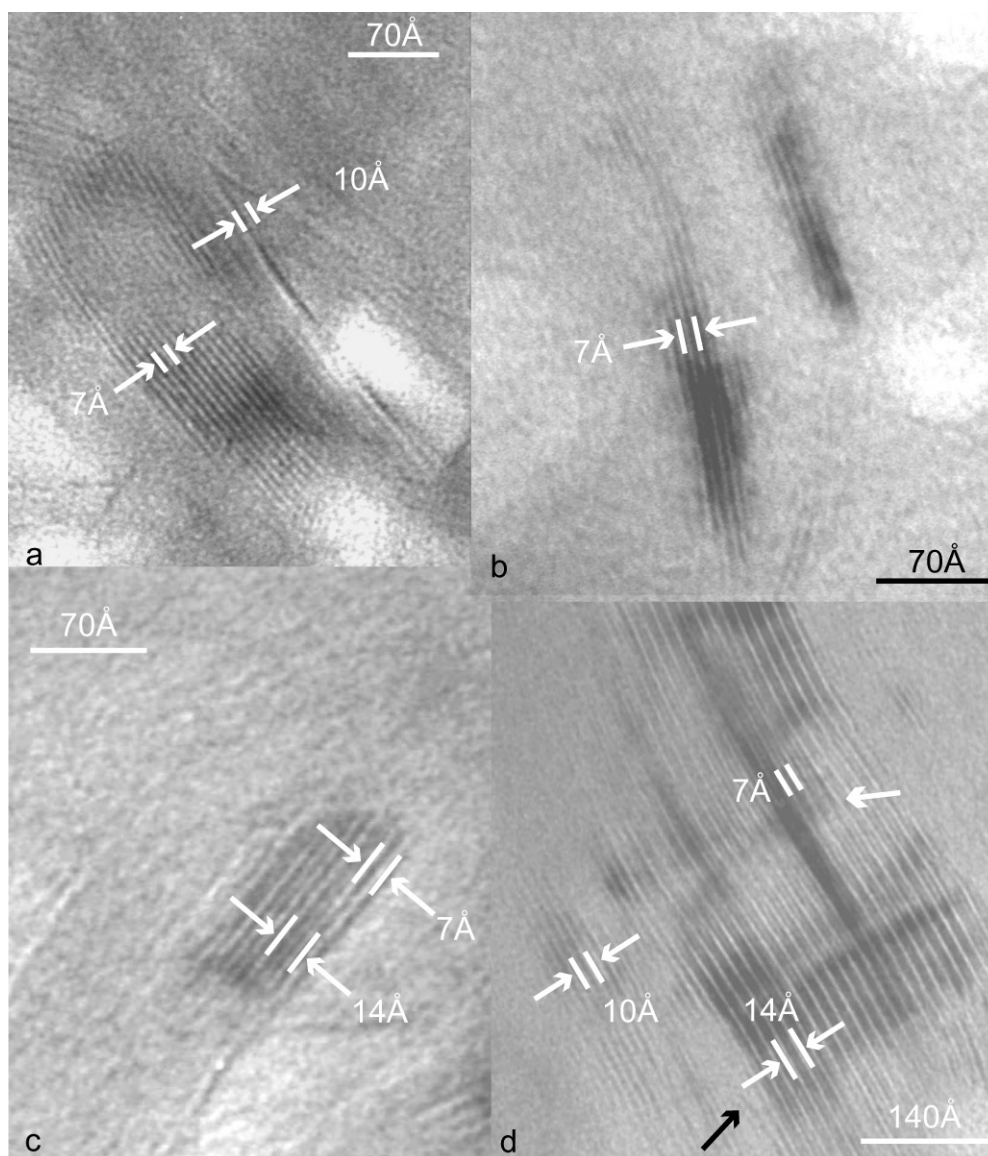


Fig. 5.9. Lattice fringe images of f-type pinite. (a) Stacking of 7 Å layers with some ≈ 10 Å layers appearing parallel and continuous. Other randomly related and poorly defined crystallites are also observable (b) Exclusive stacking of 7 Å layers. Both crystallites float in a low-contrast amorphous matrix. Small rounded areas of light contrast are an effect of electron beam damage. (c) Tiny packet of layers with random intergrowth of 7 Å and 14 Å layers. (d) Curved packet of 14 Å layers with a small region of 7 Å contrast. The single thick white arrow highlights a layer termination. In the lower left hand corner, 10 Å layers with variable contrast appearing parallel and continuous to 14 Å lattice fringes are observable. For further see section on TEM observations.

14 Å phases

Packets with exclusive stacking of 14 Å layers or of only minor interstratification with layers of other spacings were also found (Fig. 5.9d). In Fig. 5.9d, lattice fringe contrast defines a sequence of continuously bent layers with constant 14 Å spacing. There are layer terminations, TEM contrast is variable along layers and the changes in orientation of a few degrees over relatively large distances of some tens of Ångstroms is moderate. Thicknesses of observed 14 Å layer stacking range from 2 - 25 layers and bending of layers was often found. In most images, 14 Å periodicity appears at least partly as one thick bright layer and one thin

bright layer (Fig. 5.9d) or as one thick dark layer and one thin dark layer with the thin layers corresponding to brucite-like interlayer sheets (e.g. Gutherie & Veblen, 1990). The presence of both a thin and a thick fringe per 14 Å resembles chlorite 14 Å periodicity in published images (e.g. Lee & Peacor, 1985; Lee *et al.*, 1986; Ahn & Peacor, 1985; Ahn *et al.*, 1988; Amouric *et al.*, 1988). However, published images of chlorite from low-grade metamorphic environments show straight and regular lattice fringes defining relatively defect-free chlorite stacks (e.g. Ahn *et al.*, 1988; Jiang & Peacor, 1994) and not bending of lattice fringes and chlorite stacks relatively rich in defects as in this case. The presence of two layers per 14 Å clearly favours the presence of chlorite and not of vermiculite (Ruiz Cruz, 1999; Gutherie & Veblen, 1990). Moreover, Vali & Hesse (1992) reported hydrated vermiculite to collapse from 14 Å to 10 - 12 Å in TEM high vacuum.

Illite/ R₁ I/S and smectite

In Fig. 5.10a, layers appear as straight, parallel and regular lattice fringes with constant 10 Å interlayer spacing. The packet of layers is relatively defect-free, shows mottled contrast and layer terminations are absent. These features are characteristic for illite or ordered 1:1 illite-smectite (I/S) R₁ sequences (e.g. Ahn & Peacor, 1986; Ahn & Peacor, 1989; Peacor, 1992; Dong & Peacor, 1996; Nieto *et al.*, 1996). The lack of I/S R₁ 20 Å superperiodicity may be due to inappropriate image conditions or to the absence of I/S. The corresponding SAED pattern (inset in Fig. 5.10a) presents a well-defined 10 Å 00l sequence, which argues in favour of illite. In addition, another more abundant type of 10 Å layer stacking occurs within f-type pinite (Fig. 5.10b). This type was by far more sensitive to electron beam exposure with lattice fringes being lost in a few seconds at focused beam. Layers are subparallel, curved with a general wavy appearance and show variations in layer spacing (Fig. 5.10b), which may be caused by structural or compositional heterogeneities (Ahn & Buseck, 1990; Kim *et al.*, 1995). TEM contrast changes rapidly along layers and layer terminations occur (Fig. 5.10b, single black arrow). In most cases, thickness of individual 10 Å packets of layers is in the range below 150 - 200 Å. Over short distances, 20 Å superperiodicity was found to be superimposed on 10 Å substructures (Fig. 5.10b), indicating local occurrence of illite-smectite mixed layers (e.g. Gutherie & Veblen, 1989, 1990; Ahn & Peacor, 1986, 1989). All quoted features are consistent with characteristics for smectite with minor illite-smectite mixed layering (I/S R₀; e.g. Ahn & Peacor, 1986; Ahn & Peacor, 1989; Peacor, 1992; Dong & Peacor, 1996; Nieto *et al.*, 1996). Untreated smectite is well-known to collapse (dehydrate) in

TEM high vacuum, resulting in contraction of smectite 2:1 layers to $d_{(001)} \approx 10 \text{ \AA}$ spacing (e.g. Klimentidis & Mackinnon, 1986; Ahn & Peacor, 1986; Gutherie & Veblen, 1989, 1990). It is

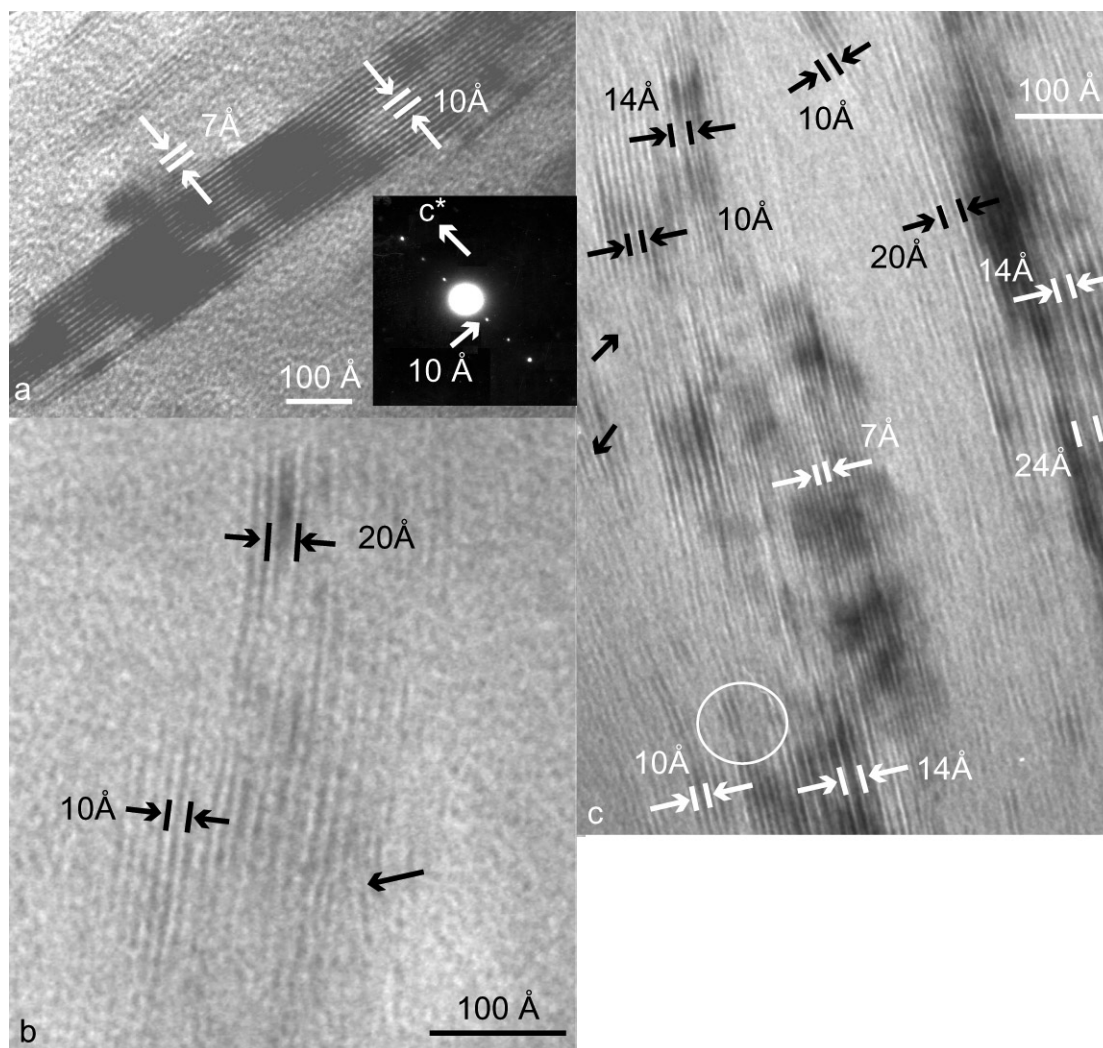


Fig. 5.10. Lattice fringe images of f-type pinite. In (a), TEM contrast defines relatively defect-free and constant lattice fringes with a 10 \AA periodicity (illite). The corresponding SAED pattern shows a well-defined and regular 001 10 \AA sequence; streaking parallel or perpendicular to c^* is absent. In (b) and (c), wavy and curved lattice fringes with a 10 \AA periodicity and variations in thickness and image contrast can be observed. Sporadically, 20 \AA superperiodicity may be imposed on the 10 \AA substructures over short distances (b and c). Single black arrow highlights a layer termination. For further see section 5.6.2.

known from the work of Gutherie and Veblen (1989, 1990) and of Ahn and Peacor (1986, 1989) that at overfocus conditions, illite/smectite compositional periodicity can be shown. However, 20 \AA superperiodicities imposed on 10 \AA substructures were rarely found here. The absence of such periodicities might be due to lack of illite-smectite ordering or of appropriate image conditions. Unfortunately, rapid beam-damage enhanced difficulties in focus control.

Complex mixed-layering

Evidence for complex random mixed-layering is given in Fig. 5.10c (stacking of 14 Å, 10 Å and 7 Å layers). 10 Å layers are mainly smectite-like, have a wavy appearance, show variable layer spacing and are subparallel (e.g. white circles, Fig. 5.10c). TEM contrast changes rapidly along layers and layer terminations occur. In general, lattice fringes are poorly ordered and rich in defects (e.g. thick arrows, Fig. 5.10c). Relatively defect-free domains with straight, regular and parallel 10 Å lattice fringes are less abundant, and over limited ranges a 20 Å periodicity may be superimposed on 10 Å substructure (Fig. 5.10c), reflecting local occurrence of 1:1 smectite-illite mixed layering (R_1) (e.g. Gutherie & Veblen, 1989, 1990; Ahn & Peacor, 1986, 1989). Random mixed layering of 10 Å layers and 14 Å chlorite layers, giving rise to single corrensite-like 24 Å superperiodicity, can also be observed in Fig. 5.10c. Ordered 24 Å mixed-layering with a thickness of about 300 Å was only found once within f-type pinite (not shown). Complex mixed-layering of 7Å and 14Å layers occurs and introduces the above quoted possibilities of interpretation.

SAED pattern

SAED patterns from f-type pinite areas do often not correspond to single crystals. Most SAED patterns show broad and diffuse 00l reflections, both parallel and normal to c^* . Spacing is only observable for low-order 00l reflections in most cases and non-00l reflections are weak, diffuse and non-periodic. Examples are given in Figs. 5.11a and b. Diffraction patterns with relatively well-defined and regular 00l rows as presented in the inset of Fig. 5.10a were rarely observed.

Orientation of f-type pinite

Fig. 5.11c presents low-magnification bright field images that give evidence for the crystallographic control of f-type pinitisation. In Fig. 5.11c, cordierite is penetrated by a pock-marked alteration vein that is oriented parallel to the crystallographic a direction. In contrast, crystallographic b direction was not found to be parallel to alteration veins (not shown). Unfortunately, bright field images and corresponding SAED patterns including the crystallographic c direction and showing its relation to alteration veins could not be obtained by TEM. Nevertheless, microscopic evidence already confirmed f-type pinite alteration veins to be parallel to c (Chapter 4).

5.6.3 I-type pinite

Prior to TEM investigations, the phase inventory and even the structural state of i-type was unclear (Chapter 4). Unfortunately, i-type pinite was not unambiguously recognised during TEM investigations. Only review of images revealed areas strongly suspected to represent i-type pinite. Fig. 5.11c shows areas of light contrast (white arrow) with irregular contours and irregular internal texture located between alteration veins and intact cordierite. Contrast of these areas is less regular and lighter than of adjacent rounded areas of light contrast induced by electron beam exposure, which indicates higher transparency for electrons. These are clearly unique features, which are in agreement with the results

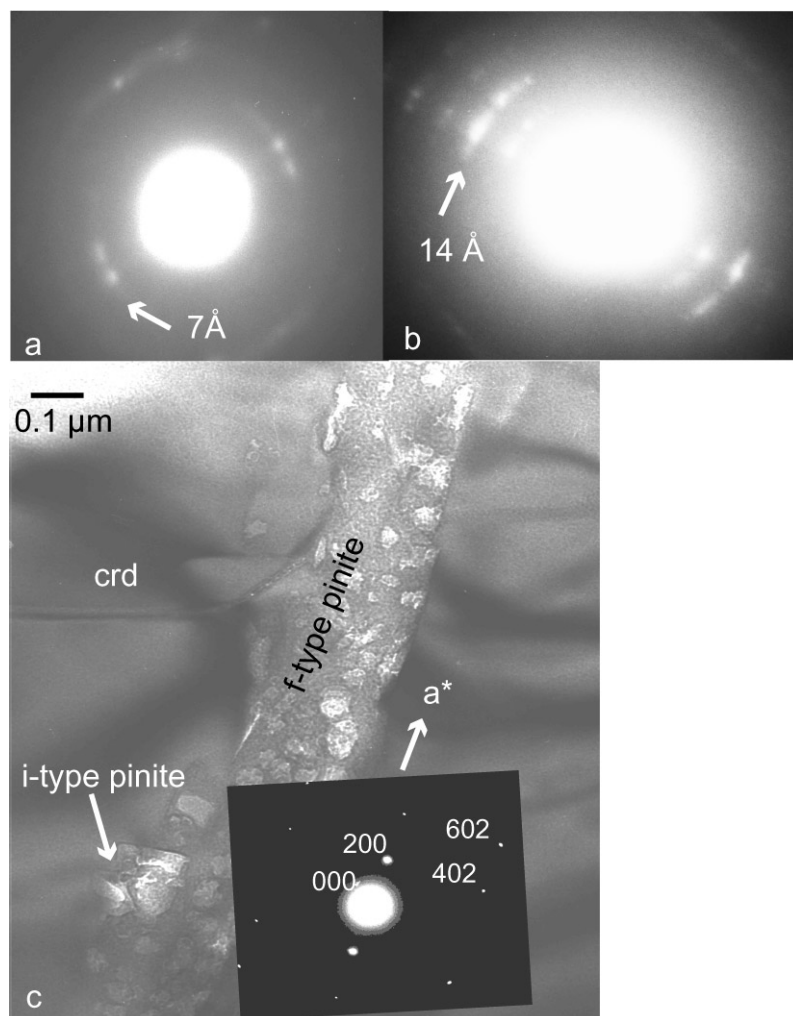


Fig. 5.11. SAED pattern (f-type pinite). (a) Poorly-defined 7 Å sequence with broad and diffuse 00l reflections. Spacing is only observable for low-order 00l reflections. Non-00l reflections are weak, diffuse and nonperiodic. (b) Poorly-defined 14 Å sequence with diffuse and broad 00l reflections. Streaking perpendicular to c^* is caused by variable layer orientation. Non-00l reflections are absent. (c) Low-magnification bright field images with corresponding electron diffraction pattern (corrected for magnetic rotation), showing crystallographic orientation of f-type pinite alteration veins parallel to a^*/a . For further see section on TEM observations.

of EM analyses, BSE imaging and petrographic microscopic investigations for i-type pinite (Chapter 4). Although TEM images show these areas to be amorphous, the true nature of i-type pinite remains unclear as amorphisation may be due to electron beam exposure and not a primary feature.

5.7 AEM data

Compositions of cordierite, f and m-type pinite based on AEM and EM data are given in Table 5.1. Due to extremely fine grain size, analyses within f-type pinite usually do not correspond to single packets of layers, but to several crystals. In contrast, within m-type pinite, thickness parallel and perpendicular to the basal plane was sufficient for analysis of individual packets of layers. However, due to mixed-layering within packets and to interstratification of packets parallel c^* , many AEM analyses of m-type also correspond to mixtures of phases. The number of the relevant mineral composition tables of the data appendix are given in the headings or in the text and have the form: Table II - 'number'.

5.7.1 M-type pinite (Table - II - 1)

M-type pinite also shows a wide range in composition. Total occupation of octahedral sites varies strongly from 3.94 - 5.45 c.p.f.u., between ideal dioctahedral and trioctahedral values. Fe ranges from 0.18 - 1.64 c.p.f.u., Mg from 0.00 to 2.53 c.p.f.u. and octahedral Al from 1.55

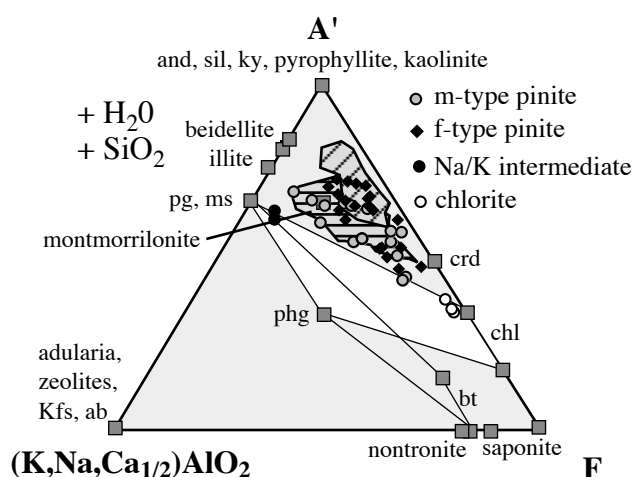


Fig. 5.12. (a) Ternary diagram A'-(K,Na,Ca_{1/2})AlO₂-F (F = FeO + MgO + MnO; A' = Al₂O₃ - (K,Na,Ca_{1/2})AlO₂) with a selected set of m and f-type pinite analyses plotted. White field: chlorite-muscovite field. Obliquely hatched grey field: EM data for f-type pinite. Horizontally hatched grey field: EM data for m-type pinite.

Table 5.1. EM and AEM data from sample Ho-10 and Ho-12.

	Crd*		f-type**												
	Crd	dark	bright	f-type**	f-type**	f-type	f-type	I/S R ₁	I/S R ₀	I/S R ₀	I/S R ₀	m-type	Na/K	chlorite	m-type**
number	1	2	3	4	6	7	8	9	10	12	13	14	15		
Si	5.02	5.01	5.85	5.77	6.23	5.01	6.60	6.82	6.40	5.40	6.45	5.62	5.77		
Al ^{IV}	3.95	3.95	2.15	2.22	1.77	2.94	1.40	1.18	1.60	2.60	1.55	2.38	2.17		
Al ^{VI}	-	-	3.30	3.05	3.46	1.69	3.47	3.49	3.22	1.56	3.70	2.93	2.82		
Ti	b.d.	b.d.	b.d.	b.d.	b.d.	b.d.	b.d.	b.d.	b.d.	b.d.	b.d.	b.d.	b.d.		
Fe ^I	0.90	0.96	0.91	1.05	0.55	2.06	0.34	0.42	0.67	1.37	0.18	3.01	1.14		
Mn	0.03	0.04	b.d.	0.02	b.d.	b.d.	b.d.	b.d.	b.d.	b.d.	b.d.	b.d.	0.02.		
Mg	1.07	1.05	0.50	0.74	0.46	1.61	0.32	0.50	0.52	2.53	0.09	5.67	0.72		
Ca	b.d.	b.d.	0.19	0.11	0.16	0.06	0.03	0.00	0.04	0.03	0.01	0.02	0.09		
Na	0.06	b.d.	0.02	0.03	0.17	0.18	0.15	0.07	0.05	0.57	1.06	0.14	0.04		
K	b.d.	b.d.	0.10	0.26	0.35	0.24	1.12	0.37	0.75	0.15	0.65	0.05	0.50		
X	-	-	0.31	0.40	0.68	0.48	1.30	0.44	0.84	0.75	1.72	0.21	0.63		
Oc	2.00	2.05	4.71	4.86	4.47	5.36	4.15	4.41	4.41	5.46	3.97	11.61	4.70		

Mineral abbreviations after Kretz (1983).

* EM analyses. Analyses without * represent AEM data. ** Average of 38 (dark f-type pinite), 49 (bright f-type pinite), 86 (m-type pinite) EM analyses.

¹ All Fe was calculated as Fe³⁺, for crd and chl as Fe²⁺.

Abbreviations are: X, Total interlayer occupancy. Oc, Total occupancy of octahedral sites.

F-type and m-type pinite analyses were normalised to 22 O, chlorite to 28 O. Fe was calculated as Fe³⁺ as reddish colours dominate within investigated pinite. Consequently, values for normalised Fe_{tot} contents and for total occupancy of octahedral sites represent lower limits.

Further AME cordierite composition data is available in the Data Appendix (Table II - 3).

- 3.70 c.p.f.u. Total X site occupancy varies strongly from 0.40 - 1.18 c.p.f.u., with majority of values between 0.5 and 1.0. K contents scatter from 0.05 - 1.17 c.p.f.u., Na from 0.00 - 0.76 c.p.f.u. and Ca does not exceed 0.07 c.p.f.u. X_{Mg} scatters between 0.17 and 0.66. The compositions are clearly outside the limited range of smectite and illite solid solution towards trioctahedral members (analyses 12, Table 5.1; e.g. Baileys, 1980; Srodon, 1986; Ransom & Helgeson, 1993). Therefore, most m-type pinites analysed by AEM represent mixtures of trioctahedral (chlorite, berthierine) and dioctahedral (I/S) phases. In $A'-(KNaCa_{1/2})O-F$ diagrams (Fig. 5.12) the data plots along the illite/smectite-chlorite join as it was found also during EM investigations (Chapter 4). Compositions corresponding to I/S R_1 mixed-layering (analysis no. 8, Table 5.1) and to random I/S with minor contamination by a trioctahedral phase (analyses no. 9 & 10, Table 5.1; Fig. 5.12) were also obtained. Additionally, compositions corresponding to chlorite with only minor contamination by alkali-bearing phyllosilicates were found (analysis 14, Table 5.1). Tetrahedral Al varies from 2.10 - 2.75 c.p.f.u., octahedral Al from 2.65 - 3.35 c.p.f.u. and $Al_{tot} : Si$ ratios from 0.93 - 1.03. Fe^{2+} ($Fe^{2+} = Fe_{tot}$) contents scatter from 3.01 - 3.25 c.p.f.u., Mg contents from 4.82 - 6.03 c.p.f.u. and X_{Mg} values from 0.61 - 0.65. Total tetrahedral and octahedral site occupancies range from 19.48 - 20.14 c.p.f.u. and X_{Mg} values from 0.61-0.65. In Fig. 5.12 these compositions plot close to the chlorite field and clearly represent trioctahedral chlorite of the chamosite-clinocllore series. Unfortunately, analyses of berthierine or chlorite/berthierine mixed-layering were not obtained.

Intermediate Na-K compositions

Compositions with $Na/(Na+K) \approx 0.63$, within the miscibility gap between muscovite and paragonite (e.g. Blencoe *et al.*, 1994), and total X site occupancies of 1.65 - 1.72 c.p.f.u., being compatible with values known for illite, were obtained (analyses 13, Table 5.1). Total occupancy of octahedral sites is close to ideal dioctahedral values (3.94 - 3.97 with all Fe assumed to be Fe^{3+}) and $Fe_{tot} + Mg$ is lower than 0.4 c.p.f.u. These analyses were made in relatively large-scale packets of layers that showed regular $\approx 20 \text{ \AA}$ superperiodicities over large distances, pulsed heavily at focused beam and were easily damaged by electron beam. Pronounced mottled contrast and lenticular voids parallel to basal planes, which were not observed in I/S mixed-layering, are further characteristics of these packets of layers. The corresponding SAED pattern (Fig. 5.13) contains only the 00l row with a relatively well-defined and sharp $\approx 10 \text{ \AA}$ and additional submultiple reflections. Some streaking parallel c^* is

observable as well. Splitting of 001 reflections, indicating occurrence of paragonite and muscovite, does not occur and the presence of only one set of reflections implies only one phase to be present. The additional reflections indicate 20 Å superstructures, may reflect some ordering in Na/K-interlayer distribution into separate layers and cannot be caused by polytypism (e.g. Peacor, 1992). The $d_{(001)}$ value ≈ 9.6 Å is close to that of paragonite. In A' -(KNaCa_{1/2})O-F diagrams Na/K intermediate analyses are close to ideal dioctahedral mica and lie on the chlorite - dioctahedral mica joint (Fig. 5.12). These packets of layers may

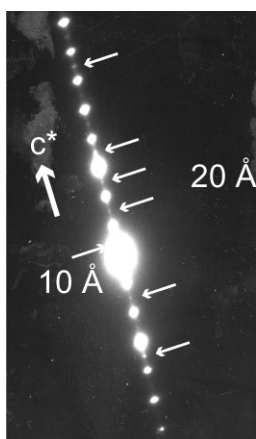


Fig. 5.13. SAED pattern from Na/K intermediate compositions with $\text{Na}/(\text{Na}+\text{K}) \approx 0.63$. A well defined ≈ 10 Å sequence and a poorly-defined ≈ 20 Å superperiodicity are observable. For further see section ‘Na-K intermediate’ in Chapter 5.7.1.

represent metastable Na/K-illite/mica with some ordering in the Na/K distribution. Similar metastable dioctahedral (Na/K)-phases have been reported earlier (Li et al.; 1992; Jiang & Peacor, 1993; Livi et al. 1997).

5.7.2 F-type pinite (Table II - 2)

Compositions of f-type pinite show large variations. Calculated occupancy of octahedral sites varies from 4.37 to 5.34 cation per formula unit (c.p.f.u.). These contents are between ideal dioctahedral and trioctahedral values. Si shows a range from 5.06 to 6.23 c.p.f.u. and octahedral Al is between 1.67 and 3.62 c.p.f.u. Total occupancy of X sites varies between 0.29 and 0.96 c.p.f.u. Average $\text{K}/(\text{K}+\text{Ca})$ ratios and $\text{K}/(\text{K}+\text{Na})$ ratios are 0.75 and 0.71, respectively, indicating K to be the principal interlayer cation. This is contrary to EM analyses, which showed Ca to be the dominant principal interlayer cation at least in dark f-type pinite. Analyses with $\text{Ca}/(\text{Ca}+\text{K}) > 0.5$ corresponding to the dark f-type pinite as well as analyses with Na as the dominating interlayer cation, both detected by EM analyses, were rarely found here. Analyses with relatively high Ca contents and $\text{Ca}/(\text{Ca}+\text{K})$ ratios were only

obtained as bulk analyses of amorphous areas, a specific Ca-bearing phase could not be identified. Obviously, f-type pinite represents complex mixtures of dioctahedral (smectite, I/S) and trioctahedral (chlorite, berthierine) phases as the compositions are clearly not compatible with the limited range of solid solution between dioctahedral and trioctahedral members (analyses 6-7, Table 5.1) (e.g. Baileys, 1980; Srodon, 1986; Ransom & Helgeson, 1993). Individual AEM analyses may be closer to ‘endmember’ compositions of phase mixtures than EM analyses due to the higher spatial resolution. This is confirmed by the arrangement of f-type pinite analyses in $A'-(KNaCa_{1/2})O$ -F diagrams (Fig. 5.12). In contrast to the EM data, the compositions of f-type pinite determined by AEM analyses do not strongly require the presence of an aluminous phase with balanced octahedral to tetrahedral charges as they plot closer to and inside the chlorite-smectite-illite field (Fig. 5.12). The remaining shift towards the A' -apex may be caused by alkali migration during AEM analyses, which is indicated to be less serious than during EM measurements by difference in $K/(K + Ca)$ ratios between AEM and EM analyses.

5.8 Discussion

TEM is a powerful tool for study of very fine-grained particles and gives detailed insight in the structure and phase inventory of fine-grained types of pinite. Especially for specifying the structural state and phase inventory of f-type pinite TEM is essential. Characterisation of pinite in focus of this study based purely on XRD data would easily have resulted in diagnosis matching most common pinite composition, namely to consist of chlorite and muscovite. Significance of XRD is limited by overlap of 00l peaks, loss of textural information and by its relatively high detection limit. In most previous studies, recognition of pinite was based on XRD and EM data. Only Abdad-Ortega & Mieto (1995) reported berthierine, chlorite and complex mixed-layering of both as products of cordierite alteration in a TEM, XRD, EM and AEM study and gave first detailed insight in structure and composition of pinite. It is clear that even their study, which focused on the thermodynamic relationship between chlorites and berthierine and not on characterisation of pinite, reflects only some details of the complex and manifold phenomenology of pinites.

5.8.1 Genesis of m-type pinite

The principal constituents of m-type pinite of this study are chlorite, berthierine, I/S R_1 mixed-layers, I/S R_0 mixed-layers, complex chlorite/berthierine mixed-layers and (Na,K)-illite. The phase inventory and crystal structure, the texture and thickness of packets of layers, the latter beyond the critical size for stable phases (e.g. Peacor, 1992), and the coexistence of packets not in line with the phase rule, match characteristics of clay mineral assemblages known from the early to late diagenetic part of burial metamorphism or from low-grade hydrothermal environments (e.g. Ahn & Peacor, 1989; Peacor, 1992; Dong *et al.*, 1997, Merriman & Peacor, 1999). These features as well as the occurrence of metastable intermediate (Na,K) illite clearly show that m-type pinite studied here lacks stable equilibrium and should have formed much below 200 °C (see below). The occurrence of overgrowth relations in trioctahedral and dioctahedral ‘subassemblages’ with berthierine and chlorite/berthierine mixed-layers replacing chlorite and I/S R_0 replacing I/S R_1 show that m-type pinite is formed by at least a two-stage process.

I/S mixed-layering has been mainly studied in burial metamorphic sequences. There, occurrence of I/S R_0 is restricted to the early diagenetic zone. At the transition from the early to the late diagenetic zone, I/S R_1 becomes the dominant dioctahedral phase (Merriman & Peacor, 1999 and reference therein). I/S R_1 is understood as a unique phase (Dong *et al.*, 1997), whose occurrence as an intermediate to smectite and illite in prograde sequences is determined by the Ostwald step rule (e.g. Ostwald, 1897, 1900; Morse & Casey, 1988; Peacor, 1992; Merriman & Peacor, 1999). The reverse reaction with smectite (I/S R_0) replacing I/S R_1 has been studied only rarely. Examples include Jiang & Peacor’s study (1990) describing alteration of diagenetic illite to I/S at very low temperatures (weathering) under hydrous conditions via dissolution and crystallisation. In analogy, the prograde transition of berthierine to chlorite is a commonly observed reaction (e.g. Nelson & Roy, 1958; Ahn & Peacor, 1985; Abdad-Ortega & Mieto, 1995; Schmidt *et al.*, 1999). The reverse reaction, with berthierine replacing chlorite, has been reported only rarely (e.g. Jiang *et al.*, 1992).

In this study, a prograde relationship between berthierine and chlorite and I/S R_0 and I/S R_1 , respectively, can be reasonably ruled out by the observed reaction textures and by the geological context. Also, low-temperature hydrothermal or retrograde replacement of one phyllosilicate by another commonly results in a wide range of overgrowth relations reflecting local and heterogeneous environments and non-equilibrium conditions (e.g. Jiang *et al.*; 1992; Jiang & Peacor, 1991, 1994), a feature that is also observed with the studied samples. In

summary, I/S R₁ mixed-layering plus chlorite represent the primary product of cordierite alteration and I/S R₀ mixed-layering and berthierine representing a secondary assemblage, resulting from the alteration of I/S R₁ and chlorite.

In burial metamorphic sequences, the coexistence of chlorite and I/S R₁ should, if at all, occur only over a very limited range as the first occurrence of chlorite is restricted to higher-grade conditions of the late diagenetic zone (Merriman & Peacor, 1999). This indicates that the formation of I/S R₁ plus chlorite should occur within a relatively narrow P-T range and/or under relatively specific fluid compositions. Most likely, the retrograde alteration in both the dioctahedral and trioctahedral subassemblages occurred within the same process and was driven by the infiltration of an additional fluid at very low-grade conditions (weathering) after the initial breakdown of cordierite to I/S R₁ plus chlorite (complex m-type pinite). The most accepted mechanism for low-temperature phyllosilicate to phyllosilicate transformation is dissolution/precipitation (e.g. Ahn & Peacor, 1986; Jiang & Peacor, 1990; Dong *et al.*, 1997).

In Chapter 4 two varieties of m-type pinite were distinguished: chlorite-muscovite and clay mineral-bearing assemblages (complex m-type pinite), the latter being the subject of this TEM study. The principle mechanism of m-type pinitisation suggested in Chapter 4 on the basis of petrography, SEM and EM data, is the breakdown of cordierite in the presence of an alkali-rich low-grade fluid ($K > Na$), which is confirmed by the TEM observations. It was suggested clay mineral-bearing (complex) m-type pinite is the low-temperature pendant of chlorite-muscovite pinite. Phase inventory, crystal size and texture of chlorite-muscovite pinite match characteristics of low-grade metamorphic assemblages and allow recognition by SEM and petrographic microscope investigations. In contrast, the phase inventory, crystal size, crystal structure and texture of complex m-type pinite resemble those of clay mineral assemblages from low to very low-grade environments and full recognition is restricted to TEM. The proportions of alkali-bearing to non-alkali-bearing phyllosilicates may be simply controlled by a_{K^+} , a_{H^+} etc. of the fluids.

5.8.2 Genesis of f-type pinite

The principal crystals or packets of layers detected by TEM within f-type pinite are berthierine, illite, smectite and chlorite, mixed-layering including 7/14 Å, 10/14 Å, I/S R₀ (and R₁?) and complex mixed-layering of 7 Å, 10 Å and 14Å layers. Coexistence of these phases clearly violates the phase rule. Most packets of layers are highly imperfect and heterogeneous in structure. Thickness of individual packets of layers is far beyond the critical values for

stable phases (e.g. Peacor, 1992). These features clearly show f-type pinitisation to be a very-low-temperature non-equilibrium process, possibly weathering.

Randomness in orientation points to direct *in situ* crystallisation of packets of layers, either from a solution present in alteration veins or from a pre-existing gel-like or amorphous material. Broad diffraction halos and lack of TEM contrast at the very beginning of electron beam exposure make it likely that amorphous material, now only partially preserved, is the primary metastable product of f-type pinitisation. This initial leaching/solution was clearly controlled crystallographically. It followed the crystallographical cell dimensions *c* and *a* of cordierite, which is reasonable as along these directions and especially along the *c* direction H₂O diffusion is relatively fast (Casey & Bunker, 1990). In fact, petrography often showed alteration veins oriented parallel to *c* to be significantly longer than in directions perpendicular to *c*. Subsequent to the formation of amorphous material, highly imperfect clay minerals as more stable secondary phases grew. It is unclear whether growth of packets of layers within f-type pinite is due to one or several processes of fluid infiltration, respectively. Material of such poor crystallinity is extremely sensitive to secondary overprint and growth of crystals during relatively younger m-type pinitisation is likely. Heterogeneity in crystal structure and in proportions of crystalline to amorphous material give evidence for local control of f-type pinitisation and possible subsequent processes.

The occurrence of corresponding chemical and optical zonation pattern (dark and bright f-type pinite) suggested that these pattern may represent discrete bands of leaching and precipitation (Chapter 4). Formation of amorphous material as a primary, but intermediate product of silicate weathering with initial etching along crystallographically controlled directions and subsequent *in situ* crystallisation of highly imperfect clay minerals as more stable secondary phases has been reported earlier (e.g. Eggleton & Buseck, 1980). Unfortunately, correlation of dark and bright f-type pinite and corresponding isotropic and slightly birefringent behaviour with specific structures in TEM images was not successful here. It is possible that the bands are simply domains with high portions of amorphous and crystalline material, respectively.

One of the key characteristics of f-type pinites is their enrichment in Ca, and the majority of f-type pinite EM analysis showed $\text{Ca}/(\text{Ca}+\text{K}) > 0.5$ (Chapter 4). EM data did not allow for an identification of the Ca-bearing phase. AEM data with similar $\text{Ca}/(\text{Ca}+\text{K})$ ratios were rarely found, which may be an effect of varying degrees of alkali migration or structural damage. AEM analyses with relatively high Ca contents and $\text{Ca}/(\text{Ca}+\text{K})$ ratios were all obtained as bulk analyses in amorphous areas. This strongly suggests that Ca is not bound in a

specific mineral, but does occur in the amorphous matrix, probably as a suspension-like component.

5.8.3 Relationship between f-type and m-type pinite

The chronological relationship between the pinite types is crucial for constructing a model of pinite genesis. In principal, there is the possibility that one type of pinite may be of secondary origin and not a primary products of cordierite breakdown.

Based on textural aspects and chemical data, f and m-type pinite were interpreted to represent primary and systematic processes of cordierite breakdown, each of which is driven by the infiltration of a hydrous fluid phase (Chapter 4). In case of the samples investigated here, f-type pinitisation was interpreted to represent the earlier process (Chapter 4). These assumptions are confirmed by the TEM investigations. The structural state, texture and grain size vary significantly between both types of pinite. Packets of layers within f-type pinite show randomness in orientation, are of a much finer grain size and their growth could be shown to be clearly not related to m-type pinite crystals. The involvement of amorphous material as the primary, but intermediate product of f-type pinitisation is likely. In analogy, m-type pinite phyllosilicates are not resorbed in contact to f-type pinite, often show a preferred orientation and can be shown to have grown directly at the expense of cordierite (Fig. 5.3). Moreover the observed reaction textures prove, that the primary m-type pinite assemblage (chlorite plus I/S R_1) reacted by transformation into secondary berthierine plus I/S R_0 along layers and not by breakdown to amorphous-like material on the infiltration of an additional very low-grade fluid. Considering that m-type pinite of this study is texturally the more interior type of pinite all these features show both types of pinite to represent separate processes of pinitisation with f-type pinitisation being the earlier process.

5.9 Summary and conclusions

Combined lattice fringe imaging, SAED and AEM allowed for a detailed characterisation of f- and m-type pinite in retrogressed HT cordierite-bearing migmatites of the Schwarzwald.

(1) Complex clay mineral-bearing m-type pinite of this study has the principal constituents chlorite, berthierine, I/S R_1 and I/S R_0 mixed-layers, Na/K-illite and random chlorite/berthierine mixed-layers. The observed features are similar to those of non-equilibrium assemblages from early to late diagenetic parts of burial metamorphic sequences.

Complex clay mineral-bearing m-type pinite lacks stable equilibrium and should have been formed much below 200 °C. In this case, its genesis is a complex two-stage process, with chlorite and I/S R₁ representing the primary product of m-type pinitisation. Secondary berthierine and I/S R₀ are formed by the replacement of chlorite and I/S R₁ via a dissolution/precipitation process driven by the infiltration of an additional very low-grade fluid.

(2) Basing on EM data, the alteration of cordierite by an alkali-rich (K > Na) low-grade hydrothermal fluid was thought to be the principle mechanism of m-type pinitisation (Chapter 4). This is in line with the TEM investigations presented here. Clay mineral-bearing (complex) m-type pinite is considered to be the low-temperature pendant of chlorite-muscovite pinite.

(3) F-type pinite consists of randomly related and randomly oriented tiny phyllosilicates, floating in an amorphous-like low contrast matrix. The principal crystals or packets of layers detected by TEM are berthierine, illite and/or I/S R₁, smectite and chlorite, mixed-layers including 7/14 Å, 10/14 Å, I/S and complex mixed-layering of 7 Å, 10 Å and 14Å layers. Lack of perfect and homogeneous structures and enhanced thickness of individual packets of layers indicate f-type pinitisation to be a very low-grade process (weathering).

(4) F-type pinitisation should be considered as the alteration of cordierite by a very low-grade hydrous fluid phase. The initial breakdown/dissolution of cordierite was clearly controlled crystallographically and followed the crystallographical cell dimensions c and a. TEM observations favour amorphous material to be the primary, but intermediate product of cordierite alteration, followed by the growth of highly imperfect clay minerals as the more stable secondary phase assemblage, most likely during several phases of crystal growth.

(5) The model of f-type pinitisation by leaching and precipitation/repolymerisation in discrete bands of distinct chemical composition and optical features (dark and bright f-type pinite; Chapter 4), could neither be confirmed nor disproved.

(6) Due to the extreme sensitivity of i-type pinite to electron beam exposure, no additional conclusions concerning its composition, structural state and genesis could be drawn in this study.

(7) Hints for a complex process of pinitisation with the isochemical breakdown of cordierite as a first step and the sericitisation of the primary breakdown assemblage as a second step (Chapter 4.2; Seifert & Schreyer, 1970) were not found.

6. FTIR: The Role of the Structural Channels in the Process of Pinitisation

6.1 Abstract

H₂O and CO₂ contents of partly pinitised cordierite from the Bayerische Wald (Bw-3) and the Schwarzwald (Ho12 and Wa-4) were determined by *in situ* FTIR measurements. In focus of this study is the possible role of the structural channels in hydrous breakdown of cordierite (pinitisation). Most spectra collected at cordierite rims in contact to pinite result from interference of pinite and cordierite spectra and do not reflect true hydration of cordierite channels. Therefore, a systematic change of cordierite channel composition as a key step within the process of pinitisation is not indicated. Despite the fact that all samples experienced infiltration of several hydrothermal aqueous fluids, recorded by the alteration of cordierite to various types of pinite, a post-peak re-equilibration with hydrous fluids can be ruled out. Nevertheless, the preferred orientation of one pinite type parallel to the crystallographic c axis indicates that the structural channels exert a major control on cordierite dissolution/leaching. Intra-grain spectra display relative homogenous volatile contents within and between grains and show cordierite volatile contents of all samples to fall substantially below the H₂O-CO₂ saturation surface. Calculation of $a_{\text{H}_2\text{O}}$ and H₂O melt contents by using published models of Harley & Carrington (2001) and Burnham (1994) show volatile contents of Bw-3 cordierite (0.59 ± 0.02 wt% H₂O and 0.052 ± 0.008 wt% CO₂) to be consistent with minimum H₂O content of granitic melt at the estimated peak conditions (850 - 900 °C and 0.50 - 0.70 GPa, published P-T conditions of...Kalt *et al.* (1999)). The volatile contents of cordierite from the Schwarzwald (0.056 ± 0.03 wt% H₂O and 0.049 ± 0.024 wt% CO₂ for Wa-4; 0.50 ± 0.07 wt% H₂O and 0.024 ± 0.009 wt% CO₂ for Ho-12) are lower than those attained during equilibration with a melt at the specified P-T conditions (730 - 780 °C and 0.40 and 0.45 GPa, published P-T conditions of Kalt *et al.* (2000a)) and could potentially result from extensive post-peak leakage. Due to uncertainties in D_w calculation and in estimation of peak P-T conditions for the samples, however, I prefer to interpret the cordierite H₂O contents of the SW samples to still record partitioning with a water-undersaturated partial melt.

6.2 Introduction

Cordierite, (Mg,Fe)₂Al₄Si₅O₁₈(nH₂O,mCO₂), is a common mineral in aluminous medium to high-grade metamorphic rocks and migmatites. It can incorporate volatiles within its large structural channels, the dominant species being molecular H₂O and CO₂ (e.g. Cohen *et al.*, 1977; Goldman *et al.*, 1977; Armbruster & Bloss, 1980, 1982; Vry, 1990). Cordierite is thus a potential monitor of fluid conditions (e.g. Vry, 1990; Kalt, 2000; Harley, 1994; Harley, & Carrington, 2001; Harley *et al.*, 2002). Detection of volatile species by infrared (IR) spectroscopy (e.g. Goldman *et al.*, 1977) revealed channel H₂O to occur in two principle orientations, I and II, and the long axis of CO₂ molecules to be oriented parallel to the crystallographic a direction. The H-H vector of H₂O I is

aligned parallel to the channels long axis (parallel to crystallographic *c*) whereas the H-H vector of H₂O II is parallel to crystallographic *b* (Fig. 1.3). H₂O II is assumed to interact with alkali cations that may be present in cordierite channels, which does not seem to be the case for H₂O I (Goldman *et al.*, 1977). On the basis of recent IR and Raman spectroscopic studies, Kolesov & Geiger (2000) additionally identified H₂O with its H-H vector parallel to crystallographic *a*, showing no interaction with alkalis.

Volatile contents of cordierite were investigated in the course of experiments, comparative studies of natural cordierites and in the context of regional of petrological studies (e.g. Hörmann *et al.*, 1980; Johannes & Schreyer, 1981; Armbruster *et al.*, 1982; Jochum, 1986; Vry *et al.*, 1988; Le Breton, 1989; Santosh *et al.*, 1991; Vry *et al.* 1990; Fitzsimons, 1994; Harley, 1994; Carrington & Harley, 1996; Harley & Carrington, 2001; Thompson *et al.*, 2001; Harley *et al.*, 2002). At fluid-present conditions the total abundance of channel H₂O, CO₂ is a function of pressure, temperature and X_{CO₂} of the coexisting fluid (Johannes & Schreyer, 1981). The volatile contents of cordierite from migmatitic and granulitic terranes turned out to be much lower than saturation values known from experiments with H₂O-CO₂ fluids at equivalent P-T conditions (e.g. Vry *et al.*, 1990; Harley, 1994; Fitzsimons, 1994; Carrington & Harley, 1996). The reason for this volatile deficiency was assigned to volatile leakage during post peak P-T evolution (Vry *et al.*, 1990) or to partitioning between cordierite and melt in environments devoid of a free volatile phase (e.g. Harley, 1994; Stevens *et al.*, 1995; Carrington & Harley, 1996, Harly & Carrington, 2001; Harley *et al.*, 2002). Recent experiments and modelling of the cordierite H₂O-CO₂ saturation surfaces (Thompson *et al.*, 2001; Harley & Carrington, 2001; Harley *et al.*, 2002) even show equilibrium channel volatile contents of cordierite at high X_{CO₂} and specified P-T conditions to be significantly lower than early models of Kurepin (1984) and Vry *et al.* (1990) had suggested. Consequently, cordierite stated as deficient in volatiles by these early models may instead be saturated in CO₂ and H₂O (Thompson *et al.*, 2001; Harley & Carrington, 2001; Harley *et al.*, 2002).

Obviously, much emphasis has been put on the question whether cordierite can serve as a monitor of fluid conditions in high-grade metamorphism and crustal anatexis (e.g. Vry *et al.*, 1988; Kalt, 2000; Harley, 1994; Fitzsimons, 1994; Carrington & Harley, 1996; Harley & Carrington, 2001; Harley *et al.* 2002). Less has been done to explore the behaviour of channel volatiles in low to very low-grade P-T settings. This is particularly of interest as hydrous alteration of cordierite takes place at these conditions (pinitisation). The term 'pinite' was established for various fine-grained breakdown products of cordierite (Chapter 4; Lacroix, 1962; Deer, 1962). The fact that some authors found pinite veins to be oriented parallel to the crystallographic *c* axis (e.g. Schreyer *et al.*, 1993) or to the *c* and *a* axis (Chapter 4) suggests that the structural channels may play a key role in the process of pinitisation and may be the major sites of dehydration or hydration. Moreover, hydration experiments in the P-T range below the stability of cordierite (200 - 400 °C, P_{tot} = P_{H₂O} ≈ 0.15 - 0.44 GPa) by Jochum (1986) resulted in rapid breakdown of natural Na-bearing and

synthetic Na-free Mg-cordierite along veins oriented parallel to crystallographic *c*. In addition, Casey & Bunker (1990) argued on a theoretical basis that the structural channels of beryl, which is quasi isostructural to cordierite, control the leaching behaviour as the channel diameter (up to 5 Å) is large enough to accelerate H₂O diffusion significantly.

In a recent *in situ* Fourier Transform Infrared Spectroscopy (FTIR) study, Kalt (2000) found the H₂O channel contents of cordierite from migmatites of the Bayerische Wald (BW) to be consistent with equilibration with a H₂O-undersaturated peraluminous melt at the peak of metamorphism. However, for one sample, she reported a systematic difference in H₂O contents between cordierite cores and rims with the rims being higher in H₂O, which could be due to retrograde modification of the channel composition, possibly in the context of pinitisation. Finally, Harley *et al.* (2002) suggested that the release of preserved 'excess' channel H₂O during decompression and cooling may provide a mechanism for hydrous alteration of cordierite (pinitisation). However, it is still unclear if and in which way the structural channels of cordierite enhance or accelerate pinitisation.

In this chapter the H₂O and CO₂ contents of partly pinitised cordierites of migmatites from the BW and the SW were analysed by *in situ* FTIR. The aim was to find out whether pinitisation of cordierite goes along with a systematic change in the cordierite channel volatile contents and to specify the possible role of the channels in the process of pinitisation.

6.3 Samples, geological settings and pinite types

All three samples investigated were selected from the sample suite of Chapter 4 and originate from the BW (Bw-3) and the SW (Ho-12, Wa-4). Both crystalline complexes are part of the internal zone of the Variscan orogenic belt in central Europe. The BW forms the south-western margin of the Bohemian Massif and the SW is located at the eastern flank of the Oberrheingraben. In both crystalline complexes, low-pressure high-temperature (LP-HT) metamorphic gneisses and migmatites and granites are the most abundant rocks.

Cordierite in the SW basement formed in the course of a final equilibration at ~730 - 780° C / 0.40 - 0.45 GPa at approximately 330 Ma. There is evidence of partial melting during the LP-HT stage, but not as widespread as in the BW (Kalt *et al.*, 1994, Kalt *et al.*, 2000a). The migmatites of the BW followed a clockwise P-T path and suffered biotite dehydration melting in the absence of an aqueous fluid during prograde P-T evolution (Kalt *et al.*, 1999). Peak metamorphic conditions of ~850 - 900° C / 0.5 - 0.7 GPa were deduced from dehydration melting experiments, but mineral equilibria reflect equilibration conditions of 770 - 846 °C and 0.44 - 0.51 GPa (Kalt *et al.*, 1999). The degree of melt segregation varies between different types of migmatites (Berger & Kalt, 1999). The thermal peak for the BW migmatites was dated at 326 - 323 Ma (Kalt *et al.*, 2000b).

Previous FTIR studies showed cordierite from the BW to contain 0.38 - 0.74 wt% H₂O and 0.04 - 0.10 wt% CO₂ (Kalt, 2000) and cordierite from the SW to contain 0.56 - 1.00 wt% H₂O and 0.02 - 0.06 wt% CO₂ (Kalt, unpublished data), respectively. One of the samples from the BW (Bw-6) showed systematic differences in H₂O content between cordierite cores and rims with the rims being higher in H₂O (Kalt, 2000).

Table 6.1: *Sample Characteristics*

sample	provenience	primary phase assemblage	degree of pinitisation of individual crd grains	types of pinite
Bw-3	Bayerische Wald	pl-qtz-ms-crd-Kfs-sil-ilm	weak to complete	b-type; m-type fi-type
Ho-12	Central Schwarzwald	crd-bt-qtz-pl-ilm-Kfs	intermediate to complete	b-type; m-type; f-type; i-type
Wa-4	Southern Schwarzwald	crd-bt-pl-Kfs-sil-ilm-qtz	intermediate to complete	b-type; m-type; f-type fi-type

Mineral abbreviations after Kretz (1983). Pinite types are: b, border; m, mat; f, fissure (vein); i, isotropic. For further information see Chapter 4.4.

All samples (Bw-3, Ho-12, Wa-4) were extensively studied by electron microprobe (EM), scanning electron microscopy (SEM) and petrographic microscopy (Chapter 4), and Ho-12 was also subject to extensive transmission electron microscope (TEM) studies (Chapter 5). Four pinite types were detected by these methods, and all of them are present in the samples investigated in this study (Table 6.1). Systematic relationships between textural position, grain size, chemical composition and, as far as could be deciphered, phase assemblages in the different pinite types suggest that each pinite type formed by a distinct process (Chapter 4). The fact that samples coming from different areas show largely the same features suggests that the suggested classification (Chapter 4) describes systematic and general features of cordierite breakdown that are at least to a certain degree independent of local late- to post-metamorphic conditions.

All pinite types contain mainly hydrous phyllosilicates and hydrous amorphous-like material. Other retrogression features, like the sericitisation of feldspar, are also present. Each type of pinite monitors the infiltration of cordierite by an aqueous fluid phase. The P-T conditions of these fluid

infiltrations cannot be determined exactly, but encompass a broad range within and mostly below the stability field of (Fe,Mg) cordierite (Chapter 4). In principle, each of the fluids bears the potential to exchange or equilibrate with the channel volatiles, as long as the breakdown of cordierite, induced by the infiltration of these fluids, is significantly slower than the exchange of volatile species.

6.4 Analytical techniques

Analytical conditions of electron microprobe (EM) investigations are described in Chapter 4. H₂O and CO₂ contents of cordierite were determined by high-resolution Fourier-Transform Infrared Spectroscopy (FTIR) using an infrared microscope IR Scope II attached to a Bruker IFS88 FTIR spectrometer purged with dry air at the Institute for Mineralogy, Hannover. Analytical equipment included a narrow band mercury cadmium telluride (MTC) detector with near-infrared (NIR) equipment (range 600 - 10000 cm⁻¹), a KBr beamsplitter and a GLOBAR light source. The spot size was 20x20 μm and the number of accumulated scans 100 per analysis. The IR spectra were collected *in situ* from doubly polished thick section with thickness of approximately 200 μm.

H₂O and CO₂ are well resolved in IR spectra of cordierite with the CO₂ peak near 2349 cm⁻¹ and peaks produced by asymmetric stretching of H₂O molecules at approximately 3689 cm⁻¹ (type I water) and at 3632 cm⁻¹ (type II water; e.g. Goldman *et al.*, 1977; Aines & Rossman, 1984; Vry *et al.* 1990). Peaks due to symmetric stretching of H₂O II are resolved near 3574 cm⁻¹ (e.g. Goldman *et al.*, 1977; Aines & Rossman, 1984; Vry *et al.* 1990). In this study, peaks for H₂O and CO₂ were observed at reported wavenumbers (Fig. 2a). Quantification of IR data was performed by using the calibration of Vry *et al.* (1990). The concentrations of H₂O and CO₂ were calculated by the equation $c = A/d \cdot \epsilon$ (c, concentration; A, measured absorbance; d, thickness of cordierite; ε, recalculated absorbance of Vry *et al.* (1990) to 1 wt% H₂O and CO₂, 1 μm thickness and 100% cordierite). The most serious errors on H₂O and CO₂ concentrations are introduced by the orientation effect, which is especially pronounced with IR on polished thick sections, because the spectra are obtained from single grains with different orientation. To reduce the orientation effect, 2 FTIR spectra collected *in situ* by rotating the sample 90° between both measurements were performed and combined to one data point.

Cordierite grains were tested for systematic core to rim variations in volatile contents, particularly rims in contact to pinitite were analysed. At the rims, carefully selected areas that did not show any sign of pinitisation under the microscope were analysed. For each sample, several profiles through areas of intact cordierite enclosed in pinitite were run. Additionally, spectra were collected from pinitites.

Calculation of activity of H₂O ($a_{\text{H}_2\text{O}}$) and CO₂ (a_{CO_2}) of high-grade melting and metamorphism and estimation of melt H₂O contents is based on recent models of the cordierite volatile saturation

surface and D_w relationships presented in Thompson *et al.* (2001), Carrington & Harley (2001) and Harley *et al.* (2002). To calculate $a_{\text{H}_2\text{O}}$ and a_{CO_2} equation (4) and (8) of Harley *et al.* (2002) were applied:

$$(4) \quad a_{\text{H}_2\text{O}} = [n/(1 - n)]\{\exp[-4203 (\pm 320)/T + 11.75 (\pm 0.33)]/f_{\text{H}_2\text{O}}\},$$

$$(8) \quad a_{\text{CO}_2} = [m/(1 - m)]\{\exp[(-3073) (\pm 200) - (0.3023P)]/T + 13.1 (\pm 1.2)]/f_{\text{CO}_2}\},$$

N and m are the number of H_2O and CO_2 molecules per formula unit of volatile-free cordierite (18 O), T is temperature in degree Kelvin, P is pressure in bar, and $f_{\text{H}_2\text{O}}$ and f_{CO_2} are the fugacities of H_2O and CO_2 at the relevant P - T conditions. The H_2O melt contents were calculated by Harley *et al.* (2002) using the equations of Burnham (1994):

$$a_{\text{H}_2\text{O}} = k_w(X_w) \text{ [at } X_w < 0.5\text{]}$$

and

$$a_{\text{H}_2\text{O}} = 0.25k_w[\exp[[6.52 - (2667/T)) X_w]] \text{ [at } X_w < 0.5\text{]}$$

where X_w is the mole fraction of water in an 8O formula unit melt and k_w is a P - T dependent coefficient experimentally determined by Harley & Carrington (2001) and Johannes & Holtz (1996) and thermodynamically defined by Burnham (1994):

$$\ln k_w = 5 + (\ln P)(4.481 \cdot 10^{-8} T^2 - 1.51 \cdot 10^{-4} - 1.137) + (\ln P)^2(1.83 \cdot 10^{-8} T^2 - 4.882 \cdot 10^5 T + 4.656 \cdot 10^2) + 7.80 \cdot 10^{-3} (\ln P)^3 - 5.012 \cdot 10^{-4} (\ln P)^4 + T(4.754 \cdot 10^{-3} - 1.62 \cdot 10^{-6} T).$$

In case of equilibrium, the $a_{\text{H}_2\text{O}}$ defined by cordierite equals $a_{\text{H}_2\text{O}}$ in melt and therefore allows calculations of the H_2O melt content. Calculations based on experimentally derived values for k_w (Harley & Carrington, 2001) gave only small deviations within error from calculations with Burnham's k_w (1994).

The partitioning coefficient D_w of H_2O between cordierite and coexisting melt in Table 6.3 was calculated by dividing the calculated melt H_2O contents by the detected cordierite H_2O contents (Harley *et al.*, 2002).

6.5 Cordierite compositions

6.5.1 Major element concentrations

The major element concentrations of cordierite are given in Chapter 4 and in Table 6.2. All investigated cordierite grains are fairly homogenous. Significant systematic core to rim variations were not found. The cordierite compositions can be viewed in Table 6.2. Minor variations can be observed for X_{Mg} , Na and Mn contents. Al/(Al+Si) ratios are constant. X_{Mg} ranges from 0.54 - 0.56 for Ho-12, from 0.48 - 0.52 for Wa-4, from 0.55 - 0.59 for Bw-3. Mn contents vary from 0.02 - 0.04 cations per formula unit (c.p.f.u.) for all samples. Ti, Ca and K are below the detection limit. Na contents scatter from 0.02 - 0.04 c.p.f.u. for the samples of the BW and SW. Systematic core to rim variations in Na have not been found for any sample. Significant changes in the Na contents along profiles through single grains are always associated with increasing K and Ca contents and with decreasing oxide totals, which clearly indicates that hydrous alteration products (pinite) have been analysed along with cordierite.

Table 6.2: Cordierite Compositions

	Ho-12 mean	Wa-4 mean	Bw-3 mean
Si	4.991±0.025	5.018±0.013	5.011±0.031
Al^{IV}	3.979±0.040	3.936±0.021	3.965±0.041
Σ^{IV}	8.970	8.954	8.976
Ti	b.d.	b.d.	b.d.
Fe*	0.895±0.016	1.010±0.034	0.848±0.031
Mn	0.035±0.003	0.031±0.003	b.d.
Mg	1.088±0.025	0.997±0.026	1.112±0.031
Σ^{VI}	2.019±0.021	2.039±0.025	1.987±0.029
Ca	b.d.	b.d.	b.d.
Na	0.047±0.015	0.037±0.005	0.066±0.008
K	b.d.	b.d.	b.d.
X_{Mg}	0.55±0.01	0.50±0.01	0.58±0.01

b.d.: below detection limit.

6.5.2 Cordierite intra-grain FTIR spectra

In all samples, well-defined cordierite IR spectra were collected on profiles from cores to marginal areas approximately 5 - 10 μ m away from the rims of grains (Fig. 6.2a). The mean volatile contents for each sample are presented in Table 6.3. The relevant tables in the data appendix are given in the headings have the form: Table - III - 'number'.

Wa-4 and Bw-3 (Table III - 3a and Table III - 1a)

The average $\text{H}_2\text{O}_{\text{tot}}$ contents of cordierite are 0.55 ± 0.03 wt% for Wa-4 and 0.59 ± 0.02 wt% for Bw-3. Intra-grain and inter-grains variations in $\text{H}_2\text{O}_{\text{tot}}$ contents exceeding the 2σ deviation within samples (6.6 % for Bw-3 and 12.4 % for Wa-4) were not detected for Bw-3 and Wa-4. In both samples $\text{H}_2\text{O I} : \text{H}_2\text{O II}$ ratios were found to be close to the usually observed 1 : 1 ratio (Tab. 6.3; Vry *et al.*, 1990). In sample Wa-4, variations in CO_2 contents in one grain slightly exceeded the 2σ deviation and may therefore not solely be due to the orientation effect. Significant inter-grain variations of CO_2 contents were not detected in sample Bw-3. The relative 2σ deviation of the average for CO_2 contents are $\sim 8\%$ for Bw-3 and $\sim 17\%$ for Wa-4.

Ho-12 (Table III - 2a)

The intra-grain spectra of sample Ho-12 show distinctive features. The vast majority of spectra shows the heights of peaks produced by asymmetric stretching of $\text{H}_2\text{O II}$ (3632 cm^{-1}) to be lower than those of peaks produced by asymmetric stretching of type I water (3689 cm^{-1} , Fig. 6.2d). In contrast, peaks produced by symmetric stretching of type II water are higher than those of type I water peaks in most cases (Fig. 6.2d). As these effects are restricted to certain grains, they are ascribed to be a result of the orientation effect (Kalt, 2000). H_2O and CO_2 contents calculated from these spectra yield 0.50 ± 0.07 wt% and 0.024 ± 0.009 wt%, respectively. $\text{H}_2\text{O I} : \text{H}_2\text{O II}$ ratios deviate strongly from the usually observed 1 : 1 ratio and come close to 3 : 2 (Table 6.3). A recalculation of H_2O contents assuming a $\text{H}_2\text{O I} : \text{H}_2\text{O II}$ ratio of 1 : 1 gives maximum H_2O contents of approximately 0.60 wt% H_2O . The relative 2σ deviation of the mean is around 30% for CO_2 and 15 % for H_2O . Significant intra or inter-grain variability in volatile contents were not detected for Ho-12.

6.5.3 Pinite FTIR spectra

Peaks collected within pinite do not represent H_2O trapped in the structural channel of cordierite, but match absorbance peaks known for free water, e.g. occurring in fluid inclusions (Fig. 6.2c). What all pinite H_2O peaks have in common is that they are in general asymmetric with a steep high wavenumber side and a smoother low wavenumber side and have a relatively high background (Fig. 6.2c). CO_2 peaks are still observable in pinite spectra, but are significantly lower than those collected from cordierite rims or cores in most cases.

6.5.4 FTIR spectra of outermost cordierite rims (Table III - 1b, III - 2b, III - 3b)

Cordierite rim spectra were collected at the outermost cordierite rims in contact to pinitite. They do not show any signs of pinitisation under the petrographic microscope. In all samples, the H₂O absorbance peaks of these spectra show systematic differences in heights and morphology

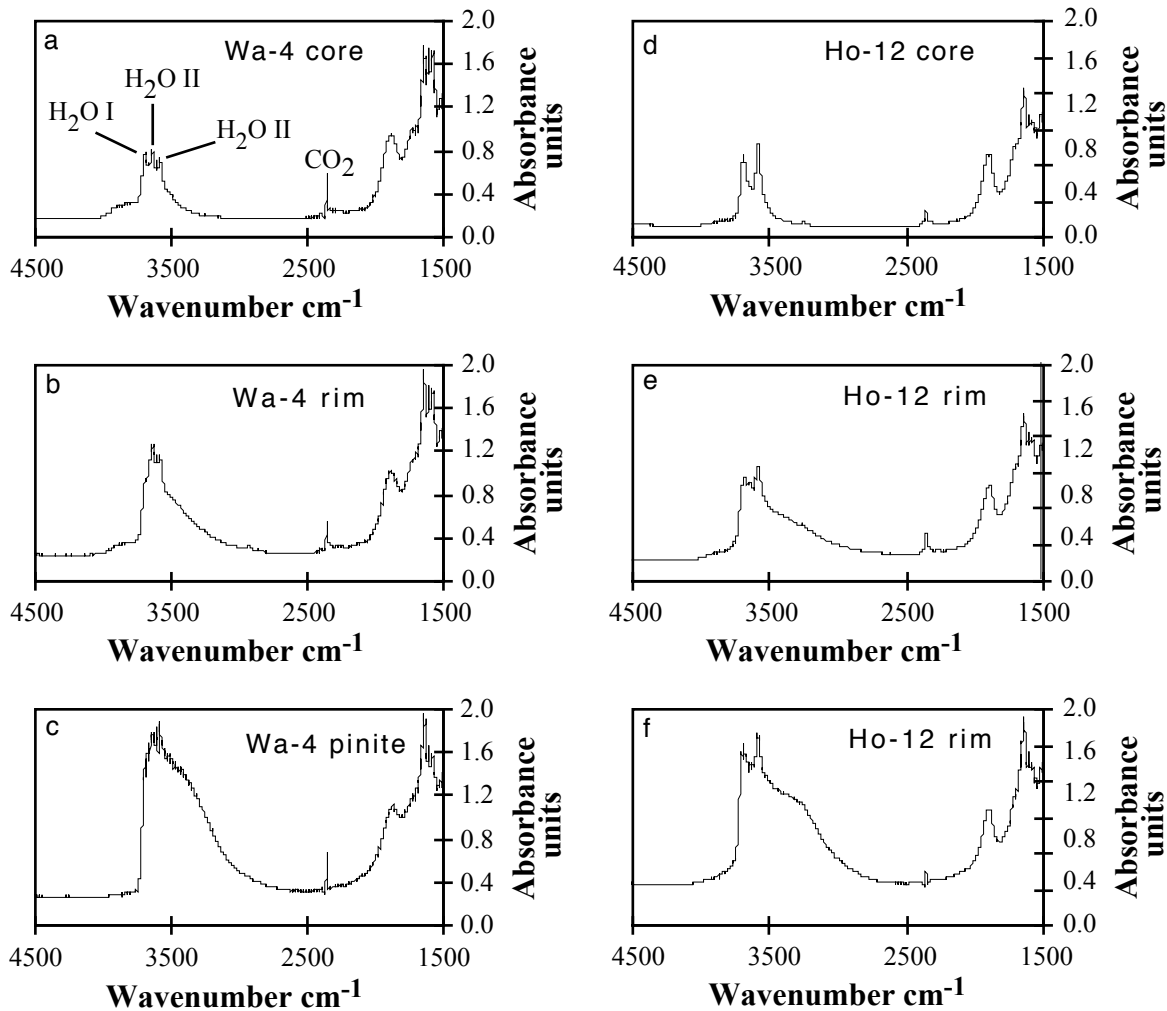


Fig. 6.2: FTIR spectra. (a) Typical intra-grain IR spectrum of cordierite obtained by *in situ* FTIR spectroscopy. The peaks of H₂O I, H₂O II and CO₂ occur at the positions reported by Vry *et al.* (1990). (b) Typical spectra obtained at cordierite rims in contact to pinitite, the H₂O peak is asymmetrically stretched to the low wavenumber side. Spectra with these characteristics are interpreted to be the result of interference between cordierite and pinitite spectra. (c) Typical pinitite spectra with steep high wavenumber side and smooth low wavenumber side. (d) Cordierite intra-grain spectra from sample Ho-12, showing high peaks produced by asymmetric stretching of H₂O I and very low peaks produced by asymmetric stretching for H₂O II. This feature most likely is a result of the orientation effect. (e), (f) Asymmetric rim spectra with varying proportions of pinitite in the analysed area (low for (e), high for (f)).

compared to the intra-grain spectra (Fig. 6.2). Most of the rim spectra show absorbance for H₂O to be higher than for intra-grain spectra and asymmetric widening of the H₂O peaks to the low wavenumber side (Figs. 6.2b, e, f). The increase in heights is positively correlated to the degree in

asymmetry. In addition, resolution of the three H₂O peaks (3632 cm⁻¹ and 3574 cm⁻¹ for H₂O II and 3689 cm⁻¹ for H₂O I) becomes increasingly poorer and in extreme cases distinction between the three H₂O peaks is impossible (Figs. 6.2b, e, f). Additionally, the background is significantly elevated compared to intragrain spectra, and this effect is also positively correlated with increase in heights and asymmetry of H₂O peaks. The strongly asymmetric morphology of H₂O peaks from cordierite rims in contact pinite is not consistent with spectra exclusively collected from cordierite (Figs. 6.2b, e, f). These peaks should rather be the result of interference between cordierite and pinite spectra as they integrate characteristics of both. This is particularly indicated by the fact that between both 'endmember' spectra several intermediate spectra with gradual changes in heights and degree of asymmetry were detected. Positive correlation between degree of asymmetry, peak heights and heights of background may be the result of varying pinite proportions in the area hit by the IR beam. In summary, it is clear that the collected spectra do not indicate hydration of the structural channels, but reflect interference of different spectra. Therefore, spectra with asymmetric H₂O-peaks were not considered for calculating the volatile contents of cordierite. Under the petrographic microscope, in thick sections, those obviously partly pinitised areas are hardly distinguishable from intact cordierite .

In contrast, CO₂ peaks show systematic differences neither in height nor in morphology. Considerable differences in CO₂ contents between cores and rims were not detected. CO₂ contents are independent of form and height of H₂O peaks.

6.6 Discussion

6.6.1 Incorporation of volatiles in cordierite

Experimental studies and modelling determining the maximum volatile contents of cordierite have been carried out for cordierite coexisting with pure H₂O (Mirwald & Schreyer, 1977; Mirwald *et al.*, 1979; Jochum, 1986; Boberski & Schreyer, 1990; Mukhopadhyay & Holdaway, 1994; Carey, 1995; Skippen & Gunter, 1996; Harley & Carrington, 2001), for cordierite coexisting with fluids in the H₂O-CO₂ system (Johannes & Schreyer, 1981; Armbruster & Bloss, 1982; Vry *et al.*, 1990; Thompson *et al.*, 2001; Harley & Carrington, 2001) and for cordierite coexisting with granitoid melt (Harley, 1994; Stevens *et al.*, 1995; Harley, & Carrington, 2001; Thompson *et al.*, 2001; Harley *et al.*, 2002).

Cordierite coexisting with H₂O-CO₂ fluids

In fluid-present metamorphic environments the total abundance of volatiles is determined by P, T and X_{CO₂} of the coexisting fluid (Johannes & Schreyer, 1981).

Experimentally, equilibrium H₂O contents have been calibrated and modelled for Mg, Fe and Fe-Mg cordierite over a broad P-T range from 0.1 - 0.9 GPa and 300 - 1000 °C (e.g. Mirwald & Schreyer, 1977; Mirwald *et al.*, 1979; Jochum, 1986; Boberski & Schreyer, 1990; McPhail *et al.*, 1990; Carey, 1995; Skippen & Gunter, 1996; Harley & Carrington, 2001). Although models as well as experimental data show differences in position, slope and curvature of isohydrans in P-T space, it is clear that the maximum H₂O content of cordierite increases strongly with pressure and decreases with temperature and does not vary with parameters such as X_{Mg} of cordierite (e.g. Boberski & Schreyer, 1990). The results of Jochum (1986) show that the presence of Na in the channels shifts the isohydrans to lower pressures. In the presence of a pure H₂O fluid, equilibrium water contents are 1.8 wt % H₂O for synthetic Na-free Mg cordierite at 800 °C and 0.6 GPa (Mirwald *et al.*, 1979) and approximately 2 wt% H₂O for synthetic Mg cordierite and natural Mg-rich cordierite with 0.04 Na c.p.f.u. at 600 °C and 0.4 GPa (Jochum, 1986). Supported by experimental data, Harley & Carrington (2001) postulated an ideal mixing one-site model for incorporation of H₂O, consistent with the internally-consistent data set of Holland & Powell (1998).

Contrasting experimental results and conflicting models leave a less well-defined situation for cordierite coexisting with fluids of the H₂O-CO₂ system (e.g. Johannes & Schreyer, 1982; Kurnepin, 1984; Vry *et al.*, 1990; Carey, 1995; Skippen & Gunter; Carrington & Harley, 1996; Thompson *et al.*, 2001). Nevertheless, the results show the total volatile abundance to decrease with increasing X_{CO₂} (e.g. Johannes & Schreyer, 1981; Vry *et al.*; 1990; Thompson *et al.*, 2001), resulting in a shift of isohydrans to higher pressures compared to the pure H₂O system. In analogy to the H₂O system, models of the CO₂ saturation surface show CO₂ contents to increase strongly with pressure and to decrease slightly with temperature (e.g. Thompson *et al.*, 2001). Le Breton & Schreyer (1993) were not successful in defining the CO₂ saturation contents for the H₂O-free system, as early results (Armbruster & Bloss, 1982) could not be reproduced and the CO₂ contents oscillated as a function of time without reaching the saturation equilibration. Based on new experimental data, Thompson *et al.* (2001) propose a one-site model for the uptake of CO₂ in the P-T range 700 - 1000 °C and 0.2 - 0.7 GPa, and an ideal behaviour for H₂O-CO₂ mixing in the cordierite channels is assumed (Harley *et al.*, 2002). The key feature of this recent modelling in the H₂O-CO₂ system is that at specified P-T conditions and high X_{CO₂}, the total abundance of channel volatiles contents is significantly lower (e.g. ~0.15 moles CO₂ at 900 °C, 0.5 GPa, X_{CO₂} = 1) than postulated by the early models of Kurepin (1984; ~0.25 moles CO₂ at 900 °C, 0.5 GPa, X_{CO₂} = 1) and by Vry *et al.* (1990; ~0.28 moles CO₂ at 900 °C, 0.5 GPa, X_{CO₂} = 1).

Cordierite coexisting with melt

In the absence of a free volatile phase and in the presence of a granitoid melt, the absolute abundance of channel volatiles is determined by the partitioning of H₂O and CO₂ between cordierite

and melt (Harley, 1994; Stevens *et al.*, 1995; Carrington & Harley, 1996). The uptake of H₂O by cordierite in coexistence with a melt is controlled by the partitioning coefficient D_w [$D_w = \text{wt\% H}_2\text{O}(\text{melt}) / \text{wt\% H}_2\text{O}(\text{cordierite})$], which is mainly temperature-dependent (e.g. Harley & Carrington, 2001; Harley *et al.*, 2002). Harley & Carrington (2001) showed D_w to be highest (5.5 - 6.5) at H₂O saturation ($a_{\text{H}_2\text{O}} = 1$) of cordierite, to undergo a minimum at medium cordierite H₂O contents (1.2 - 0.6 wt% H₂O in cordierite) to 4.5 - 2.5 and to increase at H₂O-undersaturated conditions (0.5 wt% H₂O in cordierite). CO₂ hardly effects the distribution of H₂O between cordierite and melt (Thompson *et al.*, 2001).

Table 6.3: Volatile contents of cordierite in the studied samples.

	Bw-3		Wa-4		Ho-12	
	core	rim	core	rim	core	rim
H₂O I [wt%]	0.29 ± 0.01	0.33 ± 0.03	0.27 ± 0.03	0.31 ± 0.11	0.29 ± 0.05	0.48 ± 0.21
H₂O II [wt%]	0.29 ± 0.01	0.37 ± 0.05	0.28 ± 0.03	0.32 ± 0.13	0.21 ± 0.03	0.33 ± 0.09
H₂O_{tot} [wt%]	0.59 ± 0.02	0.70 ± 0.08	0.55 ± 0.03	0.77 ± 0.31	0.50 ± 0.07	0.66 ± 0.11
CO₂ [wt%]	0.05 ± 0.01	0.05 ± 0.01	0.05 ± 0.02	0.05 ± 0.01	0.02 ± 0.01	0.03 ± 0.01
H₂O_{tot} [c.p.f.u.]	0.196 ± 0.007	0.233 ± 0.027	0.183 ± 0.010	0.256 ± 0.103	0.166 ± 0.023	0.219 ± 0.037
CO₂ [c.p.f.u.]	0.007 ± 0.001	0.007 ± 0.001	0.007 ± 0.002	0.006 ± 0.002	0.003 ± 0.001	0.004 ± 0.002
X_{CO2}	0.04	-	0.02	-	0.04	-
H₂O I : H₂O II	0.98 ± 0.03	-	0.98 ± 0.17	-	1.43 ± 0.22	-
a_{H2O}	0.10 - 0.17	-	0.12 - 0.16	-	0.11 - 0.15	-
a_{CO2}	0.02 - 0.04	-	0.03 - 0.04	-	0.02 - 0.03	-
P [GPa]	0.50 - 0.70	-	0.40 - 0.45	-	0.40 - 0.45	-
T [°C]	850 - 900	-	730 - 780	-	730 - 780	-
melt H₂O [wt%]	1.8 - 2.5	-	2.0 - 2.3	-	1.8 - 2.3	-
D_w	3.0 - 4.2	-	3.6 - 3.9	-	3.7 - 4.2	-

For calculation of H₂O melt contents k_w of Burnham (1994) was used. P-T conditions are taken from regional petrological studies, references are given in the text (e.g. Chapter 6.3.1).

6.6.2 Behaviour of volatile contents at low temperatures

The results of Jochum (1986) imply that down to 300 °C, Na and CO₂-free cordierite may rehydrate in the presence of a fluid phase or dehydrate in the absence of a fluid phase. Experiments have shown that the hydration/dehydration kinetics of cordierite do not only depend on P and T, but also on the pressure medium, the initial volatile content and on other channel fillings (Aines & Rossmann, 1984; Carey & Navrotsky, 1992; Jochum, 1986). Na and CO₂-bearing natural cordierite shows less tendency to re-equilibrate or dehydrate/decarbonise due to the presence of channel-blocking species. Below 300 °C, hydration of Na-bearing natural and synthetic cordierite was slower than its breakdown to hydrous silicates along the crystallographic c and other direction in the presence of a free fluid phase (Jochum, 1986). The observation is important for this study as most pinites form at low temperatures and low pressures. In contrast, H₂O-oversaturated cordierite (natural and synthetic) was not altered during dehydration experiments at equivalent P-T conditions (Jochum, 1986). Maximum water contents of approximately 1.6 wt% H₂O at 400 °C and 0.2 GPa and of 1.1 wt% H₂O at 250 °C and 0.05 GPa were determined by Jochum (1986).

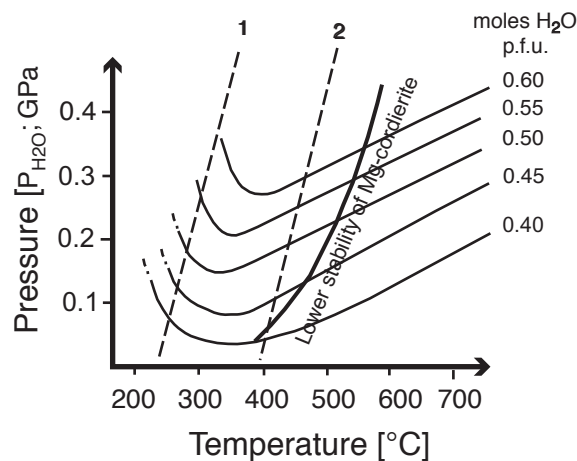


Fig. 6.3: P-T diagram depicting the cordierite - H₂O isopleths for Na-free Mg-cordierite in coexistence with a free H₂O-fluid phase after Jochum (1986) with modifications after Kalt (2000). Heavy solid curve represents the lower stability of Mg-cordierite. Contours labelled '1' and '2' represent the lower P-T limit for dehydration of synthetic Na-free cordierite and natural Na and CO₂-bearing cordierite, respectively (Jochum, 1986).

6.6.3 Volatile contents of cordierite from granulitic and migmatitic terranes

The volatile contents preserved in cordierite from migmatitic and granulitic terranes are in general below values known from equilibration with H₂O-CO₂ fluids at corresponding P-T conditions (e.g. Vry *et al.*, 1990; Thompson *et al.*, 2001; Harley *et al.*, 2002). The reasons for this volatile deficiency may be leakage or re-equilibration of volatiles during uplift and cooling (Vry *et al.*, 1990; Thompson *et al.*, 2001; Harley *et al.*, 2002) or equilibration of cordierite and melt in absence of a free fluid phase (e.g. Harley, 1994; Stevens *et al.*, 1995; Carrington & Harley, 1996, Harley & Carrington, 2001; Harley *et al.*, 2002). Recent modelling of the H₂O-CO₂ saturation surface

(Thompson *et al.*, 2001; Harley & Carrington, 2001; Harley *et al.*, 2002) even yields significantly lower H₂O + CO₂ values at high X_{CO₂} and specified P-T conditions than early models of Kurepin (1984) and Vry *et al.* (1990). In consequence, cordierite stated as deficient in volatiles by these early models may now fall within the range of equilibrium channel H₂O and CO₂ contents (Thompson *et al.*, 2001; Harley & Carrington, 2001; Harley *et al.*, 2002). Harley *et al.* (2002) illustrated by a range of case studies that whether apparent deficiency in volatile contents reflect leakage of volatiles, fluid absent situations, post-peak re-equilibration of volatile contents or dilution of H₂O and CO₂ by other components has to be considered carefully on a case by case basis.

6.6.4 Significance of the cordierite volatile contents determined in this study

The H₂O contents found in cordierite from the investigated samples Bw-3, Wa-4 and Ho-12 (Tab. 6.3) are significantly lower than values known for equilibration with a pure H₂O fluid at the specified P-T conditions (Mirwald *et al.*, 1979; Jochum, 1986; Harley *et al.*, 2002). The explanation for this volatile deficiency should be one of the following: (1) leakage of volatiles or re-equilibration during post-peak processes, possibly in the context of pinitisation, (2) equilibration with fluids containing volatiles other than H₂O or (3) equilibration with a water-undersaturated granitic melt in absence of a free H₂O phase. The three possibilities are discussed below.

(1) Re-equilibration with hydrous retrograde fluids, possibly in the context of pinitisation

For the Schwarzwald basement, fluid activity is known from late Variscan and Mesozoic times (e.g. Wernicke & Lippolt, 1997; Behr & Gerler, 1987; Behr *et al.*, 1987; von Gehlen, 1989; Markl, 1999). The infiltration of these fluids can be correlated to the formation of pinite (Table 6.4; Chapter 4.7). Given that the cordierite breakdown reactions act significantly slower than the exchange of volatile species, cordierite may have equilibrated with these fluids. Besides P and T, re-equilibration depends strongly on channel-blocking species as large CO₂ molecules and/or alkali atoms trapped in the channel necks hinder diffusion in and out of the structural channels (e.g. Zimmermann, 1981; Johannes & Schreyer, 1981; Jochum, 1986). In all investigated samples, CO₂ and Na are present.

The first and highest-grade fluid infiltration is recorded by the breakdown of cordierite to secondary greenish biotite plus muscovite (b-type pinite) and by the breakdown of K-feldspar to muscovite plus quartz assemblages (Tab. 6.4). The upper limit of the relevant temperature range (<550 - 650 °C, Table 6.4; Chapter 4.6) is well within the stability field of (Mg,Fe) cordierite (Fig. 1.2) The saturation H₂O contents of cordierite at these conditions were determined by experiments (Mirwald *et al.*, 1979; Jochum, 1986) and by thermodynamic modelling (Skipen & Gunter, 1996; McPhail *et al.*, 1990). The H₂O saturation models of cordierite of Skipen & Gunter (1996) and of McPhail *et al.* (1990) (Fig. 6.4) show differences in position, slope and curvature of H₂O isopleths compared to the experimentally derived grids of Jochum (1986) (Fig. 6.3) and Mirwald *et al.*

Table 6.4: Correlation of fluid activity and the formation of pinites in the Schwarzwald basement

Type of pinites	Fluid	Temperature range
b-type	Late to post magmatic fluids related to granite emplacement	< 550 - 650 °C
m-type	K-rich fluids related to granite alteration	200 – 400 °C
f, i-type	(Ca,Na)-rich fluids associated with the formation of Pb-Zn and fluorite-barite deposits	< 200 °C

For pinites types see Chapter 4. For further see Chapter 4.8.

(1979). They show significantly lower saturation H₂O contents at corresponding P-T conditions. Nevertheless, all of the studies show H₂O equilibrium contents to be much higher than those detected in the investigated cordierite, even when temperatures close to the lower stability limit of cordierite are considered. Therefore, a re-equilibration of cordierite volatile contents in the course of b-type pinitisation is not indicated.

The subsequent fluid infiltration is documented by chlorite-muscovite pinites in sample Wa-4. The possible P-T range of chlorite-muscovite pinitisation (< ~200 - 550 °C; Chapter 4.6) covers conditions within the stability field of (Mg,Fe) cordierite and below its lower stability. Assuming that chlorite-muscovite pinites formed within the stability field of cordierite at maximum temperatures of 550 °C, the experimental results of Jochum (1986) (Fig. 6.3) and of Mirwald *et al.* (1979) as well as the grids of Skippen & Gunter (1996) and of McPhail *et al.* (1990) show H₂O equilibrium contents to be significantly higher than the H₂O contents detected (~0.4 - 0.5 c.p.f.u. H₂O compared to 0.183 ± 0.010 c.p.f.u. H₂O; Table 6.3). Assuming that chlorite-muscovite pinitisation acted below the stability field of cordierite, the exchange of volatiles between cordierite and a coexisting fluid was most likely slower than the breakdown of cordierite (Jochum, 1986). Experimentally, the hydration of cordierite outside its stability field was determinable only over a very limited P-T range (>300 °C; Jochum, 1986). To sum up, a re-equilibration of cordierite volatile contents in the course of chlorite-muscovite pinitisation is not indicated.

The lowest-grade fluid infiltration is documented by very fine grained pinites (i, f and fi-type pinites) in all samples and of complex m-type pinites in sample Ho-12. All these types of pinites have in common that their formation should be restricted to P-T conditions (<200 °C; Chapter 4.6) far below the lower stability limit of cordierite. The results of Jochum (1986) show that below 300 °C, hydration or re-equilibration of natural Na-bearing cordierite in the presence of a free fluid phase was not determinable as the breakdown of cordierite to hydrous silicates along the crystallographic c axis and other direction was faster than the exchange of fluids. Therefore, a re-equilibration or

hydration of the investigated cordierite during i, f, fi-type or complex m-type pinites can be reasonably ruled out.

A further criterion for modification of the channel composition of cordierite by leakage of volatiles or by re-hydration during post-peak processes are inhomogeneities in volatile contents within and between cordierite grains (e.g. Vry *et al.*, 1990; Harley & Carrington, 1996). Significant inhomogeneities in volatile contents within and between grains were not detected in the investigated cordierite grains, not even in those that are pinitised. In summary, a re-equilibration (dehydration or rehydration) of cordierite volatile contents with any retrograde fluid is not indicated. It can reasonably be ruled out that pinitisation goes along with a systematic change in the cordierite channel volatile contents.

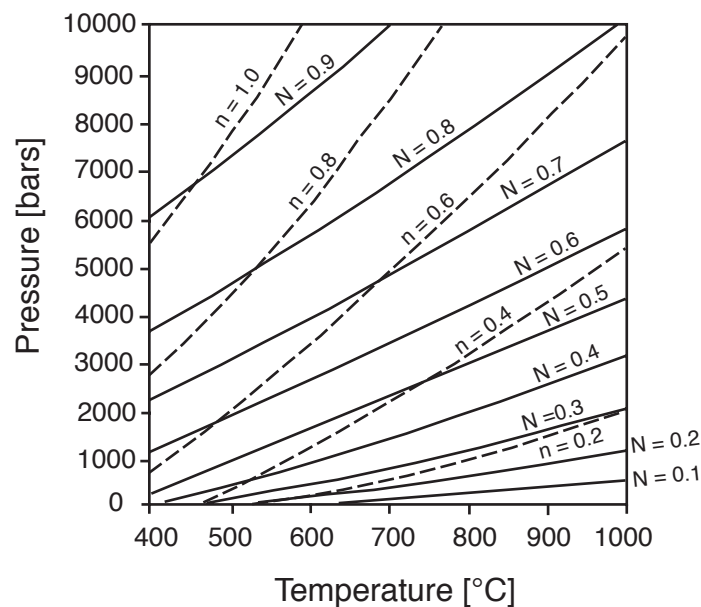


Fig. 6.4: P-T diagram showing the isohyrons for (Mg,Fe) cordierite, after Skippen & Gunter (1996; solid curves, N: mole fraction of hydrous component $(\text{Mg,Fe})_2\text{Al}_4\text{Si}_5\text{O}_{18} \cdot \text{H}_2\text{O}$) and McPhail *et al.* (1990; dashed curves, n: mole fraction of hydrous component $(\text{Mg,Fe})_2\text{Al}_4\text{Si}_5\text{O}_{18} \cdot \text{H}_2\text{O}$).

(2) Equilibration with fluids containing volatiles other than H_2O

Volatiles other than CO_2 and H_2O were not detected by IR in all samples. NH_3 , H_2S and CH_4 are infrared-active and could be qualitatively determined by FTIR. N_2 in cordierite is only Raman-active, cannot be quantified, and was only detected in one sample of the BW (Kalt, 2000). Therefore, a re-equilibration with fluids containing volatiles other than H_2O cannot be ruled out, but is very unlikely (Kalt, 2000).

(3) Equilibration with a water-undersaturated granitic melt in absence of a free H_2O phase

In both metamorphic terranes, the BW and the SW, evidence for formation of partial melts via breakdown reactions of biotite has been reported (e.g. Kalt *et al.*, 1999; Kalt *et al.*, 2000a and

references therein; Kalt, 2000; Marschall *et al.*, 2002). Therefore, partitioning of H₂O between cordierite and peraluminous water-undersaturated melt is a likely explanation for the observed water contents in cordierite of all samples. This scenario was favoured by Kalt (2000) to explain the volatile contents of samples from the BW.

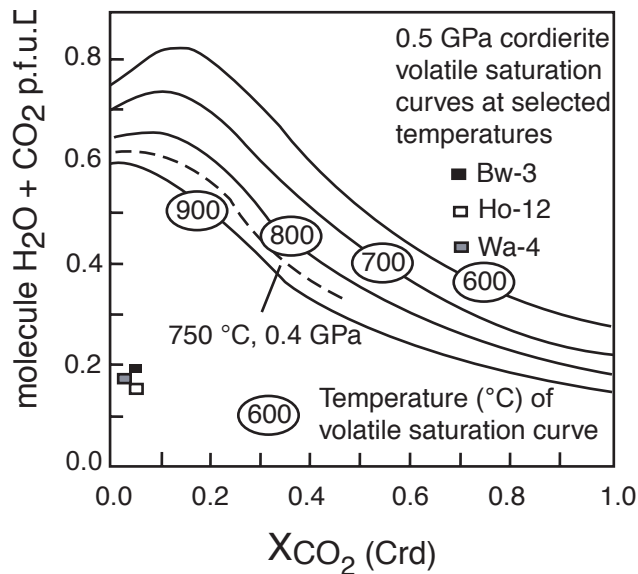


Fig. 6.5: Cordierite channel volatile diagram, after Harley *et al.* (2002), showing total abundance of H₂O + CO₂ p.f.u. of 18-oxygen cordierite coexisting with H₂O-CO₂ fluids at 0.5 GPa and 600, 700, 800, 900 °C, as a function of X_{CO₂}. The dashed line represents the volatile saturation surface at 750 °C and 0.4 GPa.

For the BW, estimates of peak conditions based on experimental results give 850 - 900 °C at 0.5 - 0.7 GPa, and mineral equilibria yield 770 - 846 °C and 0.44 - 0.51 GPa (e.g. Kalt *et al.*, 1999). Evidence for formation of peraluminous water-undersaturated melt via breakdown of biotite in the absence of an aqueous fluid is widespread in the BW (Kalt *et al.*, 1999). Sample **Bw-3** is a mesocratic type of migmatite (massive migmatite MIG1 after Kalt *et al.* (1999) that does not show a clear differentiation into leucosomes and melanosomes, which argues against segregation of melt from the rock and for continuous communication between melt and cordierite during progressive crystallisation. Cordierite is surrounded by lath-like blocks of biotite and commonly shows inclusions of sillimanite needles in the core and less often of small biotite grains and ilmenite. Release of an aqueous fluid in a late stage of crystallisation from a water-saturated melt is not indicated.

Intra-grain IR spectra from sample Bw-3 indicate 0.59 wt% H₂O in cordierite (Tab. 6.3), which allows calculation of $a_{\text{H}_2\text{O}}$ of 0.10 - 0.18 at the relevant P-T conditions. The corresponding H₂O melt contents of 1.8 - 2.5 wt% are consistent with the stability of melt at 850 - 900 °C and 0.50 - 0.70 GPa (Harley *et al.*, 2002; Fig. 6.6). This consistency and calculated a_{CO_2} values (0.02 - 0.04) both suggest equilibration of cordierite with a partial water-undersaturated melt. These results are in good

agreement with the study of Kalt (2000), concluding that cordierite preserved its volatile contents obtained at peak conditions. If at all, cordierite of sample Bw-3 should have experienced only minor H₂O loss during post-peak processes.

Sample **Wa-4** is from tectonometamorphic unit III (SSGC) of the SW. Some unit III rocks record a granulitic HP stage of approximately 1015 °C and 1.5 GPa prior to nearly isothermal decompression to a LP-HT stage (Marschall *et al.*, 2002). Formation of water-undersaturated melt occurred along the prograde path at high pressures (Marschall *et al.*, 2002). Melt kept at least partly in communication with the host rocks during isothermal decompression, which is well documented by back-reaction textures, and crystallised during nearly isobaric cooling at low pressures (Marschall *et al.*, 2002). This tectonometamorphic scenario implies that cordierite may have experienced continuous re-equilibration with coexisting melt during retrogression to the LP-HT stage at 730 - 780 °C and 0.40 - 0.45 GPa (Kalt *et al.*, 1994; Chapter 2). Sample Wa-4 is a foliated migmatite showing a layering of leucosomes and melanosomes in the mm-scale. Cordierite forms large subhedral grains rich in sillimanite inclusions in the cores. Inclusions of reddish-brown biotite and ilmenite also occur. Leucosome-like lenses and layers rich in plagioclase, quartz and K-feldspar may represent former sites of melt crystallisation. Melanosomes consist of layers of intimately intergrown cordierite, sillimanite and biotite. The preserved channel H₂O and CO₂ contents of sample Wa-4 yield low $a_{\text{H}_2\text{O}}$ (0.12 - 0.16), very low a_{CO_2} (0.03 - 0.04) and very low X_{CO_2} values ($X_{\text{CO}_2} = 0.02$), which indicate fluid-undersaturated conditions. After Harley *et al.* (2002; Fig. 6.6), the calculated H₂O melt content (2.0 - 2.3 wt%) would be entirely inconsistent with equilibrium values of melt at 730 - 780 °C and 0.40 - 0.45 GPa (3.5 wt% H₂O; Fig. 6.6). Such low volatile contents suggest a simple post-peak scenario of extensive and pervasive H₂O leakage from cordierite grains. However, uncertainties in D_w calculation, especially at low H₂O cordierite contents (Fig. 9 of Harley & Carrington, 2001), and in calculations of minimum H₂O melt contents do not allow to exclude equilibration with a melt. Assuming a D_w of 5, the calculated H₂O melt content (~2.75 wt%) is close equilibrium H₂O melt contents for cordierite coexisting with melt at the specified P-T conditions (Fig. 6.6).

An alternative scenario explaining the low volatile contents of sample **Wa-4** would be preservation of volatile contents from a higher P-T stage. Formation of melt at the specified high pressures and at the predicted melt H₂O contents (~0.8 wt%) require temperatures in excess of 950 - 1000 °C (Johannes & Holtz, 1996), which is within the P-T range reported for the HP-HT stage (Marschall *et al.*, 2002).

Sample **Ho-12** originates from the tectonometamorphic unit I of the CSGC (SW), which experienced equilibration at 730 - 780 °C and 0.40 - 0.45 GPa. In contrast to unit III, unit I does not record a granulitic HP stage (Kalt *et al.*, 2000a and references therein). Formation of partial melts is attributed to the LP-HT stage via breakdown reaction of biotite (Kalt *et al.*, 1994;

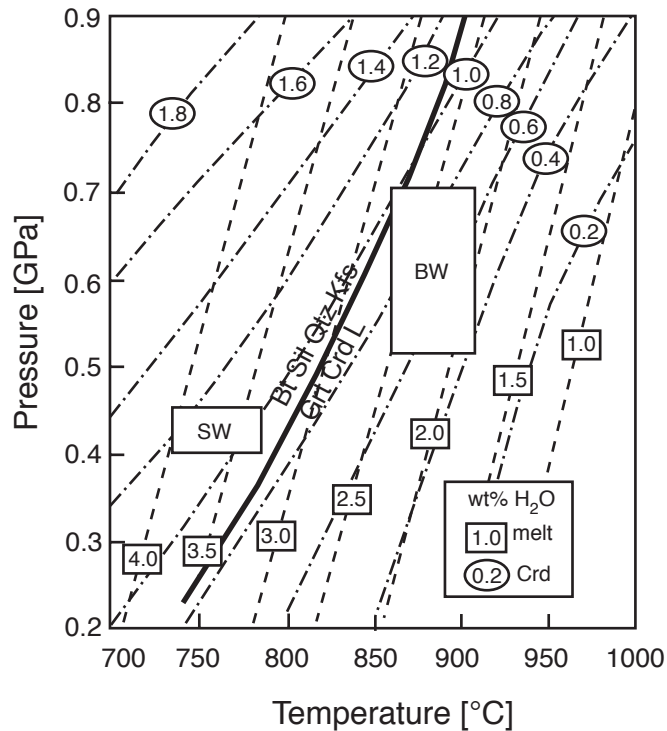


Fig. 6.6: Contoured P-T diagram after Harley *et al.* (2002), showing minimum H₂O melt contents in dependence from P and T. Isopleths (dashed lines with wt% H₂O in rectangles) for minimum H₂O wt% contents of melt are after Johannes & Holtz (1996) and Harley and Carrington (2001). Contours for cordierite H₂O wt% (dot-dashed lines with wt% H₂O in ellipses) are after Harley *et al.* (2002) and calculated from the D_w - a_{H_2O} relationships from Harley & Carrington (2001) using equation (4) in Harley *et al.* (2002). Heavy solid curve represents KFMASH reaction $Bt + Sill + Kfs + Qtz = Grt + Crd + L$. Boxes labelled 'SW' and 'BW' indicate the P-T conditions reported in regional petrological studies from the Schwarzwald (SW) (Kalt *et al.*, 1994) and from the Bayerische Wald (BW) (Kalt *et al.*, 2000b and reference therein).

Kalt *et al.* 2000a). Kalt *et al.* (1994) concluded from textures and mineral compositions that not all migmatites were formed by partial melting and favoured stromatic migmatites to have rather formed by metamorphic segregation processes at subsolidus conditions (deformation-enhanced mass transport) with, if at all, only small amounts of melt being present. Sample Ho-12 is a massive stromatic migmatite that does not show a clear differentiation into leucosomes and melanosomes. Microtextures giving evidence for dehydration melting of biotite (symplectitic intergrowth of biotite, quartz, K-feldspar and cordierite) are also absent. Therefore, it remains unclear whether cordierite of samples Ho-12 coexisted with melt. H₂O and CO₂ contents of cordierite from sample Ho-12 (0.50 ± 0.07 wt% and 0.02 ± 0.01 wt%) are low and calculation of H₂O melt contents yield only 1.8 - 2.3 wt%. After Harley *et al.* (2002), these concentrations are substantially lower than minimum melt H₂O contents required at 780 °C and 0.45 GPa (3.0 - 3.5 wt% H₂O; Harley *et al.*, 2002; Fig. 6.6). As for sample Wa-4, the preferred interpretation is that uncertainties in D_w do not point to exclude equilibration with a melt. Assuming a D_w of 5 the calculated H₂O melt contents (~ 2.5 wt%) are close to equilibrium values at the specified P-T conditions (Fig. 6.6; Harley *et al.*, 2002).

Moreover, the calculated P-T values (730 - 780 °C and 0.40 - 0.45 GPa; Kalt *et al.*, 1994; Chapter 2) do not necessarily reflect peak conditions. The values base on the Fe-Mg exchange between biotite and cordierite and are likely to record conditions on the retrograde path. Given that the psammitic lithologies of the SW experienced partial melting, minimum temperatures of approximately 800 °C are required (e.g. Stevens *et al.*, 1997). In this case, the determined H₂O contents and calculated H₂O melt contents are well in line with equilibration with partial melts.

6.7 Conclusions

All investigated samples record several distinct episodes of post-peak fluid infiltration at different P-T conditions. This is particularly documented by various hydrous alteration products, especially pinite. These fluids could have modified the volatile content of cordierite. The results of this study do not indicate any post-peak modification of the channel compositions. Most likely, the cordierite volatile contents of all samples still represent those obtained at peak conditions by equilibration with a water-undersaturated melt, which is in good agreement with the results of Kalt (2000). In consequence, it can reasonably be ruled out that pinitisation goes along with a systematic change of the channels compositions. This conclusions is probably generally valid. Nevertheless, the crystallographic control of f-type pinitisation (Chapter 4 & 5) still implies that the channels play an important role in the process of f-type pinitisation. The channel structure seems to serve as the preferred pathway of dissolution/leaching of cordierite. This is reasonable as the channels diameter is large enough to accelerate H₂O diffusion significantly (Casey & Bunker, 1990), providing the highest relative H₂O diffusion along the c direction. FTIR spectra collected at cordierite rims in contact to pinite show features consistent with interference between cordierite and pinite spectra. They do not indicate hydration of cordierite channels at cordierite rims. The findings are in line with the results of Jochum (1986), who reported the hydration of Na-bearing natural and synthetic cordierite below 300 °C in the presence of a free fluid phase to be slower than its breakdown to hydrous silicates along the crystallographic c direction.

The speculation of Harley *et al.* (2002) that the release of 'excess' H₂O, as cordierite crosses the H₂O saturation plane during decompression, may provide a mechanism for pinitisation, can be ruled out. A release of excess H₂O at low-pressure and low-temperatures should have resulted in inhomogeneities in H₂O contents of cordierite, which were never detected in this study. Moreover, pinites commonly bear alkali-bearing phyllosilicates (Chapter 4) and the amount of H₂O preserved in cordierite channels is much less than that required for pinitisation. Both facts were not considered by Harley *et al.* (2002). Finally, Jochum (1986) reported breakdown of cordierite only in the presence of a free fluid phase, but not on dehydration of H₂O-oversaturated cordierite at corresponding P-T conditions.

7. Resümee

Pinite, the ubiquitous fine-grained retrograde breakdown product of cordierite, is only insufficiently understood in terms of composition, formation conditions and genesis (Chapter 1). In order to contribute to this topic, pinite in nine cordierite-bearing high-temperature low-pressure gneisses and migmatites from the Schwarzwald and from the Bayerische Wald (Variscan belt, Chapter 2) was systematically studied. The rock samples have comparable bulk and mineralogical compositions and peak-metamorphic equilibration conditions, so that pinite should only reflect the local retrograde and/or hydrothermal environment. The aims of the study were to characterise pinite mineralogically and chemically, to possibly distinguish different pinite types and their local / regional variation, to specify the conditions and mechanisms of pinitisation, and to discuss the general implications of the results. Petrographic microscopy, EM, SEM, XRD, TEM and FTIR were used as analytical techniques (Chapter 3).

On the basis of major element composition, phase assemblage (as far as possible), textural position and grain size, four types of pinite could be distinguished that are largely independent of the sample provenience. Two of them are crystalline (b and m-type) and two of them are (partly) amorphous (f and i-type). Each pinite type formed by distinct processes acting under different P-T conditions and at different times. Although various kinds of pinite, including some of those found here, were already described by other authors (Chapter 4), this is the first systematic pinite classification that uses a combination of appropriate in-situ analytical techniques. In particular, it includes the characterisation (as far as possible) of very fine-grained material by TEM. The results place new constraints on the modes, formation conditions and formation mechanisms of pinite and therefore offer a new perspective on pinitisation. In particular, it was not known before that pinitisation encompasses several different processes that act at conditions from the greenschist facies to weathering.

B-type pinite forms predominantly at cordierite borders and consists of fine-grained aggregates of white muscovite and greenish biotite. It forms by a solution-precipitation processes driven by a fluid with high K activity within a temperature range below 550 - 650 °C and represents the highest grade type of pinite investigated in this study (Chapter 4). A coupled process of K-feldspar breakdown to muscovite plus quartz and cordierite alteration to b-type pinite is suggested in this study. Most likely, the water and some of the potassium required for this coupled reaction was derived from external reservoirs.

Fine-grained to extremely fine-grained mats of trioctahedral and dioctahedral phyllosilicate mixtures replacing cordierite pseudomorphically are called **m-type pinite** and include chlorite-muscovite pinite as well as clay mineral-bearing complex m-type pinite with illite, smectite, chlorite, berthierine and various mixed layers as the dominating phases (Chapters 4, 5). M-type pinite results

from alteration of cordierite by an alkali-bearing fluid with $K > Na$ below 500 - 550 °C. Complex m-type pinite is interpreted as the low-temperature pendant of chlorite-muscovite pinite and forms below 200 °. In this study, complex m-type pinite was shown to be the result of a complex two-stage process with I/S R_1 , Na/K-illite and chlorite as the primary products of cordierite alteration. Berthierine and I/S R_0 form at the expense of the first-stage assemblage via a dissolution/precipitation process during infiltration of an additional very low-grade fluid (Chapter 5).

F-type pinite forms alteration fissures or veins of a few to some tens of μm width, penetrating intact cordierite parallel to crystallographic c and a (Chapter 4). These veins are filled with randomly oriented and randomly related, highly imperfect crystals, floating in an amorphous matrix (Chapter 5) and show corresponding chemical and optical zonation patterns. The principal packets of layers detected are berthierine, illite, and/or I/S R_1 , smectite, chlorite and mixed-layers including 7/14 Å, 10/14 Å, I/S mixed layering and complex mixed layering of 7, 10 and 14 Å layers. *In situ* crystallisation of these packets of layers either directly from a solution or from a pre-existing gel-like material is indicated. Leaching and repolymerisation, acting in discrete band-like zones, are suggested to represent the principle mechanisms of f-type pinitisation. Most likely, f-type pinite forms at very low temperatures (weathering) by the infiltration of a very low-grade fluid.

Leaching at very low temperatures, with preferential dissolution of network-forming species, is probably the principle mechanism of **i-type pinitisation** (Chapter 4). I-type pinite is suggested to be a highly hydrated, amorphous material with a high portion of low-energy H-H bonds. Compared to cordierite, it is strongly depleted in most elements but networkforming species (Al and Si) and enriched in Ca and K with $Ca > K$. This material occurs sporadically in direct contact to cordierite, is isotropic under crossed polars and penetrated by dehydration shrinkage fissures. It shows similarities to hydrated glassy layers known from feldspar leaching. I-type pinite forms at very low temperatures (weathering).

Concerning the mechanisms of pinitisation, an important topic of this study was to investigate the role of the structural channels. It had been speculated that this role could be important (Chapter 6), but there was no systematic study so far. The H_2O and CO_2 contents of cordierite determined by FTIR in the course of this study are not consistent with release or incorporation of volatiles in the **structural channels** during pinitisation. Therefore, hydration or dehydration of the channels seems to be no key step within the process of pinitisation. The cordierite grains investigated still display volatile contents compatible with equilibration with a water-undersaturated granitoid melt at peak metamorphic conditions. Nevertheless, the structural channels (parallel to crystallographic c) probably facilitate the very low-grade dissolution and/or leaching of cordierite, because f-type pinite preferentially forms along this direction.

In this study, it was attempted to relate pinite formation to **regional-scale geological events** (Chapter 4.7). These assignments were made on the basis of pinite composition and relative age

sequence of the different types of pinite and by using published data on retrograde to post-metamorphic fluid compositions. The latter are only available for the Schwarzwald. H₂O-rich fluids with medium to low salinity and predominantly K as the major cation, related to granite emplacement, are thought to be responsible for the formation of b-type pinite. K- and Na-bearing meteoric fluids associated with granite alteration in the temperature range of 200 - 400 °C are interpreted to have driven the formation of m-type pinite in the SW. Fluids that are associated with post-Variscan hydrothermal activity at low temperatures between 150 - 180 °C in the SW, are extremely enriched in CaCl₂ and to a lesser degree in NaCl. They are interpreted as saline basinal brines and may be the potential source of f and i-type pinitisation. Local very low-grade fluids of meteoric origin (weathering) can also be considered as potential fluid sources for the formation of the amorphous types of pinite.

There are still many questions to be answered concerning pinite. Although this study has yielded a pinite classification that seems to be fairly independent of local conditions, the question is to which extent this result is of a general significance. Further studies in other regions must reveal whether the classification is generally valid or only for the Variscan basement. The structural state and phase inventory of I-type pinite could not be characterised completely. However, an in-situ, quantitative, high-resolution analytical technique that will not destroy or transform this material is not available. The formation conditions and formation mechanisms of pinitisation are not yet fully clarified. Experiments could help in this respect, but they are difficult to design and carry out under the low-grade conditions of interest, particularly for the amorphous pinite types. Specific questions of interest are: (1) Which parameters control the formation of alteration veins (f-type pinite), e.g. fluid composition, relative rates of competitive reactions of leaching and dissolution, etc.? (2) Which parameters favour the leaching of cordierite (formation of i-type pinite), e.g. pH, Eh, etc.? (3) Do the amorphous types of pinite represent weathering *sensu stricto*? To sum up, a more precise definition of the P-T-X conditions for all the different types of pinite is needed.

References

- Abdad-Ortega, M.d.M. & Mieto, F. (1995). Genetic and chemical relationship between berthierine, chlorite and cordierite in nodules associated to granitic pegmatites of Sierra Albarrana (Iberian Massif, Spain). *Contrib. Mineral. Petrol.*, **120**, 327-336.
- Ahn, J.H. & Buseck, P.R. (1990). Layer-stacking sequence and structural disorder in mixed-layer illite/smectite: Image simulation and HRTEM imaging. *Am. Mineral.*, **75**, 267-275.
- Ahn, J.H. & Peacor, D.R. (1985). Transmission electron microscopy study of diagenetic chlorite in Gulf Coast argillaceous sediments. *Clays & Clay Minerals*, **33**, 228-236.
- Ahn, J.H. & Peacor, D.R. (1986a). Transmission and analytical electron microscopy of the smectite-to-illite transition. *Clays and Clay Minerals*, **34**, 165-179.
- Ahn, J.H. & Peacor, D.R. (1986b). Transmission electron microscope data for rectorite: Implications for the origin and structure of "Fundamental Particles". *Clays & Clay Minerals*, **34**, 180-186.
- Ahn, J.H. & Peacor, D.R. (1989). Illite/smectite from Gulf Coast shales: A reappraisal of transmission electron microscope images. *Clays and Clay Minerals*, **37**, 542-546.
- Ahn, J.H., Peacor, D.R. & Coombs, D.S. (1988). Formation mechanisms of illite, chlorite and mixed layer illite-chlorite in Triassic volcanogenic sediments from the Southland syncline, New Zealand. *Contrib. Mineral. Petrol.*, **99**, 82-89.
- Aines, R.D. & Rossman, G. (1984). The high temperature behavior of water and carbon dioxide in cordierite and beryl. *Am. Mineral.*, **69**, 319-327.
- Amouric, M., Gianetto, I. & Proust, D. (1988). 7, 10 and 14 Å mixed-layer phyllosilicates studied structurally by TEM in pelitic rocks of the Piemontese zone (Venezuela). *Bull. Mineral.*, **111**, 29-37.
- Armbruster, T. & Bloss, F.D. (1980). Channel CO₂ in cordierites. *Nature*, **286**, 284-291.
- Armbruster, T. & Bloss, F.D. (1982). Orientation and effects of channel H₂O and CO₂ in cordierite. *Am. Mineral.*, **67**, 284-291.
- Bailey, S.W. (1975). Chlorites. In: *Soil components (inorganic components)*, J.E. Gieseking (Ed.). Springer, Berlin Heidelberg New York, 191-263.
- Bailey, S.W. (1980). Structures and compositions of other trioctahedral 1:1 phyllosilicate. In: *Hydrous Phyllosilicates*. S.W. Bailey (Ed.), Mineralogical Society of America, Rev. Mineral., pp. 725.
- Bailey, S.W. (1980). Summary of recommendations of AIPEA nomenclature committee on clay minerals. *Am. Mineral.*, **65**, 1-7.
- Banos, J. O. & Amouric, M. (1984). Biotite chloritization by interlayer brucitization as seen by HRTEM. *Am. Mineral.*, **69**, 869-871.

- Bayliss, P. (1975). Nomenclature of the trioctahedral chlorites. *Can. Mineral.*, **13**, 178-180.
- Beer, W. W. (1981). Die strukturelle Entwicklung der Metamorphite des Bayerischen Waldes. Ph.D. Thesis, University of Göttingen.
- Behr, H.-J. & Gerler, J. (1987). Inclusions of sedimentary brines in post-Variscan mineralizations in the Federal Republic of Germany. *Chem. Geol.*, **61**, 65-77.
- Behr, H.-J., Horn, E. E., Frenzel-Beyme, K. & Reutel, C. (1987). Fluid inclusion characteristics of the Variscan and post-Variscan mineralizing fluids in the Federal Republic of Germany. *Chem. Geol.*, **61**, 273-285.
- Bettison, L. A. & Schiffman, P. (1988). Compositional and structural variations of phyllosilicates from the Point Sal ophiolite, California. *Am. Mineral.*, **73**, 62-76.
- Bettison-Varga, L., Mackinnon, I.D.R. & Schiffmann, P. (1991). Integrated TEM, XRD and electron microprobe investigation of mixed-layer chlorite-smectite from the Point Sal ophiolite, California. *J. Metamorphic Geol.*, **9**, 697-710.
- Blencoe, J.G., Guidotti, C.V. & Sassi, F.P. (1994). The paragonite-muscovite solvus: II. Numerical geothermometers for natural, quasibinary paragonite-muscovite pairs. *Geochim. Cosmochim. Acta*, **58**, 2277-2288.
- Blümel, P. & Schreyer, W. (1976). Progressive regional low-pressure metamorphism in Moldanubian metapelites of the northern Bavarian Forest, Germany. *Krystallinikum*, **12**, 7-30.
- Blümel, P. & Schreyer, W. (1977). Phase relations in pelitic and psammitic gneisses of the sillimanite-potash-feldspar and cordierite-potash-feldspar zones in the Moldanubicum of the Lam-Bodenmais area, Bavaria. *J. Petrol.*, **18**, 431-459.
- Boberski, C. & Schreyer, W. (1990). Synthesis and water contents of Fe²⁺-bearing cordierites. *Eur. J. Mineral.*, **2**, 565.
- Bucher, K. & Frey, M. (1994). *Petrogenesis of metamorphic rocks*. Springer, Berlin Heidelberg New York, pp. 318.
- Bunker, B.C., Tallant, D.R., Headly, T.J., Turner, G.L. & Kirkpatrick, R.J. (1987). Corrosion of phosphorous oxybitride glasses in water and humid air. *J. Ceram. Soc.*, **70**, 425-430.
- Burnham, C.W. (1994). Development of the Burnham model for prediction of H₂O solubility in magmas. In: *Volatiles in Magma*. M. R. Carroll and J. R. Holloway (Eds.), Rev. Mineral., **30**, Mineralogical Society of America, Washington D.C., 123-129.
- Buseck, P.R. (Ed.) (1992). *Minerals and reaction at the atomic scale: Transmission Electron Microscopy*. Mineralogical Society of America, Washington D.C., Rev. Mineral., **27**, pp. 508.
- Carey, J.W. (1995). A thermodynamic formulation for hydrous cordierite. *Contrib. Mineral. Petrol.*, **119**, 115-165.
- Carey, J. W. & Navrotsky, A. (1992). The molar enthalpy of dehydration of cordierite. *Am. Mineral.*, **77**, 930-936.

- Carrington, D.P. & Harely, S.L. (1996). Cordierite as a monitor of fluid and melt H₂O contents in the lower crust: An experimental calibration. *Geology*, **24**, 647-650.
- Casey, W.H. & Bunker, B. (1990). Leaching of mineral and glass surfaces during dissolution. *Rev. Mineral.*, **23**, 397-426.
- Casey, W.H., Westrich, H.R., Arnold, G.W. & Banfield, J.F. (1989). The surface chemistry of dissolving labradorite feldspar. *Geochim. Cosmochim. Acta*, **53**, 821-832.
- Castaing, R. (1951). Application des sondes électroniques: une methode d'analyse ponctuelle chimique et cristallographique. Ph.D. thesis, University of Paris.
- Černý, P. (1970). Review of some secondary hypogene parageneses after early pegmatite minerals. *Freiberger Forschungshefte*, **C 270**, 47-67.
- Černý, P. & Povondra, P. (1967). Cordierite in West-Moravien pegmatites. *Acta Univ. Carol.-Geologica*, **3**, 203-221.
- Chandler, F. W. (1975). Pinite, Pressure, Temperature and Retrogressive Metamorphism, Wollaston Lake, Saskatchewan. *Geol. Surv. Can.*, **75**, 319-321.
- Chevalier, Y. & Dejou, J. (1972). Observations sur l'altération superficielle de la cordiérite extraite de quelques granites localisés dans la Provence cristalline. Comparaison des résultats avec ceux acquis dans les régions tempérés humides. *C.R. Acad. Sci., Paris sér. D*, **275**, 149-151.
- Clemens, J.D. & McMillan, P.F. (1982). A Discussion of: "Biotite melting in high-grade metamorphic Gneisses from the Haut-Allier (French Massif Central)" by Nédélec and Paquet. *Contrib. Mineral. Petrol.*, **79**, 436-438.
- Cohen, J.P., Ross, F.K. & Gibbs, G.V. (1977). An X-ray and neutron diffraction study of hydrous low cordierite. *Am. Mineral.*, **62**, 67-78.
- Cohen, J.P., Ross, F.K. & Gibbs, G.V. (1977). An X-ray and neutron diffraction study of hydrous low cordierite. *Am. Mineral.*, **62**, 67-78.
- Cotton, F. A., Wilkinson, G. & Gaus, P.L. (1987). *Basic inorganic chemistry*. John Wiley & Sons, New York, pp. 251.
- Carrington, D.P., C. & Harley, S.L. (1995). Partial melting and phase relations in high-grade metapelites: an experimental petrogenetic grid in the KFMASH system. *Contrib. Mineral. Petrol.*, **120**, 270-291.
- Deer, J.D., Howie, R. A. & Zussman, J. (1962). *Rockforming minerals, vol 1. Ortho- and ring silicates*. New York, pp 333.
- Dong, H. & Peacor, D.R. (1996). TEM observations of coherent stacking relations in smectite, I/S and illite of shales: Evidence for MacEwan crystallites and dominance of 2M₁ polytypism. *Clays and Clay Minerals*, **44**, 257-275.
- Dong, H., Peacor, D.R. & Murphy, S.F. (1998). TEM study of progressive alteration of igneous biotite to kaolinite throughout a weathered soil profile. *Geochim. Cosmochim. Acta*, **62**, 1881-1888.

- Dong, H., Peacor, R.D. & Freed, R.L. (1997). Phase relations among smectite, R₁ illite smectite, and illite. *Am. Mineral.*, **82**, 379-391.
- Echtler, H.P. & Altherr, R. (1993). Variscan crustal evolution in the Vosges mountains and the Schwarzwald: Guide to the excursion of the Swiss Geological Society and the Swiss Society of Mineralogy and Petrology (3-5 October, 1992). *Schweizerische Mineral. Petrogr. Mitt.*, **73**, 113-128.
- Echtler, H.P. & Chauvet, A. (1991-1992). Carboniferous convergence and subsequent crustal extension in the southern Schwarzwald (SW Germany). *Geodynamica Acta*, **5**, 37-49.
- Eggleton, R.A. (1980). High resolution electron microscopy of feldspar weathering. *Clays and Clay Minerals*, **28**, 173-178.
- Essene, E.J. & Peacor, D.R. (1995). Clay mineral thermometry - A critical perspective. *Clays and Clay Minerals*, **43**, 540-553.
- Feenstra, A. (1996). An EMP and TEM-AEM study of margarite, muscovite and paragonite in polymetamorphic metabauxites of Naxos (Cyclades, Greece) and the implications of fine-scale mica interlayering and multiple mica generations. *J. Petrol.*, **37**, 201-233.
- Ferrell, R.E. & Carpenter, P.K. (1990). Application of the electron microprobe and the electron microprobe in the study of clays. In: *Electron-optical methods in clay sciences*. Mackinnon, I.D.R. and F. A. Mumpton, F.A. (Eds.), Boulder, Colorado, Clay Mineral Society, 8-132.
- Fitzsimons, I.C.W. (1994). Cordierite migmatites from Antarctica: geochemical constraints on volatile distribution during crustal anatexis. *Min. Mag.*, **58A**, 274-275.
- Foster (1962). Interpretation of the composition and a classification of chlorites. *U.S.G.S. Prof. Pap*, **414-A**, 1-33.
- Franceschelli, M., Mellini, M., Memmi, I. & Ricci, C.A. (1986). Fine scale chlorite-muscovite associations in low grade metapelites from Nurra (NW Sardinia), and the possible misidentification of metamorphic vermiculite. *Contrib. Mineral. Petrol.*, **93**, 137-143.
- Franke, W. (1989). Tectonostratographic units in the Variscan belt of Europe. *Geological Society of America, Special Papers*, **230**, 395-414.
- Franz, G. & Althaus, E. (1976). Experimental investigations on the formation of solid solution in sodiu-aluminium-magnesium micas. *N. Jahrb. Mineral. Abh.*, **126**, 233-253.
- Franz, G., Hinrichsen, T. & Wannemacher, E. (1977). Determination of the miscibility gap on the solid solution series paragonite-margarite by means of the infrared spectroscopy. *Contrib. Mineral. Petrol.*, **59**, 307-316.
- Garrels, R. M. (1984). Montmorillonite/Illite stability diagram. *Clays and Clay Minerals*, **32**, 161-166.
- Goldmann, D.S., Rossman, G.R. & Dollase, W.A. (1977). Channel constituents in cordierite. *Am. Mineral.*, **62**, 1144-1157.

- Green, T.H. (1981). Synthetic high-pressure micas compositionally intermediate between the dioctahedral and trioctahedral mica series. *Contrib. Mineral. Petrol.*, **78**, 452-458.
- Green, T.H. & Vernon, R.H. (1974). Cordierite Breakdown under High-Pressure, Hydrous Conditions. *Contrib. Mineral. Petrol.*, **46**, 215-226.
- Guidotti, C.V. (1984). Micas in metamorphic rocks. *Rev. Mineral.*, **13**, 357-467.
- Gutherie, G. & Veblen, D.R. (1990). Interpreting one-dimensional high-resolution transmission electron micrographs of sheet silicates by computer simulation. *Am. Mineral.*, **75**, 276-288.
- Gutherie, G.D. J. & Veblen, D.R. (1989). High-resolution transmission electron microscopy applied to clay minerals. In: *Spectroscopic characterisation of minerals and their surfaces*. L. M. Coyne, S. W. S. McKeever and D. F. Blake. (Eds.), American Chemical Society, Washington D.C., 75-93.
- Gutherie, G.D. J. & Veblen, D.R. (1989). High-resolution transmission electron microscopy of illite/smectite: Computer simulations. *Clays and Clay Minerals*, **37**, 1-11.
- Hagedorn, B. & Lippolt, H.J. (1994). Isotopische Alter von Zerrüttungszonen als Alterschranke der Freiamt-Sexau-mineralisation (Mittlerer Schwarzwald). *Abh. Geol. Landesamt Baden-Württemberg*, **14**, 205-219.
- Hanel, M., Lippolt, H.J., Kober, B. & Wimmenauer, W. (1993). Lower Carboniferous granulites in the Schwarzwald basement near Hohengeroldseck. *Naturwissenschaften*, **80**, 25-28.
- Hanel, M., Montenari, M. & Kalt, A. (1999). Determining sedimentation ages of high-grade metamorphic gneisses by their palynological record: a case study in the northern Schwarzwald (Variscan belt, Germany). *International Journal of Earth Science*, **88**, 49-59.
- Hanel, M. & Wimmenauer, W. (1990). Petrographische Indizien für einen Deckenbau im Kristallines Schwarzwaldes. *Ber. Deutsch. Mineral. Ges., Beih. z. Eur. J. Mineral.*, **2**, 89.
- Hann, H.P. & Sawatzki, G. (2000). Neue Daten zur Tektonik des Südschwarzwaldes. *Jahresbericht der Mitteilungen der oberrheinischen geologischen Vereinigung*, **82**, 363-376.
- Harley, S.L. (1994). Cordierite as a sensor of fluid and melt distribution in crustal metamorphism. *Min. Mag.*, **58A**, 374-375.
- Harley, S.L. & Carrington, D.P. (2001). The distribution of H₂O between cordierite and granitic melt: Improved calibration of H₂O incorporation in cordierite and its application to high-grade metamorphism and crustal anatexis. *J. Petrol.*, **42**, 1595-1620.
- Harley, S.L., Thompson, B.J., Hensen, B.J. & Buick, I.S. (2002). Cordierite as a sensor of fluid conditions in high-grade metamorphism and crustal anatexis. *J. Metamorphic Geol.*, **20**, 71-86.
- Harrison, T.M., Dungan, I. & McDougall, I. (1985). Diffusion of ⁴⁰Ar in biotite: Temperature, pressure and compositional effects. *Geochim. Cosmochim. Acta*, **49**, 2461-2468.
- Haslam, H. W. (1983). An isotropic alteration product of cordierite. *Min. Mag.*, **47**, 238-240.

- Hörmann, P.K., Raith, M., Raase, P., Ackermann, D. & Seifert, F. (1980). The granulite complex of Finnish Lapland: Petrology and metamorphic conditions in the Ivaljoki-Inarijévi area. *Geol. Surv. Finland Bull.*, **308**, 1-95.
- Jiang, W.-T., Essene, E.J. & Peacor, D.R. (1990). Transmission electron microscopic study of coexisting pyrophyllite and muscovite: Direct evidence for the metastability of illite. *Clays and Clay Minerals*, **38**, 225-240.
- Jiang, W.-T. & Peacor, D.R. (1990). Transmission and analytical electron microscopy study of mixed-layer illite/smectite formed as an apparent replacement product of diagenetic illite. *Clays & Clay minerals*, **38**, 449-468.
- Jiang, W.-T. & Peacor, D.R. (1991). Transmission electron microscopic study of the kaolinitization of muscovite. *Clays & Clay Minerals.*, **39**, 1-13.
- Jiang, W.-T. & Peacor, D.R. (1993). Formation and modification of metastable intermediate sodium potassium mica, paragonite and muscovite in hydrothermally altered metabasites from northern Wales. *Am. Mineral.*, **78**, 782-793.
- Jiang, W.-T. & Peacor, D.R. (1994). Formation of corrensite, chlorite and chlorite and chlorite-mica stacks by replacement of detrital biotite in low-grade pelitic rocks. *J. Metamorphic Geol.*, **12**, 867-884.
- Jiang, W.-T. & Peacor, D.R. (1994). Prograde Transition of corrensite and chlorite in low-grade pelitic rocks from the Gaspé Peninsula, Quebec. *Clays and Clay Minerals*, **42**, 497-417.
- Jiang, W.-T., Peacor, D.R. & Buseck, P.R. (1994). Chlorite Geothermometry? - Contamination and apparent octahedral vacancies. *Clays and Clay Minerals*, **42**, 593-605.
- Jiang, W.-T., Peacor, D.R. & Slack, J.F. (1992). Microstructures, mixed-layering and polymorphism of chlorite and retrograde berthierine in the Kidd Creek Massive sulfid deposit, Ontario. *Clays and Clay Minerals*, **40**, 501-514.
- Jochum, C. (1986): Experimentelle Untersuchungen zum Wassereinbau und zur Kinetik der Hydratation und Dehydratation von synthetischen und natürlichen Cordieriten. Unpublished Ph.D. thesis, University of Bochum, pp. 235.
- Johannes, W. & Holtz, F. (1996). *Petrogenesis and experimental petrology of granitic rock*. Springer, Berlin, pp. 328.
- Johannes, W. & Schreyer, W. (1981). Experimental introduction of CO₂ and H₂O into Mg-cordierite. *American Journal of Science*, **281**, 299-317.
- Kalt, A. (2000). Cordierite channel volatiles as evidence for dehydration melting: an example from high-temperature metapelites of the Bayerische Wald (Variscan belt, Germany). *Eur. J. Mineral.*, **12**, 987-998.
- Kalt, A. & Altherr, R. (1996). Metamorphic evolution of garnet-spinel peridotites from the Variscan Schwarzwald (FRG). *Geol. Rundschau*, **85**, 211-224.

- Kalt, A., Altherr, R. & Hanel, M. (1995). Contrasting P-T conditions recorded in ultramafic high-pressure rocks from the Variscan Schwarzwald (F.R.G.). *Contrib. Mineral. Petrol.*, **121**, 45-60.
- Kalt, A., Altherr, R. & Hanel, M. (2000a). The Variscan basement of the Schwarzwald. *Beih. z. Eur. J. Mineral.*, **12**, 1-43.
- Kalt, A., Berger, A. & Blümel, P. (1999). Metamorphic evolution of cordierite-bearing migmatites from the Bayerische Wald (Variscan belt, Germany). *J. Petrol.*, **40**, 601-627.
- Kalt, A., Corfu, F. & Wijbrans, J. (2000b). Time calibration of a P-T path from a Variscan high-temperature low-pressure migmatite-gneiss complex (Bayerischer Wald, Germany) and the detection of inherited monazite. *Contrib. Mineral. Petrol.*, **138**, 143-163.
- Kalt, A., Grauert, B. & Baumann, A. (1994). Rb-Sr and U-Pb isotope studies on migmatites from the Schwarzwald (Germany): constraints on isotopic resetting during Variscan high-temperature metamorphism. *J. Metamorphic Geol.*, **12**, 667-680.
- Kalt, A., Kober, B. & Hanel, M. (2000c). Further time constraints on Variscan high-pressure metamorphism in the Schwarzwald (Germany). *Ber. Deutsch. Mineral. Ges., Beih. 1 z. Eur. J. Mineral.*, **12**, 91.
- Kawano, M. & Tomita, K. (1994). Growth of smectite from leached layer during experimental alteration of albite. *Clays and Clay Minerals*, **42**, 7-17.
- Kawano, M. & Tomita, K. (1996). Amorphous aluminium hydroxide formed at the earliest weathering stages of K-feldspar. *Clays and Clay Minerals*, **44**, 672-676.
- Kawano, M. & Tomita, K. (2001). TEM-EDX study of weathered layers on the surface of volcanic glass, bytownite and hypersthene in volcanic ash from Sakurjiam volcano, Japan. *Am. Mineral.*, **86**, 284-292.
- Kim, J.-W. & Peacor, D.R. (1995). A technique maintaining texture and permanent expansion of smectite interlayers for TEM observations. *Clays and Clay Minerals*, **43**, 51-57.
- Kleber, I., Bausch, H.-J. & Bohn, J. (1990). *Einführung in die Kristallographie*. Verlag Technik GmbH, Berlin, pp. 406.
- Klein, H. & Wimmenauer, W. (1984). Eclogites and their retrograde transformation in the Schwarzwald. *N. Jb. Mineral. Mitt.*, **12**, 25-38.
- Klimentidis, R.E. & Mackinnon, D.R. (1986). High-resolution imaging of ordered mixed-layer clays. *Clays and Clay Minerals*, **34**, 155-164.
- Kolesov, B.A. & Geiger, C.A. (1999). Cordierite II: The role of CO₂ and H₂O. *Ber. Deutsh. Mineral. Ges., Beih. z. Eur. J. Mineral.*, **11**, 131.
- Kolesov, B.A. & Geiger, C.A. (2000). Cordierite II: The role of CO₂ and H₂O. *Am. Mineral.*, **85**, 1265-1274.
- Kosmat, F. (1927). Gliederung des variszischen Gebirgsbaus. *Abhandlungen des Sächsischen Geologischen Landesamtes*, **1**, 1-39.
- Kretz, R. (1983). Symbols for rock-forming minerals. *Am. Mineral.*, **68**, 227-279.

- Lacroix, A. (1962) - Minéralogie de la France et de ses anciens territoires d'outre-mer. Tome 1. A. Blanchard (Ed.) Nouvelle édition, Paris, 15-19.
- Lal, R.K. (1969). Retrogression of cordierite to kyanite and andalusite at Fishtal Lake, Ontario, Canada. *Min. Mag.*, **37**, 466-471.
- Layman, F.G. (1963). Alteration of Cordierite. *Program 1963 Annual Meeting GSA*, 100A.
- Le Breton, N. (1989). Infrared investigation of CO₂-bearing cordierites. *Contrib. Mineral. Petrol.*, **103**, 387-396.
- Leake, B.E. (1960). Compilation of chemical analyses and physical constants of natural cordierite. *Am. Mineral.*, **54**, 282-298.
- Lee, H.J. & Peacor, D.R. (1985). Ordered 1:1 interstratification of illite and chlorite: A transmission and analytical electron microscope study. *Clays and Clay Minerals*, **33**, 463-467.
- Lee, J.H., Peacor, D.R., Lewis, D.D. & Wintsch, R.P. (1986). Chlorite, illite/muscovite interlayered and interstratified crystals: A TEM/STEM study. *Contrib. Mineral. Petrol.*, **88**, 372-385.
- Li, G., Peacor, D.R., Merriman, R.J. & Roberts, B. (1994). The diagenetic to low-grade metamorphic evolution of matrix white micas in the system muscovite-paragonite in a mudrock from Central Wales, United Kingdom. *Clays and Clay Minerals*, **42**, 369-381.
- Lippmann, F. (1981). Stability diagrams involving clay minerals. In: *8th Conference on Clay Mineralogy and Petrology Teplice, 1979*, J. Konata (Ed.).
- Lippmann, F. (1982). The thermodynamic status of clay minerals. In: *Proceedings of the 7th international clay conference*, Bologna, Pavaia, H. van Olphen & F. Veniale (Eds.).
- Lippolt, H.J., Hradetzky, H. & Hautmann, S. (1994). K-Ar dating of amphibole-bearing rocks in the Schwarzwald, SW Germany: I. ⁴⁰Ar/³⁹Ar age constraints to Hercynian HT-metamorphism. *N. Jb. Mineral. Mh.*, **1994/10**, 433-448.
- Livi, K. J.T., Veblen, D. R., Ferry, J. M. & Frey, M. (1997). Evolution of 2:1 layered silicates in low grade metamorphosed Liassic shales of Central Switzerland. *J. Metamorphic Geol.*, **15**, 323-344.
- Loeschke, J., Guldenpfennig, M., Hann, H.P. & Sawatzki, G. (1998). Die Zone von Badenweiler-Lenzkirch (Schwarzwald): Eine variskische Suturezone. *Zeitschrift der deutschen geologischen Gesellschaft*, **149**, 197-212.
- Loucks, R.R. (1991). The bound interlayer H₂O content of potassic white mica: muscovite-hydromuscovite-hydrophyphyllite solutions. *Am. Mineral.*, **76**, 1563-1579.
- Lüders, V. (1994). Geochemische Untersuchungen an Gangmineralen aus dem Berbaurevier Freiamt-Sexau und dem Badenweiler-Quarzriff (Schwarzwald). *Abh. geol. Landesamt Baden-Württemberg*, **14**, 173-190.
- Marchand, J., Bossiere, G. & Leyleroup, A. (1982). Pinite and Pseudo-"Glass" in High-Grade Metamorphic Gneisses. *Contrib. Mineral. Petrol.*, **79**, 439-442.

- Markl, G. (1999). Wollastonite formation during Variscan post-tectonic cooling in the Schwarzwald. *Mineralogy and Petrology*, **66**, 193-213.
- Marschall, H.R., Kalt, A. & Hanel, M. (2002). P-T evolution of a Variscan lower Crustal segment: a study of granulite from the Schwarzwald, Germany. *J Petrol.*, **in press**.
- Masch, L. & Cetin B. (1991). Gefüge, Deformationsmechanismen und Kinematik in ausgewählten HT-Mylonitzonen im Moldanubikum des Bayerischen Waldes. *Geologia Bavarica*, **96**, 7-26.
- Massonne, H. J. & Schreyer, W. (1983). Stability of the talc-kyanite assemblage revisited. *Terra Cognita*, **39**, 187.
- Mathias, M. (1952). An unusual cordierite-rock from Upington, Cape Province. *Min. Mag.*, **29**, 936-945.
- Matte, P. (1986). Tectonics and plate tectonics for the Variscan belt in Europe. *Tectonophysics*, **126**, 329-374.
- Mazer, J.J., Bates, J.K., Bradley, J.P., Bradley, C.R. & Stevenson, C.M. (1992). Alteration of tektite to form weathering products. *Nature*, **357**, 573-576.
- McPhail, D.C., Berman, R.G. & Greenwood, H.J. (1990). Experimental and theoretical constraints on aluminium substitution in magnesium chlorite, and a thermodynamic model for H₂O in magnesian cordierite. *Can. Mineral.*, **28**, 859-874.
- Medaris, L.G., Jelinek, E. & Misar, Z. (1995). Czech eclogites: terrane settings and implications for the Variscan evolution of the Bohemian Massif. *Eur. J. Mineral.*, **7**, 7-28.
- Merriman, R.J. & Peacor, D.R. (1999). Very low-grade metapelites: mineralogy, microfabrics and measuring reaction progress. In: *Low-grade metamorphism*. (Eds.) M. Frey and D. Robinson, 10-60.
- Mirwald, P.W., Maresch, W.V. & Schreyer, W. (1979). Der Wassergehalt von Mg-Cordierit zwischen 500 °C und 800 °C sowie 0.5 und 11 kbar. *Fortschr. Mineral.*, **57**, 101-102.
- Mirwald, P.W. & Schreyer, W. (1977). Die stabile und metastabile Abbaureaktion von Mg-Cordierit in Talk, Disthen und Quarz und ihre Abhängigkeit vom Gleichgewichtswassergehalt des Cordierits. *Fortschr. Mineral.*, **55**, 95-97.
- Moore, D.M. & Reynolds, R.C.J. (1997). *X-ray diffraction and the identification of clay minerals*. Oxford University Press, Oxford, pp. 325.
- Morse, J.S. & Casey, W.H. (1988). Ostwald processes and mineral paragenesis in sediments. *American Journal of Science*, **288**, 537-560.
- Mukhopadhyay, B., Holdaway, M.L. & Dyar, M.D. (1994). Cordierite-garnet-sillimanite-quartz equilibrium: New experimental calibration in the system FeO-Al₂O₃-SiO₂-H₂O and certain P-T-XH₂O relations. *Contrib. Mineral. Petrol.*, **116**, 462-472.
- Nadeau, P.H. & Bain, D.C. (1986). Composition of some smectites and diagenetic illitic clay and implications for their origin. *Clays and Clay Minerals*, **34**, 453-464.

- Nedelec, A. & Paquet, J. (1981). Biotite melting in high-grade metamorphic gneisses from the Haut-Allier (French Massif Central). *Contrib. Mineral. Petrol.*, **77**, 1-10.
- Nelson, B.W. & Roy, R. (1958). Synthesis of the chlorites and their structural and chemical constitution. *Am. Mineral.*, **43**, 707-725.
- Nesbitt, H.W. & Muir, I.J. (1988). SIMS depth profiles of weathered plagioclase and processes affecting dissolved Al and Si in some acidic soil solutions. *Nature*, **334**, 336-338.
- Newton, R.C. (1972). An experimental determination of the high pressure stability limits of magnesian cordierite under wet and dry conditions. *J. Geol.*, **80**, 398-420.
- Nieto, F., Ortega-Huertas, M., Peacor, D.R. & Arostegui, J. (1996). Evolution of illite/smectite from early diagenesis through incipient metamorphism in sediments of the Basque-Cantabrian Basin. *Clays and Clay Minerals*, **44**, 304-323.
- Ostwald, W.Z. (1897). Studien über die Bildung und Umwandlung fester Körper. 1. *Abhandlung: Zeitung Physik Chemie*, **22**, 289-330.
- Ostwald, Z.W. (1900). Über die vermeintliche Isomerie des roten und gelben Quecksilberoxyds und die Oberflächenspannung fester Körper. *Zeitung Physik Chemie Stoechiom. Verwandtschaftsl.*, **34**, 495-503.
- Pavicevic, M.K., Amthauer, G. (Eds.) (2001). *Physikalisch-chemische Untersuchungsmethoden in den Geowissenschaften.*: E. Schweizerbartsche Verlagsbuchhandlung (Nägele u. Obermiller), Stuttgart, pp. 252.
- Peacor, D.R. (1992). Diagenesis and low-grade metamorphism of shales and slates. *Rev. Mineral.*, **27**, 335-380.
- Petit, J.C., Della, M., G., Dran, J.-C., Magonthier, M.-C., Mando, P.A. & Paccagnella, A. (1990). Hydrated-layer formation during dissolution silicate glasses and minerals. *Geochim. Cosmochim. Acta*, **54**, 1949-1955.
- Potts, P.J., Bowles, J.F.W., Reed, S.J.B. & Cave, M.R. (Eds.) (1995). *Microprobe Techniques in the Earth Sciences*. Chapman & Hall, London, New York, pp. 419.
- Pouchou, J.L. & Pichoir, F. (1985). "PAP" F(rZ) Procedure for Improved Quantitative Microanalysis. In: *Microbeam Analysis 1985*. J.T Armstrong (Ed.), San Francisco, California, USA, 104-106.
- Çech, F. & Burke, E.A. (1984). Sodian-beryllian cordierite from Gammelmorskörr, Kemiö Island, Finland, and its decomposition products. *N. Jb. Mineral. Mh.*, **H(3)**, 125-136.
- Radoslovich, E.W. (1963). The cell dimensions and symmetry of layer-lattice silicates. V. Composition limits. *Am. Mineral.*, **48**, 348-367.
- Ransom, B. & Helgeson, H.C. (1993). Compositional endmembers and thermodynamic components of illitic and dioctahedral aluminous smectite solid solutions. *Clays and Clay Minerals*, **41**, 537-550.

- Rehfeld, U. (1983). A relictic staurolite-kyanite mineral paragenesis in paragneisses of the Central Schwarzwald. *N. Jb. Mineral. Abh.*, **146**, 170-181.
- Reynolds, R.C.J. (1988). Mixed layer chlorite minerals. In: *Hydrous Phyllosilicates*. S. W. Bailey (Ed.). Mineralogical Society of America., Washington D.C., 601-629.
- Richardson, S. W. (1968). Staurolite stability in a part of the system Fe-Al-Si-O-H. *J. Petrol.*, **9**, 467-488.
- Ruiz Cruz, M.D. (1999). New data for metamorphic vermiculite. *Eur. J. Mineral.*, **11**, 533-548.
- Santosh, M., Jackson, D.H. & Johnston, A.D. (1991). The significance of channel and fluid inclusion CO₂ in cordierite: evidence from carbon isotopes. *J. Petrol.*, **34**, 233-258.
- Schaltegger, U. (2000). U-Pb geochronology of the Southern Black Forest Batholith (Central Variscan belt): timing of exhumation and granite emplacement. *Inter. J. Earth Science*, **88**, 814-828.
- Schenk, K. & Armbruster, T. (1985). Beidellite-nontronite, an alteration product of cordierite in the rhyolite from Torniella (Tuscany, Italy). *N. Jb. Mineral. Mh.*, **9**, 385-395.
- Schiffman, P. & Day, H.W. (Eds.) (1992). Low-grade metamorphism of mafic rocks. *Special Paper 269*. Geological Society of America. Boulder, Colorado, pp. 261.
- Schiffman, P. & Fridleifsson, G.O. (1991). The smectite to chlorite transition in drillhole NJ-15, Nesjavellier Geothermal Field, Iceland: XRD, BSE and electron microprobe investigations. *J. Metamorphic Geol.*, **9**, 679-696.
- Schmidt, D., Livi, K.J.T. & Frey, M. (1999). Reaction progress in chloritic material: an electron microbeam study of the Tavayanne greywacke, Switzerland. *J. Metamorphic Geol.*, **17**, 229-241.
- Schreyer, W. (1965a). Synthetische und natürliche Cordierite II. *N. Jb. Mineral. Abh.*, **103**, 35-79.
- Schreyer, W. (1965b). Zur Stabilität des Ferrocordierites. *Contrib. Mineral. Petrol.*, **11**, 297-322.
- Schreyer, W. (1986). The mineral cordierite: structure and reactions in the presence of fluid phases. *Berichte der Bunsen-Gesellschaft für physikalische Chemie*, **90**, 748-755.
- Schreyer, W. & Blümel, P. (1974). Progressive metamorphism in the Moldanubicum of the Northern Bavarian Forest. *Fortschr. Mineral.*, **52**, 151-165.
- Schreyer, W. & Yoder, H.S. (1958). Cordierite-H₂O system. *Carnegie Inst. Yearb.*, **57**, 195-197.
- Schreyer, W. & Yoder, H.S. (1961). Petrographic guides to the experimental petrology of cordierite. *Carnegie Inst. Yearb.*, **60**, 147-152.
- Schreyer, W. & Yoder, H.S. (1964). The system Mg-cordierite-H₂O and related rocks. *N. Jb. Mineral.*, **101**, 271-342.
- Schreyer, W. H.-J., Bernhardt, H.-J. & Medenbach, O. (1993). Ferrogredite, Siderophyllite, Septechamosite, Andalusite and Chloritoid as alteration products of Sekaninaite (Ferrocordierite) from the Dolni Bory Pegmatite, Moravia. *Russian Geology and Geophysics*, **34**, 125-131.
- Seifert, F. (1976). Stability of the Assemblage Cordierite + K-Feldspar + Quartz. *Contrib. Mineral. Petrol.*, **57**, 179-185.

- Seifert, F. & Schreyer, W. (1970). Lower temperature stability limit of Mg cordierite in the range 1-7 kbar water pressure: a redetermination. *Contrib. Mineral. Petrol.*, **27**, 225-238.
- Shau, Y.-H., Peacor, D.R. & Essene, E.J. (1990). Corrensite and mixed-layer chlorite/corrensite in metabasalts from northern Taiwan: TEM/AEM, EMPA, XRD and optical studies. *Contrib. Mineral. Petrol.*, **105**, 123-142.
- Simon, K. (1990). Hydrothermal alteration of Variscan granites, Southern Schwarzwald, Federal Republic of Germany. *Contrib. Mineral. Petrol.*, **105**, 177-196.
- Simon, K. & Hoefs, J. (1987). Effects of meteoric water interaction on Hercynian granites from the Südschwarzwald, Southwest Germany. *Chemical Geology*, **61**, 253-261.
- Skippen, G.B. & Gunter, A.E.. (1996). The thermodynamic properties of H₂O in magnesian and iron cordierite. *Contrib. Mineral. Petrol.*, **124**, 82-89.
- Spear, F.S. (1993). *Metamorphic phase equilibria and pressure-temperature-time paths*. Washington : Mineralogical Society of America, pp. 799.
- Spear, F.S. & Cheney, J.T. (1989). A petrogenetic grid for pelitic schists in the system SiO₂-Al₂O₃-FeO-MgO-K₂O-H₂O. *Contrib. Mineral. Petrol.*, **101**, 149-164.
- Srodon, J., Morgan, D.J., Eslinger, E.V., Eberl, D.D. & Karlinger, M.R. (1986). Chemistry of illite/smectite and end-member illite. *Clays and Clay Minerals*, **34**, 368-378.
- Steeds, J. W. & Morniroli, J.-P. (1992). Electron diffraction - SAED & CBED. In: *Minerals and reaction on the atomic scale: Transmission electron microscopy*. (Ed.) P. R. Buseck, Washington D.C., 37-83.
- Stevens, G., Clemens, J.D. & Droop, G.T.R. (1993). Hydrous cordierite in granulites and crustal magma production. *Geology*, **23**, 925-928.
- Stevens, G., Clemens, J.D. & Droop, G.T.R. (1997). Melt production during granulite-facies anatexis: experimental data from 'primitive' metasedimentary protoliths. *Contrib. Mineral. Petrol.*, **128**, 325-370.
- Thompson, P., Harley, S.L. & Carrington, D.P. (2001). The distribution of H₂O-CO₂ between cordierite and granitic melt under fluid-saturated conditions at 5kabr and 900 °C. *Contrib. Mineral. Petrol.*, **142**, 107-118.
- Troll, G. (1967). Geologischen Übersichtskarte des Bayerischen Waldes 1:100 000. *Supplement to Geologica Bavaria*, **58**,
- Troll, G. (1968). Geologische Übersichtskarte des Regensburger Waldes 1:100 000. *Supplement Geologica Bavaria*, **59**,
- Vali, H. & Hesse, R. (1990). Alkylammonium ion treatment of clay minerals in ultrathin section: A new method for HRTEM examination of expandable layers. *Am. Mineral.*, **75**, 1443-1446.
- Vali, H. & Hesse, R. (1992). Identification of vermiculite by transmission electron microscopy and XRD. *Clay Minerals*, **27**, 185-192.

- Veblen, D.R., Gutherie, G.D.J., Livi, K.J.T. & Reynolds, R.C. (1990). High-resolution transmission electron microscopy and electron diffraction of mixed-layer illite/smectite: Experimental results. *Clays and Clay Minerals*, **38**, 1-13.
- Vrana, S. (1979). A secondary magnesium-bearing beryl in pseudomorphs after pegmatitic cordierite. *Čas. Miner. Geol.*, **24**, 65-69.
- Vry, J.K., Brown, P.E., Valley, J.W. & Morrison, J. (1988). Constraints on granulite genesis from carbon isotope compositions of cordierite and graphite. *Nature*, **332**, 66-68.
- Vry, J.K., Brown, P.E. & Valley, J.W. (1990). Cordierite volatile content and the role of CO₂ in high-grade metamorphism. *Am. Mineral.*, **75**, 71-88.
- von Gehlen, K. (1989). Ore and mineral deposits of the Schwarzwald. In: Emmermann, R. & Wohlenberg, J. (eds) *The German Continental Deep Drilling Program (KTB). Site selection studies in the Oberpfalz and Schwarzwald*. Springer, Heidelberg, 277-295.
- Wernicke, R.S. & Lippolt, H.J. (1997). (U+Th)-He evidence of Jurassic continuous hydrothermal activity in the Schwarzwald basement, Germany. *Chem. Geol.*, **138**, 273-285.
- White, S.H., Hugget, J.M. & Shaw, H.F. (1985). Electron-optical studies of phyllosilicate intergrowth in sedimentary and metamorphic rocks. *Min. Mag.*, **49**, 413-423.
- Williams, D.B. & Carter, C.B. (1996). *Transmission electron microscopy - A textbook for material science*. Plenum Press, New York, pp. 750.
- Wimmenauer, W. (1980). Lithology of Precambrian in the Schwarzwald. An interim report. *N. Jb. Mineral. Mh.*, **1980**, 364-372.
- Wimmenauer, W. (1984). Das prävariszische Kristallin im Schwarzwald. *Forschr. Mineral.*, **62**, 69-86.
- Xie, X., Byerly, G.R. & Ferrell, R.E.J. (1997). I1b trioctahedral chlorite from the Baberton greenstone belt: crystal structure and rock composition constraints with implications to geothermometry. *Contrib. Mineral. Petrol.*, **126**, 275-291.
- Zaluzec, N.J., Maher, D.M. & Mochel, P.E. (1982). *Analytical Electron Microscopy-1981*. (Eds.) R. H. Geiss, San Francisco Press, San Francisco, California, pp. 25.
- Zimmermann, J.-L. (1981). La libération de l'eau, du gaz carbonique et des hydrocarbures des cordiérites. *Bulletin Minéralogie*, **104**, 325-328.
- Zoubek, V. (1965). Das Moldanubikum und seine Stellung im geologischen Bau Europas. *Freiberger Forschungshefte*, **C190**, 129-148.

Data appendix

The following pages present selected EM, AEM and FTIR data. The attached CD-Rom includes

TEM images

BSE images

XRD spectra

FTIR spectra

EM data

AEM data.

Abbreviations:

All mineral abbreviations are after Kretz (1983).

Table I: EM data

overpr. f:	overprinted f-type pinite
d. f-type:	dark f-type pinite
b. f-type:	bright f-type pinite
d. fi-type:	dark fi-type pinite
b. fi-type:	bright fi-type pinite
m-type:	m-type pinite
i-type:	i-type pinite
Na.-mix:	analysis representing a phase mixture including a Na-bearing phase
sec. bt:	secondary biotite
primary bt	primary biotite
chl-ms pi:	chlorite-muscovite pinite
ms-bt:	analysis representing mixture of muscovite and biotite
chl-ms:	analysis representing mixture of chlorite and muscovite
text. pos.:	textural position
pi. cont.:	analysis obtained at a mineral rim in contact to pinite
Al ^{IV} :	tetrahedrally coordinated Al
∑ IV:	sum of the tetrahedrally coordinated cations
Al ^{IV} :	octahedrally coordinated Al
FeO*, Fe**:	All Fe was calculated as Fe ²⁺ in all mineral formula, except for i, fi, f-type pinite and (complex) m-type pinite. Here all Fe was calculated as Fe ³⁺ .
∑ VI:	sum of the octahedrally coordinated cations
∑ X:	sum of cations on the X-site of phyllosilicates with inter-layers
X _{Mg} :	$X_{Mg} = Mg / (Mg + Fe)$

Table II: AEM data

bulk anal.:	bulk analysis
text. pos.:	textural position
dioc.:	dioctahedral
di.-trioct.:	Analysis representing a mixture of dioctahedral and trioctahedral phyllosilicates
Na-K:	Analysis with Na and K values intermediate to ideal endmember composition
Na:	Analysis with Na close to ideal Na endmember composition
Al ^{IV} :	tetrahedrally coordinated Al
∑ IV:	sum of the tetrahedrally coordinated cations
Al ^{IV} :	octahedrally coordinated Al
FeO*, Fe**:	All Fe was calculated as Fe ²⁺ in all mineral formula, except for f-type pinite and complex m-type pinite. Here all Fe was calculated as Fe ³⁺ .
∑ VI:	sum of the octahedrally coordinated cations
∑ X:	sum of cations on the X-site of phyllosilicates with inter-layers
X _{Mg} :	$X_{Mg} = Mg / (Mg + Fe)$

Table III: FTIR data

A and B refer to two FTIR measurements obtained *in situ* at one point with a rotation of 90° between both measurements.

p. height: peak height

Table I-1

sample phase core/rim* number text. pos.	Al-20 overpr. f -	Al-20 overpr. f -	Al-20 overpr. f -	Al-20 overpr. f -	Al-20 overpr. f -	Al-20 overpr. f -	Al-20 overpr. f -	Al-20 overpr. f -	Al-20 overpr. f -	Al-20 overpr. f -	Al-20 overpr. f -	Al-20 overpr. f -	Al-20 overpr. f -
	Al20-55	Al20-56	Al20-61	Al20-69	Al20-70	Al20-84	Al20-85	Al20-91	Al20-92	Al20-93	Al20-94	Al20-401	Al20-403
wt%													
SiO ₂	41.18	40.58	40.63	41.79	41.26	41.40	39.59	41.58	41.15	42.06	42.12	40.59	41.25
TiO ₂	0.01	0.03	0.00	0.00	0.00	0.02	0.03	0.01	0.04	0.00	0.00	0.00	0.02
Al ₂ O ₃	28.11	27.72	28.58	28.94	28.84	27.95	26.27	28.81	27.23	28.76	28.66	27.32	28.89
FeO**	8.08	8.70	8.48	8.12	9.13	9.55	11.09	7.13	11.28	7.06	7.83	10.36	8.64
MnO	0.31	0.31	0.17	0.31	0.18	0.28	0.29	0.34	0.25	0.21	0.26	0.22	0.25
MgO	9.10	8.98	8.98	8.91	8.92	9.37	9.26	8.60	9.70	9.26	9.53	9.10	8.87
CaO	0.62	0.66	0.62	0.67	0.71	0.70	0.70	0.59	0.67	0.61	0.59	0.60	0.69
Na ₂ O	0.05	0.03	0.04	0.04	0.05	0.04	0.04	0.07	0.04	0.05	0.06	0.04	0.04
K ₂ O	1.54	1.51	1.58	1.61	1.57	1.60	1.58	1.61	1.74	1.86	1.62	1.47	1.59
Total	89.02	88.51	89.08	90.38	90.66	90.91	88.84	88.75	92.13	89.90	90.66	89.70	90.24
cation basis							22 O						
Si	5.78	5.75	5.71	5.77	5.71	5.73	5.66	5.83	5.67	5.83	5.80	5.70	5.72
Al ^{IV}	2.22	2.25	2.29	2.23	2.29	2.27	2.34	2.17	2.33	2.17	2.20	2.30	2.28
$\sum IV$	8.00	8.00	8.00	8.00	8.00	8.00	8.00	8.00	8.00	8.00	8.00	8.00	8.00
Al ^{VI}	2.43	2.37	2.44	2.49	2.41	2.28	2.08	2.58	2.09	2.52	2.44	2.23	2.45
Ti	0.00	0.00	0.00	0.00	0.00	0.00	0.00	0.00	0.00	0.00	0.00	0.00	0.00
Fe*	0.85	0.93	0.90	0.84	0.95	0.99	1.19	0.75	1.17	0.74	0.81	1.09	0.90
Mn	0.04	0.04	0.02	0.04	0.02	0.03	0.04	0.04	0.03	0.02	0.03	0.03	0.03
Mg	1.90	1.90	1.88	1.83	1.84	1.93	1.97	1.80	1.99	1.91	1.95	1.91	1.84
$\sum VI$	5.23	5.23	5.24	5.20	5.22	5.24	5.28	5.18	5.28	5.19	5.24	5.26	5.21
Ca	0.09	0.10	0.09	0.10	0.10	0.10	0.11	0.09	0.10	0.09	0.09	0.09	0.10
Na	0.01	0.01	0.01	0.01	0.01	0.01	0.01	0.02	0.01	0.01	0.02	0.01	0.01
K	0.28	0.27	0.28	0.28	0.28	0.28	0.29	0.29	0.31	0.33	0.28	0.26	0.28
$\sum X$	0.38	0.38	0.39	0.39	0.40	0.40	0.40	0.40	0.42	0.43	0.39	0.36	0.39
$\sum cations$	13.61	13.61	13.62	13.59	13.61	13.64	13.68	13.57	13.69	13.63	13.62	13.62	13.61
X _{Mg}	0.69	0.67	0.68	0.68	0.66	0.66	0.62	0.71	0.63	0.72	0.71	0.64	0.67

Table I-1

sample phase core/rim* number text. pos.	Al-20 overpr. f -	Al-20 overpr. f -	Al-20 overpr. f -	Al-20 overpr. f -	Al-20 overpr. f -	Al-20 overpr. f -	Al-20 overpr. f -	Al-20 overpr. f -	Al-20 overpr. f -	Al-20 overpr. f -	Al-20 overpr. f -	Al-20 overpr. f -	Al-20 overpr. f -
	Al20-405	Al20-406	Al20-407	Al20-408	Al20-404	Al20-404	Al20-702	Al20-706	Al20-707	Al20-714	Al20-715	Al20-716	Al20-717
wt%													
SiO ₂	42.38	41.16	41.23	40.05	38.21	38.21	41.33	42.17	41.81	39.58	38.61	42.53	42.81
TiO ₂	0.02	0.01	0.00	0.01	0.03	0.03	0.00	0.00	0.03	0.04	0.02	0.00	0.05
Al ₂ O ₃	29.48	28.64	27.33	26.13	25.24	25.24	28.34	29.38	28.47	25.71	25.20	28.02	28.41
FeO**	8.11	9.19	9.91	11.74	8.32	8.32	8.90	7.23	8.41	11.25	11.55	8.01	7.67
MnO	0.22	0.25	0.29	0.24	0.28	0.28	0.20	0.15	0.25	0.28	0.28	0.25	0.24
MgO	8.99	8.87	9.17	9.30	9.03	9.03	8.97	6.68	8.92	9.20	9.13	8.51	8.95
CaO	0.71	0.66	0.62	0.56	0.74	0.74	0.71	0.58	0.73	0.63	0.61	0.68	0.70
Na ₂ O	0.05	0.05	0.05	0.02	0.03	0.03	0.05	0.05	0.09	0.04	0.03	0.05	0.06
K ₂ O	1.58	1.60	1.65	1.76	1.54	1.54	1.58	1.84	1.72	1.53	1.57	2.00	1.73
Total	91.54	90.47	90.30	89.81	83.41	83.41	90.07	88.11	90.41	88.25	87.01	90.07	90.63
cation basi							22 O						
Si	5.77	5.71	5.75	5.67	5.76	5.76	5.75	5.93	5.79	5.69	5.65	5.90	5.89
Al ^{IV}	2.23	2.29	2.25	2.33	2.24	2.24	2.25	2.07	2.21	2.31	2.35	2.10	2.11
$\sum IV$	8.00	8.00	8.00	8.00	8.00	8.00	8.00	8.00	8.00	8.00	8.00	8.00	8.00
Al ^{VI}	2.51	2.39	2.25	2.03	2.24	2.24	2.40	2.80	2.43	2.05	1.99	2.48	2.49
Ti	0.00	0.00	0.00	0.00	0.00	0.00	0.00	0.00	0.00	0.00	0.00	0.00	0.00
Fe*	0.83	0.96	1.04	1.25	0.94	0.94	0.93	0.77	0.88	1.22	1.27	0.84	0.79
Mn	0.03	0.03	0.03	0.03	0.04	0.04	0.02	0.02	0.03	0.03	0.03	0.03	0.03
Mg	1.83	1.84	1.91	1.96	2.03	2.03	1.86	1.40	1.84	1.97	1.99	1.76	1.83
$\sum VI$	5.19	5.22	5.23	5.28	5.25	5.25	5.21	4.99	5.18	5.27	5.29	5.11	5.15
Ca	0.10	0.10	0.09	0.09	0.12	0.12	0.11	0.09	0.11	0.10	0.10	0.10	0.10
Na	0.01	0.01	0.01	0.01	0.01	0.01	0.01	0.01	0.02	0.01	0.01	0.01	0.02
K	0.27	0.28	0.29	0.32	0.30	0.30	0.28	0.33	0.30	0.28	0.29	0.35	0.30
$\sum X$	0.39	0.39	0.40	0.41	0.42	0.42	0.40	0.43	0.43	0.39	0.40	0.47	0.42
$\sum cations$	13.58	13.62	13.63	13.68	13.68	13.68	13.61	13.42	13.61	13.66	13.69	13.57	13.57
X _{Mg}	0.69	0.66	0.65	0.61	0.68	0.68	0.67	0.65	0.68	0.62	0.61	0.68	0.70

Table I-2

sample phase core/rim* number text. pos.	Bw-29 d. f-type	Bw-29 d. f-type	Bw-29 d. f-type	Bw-29 d. f-type	Bw-29 d. f-type	Bw-29 d. f-type	Bw-29 d. f-type	Bw-29 d. f-type	Bw-29 d. f-type	Bw-29 d. f-type	Bw-29 d. f-type	Bw-29 d. f-type	Bw-29 d. f-type
	Bw29-221	Bw29-223	Bw29-224	Bw29-225	Bw29-250	Bw29-288	Bw29-289	Bw29-290	Bw29-291	Bw29-292	Bw29-294	Bw29-413	Bw29-67
wt%													
SiO ₂	39.37	38.19	39.43	38.10	40.00	39.83	39.05	39.50	39.37	37.16	41.58	41.21	38.98
TiO ₂	0.00	0.03	0.00	0.01	0.00	0.01	0.01	0.02	0.00	0.00	0.02	0.00	0.00
Al ₂ O ₃	33.45	33.19	33.11	32.32	33.17	36.72	30.89	36.61	32.14	36.65	35.36	33.51	33.63
FeO**	6.10	5.91	6.39	5.52	6.62	5.96	6.78	5.79	5.53	6.84	6.92	0.94	5.59
MnO	0.11	0.09	0.06	0.16	0.13	0.13	0.10	0.13	0.15	0.24	0.18	0.05	0.10
MgO	1.52	1.58	1.67	1.51	1.64	1.44	1.74	1.64	1.56	4.80	1.94	0.37	1.44
CaO	0.78	0.86	0.94	1.21	0.95	0.97	1.08	0.85	0.80	0.99	1.09	0.12	0.64
Na ₂ O	0.10	0.09	0.16	0.13	0.12	0.19	0.17	0.31	0.21	0.15	0.25	0.31	0.24
K ₂ O	0.34	0.30	0.53	0.51	0.60	0.82	0.66	0.98	0.91	0.09	0.73	5.03	0.49
Total	81.77	80.24	82.30	79.47	83.25	86.09	80.50	85.82	80.65	86.92	88.09	81.62	81.10
cation basi							22 O						
Si	5.84	5.78	5.84	5.83	5.86	5.64	5.93	5.62	5.94	5.26	5.77	6.17	5.83
Al ^{IV}	2.16	2.22	2.16	2.17	2.14	2.36	2.07	2.38	2.06	2.74	2.23	1.83	2.17
∑ IV	8.00	8.00	8.00	8.00	8.00	8.00	8.00	8.00	8.00	8.00	8.00	8.00	8.00
Al ^{VI}	3.69	3.70	3.61	3.66	3.59	3.77	3.46	3.76	3.65	3.37	3.56	4.08	3.75
Ti	0.00	0.00	0.00	0.00	0.00	0.00	0.00	0.00	0.00	0.00	0.00	0.00	0.00
Fe*	0.68	0.67	0.71	0.64	0.73	0.64	0.78	0.62	0.63	0.73	0.72	0.11	0.63
Mn	0.01	0.01	0.01	0.02	0.02	0.02	0.01	0.02	0.02	0.03	0.02	0.01	0.01
Mg	0.34	0.36	0.37	0.35	0.36	0.30	0.39	0.35	0.35	1.01	0.40	0.08	0.32
∑ VI	4.72	4.74	4.70	4.67	4.69	4.73	4.65	4.74	4.65	5.14	4.71	4.28	4.71
Ca	0.12	0.14	0.15	0.20	0.15	0.15	0.18	0.13	0.13	0.15	0.16	0.02	0.10
Na	0.03	0.02	0.04	0.04	0.03	0.05	0.05	0.09	0.06	0.04	0.07	0.09	0.07
K	0.06	0.06	0.10	0.10	0.11	0.15	0.13	0.18	0.17	0.02	0.13	0.96	0.09
∑ X	0.22	0.22	0.29	0.34	0.29	0.35	0.35	0.39	0.37	0.21	0.36	1.07	0.26
∑ cations	12.94	12.96	12.99	13.00	12.98	13.08	13.00	13.13	13.01	13.35	13.07	13.35	12.98
X _{Mg}	0.33	0.35	0.34	0.35	0.33	0.32	0.34	0.36	0.36	0.58	0.36	0.43	0.34

Table I-3

sample phase core/rim* number text. pos.	Bw-29 d. f-type	Bw-29 d. f-type	Bw-29 d. f-type	Bw-29 d. f-type	Bw-29 d. f-type	Bw-29 d. f-type	Bw-29 d. f-type	Bw-29 d. f-type	Bw-29 d. f-type	Bw-29 d. f-type	Bw-29 d. f-type	Bw-29 d. f-type	Bw-29 d. f-type
	Bw29-153	Bw3-400	Bw29-416	Bw29-418	Bw29-424	Bw29-425	Bw29-426	Bw29-429	Bw29-430	Bw29-431	Bw29-432	Bw29-433	Bw29-445
wt%													
SiO ₂	37.28	42.07	38.90	40.81	38.47	42.21	41.82	41.20	42.44	42.83	43.76	42.03	38.91
TiO ₂	0.00	0.00	0.04	0.00	0.02	0.00	0.00	0.00	0.00	0.01	0.00	0.00	0.03
Al ₂ O ₃	33.80	33.28	35.77	32.70	32.82	34.08	33.56	36.88	35.76	36.77	36.13	36.97	34.50
FeO**	6.56	6.85	5.42	7.71	5.99	6.49	7.45	6.23	5.41	5.91	5.14	6.29	6.32
MnO	0.21	0.10	0.08	0.11	0.02	0.04	0.13	0.16	0.05	0.12	0.01	0.05	0.06
MgO	1.70	2.53	1.42	2.56	1.81	2.33	2.53	1.56	1.56	1.39	1.32	1.55	1.54
CaO	0.87	0.43	0.60	0.53	0.38	0.37	0.40	0.73	1.33	0.84	0.98	1.08	0.75
Na ₂ O	0.16	0.20	0.37	0.25	0.65	0.17	0.24	0.41	0.38	0.36	0.29	0.38	0.37
K ₂ O	0.32	1.78	0.80	1.27	2.06	1.91	1.37	0.73	0.81	0.87	0.68	0.79	0.90
Total	80.90	87.23	83.41	85.95	83.21	87.60	87.55	87.93	87.75	89.10	88.32	89.16	83.41
cation basi							22 O						
Si	5.63	5.92	5.67	5.84	6.90	5.90	5.87	5.71	5.88	5.84	5.98	5.75	5.70
Al ^{IV}	2.37	2.08	2.33	2.16	1.10	2.10	2.13	2.29	2.12	2.16	2.02	2.25	2.30
∑ IV	8.00	8.00	8.00	8.00	8.00	8.00	8.00	8.00	8.00	8.00	8.00	8.00	8.00
Al ^{VI}	3.64	3.44	3.82	3.36	2.87	3.52	3.42	3.73	3.71	3.75	3.80	3.71	3.67
Ti	0.00	0.00	0.00	0.00	0.00	0.00	0.00	0.00	0.00	0.00	0.00	0.00	0.00
Fe*	0.75	0.73	0.59	0.83	0.85	0.68	0.79	0.65	0.56	0.61	0.53	0.65	0.70
Mn	0.03	0.01	0.01	0.01	0.00	0.00	0.02	0.02	0.01	0.01	0.00	0.01	0.01
Mg	0.38	0.53	0.31	0.55	0.51	0.49	0.53	0.32	0.32	0.28	0.27	0.32	0.34
∑ VI	4.80	4.71	4.73	4.75	4.24	4.70	4.75	4.72	4.60	4.65	4.60	4.67	4.71
Ca	0.14	0.06	0.09	0.08	0.08	0.06	0.06	0.11	0.20	0.12	0.14	0.16	0.12
Na	0.05	0.05	0.11	0.07	0.24	0.05	0.06	0.11	0.10	0.10	0.08	0.10	0.11
K	0.06	0.32	0.15	0.23	0.50	0.34	0.25	0.13	0.14	0.15	0.12	0.14	0.17
∑ X	0.25	0.44	0.35	0.38	0.81	0.44	0.37	0.35	0.44	0.37	0.34	0.40	0.39
∑ cations	13.05	13.14	13.08	13.13	13.05	13.14	13.12	13.07	13.05	13.02	12.94	13.07	13.10
X _{Mg}	0.34	0.42	0.34	0.40	0.37	0.42	0.40	0.33	0.36	0.32	0.34	0.33	0.33

Table I-4

sample phase core/rim* number text. pos.	Bw-29 b. f-type	Bw-29 b. f-type	Bw-29 b. f-type	Bw-29 b. f-type	Bw-29 b. f-type	Bw-29 b. f-type	Bw-29 b. f-type	Bw-29 b. f-type	Bw-29 b. f-type	Bw-29 b. f-type	Bw-29 b. f-type	Bw-29 b. f-type	Bw-29 b. f-type
	Bw29-143	Bw29-144	Bw29-146	Bw29-154	Bw29-185	Bw29-192	Bw29-24	Bw29-227	Bw29-228	Bw29-229	Bw29-230	Bw29-231	Bw29-233
wt%													
SiO ₂	39.83	42.85	38.32	41.04	40.43	43.88	44.12	37.24	37.84	40.95	38.93	39.89	39.99
TiO ₂	0.01	0.00	0.00	0.01	0.00	0.01	0.04	0.01	0.02	0.02	0.00	0.00	0.00
Al ₂ O ₃	31.60	31.96	31.15	33.20	31.77	31.37	29.91	27.20	29.13	31.13	29.40	31.22	31.54
FeO**	8.80	10.35	8.75	8.06	8.63	10.09	12.12	14.84	9.48	8.90	11.72	10.41	10.03
MnO	0.17	0.23	0.19	0.16	0.16	0.21	0.24	0.17	0.11	0.15	0.19	0.19	0.19
MgO	1.93	3.41	2.09	2.33	2.60	3.46	4.54	3.61	2.48	2.29	2.85	2.58	2.59
CaO	1.03	0.57	0.87	0.68	0.62	0.53	0.37	0.77	1.17	1.25	1.19	1.17	0.85
Na ₂ O	0.04	0.14	0.21	0.13	0.19	0.11	0.28	0.15	0.14	0.19	0.16	0.17	0.12
K ₂ O	0.12	0.11	0.38	0.50	0.82	0.36	0.28	0.32	0.54	0.60	0.48	0.53	0.35
Total	83.54	89.61	81.96	86.12	85.20	90.02	91.90	84.30	80.93	85.47	84.92	86.15	85.69
cation basi							22 O						
Si	5.85	5.89	5.77	5.84	5.85	6.00	5.97	5.61	5.80	5.91	5.74	5.76	5.78
Al ^{IV}	2.15	2.11	2.23	2.16	2.15	2.00	2.03	2.39	2.20	2.09	2.26	2.24	2.22
∑ IV	8.00	8.00	8.00	8.00	8.00	8.00	8.00	8.00	8.00	8.00	8.00	8.00	8.00
Al ^{VI}	3.32	3.07	3.29	3.40	3.26	3.06	2.73	2.44	3.07	3.20	2.85	3.06	3.14
Ti	0.00	0.00	0.00	0.00	0.00	0.00	0.00	0.00	0.00	0.00	0.00	0.00	0.00
Fe*	0.97	1.07	0.99	0.86	0.94	1.04	1.23	1.68	1.09	0.97	1.30	1.13	1.09
Mn	0.02	0.03	0.02	0.02	0.02	0.02	0.03	0.02	0.01	0.02	0.02	0.02	0.02
Mg	0.42	0.70	0.47	0.49	0.56	0.71	0.92	0.81	0.57	0.49	0.63	0.55	0.56
∑ VI	4.74	4.87	4.77	4.78	4.78	4.83	4.91	4.96	4.75	4.68	4.80	4.77	4.82
Ca	0.16	0.08	0.14	0.10	0.10	0.08	0.05	0.12	0.19	0.19	0.19	0.18	0.13
Na	0.01	0.04	0.06	0.04	0.05	0.03	0.07	0.04	0.04	0.05	0.05	0.05	0.03
K	0.02	0.02	0.07	0.09	0.15	0.06	0.05	0.06	0.11	0.11	0.09	0.10	0.07
∑ X	0.20	0.14	0.27	0.23	0.30	0.17	0.18	0.23	0.34	0.36	0.32	0.33	0.23
∑ cations	12.94	13.01	13.04	13.01	13.08	13.00	13.09	13.19	13.09	13.04	13.12	13.10	13.04
X _{Mg}	0.30	0.40	0.32	0.36	0.37	0.40	0.43	0.33	0.34	0.34	0.33	0.33	0.34

Table I-4

sample phase core/rim* number text. pos.	Bw-29 b. f-type	Bw-29 b. f-type	Bw-29 b. f-type	Bw-29 b. f-type	Bw-29 b. f-type	Bw-29 b. f-type	Bw-29 b. f-type	Bw-29 b. f-type	Bw-29 b. f-type	Bw-29 b. f-type	Bw-29 b. f-type	Bw-29 b. f-type	Bw-29 b. f-type
	Bw29-234	Bw29-235	Bw29-236	Bw29-237	Bw29-238	Bw29-239	Bw29-249	Bw29-252	Bw29-254	Bw29-703	Bw29-7004	Bw29-705	Bw29-706
wt%													
SiO ₂	40.00	39.42	40.08	38.70	40.44	38.79	40.35	40.71	39.78	38.89	38.23	38.97	38.57
TiO ₂	0.01	0.04	0.00	0.00	0.00	0.02	0.00	0.00	0.00	0.00	0.00	0.00	0.00
Al ₂ O ₃	31.94	31.40	31.26	32.13	31.50	31.89	32.43	29.66	30.78	31.61	33.97	35.46	34.01
FeO**	9.93	10.16	9.73	10.27	11.09	10.68	8.99	10.73	11.14	10.75	5.36	5.02	7.55
MnO	0.13	0.20	0.19	0.18	0.17	0.19	0.10	0.17	0.17	0.22	0.08	0.09	0.15
MgO	2.59	2.51	2.67	2.48	2.97	2.62	2.23	2.78	2.76	2.65	1.44	1.40	2.05
CaO	0.82	0.84	0.87	0.93	0.81	0.80	0.99	1.07	1.29	0.71	1.09	1.52	1.01
Na ₂ O	0.17	0.18	0.16	0.19	0.25	0.16	0.17	0.18	0.22	0.29	0.14	0.22	0.14
K ₂ O	0.34	0.33	0.32	0.53	0.52	0.27	0.42	0.55	0.58	0.43	0.34	0.53	0.30
Total	85.92	85.09	85.31	85.40	87.75	85.43	85.69	85.86	86.71	85.55	80.64	83.25	83.78
cation basi													
Si	5.76	5.74	5.81	5.63	5.74	5.64	5.80	5.89	5.73	5.66	5.75	5.69	5.64
Al ^{IV}	2.24	2.26	2.19	2.37	2.26	2.36	2.20	2.11	2.27	2.34	2.25	2.31	2.36
∑ IV	8.00	8.00	8.00	8.00	8.00	8.00	8.00	8.00	8.00	8.00	8.00	8.00	8.00
Al ^{VI}	3.17	3.13	3.15	3.14	3.00	3.11	3.29	2.96	2.95	3.08	3.77	3.79	3.51
Ti	0.00	0.00	0.00	0.00	0.00	0.00	0.00	0.00	0.00	0.00	0.00	0.00	0.00
Fe*	1.08	1.11	1.06	1.12	1.18	1.17	0.97	1.17	1.21	1.18	0.61	0.55	0.83
Mn	0.02	0.02	0.02	0.02	0.02	0.02	0.01	0.02	0.02	0.03	0.01	0.01	0.02
Mg	0.56	0.55	0.58	0.54	0.63	0.57	0.48	0.60	0.59	0.57	0.32	0.31	0.45
∑ VI	4.82	4.82	4.81	4.83	4.83	4.87	4.75	4.75	4.77	4.85	4.71	4.66	4.80
Ca	0.13	0.13	0.14	0.15	0.12	0.12	0.15	0.17	0.20	0.11	0.18	0.24	0.16
Na	0.05	0.05	0.05	0.05	0.07	0.04	0.05	0.05	0.06	0.08	0.04	0.06	0.04
K	0.06	0.06	0.06	0.10	0.09	0.05	0.08	0.10	0.11	0.08	0.06	0.10	0.06
∑ X	0.23	0.24	0.24	0.30	0.28	0.22	0.28	0.32	0.37	0.27	0.28	0.40	0.25
∑ cations	13.05	13.06	13.05	13.12	13.12	13.09	13.03	13.07	13.14	13.13	12.99	13.06	13.06
X _{Mg}	0.34	0.33	0.35	0.32	0.35	0.33	0.33	0.34	0.33	0.33	0.35	0.36	0.35

Table I-5

sample phase core/rim* number text. pos.	Bw-3 d. fi-type	Bw-3 d. fi-type	Bw-3 d. fi-type	Bw-3 d. fi-type	Bw-3 d. fi-type	Bw-3 d. fi-type	Bw-3 d. fi-type	Bw-3 d. fi-type	Bw-3 d. fi-type	Bw-3 d. fi-type	Bw-3 d. fi-type	Bw-3 d. fi-type	Bw-3 d. fi-type
	Bw3-263	Bw3-264	Bw3-397	Bw3-703	Bw3-704	Bw3-705	Bw3-708	Bw3-710	Bw3-718	Bw3-719	Bw3-722	Bw3-723	Bw3-724
wt%													
SiO ₂	40.74	40.06	39.82	39.80	41.21	41.21	40.39	38.37	44.62	43.38	41.04	44.43	40.90
TiO ₂	0.00	0.03	0.05	0.01	0.01	0.00	0.00	0.02	0.02	0.00	0.00	0.02	0.00
Al ₂ O ₃	27.66	34.12	28.35	30.33	30.79	30.78	30.27	31.96	35.32	35.77	30.78	35.54	32.19
FeO**	5.97	5.65	7.30	6.81	5.92	5.88	8.92	7.75	4.49	4.26	7.56	4.77	4.80
MnO	0.17	0.16	0.15	0.20	0.23	0.16	0.14	0.16	0.11	0.12	0.19	0.09	0.05
MgO	3.07	3.07	4.47	7.04	6.74	6.73	5.84	5.92	2.73	2.85	5.42	2.83	3.05
CaO	2.32	1.66	1.32	0.66	0.58	0.58	0.53	0.56	1.90	1.94	0.61	2.09	1.38
Na ₂ O	0.12	0.33	0.15	0.04	0.06	0.05	0.04	0.08	0.41	0.43	0.16	0.53	0.36
K ₂ O	0.64	0.68	1.10	0.85	1.24	1.22	1.12	1.19	1.14	1.00	1.81	1.11	0.92
Total	80.69	85.74	82.71	85.76	86.77	86.61	87.23	86.02	90.75	89.76	87.58	91.41	83.65
cation basi							22 O						
Si	6.19	5.72	5.95	5.73	5.84	5.85	5.75	5.54	5.98	5.88	5.82	5.93	5.95
Al ^{IV}	1.81	2.28	2.05	2.27	2.16	2.15	2.25	2.46	2.02	2.12	2.18	2.07	2.05
∑ IV	8.00	8.00	8.00	8.00	8.00	8.00	8.00	8.00	8.00	8.00	8.00	8.00	8.00
Al ^{VI}	3.14	3.46	2.95	2.87	2.98	2.99	2.83	2.98	3.56	3.60	2.96	3.52	3.48
Ti	0.00	0.00	0.01	0.00	0.00	0.00	0.00	0.00	0.00	0.00	0.00	0.00	0.00
Fe*	0.68	0.61	0.82	0.74	0.63	0.63	0.96	0.84	0.45	0.43	0.81	0.48	0.53
Mn	0.02	0.02	0.02	0.02	0.03	0.02	0.02	0.02	0.01	0.01	0.02	0.01	0.01
Mg	0.69	0.65	1.00	1.51	1.42	1.42	1.24	1.27	0.55	0.58	1.15	0.56	0.66
∑ VI	4.54	4.74	4.79	5.15	5.06	5.06	5.04	5.11	4.58	4.62	4.93	4.57	4.67
Ca	0.38	0.25	0.21	0.10	0.09	0.09	0.08	0.09	0.27	0.28	0.09	0.30	0.22
Na	0.04	0.09	0.04	0.01	0.02	0.01	0.01	0.02	0.11	0.11	0.04	0.14	0.10
K	0.12	0.12	0.21	0.16	0.22	0.22	0.20	0.22	0.19	0.17	0.33	0.19	0.17
∑ X	0.54	0.47	0.47	0.27	0.33	0.32	0.29	0.33	0.57	0.57	0.46	0.63	0.49
∑ cations	13.08	13.21	13.26	13.41	13.39	13.38	13.34	13.44	13.15	13.19	13.40	13.20	13.16
X _{Mg}	0.50	0.52	0.55	0.67	0.69	0.69	0.56	0.60	0.55	0.57	0.59	0.54	0.56

Table I-6

sample phase core/rim* number text. pos.	Bw-3 b. fi-type	Bw-3 b. fi-type	Bw-3 b. fi-type	Bw-3 b. fi-type	Bw-3 b. fi-type	Bw-3 b. fi-type	Bw-3 b. fi-type	Bw-3 b. fi-type	Bw-3 b. fi-type	Bw-3 b. fi-type	Bw-3 b. fi-type	Bw-3 b. fi-type	Bw-3 b. fi-type
	Bw3-276	Bw3-329	Bw3-376	Bw3-377	Bw3-378	Bw3-379	Bw3-380	Bw3-381	Bw3-382	Bw3-383	Bw3-384	Bw3-274	Bw3-722
wt%													
SiO ₂	40.49	42.46	44.00	46.25	38.58	38.75	39.04	38.92	42.18	43.24	47.57	43.24	41.04
TiO ₂	0.00	0.00	0.00	0.00	0.03	0.01	0.01	0.03	0.03	0.00	0.03	0.00	0.00
Al ₂ O ₃	29.72	35.02	31.21	30.49	29.10	30.29	28.94	29.96	28.27	28.54	31.37	31.60	30.78
FeO**	5.13	4.30	7.80	7.53	8.80	8.12	7.58	8.14	7.72	7.38	6.52	7.44	7.56
MnO	0.11	0.11	0.16	0.21	0.17	0.09	0.12	0.17	0.17	0.17	0.19	0.23	0.19
MgO	2.59	2.10	5.01	5.04	4.43	4.58	4.26	4.53	4.71	5.08	4.74	3.82	5.42
CaO	1.25	1.15	1.33	1.41	1.74	1.76	1.64	1.74	1.43	1.36	1.39	1.09	0.61
Na ₂ O	0.33	0.36	0.34	0.34	0.16	0.21	0.08	0.14	0.24	0.27	0.30	0.41	0.16
K ₂ O	1.15	1.55	0.56	0.67	0.61	0.65	0.41	0.54	0.67	0.58	0.66	1.09	1.81
Total	80.76	87.08	90.42	91.97	83.62	84.50	82.07	84.16	85.42	86.64	92.81	88.96	87.58
cation basi							22 O						
Si	6.28	6.06	6.21	6.39	6.01	5.94	6.11	5.98	6.33	6.36	6.44	6.21	5.82
Al ^{IV}	1.72	1.94	1.79	1.61	1.99	2.06	1.89	2.02	1.67	1.64	1.56	1.79	2.18
∑ IV	8.00	8.00	8.00	8.00	8.00	8.00	8.00	8.00	8.00	8.00	8.00	8.00	8.00
Al ^{VI}	3.72	3.94	3.40	3.36	3.36	3.41	3.44	3.41	3.33	3.31	3.44	3.55	2.96
Ti	0.00	0.00	0.00	0.00	0.00	0.00	0.00	0.00	0.00	0.00	0.00	0.00	0.00
Fe*	0.20	0.15	0.28	0.26	0.34	0.31	0.30	0.31	0.29	0.27	0.22	0.27	0.81
Mn	0.01	0.01	0.02	0.02	0.02	0.01	0.02	0.02	0.02	0.02	0.02	0.03	0.02
Mg	0.60	0.45	1.05	1.04	1.03	1.05	0.99	1.04	1.05	1.11	0.96	0.82	1.15
∑ VI	4.53	4.56	4.75	4.68	4.76	4.78	4.75	4.78	4.70	4.72	4.65	4.66	4.93
Ca	0.21	0.18	0.20	0.21	0.29	0.29	0.27	0.29	0.23	0.21	0.20	0.17	0.09
Na	0.10	0.10	0.09	0.09	0.05	0.06	0.02	0.04	0.07	0.08	0.08	0.11	0.04
K	0.23	0.28	0.10	0.12	0.12	0.13	0.08	0.11	0.13	0.11	0.11	0.20	0.33
∑ X	0.53	0.56	0.40	0.42	0.46	0.48	0.38	0.43	0.43	0.40	0.39	0.48	0.46
∑ cations	13.06	13.11	13.15	13.10	13.22	13.26	13.13	13.22	13.12	13.12	13.04	13.15	13.40
X _{Mg}	0.75	0.74	0.79	0.80	0.75	0.77	0.77	0.77	0.78	0.80	0.81	0.75	0.59

Table I-7

sample phase core/rim* number text. pos.	Bw-8 d. f-type	Bw-8 d. f-type	Bw-8 d. f-type	Bw-8 d. f-type	Bw-8 d. f-type	Bw-8 d. f-type	Bw-8 d. f-type	Bw-8 d. f-type	Bw-8 d. f-type	Bw-8 d. f-type	Bw-8 d. f-type	Bw-8 d. f-type	Bw-8 d. f-type
	Bw8-155	Bw8-156	Bw8-157	Bw8-160	Bw8-175	Bw8-179	Bw8-180	Bw8-185	Bw8-191	Bw8-193	Bw8-194	Bw8-200	Bw8-201
wt%													
SiO ₂	40.74	40.48	39.26	40.23	42.22	39.01	39.86	39.84	40.45	41.30	41.20	42.73	41.73
TiO ₂	0.01	0.02	0.02	0.02	0.01	0.01	0.00	0.03	0.00	0.00	0.01	0.00	0.01
Al ₂ O ₃	32.41	31.55	31.27	32.08	31.54	33.24	33.85	33.68	34.25	34.63	31.85	33.19	33.48
FeO**	7.38	8.52	8.35	9.47	9.03	6.60	6.89	7.17	7.58	7.12	8.45	7.34	7.10
MnO	0.12	0.17	0.18	0.25	0.19	0.08	0.14	0.23	0.13	0.14	0.24	0.24	0.21
MgO	2.81	3.54	3.16	3.79	4.26	2.20	2.33	2.21	2.13	2.41	3.96	3.28	3.18
CaO	1.33	1.13	1.37	0.95	0.91	1.27	1.14	1.35	1.27	1.10	0.87	1.11	1.01
Na ₂ O	0.18	0.22	0.27	0.18	0.23	0.08	0.09	0.11	0.06	0.15	0.16	0.17	0.15
K ₂ O	0.25	0.39	0.46	0.27	0.28	0.15	0.14	0.16	0.12	0.31	0.18	0.36	0.17
Total	85.28	86.07	84.33	87.27	88.67	82.63	84.43	84.78	85.99	87.16	86.93	88.43	87.06
cation basi							22 O						
Si	5.85	5.80	5.75	5.71	5.87	5.76	5.76	5.75	5.75	5.78	5.83	5.91	5.85
Al ^{IV}	2.15	2.20	2.25	2.29	2.13	2.24	2.24	2.25	2.25	2.22	2.17	2.09	2.15
∑ IV	8.00	8.00	8.00	8.00	8.00	8.00	8.00	8.00	8.00	8.00	8.00	8.00	8.00
Al ^{VI}	3.34	3.13	3.15	3.07	3.03	3.54	3.52	3.47	3.49	3.50	3.13	3.32	3.38
Ti	0.00	0.00	0.00	0.00	0.00	0.00	0.00	0.00	0.00	0.00	0.00	0.00	0.00
Fe*	0.80	0.92	0.92	1.01	0.94	0.73	0.75	0.78	0.81	0.75	0.90	0.76	0.75
Mn	0.01	0.02	0.02	0.03	0.02	0.01	0.02	0.03	0.02	0.02	0.03	0.03	0.02
Mg	0.60	0.76	0.69	0.80	0.88	0.48	0.50	0.47	0.45	0.50	0.84	0.68	0.67
∑ VI	4.75	4.83	4.79	4.91	4.88	4.76	4.79	4.76	4.76	4.77	4.90	4.79	4.82
Ca	0.21	0.17	0.22	0.14	0.14	0.20	0.18	0.21	0.19	0.17	0.13	0.16	0.15
Na	0.05	0.06	0.08	0.05	0.06	0.02	0.02	0.03	0.02	0.04	0.04	0.05	0.04
K	0.05	0.07	0.09	0.05	0.05	0.03	0.03	0.03	0.02	0.05	0.03	0.06	0.03
∑ X	0.30	0.31	0.38	0.24	0.25	0.25	0.23	0.27	0.23	0.26	0.21	0.27	0.22
∑ cations	13.05	13.14	13.17	13.16	13.13	13.01	13.01	13.03	13.00	13.03	13.11	13.06	13.04
X _{Mg}	0.43	0.45	0.43	0.44	0.48	0.40	0.40	0.38	0.36	0.40	0.48	0.47	0.47

Table I-8

sample phase core/rim* number text. pos.	Bw-8 d. f-type	Bw-8 b. f-type	Bw-8 b. f-type	Bw-8 b. f-type	Bw-8 b. f-type	Bw-8 b. f-type	Bw-8 b. f-type	Bw-8 b. f-type	Bw-8 b. f-type	Bw-8 b. f-type	Bw-8 b. f-type	Bw-8 b. f-type	Bw-8 b. f-type
	Bw8-201	Bw8-283	Bw8-284	Bw8-287	Bw8-290	Bw8-298	Bw8-305	Bw8-306	Bw8-315	Bw8-321	Bw8-130	Bw8-299	Bw8-176
wt%													
SiO ₂	41.73	41.97	42.58	39.68	42.58	39.91	43.08	43.51	39.35	39.07	42.86	39.08	36.75
TiO ₂	0.01	0.00	0.00	0.00	0.00	0.00	0.02	0.03	0.01	0.00	0.03	0.01	0.03
Al ₂ O ₃	33.48	34.97	34.63	34.92	34.13	34.60	34.27	34.35	31.19	30.86	28.39	30.45	28.77
FeO**	7.10	7.29	6.90	8.73	7.41	7.10	6.96	6.82	9.98	8.54	12.38	10.61	11.11
MnO	0.21	0.04	0.09	0.07	0.06	0.16	0.07	0.11	0.18	0.21	0.40	0.13	0.18
MgO	3.18	3.80	3.70	3.99	4.25	2.55	3.92	3.49	3.73	3.17	8.53	5.36	3.97
CaO	1.01	0.27	0.30	0.36	0.31	1.31	0.20	0.18	1.57	1.34	0.04	0.73	1.27
Na ₂ O	0.15	0.06	0.08	0.12	0.12	0.30	0.07	0.04	0.26	0.09	0.17	0.14	0.09
K ₂ O	0.17	0.48	0.55	0.34	0.47	0.30	0.46	0.18	0.46	0.20	0.06	0.42	0.24
Total	87.06	88.88	88.80	88.21	89.33	86.23	89.05	88.72	86.75	83.47	92.85	86.98	82.41
cation basi							22 O						
Si	5.85	5.76	5.84	5.54	5.82	5.67	5.88	5.94	5.66	5.77	5.91	5.73	5.72
Al ^{IV}	2.15	2.24	2.16	2.46	2.18	2.33	2.12	2.06	2.34	2.23	2.09	2.27	2.28
∑ IV	8.00	8.00	8.00	8.00	8.00	8.00	8.00	8.00	8.00	8.00	8.00	8.00	8.00
Al ^{VI}	3.38	3.41	3.43	3.28	3.32	3.47	3.40	3.47	2.94	3.15	2.52	2.98	3.00
Ti	0.00	0.00	0.00	0.00	0.00	0.00	0.00	0.00	0.00	0.00	0.00	0.00	0.00
Fe*	0.75	0.75	0.71	0.92	0.76	0.76	0.71	0.70	1.08	0.95	1.43	1.30	1.45
Mn	0.02	0.00	0.01	0.01	0.01	0.02	0.01	0.01	0.02	0.03	0.05	0.02	0.02
Mg	0.67	0.78	0.76	0.83	0.87	0.54	0.80	0.71	0.80	0.70	1.75	1.17	0.92
∑ VI	4.82	4.95	4.91	5.03	4.95	4.78	4.92	4.89	4.84	4.82	5.75	5.47	5.39
Ca	0.15	0.04	0.04	0.05	0.05	0.20	0.03	0.03	0.24	0.21	0.01	0.12	0.21
Na	0.04	0.02	0.02	0.03	0.03	0.08	0.02	0.01	0.07	0.03	0.04	0.04	0.03
K	0.03	0.08	0.10	0.06	0.08	0.05	0.08	0.03	0.08	0.04	0.01	0.08	0.05
∑ X	0.22	0.14	0.16	0.15	0.16	0.34	0.13	0.07	0.40	0.27	0.06	0.23	0.28
∑ cations	13.04	13.09	13.07	13.18	13.11	13.12	13.05	12.96	13.24	13.10	13.81	13.70	13.67
X _{Mg}	0.47	0.51	0.52	0.48	0.53	0.42	0.53	0.50	0.43	0.42	0.55	0.47	0.39

Table I-9

sample phase	Ho-10 d. f-type	Ho-10 d. f-type	Ho-10 d. f-type	Ho-10 d. f-type	Ho-10 d. f-type	Ho-10 d. f-type	Ho-10 d. f-type	Ho-10 d. f-type	Ho-10 d. f-type	Ho-10 d. f-type	Ho-10 d. f-type	Ho-10 d. f-type	Ho-10 d. f-type
core/rim*	-	-	-	-	-	-	-	-	-	-	-	-	-
number	Ho10-17	Ho10-57	Ho10-58	Ho10-87	Ho10-88	Ho10-90	Ho10-96	Ho10-39	Ho10-40	Ho10-41	Ho10-42	Ho10-43	Ho10-29
textural pos.	-	-	-	-	-	-	-	-	-	-	-	-	-
wt%													
SiO ₂	41.85	45.20	40.59	38.56	42.50	41.43	43.87	43.30	42.06	43.14	40.93	41.62	41.30
TiO ₂	0.01	0.00	0.01	0.02	0.00	0.01	0.01	0.00	0.02	0.00	0.00	0.01	0.01
Al ₂ O ₃	34.60	33.03	35.31	31.18	34.98	34.16	34.22	34.04	34.43	34.43	35.08	34.93	34.91
FeO**	5.84	4.10	6.70	9.89	4.58	6.59	4.85	5.34	6.04	5.38	6.53	6.23	6.16
MnO	0.00	0.05	0.03	0.10	0.07	0.02	0.10	0.08	0.00	0.07	0.03	0.07	0.04
MgO	1.66	0.74	1.68	4.43	1.20	1.82	1.81	1.56	1.67	1.50	1.68	1.76	1.67
CaO	0.75	1.02	0.81	0.52	0.99	0.69	0.90	0.67	0.76	0.63	0.78	0.67	0.76
Na ₂ O	0.05	0.10	0.07	0.07	0.15	0.08	0.21	0.08	0.07	0.09	0.07	0.08	0.12
K ₂ O	1.26	1.62	0.54	1.08	0.85	1.38	1.10	2.16	1.25	1.97	0.65	1.12	1.25
Total	86.02	85.88	85.73	85.86	85.35	86.17	87.07	87.24	86.29	87.20	85.75	86.52	86.22
cation basis							22 O						
Si	5.92	6.34	5.76	5.60	6.01	5.88	6.09	6.05	5.93	6.02	5.81	5.86	5.84
Al ^{IV}	2.08	1.66	2.24	2.40	1.99	2.12	1.91	1.95	2.07	1.98	2.19	2.14	2.16
∑ IV	8.00	8.00	8.00	8.00	8.00	8.00	8.00	8.00	8.00	8.00	8.00	8.00	8.00
Al ^{VI}	3.68	3.81	3.67	2.94	3.84	3.59	3.70	3.66	3.65	3.69	3.67	3.66	3.66
Ti	0.00	0.00	0.00	0.00	0.00	0.00	0.00	0.00	0.00	0.00	0.00	0.00	0.00
Fe*	0.62	0.43	0.72	1.00	0.49	0.70	0.51	0.56	0.64	0.56	0.70	0.66	0.66
Mn	0.00	0.01	0.00	0.01	0.01	0.00	0.01	0.01	0.00	0.01	0.00	0.01	0.01
Mg	0.35	0.16	0.36	0.96	0.25	0.39	0.37	0.32	0.35	0.31	0.35	0.37	0.35
∑ VI	4.65	4.40	4.75	5.00	4.59	4.68	4.59	4.56	4.65	4.58	4.73	4.70	4.67
Ca	0.11	0.15	0.12	0.08	0.15	0.11	0.13	0.10	0.12	0.09	0.12	0.10	0.12
Na	0.01	0.03	0.02	0.02	0.04	0.02	0.06	0.02	0.02	0.02	0.02	0.02	0.03
K	0.23	0.29	0.10	0.20	0.15	0.25	0.20	0.39	0.22	0.35	0.12	0.20	0.23
∑ X	0.35	0.47	0.24	0.30	0.34	0.38	0.39	0.51	0.36	0.47	0.26	0.33	0.37
∑ cations	13.01	12.87	12.98	13.30	12.93	13.05	12.98	13.07	13.01	13.05	12.98	13.02	13.05
X _{Mg}	0.36	0.26	0.33	0.47	0.34	0.35	0.42	0.37	0.35	0.36	0.34	0.36	0.35

Table I-9

sample phase	Ho-10 d. f-type	Ho-10 d. f-type	Ho-10 d. f-type	Ho-10 d. f-type	Ho-10 d. f-type	Ho-10 d. f-type	Ho-10 d. f-type	Ho-10 d. f-type	Ho-10 d. f-type	Ho-10 d. f-type	Ho-10 d. f-type	Ho-10 b. f-type	Ho-10 b. f-type
core/rim*	-	-	-	-	-	-	-	-	-	-	-	-	-
number	Ho10-416	Ho10-417	Ho10-418	Ho10-419	Ho10-705	Ho10-711	Ho10-714	Ho10-715	Ho10-717	Ho10-752	Ho10-18	Ho10-47	Ho10-402
textural po:	-	-	-	-	-	-	-	-	-	-	-	-	-
wt%													
SiO ₂	40.02	39.73	40.78	39.81	46.31	40.54	40.92	40.02	41.77	44.45	41.09	38.58	35.23
TiO ₂	0.00	0.02	0.00	0.00	0.00	0.03	0.03	0.00	0.00	0.00	0.02	0.00	0.03
Al ₂ O ₃	32.97	32.51	33.32	32.39	34.39	35.06	35.33	32.34	35.00	34.80	34.54	30.77	26.33
FeO**	9.29	9.63	7.83	8.88	2.34	6.20	6.12	8.39	6.18	3.88	6.33	10.08	20.12
MnO	0.09	0.04	0.11	0.07	0.04	0.05	0.08	0.10	0.05	0.02	0.06	0.12	0.15
MgO	3.65	4.30	4.11	3.83	0.56	1.68	1.65	3.51	1.68	1.61	1.64	4.96	2.97
CaO	0.56	0.49	0.39	0.47	1.26	0.77	0.77	0.50	0.66	0.55	0.69	0.50	0.48
Na ₂ O	0.03	0.07	0.03	0.07	0.05	0.11	0.11	0.07	0.13	0.10	0.07	0.06	0.08
K ₂ O	0.96	1.12	0.99	1.07	1.57	0.89	0.80	1.01	1.67	2.70	1.29	1.33	2.16
Total	87.60	87.93	87.59	86.64	86.51	85.32	85.81	85.94	87.13	88.10	85.74	86.37	87.61
cation basi							22 O						
Si	5.66	5.62	5.73	5.69	6.39	5.79	5.80	5.75	5.86	6.13	5.85	5.59	5.30
Al ^{IV}	2.34	2.38	2.27	2.31	1.61	2.21	2.20	2.25	2.14	1.87	2.15	2.41	2.70
∑ IV	8.00	8.00	8.00	8.00	8.00	8.00	8.00	8.00	8.00	8.00	8.00	8.00	8.00
Al ^{VI}	3.15	3.04	3.25	3.15	3.99	3.68	3.70	3.22	3.65	3.78	3.64	2.84	1.97
Ti	0.00	0.00	0.00	0.00	0.00	0.00	0.00	0.00	0.00	0.00	0.00	0.00	0.00
Fe*	0.99	1.02	0.83	0.96	0.24	0.67	0.65	0.91	0.65	0.40	0.68	1.10	2.28
Mn	0.01	0.00	0.01	0.01	0.00	0.01	0.01	0.01	0.01	0.00	0.01	0.01	0.02
Mg	0.77	0.91	0.86	0.82	0.11	0.36	0.35	0.75	0.35	0.33	0.35	1.07	0.67
∑ VI	4.92	4.97	4.95	4.93	4.35	4.72	4.71	4.89	4.66	4.51	4.68	5.03	4.93
Ca	0.08	0.07	0.06	0.07	0.19	0.12	0.12	0.08	0.10	0.08	0.10	0.08	0.08
Na	0.01	0.02	0.01	0.02	0.01	0.03	0.03	0.02	0.04	0.03	0.02	0.02	0.02
K	0.17	0.20	0.18	0.19	0.28	0.16	0.15	0.18	0.30	0.47	0.23	0.25	0.41
∑ X	0.27	0.30	0.24	0.29	0.48	0.31	0.29	0.28	0.43	0.58	0.36	0.34	0.51
∑ cations	13.19	13.27	13.19	13.21	12.83	13.03	13.01	13.17	13.09	13.10	13.04	13.36	13.44
X _{Mg}	0.44	0.47	0.51	0.46	0.32	0.35	0.35	0.45	0.35	0.45	0.34	0.49	0.23

Table I-10

sample phase	Ho-10 b. f-type	Ho-10 b. f-type	Ho-10 b. f-type	Ho-10 b. f-type	Ho-10 b. f-type	Ho-10 b. f-type	Ho-10 b. f-type	Ho-10 b. f-type	Ho-10 b. f-type	Ho-10 b. f-type	Ho-10 b. f-type	Ho-10 b. f-type	Ho-10 b. f-type
core/rim*	-	-	-	-	-	-	-	-	-	-	-	-	-
number	Ho10-403	Ho12-404	Ho12-406	Ho12-407	Ho10-408	Ho10-22	Ho10-23	Ho10-34	Ho10-44	Ho10-45	Ho10-46	Ho10-21	Ho10-31
textural po:	-	-	-	-	-	-	-	-	-	-	-	-	-
wt%													
SiO ₂	36.15	35.47	35.93	40.50	39.06	43.12	42.42	42.98	37.69	38.32	38.89	45.42	41.85
TiO ₂	0.00	0.00	0.02	0.00	0.02	0.01	0.01	0.04	0.00	0.01	0.00	0.05	0.00
Al ₂ O ₃	26.49	26.12	26.71	33.66	30.94	32.46	29.84	29.60	31.27	30.80	30.72	32.60	29.09
FeO**	19.40	21.38	19.48	8.64	10.39	7.11	9.15	9.08	10.48	10.25	9.82	3.98	11.28
MnO	0.11	0.17	0.10	0.04	0.04	0.02	0.08	0.06	0.10	0.07	0.09	0.04	0.06
MgO	2.80	2.86	2.85	1.99	5.52	1.21	1.80	1.84	4.84	4.84	4.72	0.81	2.22
CaO	0.50	0.53	0.51	0.96	0.38	0.64	0.52	0.54	0.49	0.54	0.48	0.67	0.52
Na ₂ O	0.10	0.07	0.08	0.13	0.08	0.07	0.13	0.17	0.06	0.07	0.09	0.14	0.09
K ₂ O	2.46	1.56	2.12	1.01	1.80	2.95	4.16	4.33	1.14	1.02	1.27	3.90	3.96
Total	88.02	88.22	87.79	86.91	88.25	87.61	88.13	88.65	86.08	85.92	86.06	87.60	89.07
cation basi													
Si	5.39	5.30	5.36	5.75	5.56	6.08	6.06	6.10	5.49	5.57	5.64	6.34	5.96
Al ^{IV}	2.61	2.70	2.64	2.25	2.44	1.92	1.94	1.90	2.51	2.43	2.36	1.66	2.04
$\sum IV$	8.00	8.00	8.00	8.00	8.00	8.00	8.00	8.00	8.00	8.00	8.00	8.00	8.00
Al ^{VI}	2.05	1.90	2.06	3.38	2.76	3.47	3.08	3.06	2.85	2.85	2.89	3.70	2.85
Ti	0.00	0.00	0.00	0.00	0.00	0.00	0.00	0.00	0.00	0.00	0.00	0.00	0.00
Fe*	2.18	2.40	2.19	0.92	1.11	0.75	0.98	0.97	1.15	1.12	1.07	0.42	1.21
Mn	0.01	0.02	0.01	0.00	0.01	0.00	0.01	0.01	0.01	0.01	0.01	0.01	0.01
Mg	0.62	0.64	0.63	0.42	1.17	0.26	0.38	0.39	1.05	1.05	1.02	0.17	0.47
$\sum VI$	4.86	4.96	4.90	4.72	5.05	4.48	4.46	4.43	5.06	5.04	4.99	4.30	4.54
Ca	0.08	0.08	0.08	0.15	0.06	0.10	0.08	0.08	0.08	0.08	0.07	0.10	0.08
Na	0.03	0.02	0.02	0.04	0.02	0.02	0.04	0.05	0.02	0.02	0.02	0.04	0.02
K	0.47	0.30	0.40	0.18	0.33	0.53	0.76	0.78	0.21	0.19	0.23	0.69	0.72
$\sum X$	0.58	0.40	0.51	0.36	0.41	0.65	0.87	0.91	0.31	0.29	0.33	0.83	0.82
$\sum cations$	13.44	13.36	13.40	13.09	13.46	13.12	13.33	13.34	13.37	13.33	13.33	13.13	13.36
X _{Mg}	0.22	0.21	0.22	0.31	0.51	0.25	0.28	0.29	0.48	0.48	0.49	0.29	0.28

Table I-11

sample phase	Ho-12 d. f-type	Ho-12 d. f-type	Ho-12 d. f-type	Ho-12 d. f-type	Ho-12 d. f-type	Ho-12 d. f-type	Ho-12 d. f-type	Ho-12 d. f-type	Ho-12 d. f-type	Ho-12 d. f-type	Ho-12 d. f-type	Ho-12 d. f-type	Ho-12 d. f-type
core/rim*	-	-	-	-	-	-	-	-	-	-	-	-	-
number	Ho12-14	Ho12-16	Ho12-19	Ho12-21	Ho12-29	Ho12-31	Ho12-32	Ho12-55	Ho12-57	Ho12-58	Ho12-59	Ho12-67	
textural po:	-	-	-	-	-	-	-	-	-	-	-	-	
wt%													
SiO ₂	41.21	40.11	40.14	40.30	41.82	41.43	39.64	39.83	40.57	40.32	39.97	40.73	39.29
TiO ₂	0.02	0.02	0.00	0.00	0.02	0.00	0.00	0.02	0.02	0.04	0.07	0.02	0.01
Al ₂ O ₃	32.66	32.59	31.73	32.45	33.34	32.31	33.53	32.70	31.96	32.31	32.56	32.52	31.50
FeO**	8.07	9.01	8.31	8.58	7.11	7.71	8.54	9.12	8.51	8.58	8.51	7.88	9.12
MnO	0.09	0.05	0.14	0.11	0.11	0.12	0.11	0.17	0.07	0.17	0.15	0.09	0.20
MgO	3.03	2.10	2.73	2.12	2.75	1.92	2.11	2.15	1.98	2.15	2.11	1.93	3.59
CaO	0.80	1.11	1.15	1.17	0.76	1.31	1.18	1.15	1.26	1.17	1.22	1.20	1.06
Na ₂ O	0.08	0.08	0.05	0.06	0.04	0.06	0.10	0.05	0.05	0.09	0.07	0.07	0.05
K ₂ O	0.72	0.36	0.50	0.64	0.87	0.36	0.40	0.54	0.43	0.50	0.58	0.54	0.54
Total	86.70	85.42	84.75	85.43	86.85	85.23	85.61	85.74	84.83	85.35	85.24	84.99	85.35
cation basi													
Si	5.84	5.78	5.83	5.81	5.89	5.94	5.70	5.74	5.87	5.82	5.78	5.87	5.70
Al ^{IV}	2.16	2.22	2.17	2.19	2.11	2.06	2.30	2.26	2.13	2.18	2.22	2.13	2.30
$\sum IV$	8.00	8.00	8.00	8.00	8.00	8.00	8.00	8.00	8.00	8.00	8.00	8.00	8.00
Al ^{VI}	3.29	3.31	3.26	3.32	3.42	3.41	3.38	3.29	3.33	3.31	3.32	3.40	3.09
Ti	0.00	0.00	0.00	0.00	0.00	0.00	0.00	0.00	0.00	0.00	0.01	0.00	0.00
Fe*	0.86	0.98	0.91	0.93	0.75	0.83	0.92	0.99	0.93	0.93	0.92	0.85	1.00
Mn	0.01	0.01	0.02	0.01	0.01	0.01	0.01	0.02	0.01	0.02	0.02	0.01	0.02
Mg	0.64	0.45	0.59	0.46	0.58	0.41	0.45	0.46	0.43	0.46	0.45	0.42	0.78
$\sum VI$	4.81	4.75	4.77	4.72	4.77	4.66	4.77	4.76	4.69	4.73	4.73	4.69	4.89
Ca	0.12	0.17	0.18	0.18	0.11	0.20	0.18	0.18	0.19	0.18	0.19	0.19	0.16
Na	0.02	0.02	0.01	0.02	0.01	0.02	0.03	0.01	0.01	0.03	0.02	0.02	0.02
K	0.13	0.07	0.09	0.12	0.16	0.07	0.07	0.10	0.08	0.09	0.11	0.10	0.10
$\sum X$	0.27	0.26	0.28	0.32	0.28	0.29	0.28	0.29	0.29	0.30	0.31	0.31	0.28
$\sum cations$	13.08	13.01	13.06	13.04	13.05	12.95	13.05	13.05	12.98	13.03	13.04	12.99	13.16
X _{Mg}	0.43	0.32	0.39	0.33	0.43	0.33	0.33	0.32	0.32	0.33	0.33	0.33	0.44

Table I-12

sample phase	Ho-12 b. f-type	Ho-12 b. f-type	Ho-12 b. f-type	Ho-12 b. f-type	Ho-12 b. f-type	Ho-12 b. f-type	Ho-12 b. f-type	Ho-12 b. f-type	Ho-12 b. f-type	Ho-12 b. f-type	Ho-12 b. f-type	Ho-12 b. f-type	Ho-12 b. f-type
core/rim*	-	-	-	-	-	-	-	-	-	-	-	-	-
number	Ho12-487	Ho12-488	Ho12-238	Ho12-239	Ho12-17	Ho12-144	Ho12-145	Ho12-148	Ho12-20	Ho12-28	Ho12-30	Ho12-46	Ho12-61
textural po:	-	-	-	-	-	-	-	-	-	-	-	-	-
wt%													
SiO ₂	41.03	39.04	39.51	39.79	41.49	41.13	39.33	37.97	40.53	41.43	40.92	40.28	41.17
TiO ₂	0.00	0.00	0.04	0.00	0.00	0.01	0.00	0.00	0.01	0.01	0.01	0.02	0.03
Al ₂ O ₃	30.89	29.28	31.07	29.34	32.98	30.70	30.29	30.77	32.76	33.00	32.56	32.33	33.18
FeO**	9.00	11.85	11.50	11.19	7.93	8.56	12.26	13.87	8.23	8.07	8.24	8.41	8.26
MnO	0.05	0.06	0.12	0.12	0.17	0.15	0.15	0.17	0.16	0.09	0.09	0.11	0.19
MgO	3.42	2.84	3.20	2.92	3.93	3.24	3.16	3.36	4.17	3.97	2.70	4.02	4.09
CaO	0.74	1.08	1.03	1.14	0.45	0.56	0.73	0.66	0.47	0.42	0.97	0.55	0.41
Na ₂ O	0.04	0.05	0.11	0.02	0.09	0.17	0.12	0.11	0.08	0.10	0.06	0.07	0.07
K ₂ O	0.74	0.52	0.51	0.53	2.03	2.49	2.07	1.63	1.50	1.93	0.62	1.39	1.82
Total	85.91	84.71	87.11	85.04	89.09	87.00	88.10	88.53	87.91	89.02	86.17	87.18	89.24
cation basi													
Si	5.89	5.76	5.67	5.83	5.77	5.89	5.65	5.46	5.71	5.76	5.83	5.72	5.72
Al ^{IV}	2.11	2.24	2.33	2.17	2.23	2.11	2.35	2.54	2.29	2.24	2.17	2.28	2.28
$\sum IV$	8.00	8.00	8.00	8.00	8.00	8.00	8.00	8.00	8.00	8.00	8.00	8.00	8.00
Al ^{VI}	3.11	2.86	2.92	2.90	3.18	3.08	2.78	2.68	3.15	3.18	3.30	3.13	3.16
Ti	0.00	0.00	0.00	0.00	0.00	0.00	0.00	0.00	0.00	0.00	0.00	0.00	0.00
Fe*	0.97	1.32	1.24	1.23	0.83	0.92	1.33	1.50	0.87	0.84	0.88	0.90	0.86
Mn	0.01	0.01	0.01	0.01	0.02	0.02	0.02	0.02	0.02	0.01	0.01	0.01	0.02
Mg	0.73	0.63	0.68	0.64	0.81	0.69	0.68	0.72	0.88	0.82	0.57	0.85	0.85
$\sum VI$	4.83	4.81	4.86	4.79	4.85	4.71	4.80	4.92	4.92	4.86	4.77	4.90	4.89
Ca	0.11	0.17	0.16	0.18	0.07	0.09	0.11	0.10	0.07	0.06	0.15	0.08	0.06
Na	0.01	0.01	0.03	0.01	0.02	0.05	0.03	0.03	0.02	0.03	0.02	0.02	0.02
K	0.14	0.10	0.09	0.10	0.36	0.45	0.38	0.30	0.27	0.34	0.11	0.25	0.32
$\sum X$	0.26	0.28	0.28	0.28	0.45	0.59	0.52	0.43	0.36	0.43	0.28	0.35	0.40
$\sum cations$	13.09	13.09	13.14	13.07	13.30	13.30	13.33	13.35	13.28	13.29	13.05	13.25	13.30
X _{Mg}	0.43	0.32	0.36	0.34	0.50	0.43	0.34	0.32	0.50	0.49	0.39	0.49	0.50

Table I-13

sample phase	To-2 overpr. f	To-2 overpr. f	To-2 overpr. f	To-2 overpr. f	To-2 overpr. f	To-2 overpr. f	To-2 overpr. f	To-2 overpr. f	To-2 overpr. f	To-2 overpr. f	To-2 overpr. f	To-2 overpr. f	To-2 overpr. f
core/rim*	-	-	-	-	-	-	-	-	-	-	-	-	-
number	To2-95	To2-97	To2-101	To2-145	To2-146	To2-148	To2-149	To2-150	To2-151	To2-152	To2-153	To2-404	To2-407
textural po:	-	-	-	-	-	-	-	-	-	-	-	-	-
wt%													
SiO ₂	41.43	40.95	42.00	41.38	44.08	42.25	42.60	42.75	43.28	45.25	44.87	39.75	40.07
TiO ₂	0.03	0.03	0.03	0.00	0.00	0.02	0.00	0.00	0.00	0.04	0.04	0.07	0.02
Al ₂ O ₃	31.03	29.43	29.24	29.81	31.17	30.59	30.24	30.43	30.46	30.98	30.71	25.93	27.87
FeO**	8.36	8.46	9.05	8.41	7.13	7.69	8.41	8.21	7.30	6.15	6.76	10.12	10.11
MnO	0.21	0.27	0.17	0.17	0.12	0.16	0.12	0.19	0.15	0.15	0.14	0.28	0.17
MgO	5.93	7.04	7.23	6.16	5.14	5.44	5.85	5.90	5.10	4.54	4.94	7.72	8.43
CaO	0.71	0.63	0.72	0.75	0.69	0.71	0.73	0.70	0.68	0.77	0.74	0.79	0.73
Na ₂ O	0.10	0.04	0.04	0.07	0.08	0.07	0.05	0.06	0.08	0.09	0.09	0.03	0.02
K ₂ O	2.99	2.24	2.44	2.10	3.02	2.63	2.24	2.18	3.46	3.71	3.22	1.41	1.54
Total	90.78	89.09	90.92	88.88	91.43	89.57	90.23	90.42	90.51	91.68	91.51	86.10	88.95
cation basi													
Si	5.73	5.76	5.80	5.82	5.99	5.88	5.89	5.89	5.97	6.13	6.09	5.82	5.68
Al ^{IV}	2.27	2.24	2.20	2.18	2.01	2.12	2.11	2.11	2.03	1.87	1.91	2.18	2.32
$\sum IV$	8.00	8.00	8.00	8.00	8.00	8.00	8.00	8.00	8.00	8.00	8.00	8.00	8.00
Al ^{VI}	2.79	2.64	2.56	2.76	2.99	2.90	2.81	2.83	2.93	3.07	3.00	2.29	2.33
Ti	0.00	0.00	0.00	0.00	0.00	0.00	0.00	0.00	0.00	0.00	0.00	0.01	0.00
Fe*	0.87	0.90	0.94	0.89	0.73	0.81	0.87	0.85	0.76	0.63	0.69	1.11	1.08
Mn	0.02	0.03	0.02	0.02	0.01	0.02	0.01	0.02	0.02	0.02	0.02	0.03	0.02
Mg	1.22	1.48	1.49	1.29	1.04	1.13	1.20	1.21	1.05	0.92	1.00	1.68	1.78
$\sum VI$	4.92	5.05	5.02	4.96	4.77	4.85	4.90	4.91	4.75	4.64	4.71	5.13	5.21
Ca	0.10	0.09	0.11	0.11	0.10	0.11	0.11	0.10	0.10	0.11	0.11	0.12	0.11
Na	0.03	0.01	0.01	0.02	0.02	0.02	0.01	0.02	0.02	0.02	0.02	0.01	0.01
K	0.53	0.40	0.43	0.38	0.52	0.47	0.39	0.38	0.61	0.64	0.56	0.26	0.28
$\sum X$	0.66	0.51	0.55	0.51	0.64	0.59	0.52	0.50	0.73	0.78	0.69	0.40	0.39
$\sum cations$	13.57	13.55	13.56	13.46	13.42	13.45	13.42	13.42	13.48	13.41	13.40	13.52	13.60
X _{Mg}	0.58	0.62	0.61	0.59	0.59	0.58	0.58	0.59	0.58	0.59	0.59	0.60	0.62

Table I-14

sample phase core/rim* number textural po:	Wa-4 fi-type	Wa-4 fi-type	Wa-4 fi-type	Wa-4 fi-type	Wa-4 fi-type	Wa-4 fi-type	Wa-4 fi-type	Wa-4 fi-type	Wa-4 fi-type	Wa-4 fi-type	Wa-4 fi-type	Wa-4 fi-type	Wa-4 fi-type
	Wa4-88	Wa4-89	Wa4-40	Wa4-99	Wa4-100	Wa4-102	Wa4-107	Wa4-115	Wa4-124	Wa4-128	Wa4-129	Wa4-143	Wa4-144
wt%													
SiO ₂	38.65	42.12	40.63	41.14	34.24	41.83	39.62	41.32	40.20	41.61	40.42	40.36	42.44
TiO ₂	0.00	0.00	0.00	0.01	0.04	0.00	0.01	0.00	0.00	0.00	0.01	0.01	0.01
Al ₂ O ₃	32.25	29.14	28.13	28.97	30.61	30.91	32.80	29.94	28.58	30.29	30.55	33.50	31.85
FeO**	6.01	8.81	8.89	8.70	5.96	8.69	6.03	9.08	7.17	8.87	8.81	5.97	7.69
MnO	0.08	0.19	0.14	0.16	0.07	0.20	0.10	0.23	0.12	0.17	0.18	0.06	0.16
MgO	1.96	3.67	3.00	3.32	1.87	3.29	2.09	3.67	2.57	3.78	3.81	2.03	2.71
CaO	1.55	1.34	1.83	1.54	1.42	1.02	1.40	1.32	1.78	1.24	1.24	1.36	1.61
Na ₂ O	0.15	0.05	0.06	0.21	0.23	0.22	0.11	0.21	0.10	0.06	0.09	0.14	0.31
K ₂ O	0.53	0.55	0.46	0.82	0.70	1.49	0.50	0.83	0.48	0.45	0.49	0.38	0.70
Total	81.23	85.88	83.14	84.90	75.14	87.67	82.66	86.61	80.99	86.47	85.61	83.80	87.47
cation basi							22 O						
Si	5.82	6.05	6.04	6.00	5.60	5.92	5.84	5.92	6.09	5.94	5.84	5.86	5.96
Al ^{IV}	2.18	1.95	1.96	2.00	2.40	2.08	2.16	2.08	1.91	2.06	2.16	2.14	2.04
$\sum IV$	8.00	8.00	8.00	8.00	8.00	8.00	8.00	8.00	8.00	8.00	8.00	8.00	8.00
Al ^{VI}	3.53	2.98	2.97	2.98	3.51	3.08	3.54	2.97	3.19	3.03	3.04	3.59	3.24
Ti	0.00	0.00	0.00	0.00	0.00	0.00	0.00	0.00	0.00	0.00	0.00	0.00	0.00
Fe*	0.68	0.95	0.99	0.96	0.73	0.92	0.67	0.98	0.82	0.95	0.96	0.65	0.81
Mn	0.01	0.02	0.02	0.02	0.01	0.02	0.01	0.03	0.02	0.02	0.02	0.01	0.02
Mg	0.44	0.79	0.66	0.72	0.46	0.69	0.46	0.78	0.58	0.80	0.82	0.44	0.57
$\sum VI$	4.66	4.74	4.65	4.68	4.71	4.72	4.69	4.76	4.60	4.80	4.83	4.69	4.64
Ca	0.25	0.21	0.29	0.24	0.25	0.15	0.22	0.20	0.29	0.19	0.19	0.21	0.24
Na	0.04	0.01	0.02	0.06	0.07	0.06	0.03	0.06	0.03	0.02	0.03	0.04	0.08
K	0.10	0.10	0.09	0.15	0.15	0.27	0.09	0.15	0.09	0.08	0.09	0.07	0.13
$\sum X$	0.40	0.32	0.40	0.45	0.47	0.48	0.35	0.41	0.41	0.29	0.31	0.32	0.45
$\sum cations$	13.06	13.07	13.05	13.13	13.18	13.20	13.03	13.17	13.01	13.09	13.14	13.01	13.09
X _{Mg}	0.39	0.45	0.40	0.43	0.38	0.43	0.41	0.44	0.41	0.46	0.46	0.40	0.41

Table I-15

sample phase core/rim* number textural po:	Wa-4 ovepr. f	Wa-4 ovepr. f	Wa-4 ovepr. f	Wa-4 ovepr. f	Wa-4 ovepr. f	Wa-4 ovepr. f	Wa-4 ovepr. f	Wa-4 ovepr. f	Wa-4 ovepr. f	Wa-4 ovepr. f	Wa-4 ovepr. f	Wa-4 ovepr. f	Wa-4 ovepr. f
	Wa4r-3	Wa4r-4	Wa4r-6	Wa4-14	Wa4-15	Wa4-17	Wa4-20	Wa4-21	Wa4-22	Wa4-23	Wa4-26	Wa4-29	Wa4-36
wt%													
SiO ₂	45.46	39.25	40.28	43.15	41.72	43.67	41.68	41.86	40.06	42.89	42.58	42.73	41.03
TiO ₂	0.04	0.00	0.00	0.00	0.00	0.03	0.00	0.06	0.04	0.01	0.00	0.00	0.06
Al ₂ O ₃	32.87	30.05	31.10	30.46	28.14	29.17	30.53	30.68	29.80	30.14	30.17	28.33	30.64
FeO**	4.80	10.95	10.05	7.73	10.20	8.69	9.83	9.06	10.95	8.51	8.62	9.04	9.58
MnO	0.14	0.19	0.22	0.16	0.18	0.12	0.20	0.17	0.21	0.13	0.26	0.15	0.18
MgO	1.91	5.38	5.10	2.92	3.54	3.05	4.59	4.24	5.32	3.91	4.30	3.11	4.63
CaO	1.25	0.43	0.41	0.81	0.93	0.86	0.34	0.31	0.38	0.27	0.25	0.90	0.32
Na ₂ O	0.15	0.04	0.06	0.16	0.12	0.25	0.10	0.11	0.07	0.14	0.09	0.08	0.08
K ₂ O	3.04	1.58	1.84	2.77	2.74	3.32	3.49	3.69	1.93	4.99	3.50	2.83	2.90
Total	89.65	87.88	89.09	88.16	87.57	89.21	90.75	90.17	88.75	90.99	89.76	87.16	89.41
cation basi							22 O						
Si	6.22	5.62	5.67	6.08	6.00	6.13	5.80	5.85	5.69	5.96	5.95	6.13	5.77
Al ^{IV}	1.78	2.38	2.33	1.92	2.00	1.87	2.20	2.15	2.31	2.04	2.05	1.87	2.23
$\sum IV$	8.00	8.00	8.00	8.00	8.00	8.00	8.00	8.00	8.00	8.00	8.00	8.00	8.00
Al ^{VI}	3.51	2.69	2.83	3.14	2.77	2.96	2.81	2.90	2.67	2.90	2.92	2.92	2.85
Ti	0.00	0.00	0.00	0.00	0.00	0.00	0.00	0.01	0.00	0.00	0.00	0.00	0.01
Fe*	0.49	1.18	1.06	0.82	1.10	0.92	1.03	0.95	1.17	0.89	0.91	0.98	1.01
Mn	0.02	0.02	0.03	0.02	0.02	0.01	0.02	0.02	0.02	0.02	0.03	0.02	0.02
Mg	0.39	1.15	1.07	0.61	0.76	0.64	0.95	0.88	1.13	0.81	0.90	0.67	0.97
$\sum VI$	4.42	5.04	4.99	4.59	4.65	4.53	4.81	4.76	4.99	4.62	4.75	4.58	4.86
Ca	0.18	0.07	0.06	0.12	0.14	0.13	0.05	0.05	0.06	0.04	0.04	0.14	0.05
Na	0.04	0.01	0.02	0.04	0.03	0.07	0.03	0.03	0.02	0.04	0.02	0.02	0.02
K	0.53	0.29	0.33	0.50	0.50	0.59	0.62	0.66	0.35	0.88	0.62	0.52	0.52
$\sum X$	0.75	0.37	0.41	0.66	0.68	0.79	0.70	0.73	0.43	0.96	0.69	0.68	0.59
$\sum cations$	13.17	13.41	13.39	13.25	13.33	13.32	13.51	13.49	13.42	13.58	13.44	13.26	13.45
X _{Mg}	0.44	0.49	0.50	0.43	0.41	0.41	0.48	0.48	0.49	0.48	0.50	0.41	0.49

Table I-16

sample phase core/rim* number textural po:	We-9 d. f-type	We-9 d. f-type	We-9 d. f-type	We-9 d. f-type	We-9 d. f-type	We-9 d. f-type	We-9 d. f-type	We-9 d. f-type	We-9 d. f-type	We-9 d. f-type	We-9 d. f-type	We-9 d. f-type	We-9 d. f-type
	We9-5	We9-6	We9-7	We9-8f	We9-9f	We9-10f	We9-13	We9-14	We9-15	We9-26f	We9-40f	We9-41	We9-45
wt%													
SiO ₂	40.61	39.54	41.29	39.63	44.52	42.45	41.02	42.62	42.77	40.23	41.99	39.33	39.67
TiO ₂	0.00	0.02	0.00	0.02	0.02	0.01	0.02	0.00	0.00	0.00	0.00	0.01	0.01
Al ₂ O ₃	35.70	36.73	34.56	36.59	33.95	32.11	33.29	32.50	32.77	35.50	34.27	35.94	35.49
FeO**	6.18	6.82	6.15	6.88	5.82	6.26	6.47	7.15	7.13	7.21	6.60	6.94	6.79
MnO	0.08	0.05	0.03	0.08	0.11	0.12	0.13	0.03	0.09	0.06	0.07	0.08	0.01
MgO	2.20	1.95	2.20	2.36	2.22	2.43	2.45	2.76	2.79	2.34	2.40	2.27	2.23
CaO	1.18	0.94	1.11	0.87	1.42	1.35	1.22	0.90	0.89	1.07	1.05	0.88	0.93
Na ₂ O	0.10	0.20	0.10	0.15	0.19	0.10	0.09	0.09	0.11	0.16	0.18	0.09	0.16
K ₂ O	0.30	0.44	0.34	0.19	0.58	0.39	0.37	0.96	1.01	0.35	0.62	0.25	0.34
Total	86.38	86.69	85.78	86.79	88.83	85.23	85.04	87.00	87.58	86.92	87.18	85.80	85.64
cation basi							22 O						
Si	5.72	5.57	5.84	5.57	6.08	6.05	5.88	5.99	5.98	5.66	5.87	5.59	5.65
Al ^{IV}	2.28	2.43	2.16	2.43	1.92	1.95	2.12	2.01	2.02	2.34	2.13	2.41	2.35
∑ IV	8.00	8.00	8.00	8.00	8.00	8.00	8.00	8.00	8.00	8.00	8.00	8.00	8.00
Al ^{VI}	3.65	3.67	3.61	3.63	3.54	3.45	3.49	3.37	3.37	3.54	3.52	3.62	3.61
Ti	0.00	0.00	0.00	0.00	0.00	0.00	0.00	0.00	0.00	0.00	0.00	0.00	0.00
Fe*	0.66	0.72	0.65	0.73	0.60	0.67	0.70	0.76	0.75	0.76	0.69	0.74	0.73
Mn	0.01	0.01	0.00	0.01	0.01	0.01	0.02	0.00	0.01	0.01	0.01	0.01	0.00
Mg	0.46	0.41	0.46	0.49	0.45	0.52	0.52	0.58	0.58	0.49	0.50	0.48	0.47
∑ VI	4.77	4.81	4.73	4.86	4.61	4.66	4.73	4.71	4.71	4.80	4.72	4.85	4.81
Ca	0.18	0.14	0.17	0.13	0.21	0.21	0.19	0.14	0.13	0.16	0.16	0.13	0.14
Na	0.03	0.05	0.03	0.04	0.05	0.03	0.03	0.02	0.03	0.04	0.05	0.02	0.05
K	0.05	0.08	0.06	0.03	0.10	0.07	0.07	0.17	0.18	0.06	0.11	0.05	0.06
∑ X	0.26	0.28	0.26	0.21	0.36	0.30	0.28	0.33	0.34	0.27	0.32	0.20	0.25
∑ cations	13.03	13.08	12.99	13.07	12.96	12.96	13.01	13.04	13.06	13.07	13.04	13.06	13.06
X _{Mg}	0.41	0.36	0.42	0.40	0.43	0.43	0.43	0.43	0.44	0.39	0.42	0.39	0.39

Table I-17

sample phase core/rim* number textural po:	We-9 d. f-type	We-9 b. fype	We-9 b. fype	We-9 b. fype	We-9 b. fype	We-9 b. fype	We-9 b. fype	We-9 b. fype	We-9 b. fype	We-9 b. fype	We-9 b. fype	We-9 b. fype	We-9 b. fype
	We9-48f	We9-12f	We9-24	We9-25f	We9-42	We9-44f	We9-47	We9-59f	We9-60f	We9-61	We9-66	We9-67	We9-93
wt%													
SiO ₂	42.67	41.79	41.62	41.79	42.53	41.51	42.64	42.58	42.29	42.36	42.20	42.81	42.36
TiO ₂	0.00	0.00	0.00	0.00	0.00	0.03	0.02	0.00	0.01	0.03	0.02	0.00	0.00
Al ₂ O ₃	33.88	31.77	30.89	31.10	31.10	32.77	31.81	31.17	31.34	30.66	31.46	31.23	30.76
FeO**	6.79	7.73	9.10	8.35	8.54	7.22	7.68	8.05	8.08	8.31	7.81	8.50	8.79
MnO	0.11	0.11	0.15	0.08	0.09	0.08	0.06	0.15	0.14	0.15	0.10	0.18	0.10
MgO	2.60	2.94	2.89	2.86	2.98	2.76	3.13	3.09	2.94	2.90	2.84	2.99	2.90
CaO	1.16	0.77	0.79	0.86	0.81	0.98	0.66	0.74	0.77	0.74	0.67	0.76	0.76
Na ₂ O	0.24	0.21	0.12	0.18	0.12	0.21	0.20	0.11	0.15	0.12	0.14	0.16	0.11
K ₂ O	1.04	1.69	1.05	1.30	1.54	1.16	1.74	1.59	1.40	1.40	1.60	1.43	1.22
Total	88.50	87.01	86.61	86.52	87.75	86.71	87.93	87.49	87.13	86.66	86.85	88.07	87.01
cation basi							22 O						
Si	5.90	5.93	5.94	5.96	5.99	5.88	5.98	6.00	5.98	6.03	5.99	6.00	6.01
Al ^{IV}	2.10	2.07	2.06	2.04	2.01	2.12	2.02	2.00	2.02	1.97	2.01	2.00	1.99
∑ IV	8.00	8.00	8.00	8.00	8.00	8.00	8.00	8.00	8.00	8.00	8.00	8.00	8.00
Al ^{VI}	3.43	3.24	3.13	3.19	3.16	3.35	3.23	3.19	3.21	3.17	3.25	3.16	3.15
Ti	0.00	0.00	0.00	0.00	0.00	0.00	0.00	0.00	0.00	0.00	0.00	0.00	0.00
Fe*	0.71	0.83	0.98	0.90	0.91	0.77	0.81	0.85	0.86	0.89	0.83	0.90	0.94
Mn	0.01	0.01	0.02	0.01	0.01	0.01	0.01	0.02	0.02	0.02	0.01	0.02	0.01
Mg	0.54	0.62	0.61	0.61	0.63	0.58	0.65	0.65	0.62	0.61	0.60	0.62	0.61
∑ VI	4.68	4.70	4.74	4.70	4.70	4.72	4.71	4.71	4.71	4.70	4.70	4.71	4.71
Ca	0.17	0.12	0.12	0.13	0.12	0.15	0.10	0.11	0.12	0.11	0.10	0.11	0.12
Na	0.07	0.06	0.03	0.05	0.03	0.06	0.05	0.03	0.04	0.03	0.04	0.04	0.03
K	0.18	0.31	0.19	0.24	0.28	0.21	0.31	0.29	0.25	0.25	0.29	0.26	0.22
∑ X	0.42	0.48	0.34	0.42	0.43	0.41	0.46	0.43	0.41	0.40	0.43	0.41	0.37
∑ cations	13.10	13.18	13.09	13.12	13.13	13.13	13.17	13.14	13.12	13.10	13.13	13.12	13.08
X _{Mg}	0.43	0.43	0.39	0.40	0.41	0.43	0.45	0.43	0.42	0.41	0.42	0.41	0.40

Table I-18

sample phase core/rim* number text. pos.	Al-20 m-type -	Al-20 m-type -	Al-20 m-type -	Al-20 m-type -	Al-20 m-type -	Al-20 m-type -	Al-20 m-type -	Al-20 m-type -	Al-20 m-type -	Al-20 m-type -	Al-20 m-type -	Al-20 m-type -	Al-20 m-type -
	Al20-479	Al20-409	Al20-413	Al20-422	Al20-410	Al20-4-1	Al20-412	Al20-414	Al20-453	Al20-454	Al20-473	Al20-480	Al20-476
wt%													
SiO ₂	40.98	44.27	44.61	44.05	48.05	47.66	48.24	48.29	41.31	40.83	41.74	38.39	43.83
TiO ₂	0.01	0.00	0.00	0.00	0.00	0.02	0.01	0.02	0.02	0.02	0.02	0.05	0.00
Al ₂ O ₃	26.10	27.58	27.87	28.07	30.82	30.78	31.17	30.89	29.87	29.07	30.07	25.09	29.30
FeO**	7.33	5.36	4.21	7.08	4.32	4.64	3.67	4.13	7.31	8.45	7.09	12.61	7.13
MnO	0.12	0.17	0.16	0.12	0.13	0.14	0.11	0.12	0.16	0.26	0.18	0.28	0.18
MgO	8.23	5.10	5.26	5.90	4.97	5.11	4.70	4.99	8.57	9.60	8.62	10.88	6.45
CaO	0.59	0.54	0.61	0.77	0.63	0.85	0.60	0.76	0.48	0.63	0.52	0.66	0.36
Na ₂ O	0.08	0.06	0.07	0.10	0.12	0.11	0.14	0.12	0.06	0.04	0.07	0.04	0.13
K ₂ O	2.62	4.62	4.32	4.41	4.91	4.86	5.03	4.93	2.15	1.16	2.20	1.17	5.74
Total	86.06	87.72	87.11	90.50	93.95	94.18	93.68	94.25	89.93	90.05	90.53	89.18	93.17
cation basis							22 O						
Si	5.97	6.30	6.34	6.12	6.33	6.28	6.36	6.34	5.73	5.66	5.75	5.51	5.97
Al ^{IV}	2.03	1.70	1.66	1.88	1.67	1.72	1.64	1.66	2.27	2.34	2.25	2.49	2.03
$\sum IV$	8.00	8.00	8.00	8.00	8.00	8.00	8.00	8.00	8.00	8.00	8.00	8.00	8.00
Al ^{VI}	2.44	2.92	3.02	2.72	3.12	3.07	3.21	3.13	2.62	2.42	2.63	1.75	2.68
Ti	0.00	0.00	0.00	0.00	0.00	0.00	0.00	0.00	0.00	0.00	0.00	0.01	0.00
Fe*	0.80	0.57	0.45	0.74	0.43	0.46	0.36	0.41	0.76	0.88	0.73	1.36	0.73
Mn	0.02	0.02	0.02	0.01	0.01	0.02	0.01	0.01	0.02	0.03	0.02	0.03	0.02
Mg	1.79	1.08	1.12	1.22	0.98	1.00	0.92	0.98	1.77	1.99	1.77	2.33	1.31
$\sum VI$	5.05	4.60	4.60	4.69	4.54	4.55	4.51	4.53	5.17	5.32	5.16	5.47	4.74
Ca	0.09	0.08	0.09	0.11	0.09	0.12	0.08	0.11	0.07	0.09	0.08	0.10	0.05
Na	0.02	0.02	0.02	0.03	0.03	0.03	0.04	0.03	0.02	0.01	0.02	0.01	0.03
K	0.49	0.84	0.78	0.78	0.83	0.82	0.85	0.83	0.38	0.20	0.39	0.21	1.00
$\sum X$	0.60	0.94	0.90	0.92	0.95	0.97	0.97	0.96	0.47	0.31	0.48	0.33	1.08
$\sum cations$	13.65	13.53	13.50	13.62	13.49	13.52	13.48	13.49	13.64	13.62	13.64	13.80	13.82
X _{Mg}	0.69	0.65	0.71	0.62	0.70	0.69	0.72	0.71	0.70	0.69	0.71	0.63	0.64

Table I-19

sample phase core/rim* number text. pos.	Bw-3 m-type -	Bw-3 m-type -	Bw-3 m-type -	Bw-3 m-type -	Bw-3 m-type -	Bw-3 m-type -	Bw-3 m-type -	Bw-3 m-type -	Bw-3 m-type -	Bw-3 m-type -	Bw-3 m-type -	Bw-3 m-type -	Bw-3 m-type -
	Bw3256	Bw3-244	Bw3-245	Bw3-239	Be31-174	Bw3-130	Bw3-128	Bw3-127	Bw3-12	Bw3-106	Bw3-98	Bw3-99	Bw3-97
wt%													
SiO ₂	41.69	38.94	39.03	40.96	41.38	42.47	41.06	38.54	38.76	42.24	38.18	37.64	37.58
TiO ₂	0.00	0.00	0.03	0.02	0.00	0.00	0.01	0.01	0.00	0.01	0.02	0.00	0.03
Al ₂ O ₃	30.38	30.74	31.16	29.93	30.14	29.58	29.63	28.84	28.99	30.38	29.14	29.08	28.23
FeO**	7.43	8.82	8.73	8.75	8.01	7.50	8.48	10.11	9.93	7.10	10.33	10.33	10.16
MnO	0.11	0.09	0.08	0.09	0.13	0.16	0.15	0.19	0.10	0.13	0.18	0.18	0.12
MgO	4.72	6.30	6.42	5.36	4.99	4.85	5.00	6.87	6.75	4.22	7.26	7.02	7.20
CaO	0.70	0.53	0.46	0.29	0.40	0.57	0.34	0.44	0.48	0.81	0.52	0.51	0.50
Na ₂ O	0.14	0.07	0.08	0.09	0.09	0.21	0.08	0.05	0.07	0.16	0.05	0.07	0.05
K ₂ O	3.08	1.11	1.18	4.26	3.47	3.45	3.18	1.64	1.89	3.45	1.19	1.35	1.32
Total	88.27	86.60	87.17	89.77	88.62	88.83	87.96	86.72	86.95	88.50	86.87	86.18	85.19
cation basi							22 O						
Si	5.90	5.60	5.58	5.78	5.86	5.99	5.86	5.60	5.61	5.96	5.53	5.50	5.55
Al ^{IV}	2.10	2.40	2.42	2.22	2.14	2.01	2.14	2.40	2.39	2.04	2.47	2.50	2.45
$\sum IV$	8.00	8.00	8.00	8.00	8.00	8.00	8.00	8.00	8.00	8.00	8.00	8.00	8.00
Al ^{VI}	2.97	2.81	2.82	2.76	2.89	2.90	2.84	2.53	2.56	3.02	2.50	2.52	2.47
Ti	0.00	0.00	0.00	0.00	0.00	0.00	0.00	0.00	0.00	0.00	0.00	0.00	0.00
Fe*	0.79	0.95	0.94	0.93	0.85	0.79	0.91	1.10	1.08	0.75	1.13	1.14	1.13
Mn	0.01	0.01	0.01	0.01	0.02	0.02	0.02	0.02	0.01	0.02	0.02	0.02	0.02
Mg	1.00	1.35	1.37	1.13	1.05	1.02	1.06	1.49	1.46	0.89	1.57	1.53	1.59
$\sum VI$	4.77	5.13	5.14	4.83	4.81	4.73	4.84	5.15	5.11	4.68	5.22	5.21	5.21
Ca	0.11	0.08	0.07	0.04	0.06	0.09	0.05	0.07	0.07	0.12	0.08	0.08	0.08
Na	0.04	0.02	0.02	0.03	0.03	0.06	0.02	0.01	0.02	0.04	0.01	0.02	0.01
K	0.56	0.20	0.21	0.77	0.63	0.62	0.58	0.30	0.35	0.62	0.22	0.25	0.25
$\sum X$	0.70	0.30	0.31	0.84	0.71	0.76	0.65	0.39	0.44	0.79	0.31	0.35	0.34
$\sum cations$	13.47	13.43	13.45	13.66	13.52	13.50	13.49	13.54	13.55	13.46	13.54	13.56	13.55
X _{Mg}	0.56	0.59	0.59	0.55	0.55	0.56	0.54	0.57	0.57	0.54	0.58	0.57	0.58

Table I-20

sample phase core/rim* number text. pos.	Ho-10 m-type -	Ho-10 m-type -	Ho-10 m-type -	Ho-10 m-type -	Ho-10 m-type -	Ho-10 m-type -	Ho-10 m-type -	Ho-10 m-type -	Ho-10 m-type -	Ho-10 m-type -	Ho-10 m-type -	Ho-10 m-type -	Ho-10 m-type -
	Ho10-706	Ho10-707	Ho10-708	Ho10-709	Ho10-751	Ho10-49	Ho10-51	Ho10-53	Ho10-54	Ho10-55	Ho10-71	Ho10-74	Ho10-77
wt%													
SiO ₂	42.70	38.51	39.26	39.31	41.89	46.12	39.59	42.94	41.70	43.67	39.33	43.34	41.25
TiO ₂	0.01	0.00	0.06	0.00	0.00	0.00	0.00	0.00	0.00	0.00	0.00	0.00	0.00
Al ₂ O ₃	29.81	28.17	28.41	28.84	30.09	32.69	26.62	29.65	29.15	34.65	27.85	28.73	28.38
FeO**	9.65	13.44	13.87	13.83	8.34	3.92	10.82	8.51	11.60	5.89	12.18	8.23	10.07
MnO	0.04	0.07	0.08	0.07	0.14	0.00	0.28	0.17	0.10	0.04	0.13	0.09	0.18
MgO	2.25	2.68	2.83	2.74	3.73	0.75	8.54	2.85	2.26	1.64	5.67	4.96	5.66
CaO	0.30	0.39	0.40	0.42	0.23	0.81	0.00	0.45	0.52	0.56	0.23	0.19	0.12
Na ₂ O	0.10	0.11	0.07	0.07	0.11	0.07	0.14	0.48	0.11	0.08	0.19	0.13	0.26
K ₂ O	4.80	3.42	3.24	3.16	5.85	3.30	5.08	4.14	3.74	2.33	4.16	6.21	5.72
Total	89.65	86.81	88.24	88.45	90.38	87.67	91.07	89.17	89.17	88.88	89.77	91.88	91.63
cation basi							22 O						
Si	6.03	5.70	5.71	5.69	5.90	6.40	5.63	6.06	5.94	6.01	5.64	6.02	5.79
Al ^{IV}	1.97	2.30	2.29	2.31	2.10	1.60	2.37	1.94	2.06	1.99	2.36	1.98	2.21
∑ IV	8.00	8.00	8.00	8.00	8.00	8.00	8.00	8.00	8.00	8.00	8.00	8.00	8.00
Al ^{VI}	2.99	2.61	2.58	2.62	2.90	3.74	2.09	2.99	2.83	3.63	2.36	2.71	2.49
Ti	0.00	0.00	0.01	0.00	0.00	0.00	0.00	0.00	0.00	0.00	0.00	0.00	0.00
Fe*	1.02	1.50	1.52	1.51	0.88	0.41	1.16	0.90	1.24	0.61	1.32	0.86	1.06
Mn	0.00	0.01	0.01	0.01	0.02	0.00	0.03	0.02	0.01	0.01	0.02	0.01	0.02
Mg	0.47	0.59	0.61	0.59	0.78	0.15	1.81	0.60	0.48	0.34	1.21	1.03	1.18
∑ VI	4.49	4.70	4.72	4.72	4.58	4.30	5.09	4.52	4.56	4.58	4.90	4.61	4.76
Ca	0.05	0.06	0.06	0.07	0.03	0.12	0.00	0.07	0.08	0.08	0.04	0.03	0.02
Na	0.03	0.03	0.02	0.02	0.03	0.02	0.04	0.13	0.03	0.02	0.05	0.03	0.07
K	0.86	0.64	0.60	0.58	1.05	0.58	0.92	0.74	0.68	0.41	0.76	1.10	1.02
∑ X	0.94	0.74	0.68	0.67	1.12	0.72	0.96	0.94	0.79	0.51	0.85	1.16	1.11
∑ cations	13.43	13.44	13.40	13.39	13.70	13.03	14.04	13.46	13.35	13.09	13.75	13.77	13.87
X _{Mg}	0.32	0.28	0.29	0.28	0.47	0.27	0.61	0.40	0.28	0.36	0.48	0.54	0.53

Table I-21

sample phase core/rim* number text. pos.	Ho-12 m-type -	Ho-12 m-type -	Ho-12 m-type -	Ho-12 m-type -	Ho-12 m-type -	Ho-12 m-type -	Ho-12 m-type -	Ho-12 m-type -	Ho-12 m-type -	Ho-12 m-type -	Ho-12 m-type -	Ho-12 m-type -	Ho-12 m-type -
	Ho12-9	Ho12-12	Ho12-15	Ho12-22	Ho12-26	Ho12-27	Ho12-33	Ho12-48	Ho12-49	Ho12-50	Ho12-52	Ho12-53	Ho12-54
wt%													
SiO ₂	38.84	40.27	38.74	40.29	39.52	39.68	39.24	37.22	38.88	38.47	40.09	38.23	39.00
TiO ₂	0.01	0.01	0.00	0.00	0.00	0.01	0.02	0.02	0.03	0.00	0.01	0.01	0.00
Al ₂ O ₃	28.83	28.88	27.21	28.84	28.39	28.54	28.84	27.49	27.79	28.05	27.47	27.16	27.90
FeO**	15.04	13.59	16.24	14.32	15.44	14.63	15.25	16.77	15.74	16.25	14.33	16.31	16.09
MnO	0.20	0.21	0.18	0.21	0.17	0.18	0.27	0.23	0.18	0.20	0.17	0.29	0.14
MgO	3.38	3.26	3.02	2.74	3.26	3.31	3.43	3.03	3.16	3.16	3.20	2.98	2.89
CaO	0.62	0.56	0.67	0.71	0.66	0.61	0.62	0.73	0.72	0.65	0.64	0.67	0.72
Na ₂ O	0.21	0.18	0.14	0.15	0.16	0.15	0.19	0.17	0.16	0.16	0.14	0.12	0.13
K ₂ O	1.89	2.25	1.67	2.09	2.00	2.17	1.70	1.49	1.62	1.65	2.19	1.70	1.86
Total	89.02	89.20	87.89	89.34	89.59	89.33	89.55	87.14	88.29	88.58	88.24	87.47	88.73
cation basi							22 O						
Si	5.59	5.75	5.66	5.75	5.65	5.68	5.61	5.51	5.64	5.58	5.80	5.63	5.64
Al ^{IV}	2.41	2.25	2.34	2.25	2.35	2.32	2.39	2.49	2.36	2.42	2.20	2.37	2.36
∑ IV	8.00	8.00	8.00	8.00	8.00	8.00	8.00	8.00	8.00	8.00	8.00	8.00	8.00
Al ^{VI}	2.48	2.60	2.35	2.60	2.44	2.50	2.46	2.31	2.40	2.38	2.48	2.34	2.40
Ti	0.00	0.00	0.00	0.00	0.00	0.00	0.00	0.00	0.00	0.00	0.00	0.00	0.00
Fe*	1.63	1.46	1.79	1.54	1.66	1.58	1.64	1.87	1.72	1.77	1.56	1.81	1.75
Mn	0.02	0.03	0.02	0.03	0.02	0.02	0.03	0.03	0.02	0.02	0.02	0.04	0.02
Mg	0.72	0.69	0.66	0.58	0.69	0.71	0.73	0.67	0.68	0.68	0.69	0.65	0.62
∑ VI	4.85	4.78	4.82	4.74	4.82	4.81	4.87	4.88	4.83	4.86	4.76	4.83	4.80
Ca	0.10	0.09	0.10	0.11	0.10	0.09	0.09	0.12	0.11	0.10	0.10	0.11	0.11
Na	0.06	0.05	0.04	0.04	0.04	0.04	0.05	0.05	0.05	0.04	0.04	0.03	0.04
K	0.35	0.41	0.31	0.38	0.37	0.40	0.31	0.28	0.30	0.31	0.40	0.32	0.34
∑ X	0.50	0.55	0.46	0.53	0.51	0.53	0.46	0.44	0.46	0.45	0.54	0.46	0.49
∑ cations	13.36	13.33	13.27	13.27	13.33	13.34	13.32	13.32	13.29	13.31	13.30	13.29	13.29
X _{Mg}	0.31	0.32	0.27	0.27	0.29	0.31	0.31	0.26	0.28	0.28	0.31	0.27	0.26

Table I-22

sample phase core/rim* number text. pos.	To-2 m-type - To2-12	To-2 m-type - To2-25	To-2 m-type - To2-26	To-2 m-type - To2-32	To-2 m-type - To2-35	To-2 m-type - To2-37	To-2 m-type - To2-39	To-2 m-type - To2-40	To-2 m-type - To2-98	To-2 m-type - To2-104	To-2 m-type - To2-133	To-2 m-type - To2-134	To-2 m-type - To2-174
wt%													
SiO ₂	40.90	39.19	39.07	44.21	42.61	41.70	43.33	48.90	43.30	42.78	42.51	42.12	41.99
TiO ₂	0.01	0.03	0.01	0.02	0.01	0.03	0.00	0.03	0.02	0.04	0.01	0.02	0.00
Al ₂ O ₃	29.35	26.51	25.80	30.47	28.67	30.33	28.43	33.93	30.13	27.24	30.74	29.07	28.80
FeO**	8.14	10.40	10.66	6.80	7.95	7.73	6.96	1.39	7.56	9.57	7.79	7.24	7.43
MnO	0.32	0.47	0.37	0.17	0.18	0.23	0.23	0.02	0.23	0.25	0.18	0.17	0.28
MgO	4.86	7.09	8.17	4.43	5.79	4.84	5.56	1.40	4.72	5.27	4.81	4.82	5.59
CaO	0.02	0.09	0.04	0.37	0.49	0.66	0.05	0.05	0.06	0.31	0.10	0.11	0.03
Na ₂ O	0.18	0.16	0.24	0.11	0.11	0.07	0.33	1.38	0.21	0.19	0.16	0.17	0.24
K ₂ O	7.45	6.18	7.32	5.52	5.49	3.16	7.92	7.69	7.54	6.36	7.90	7.99	7.68
Total	91.25	90.12	91.69	92.10	91.30	88.75	92.80	94.77	93.76	92.01	94.22	91.72	92.08
cation basi							22 O						
Si	5.79	5.67	5.61	6.05	5.94	5.88	6.01	6.41	5.93	5.99	5.82	5.92	5.88
Al ^{IV}	2.21	2.33	2.39	1.95	2.06	2.12	1.99	1.59	2.07	2.01	2.18	2.08	2.12
∑ IV	8.00	8.00	8.00	8.00	8.00	8.00	8.00	8.00	8.00	8.00	8.00	8.00	8.00
Al ^{VI}	2.69	2.18	1.97	2.96	2.65	2.92	2.65	3.66	2.79	2.48	2.77	2.73	2.64
Ti	0.00	0.00	0.00	0.00	0.00	0.00	0.00	0.00	0.00	0.00	0.00	0.00	0.00
Fe*	0.87	1.13	1.15	0.70	0.83	0.82	0.73	0.14	0.78	1.01	0.80	0.77	0.78
Mn	0.04	0.06	0.05	0.02	0.02	0.03	0.03	0.00	0.03	0.03	0.02	0.02	0.03
Mg	1.03	1.53	1.75	0.90	1.20	1.02	1.15	0.27	0.96	1.10	0.98	1.01	1.17
∑ VI	4.62	4.90	4.92	4.59	4.71	4.79	4.55	4.07	4.56	4.62	4.58	4.53	4.62
Ca	0.00	0.01	0.01	0.05	0.07	0.10	0.01	0.01	0.01	0.05	0.01	0.02	0.00
Na	0.05	0.05	0.07	0.03	0.03	0.02	0.09	0.35	0.05	0.05	0.04	0.05	0.06
K	1.35	1.14	1.34	0.96	0.98	0.57	1.40	1.29	1.32	1.14	1.38	1.43	1.37
∑ X	1.40	1.20	1.41	1.05	1.08	0.69	1.50	1.64	1.38	1.23	1.44	1.50	1.44
∑ cations	14.02	14.10	14.34	13.64	13.79	13.48	14.05	13.71	13.94	13.85	14.01	14.03	14.07
X _{Mg}	0.54	0.57	0.60	0.56	0.59	0.55	0.61	0.67	0.55	0.52	0.55	0.57	0.60

Table I-23

sample phase core/rim* number text. pos.	Wa-4 m-type - Wa4-2	Wa-4 m-type - Wa4r-5	Wa-4 m-type - Wa4-13	Wa-4 m-type - Wa4-19	Wa-4 m-type - Wa4-24	Wa-4 m-type - Wa4-25	Wa-4 m-type - Wa4-27	Wa-4 m-type - Wa4-30	Wa-4 m-type - Wa4-44	Wa-4 m-type - Wa4-45	Wa-4 m-type - Wa4-59	Wa-4 m-type - Wa4-87	Wa-4 m-type - Wa4-94
wt%													
SiO ₂	45.86	45.69	45.87	45.62	45.89	44.66	46.55	44.94	45.58	45.54	44.09	45.05	45.12
TiO ₂	0.00	0.00	0.00	0.01	0.00	0.00	0.02	0.00	0.01	0.04	0.03	0.00	0.03
Al ₂ O ₃	30.79	29.94	30.57	30.42	30.18	30.54	30.85	29.75	30.05	30.51	30.61	29.89	29.38
FeO**	6.34	7.25	6.30	6.28	6.02	6.78	5.35	5.87	6.58	6.45	7.99	7.58	6.78
MnO	0.07	0.16	0.15	0.14	0.12	0.17	0.05	0.12	0.12	0.12	0.20	0.08	0.07
MgO	2.97	3.02	2.74	2.49	2.61	2.89	2.11	2.54	2.84	2.89	3.59	3.26	3.04
CaO	0.07	0.08	0.09	0.05	0.06	0.08	0.08	0.07	0.04	0.06	0.23	0.08	0.06
Na ₂ O	0.18	0.19	0.15	0.13	0.16	0.19	0.15	0.12	0.16	0.17	0.12	0.20	0.17
K ₂ O	8.23	7.96	7.91	8.31	7.94	6.93	8.76	8.48	7.94	8.22	5.69	7.52	7.77
Total	94.50	94.31	93.80	93.49	92.98	92.45	93.95	91.91	93.29	94.02	92.54	93.65	92.41
cation basi							22 O						
Si	6.25	6.27	6.29	6.29	6.33	6.21	6.35	6.30	6.29	6.25	6.12	6.22	6.30
Al ^{IV}	1.75	1.73	1.71	1.71	1.67	1.79	1.65	1.70	1.71	1.75	1.88	1.78	1.70
∑ IV	8.00	8.00	8.00	8.00	8.00	8.00	8.00	8.00	8.00	8.00	8.00	8.00	8.00
Al ^{VI}	3.20	3.11	3.22	3.23	3.24	3.21	3.32	3.22	3.18	3.18	3.13	3.09	3.13
Ti	0.00	0.00	0.00	0.00	0.00	0.00	0.00	0.00	0.00	0.00	0.00	0.00	0.00
Fe*	0.48	0.55	0.48	0.48	0.46	0.53	0.41	0.46	0.51	0.49	0.62	0.58	0.53
Mn	0.01	0.02	0.02	0.02	0.01	0.02	0.01	0.01	0.01	0.01	0.02	0.01	0.01
Mg	0.60	0.62	0.56	0.51	0.54	0.60	0.43	0.53	0.58	0.59	0.74	0.67	0.63
∑ VI	4.29	4.30	4.28	4.24	4.25	4.35	4.16	4.22	4.29	4.28	4.51	4.35	4.30
Ca	0.01	0.01	0.01	0.01	0.01	0.04	0.01	0.01	0.01	0.01	0.03	0.01	0.01
Na	0.05	0.05	0.04	0.03	0.04	0.05	0.04	0.03	0.04	0.05	0.03	0.05	0.05
K	1.43	1.39	1.38	1.46	1.40	1.23	1.53	1.52	1.40	1.44	1.01	1.32	1.38
∑ X	1.49	1.45	1.44	1.50	1.45	1.32	1.58	1.56	1.44	1.49	1.07	1.39	1.44
∑ cations	13.78	13.76	13.72	13.75	13.70	13.67	13.74	13.78	13.73	13.78	13.59	13.74	13.73
X _{Mg}	0.56	0.53	0.54	0.51	0.54	0.53	0.51	0.54	0.54	0.54	0.55	0.54	0.55

Table I-24

sample phase core/rim* number text. pos.	We-9 m-type	We-9 m-type	We-9 m-type	We-9 m-type	We-9 m-type	We-9 m-type	We-9 m-type	We-9 m-type	We-9 m-type	We-9 m-type	We-9 m-type	We-9 m-type	We-9 m-type
	We9-33	We9-34f	We9-36f	We9-37f	We9-38	We9-43	We9-46	We9-52	We9-53	We9-65	We9-86	We9-105	We9-106
wt%													
SiO ₂	45.77	44.46	48.76	46.28	38.25	42.83	41.12	47.43	45.73	43.59	44.45	43.80	47.36
TiO ₂	0.00	0.00	0.00	0.03	0.02	0.00	0.00	0.01	0.03	0.01	0.03	0.02	0.20
Al ₂ O ₃	30.13	30.27	32.42	31.17	27.20	29.76	27.95	31.39	30.86	28.83	30.89	29.88	34.83
FeO**	6.22	8.28	2.93	8.95	12.38	7.76	10.15	7.46	10.00	8.57	8.82	6.91	1.66
MnO	0.13	0.24	0.09	0.29	0.28	0.15	0.26	0.27	0.34	0.33	0.25	0.18	0.13
MgO	5.10	6.26	1.96	6.22	8.33	5.37	8.22	5.62	7.29	8.36	5.76	4.89	2.90
CaO	0.01	0.01	0.03	0.02	0.05	0.00	0.02	0.02	0.02	0.06	0.04	0.00	0.00
Na ₂ O	0.38	0.47	0.96	0.46	0.29	0.50	0.35	1.34	0.46	0.38	2.27	0.74	0.77
K ₂ O	6.67	3.91	6.55	2.52	4.82	5.86	4.75	2.01	0.88	3.69	1.85	5.74	7.86
Total	94.41	93.88	93.69	95.94	91.62	92.24	92.80	95.54	95.61	93.81	94.36	92.17	95.71
cation basi							22 O						
Si	6.13	5.96	6.45	6.01	5.44	5.91	5.69	6.14	5.93	5.87	5.90	6.02	6.18
Al ^{IV}	1.87	2.04	1.55	1.99	2.56	2.09	2.31	1.86	2.07	2.13	2.10	1.98	1.82
∑ IV	8.00	8.00	8.00	8.00	8.00	8.00	8.00	8.00	8.00	8.00	8.00	8.00	8.00
Al ^{VI}	2.89	2.73	3.51	2.78	2.00	2.75	2.25	2.93	2.65	2.45	2.73	2.86	3.53
Ti	0.00	0.00	0.00	0.00	0.00	0.00	0.00	0.00	0.00	0.00	0.00	0.00	0.02
Fe*	0.63	0.83	0.29	0.87	1.32	0.81	1.06	0.73	0.98	0.87	0.88	0.71	0.16
Mn	0.01	0.03	0.01	0.03	0.03	0.02	0.03	0.03	0.04	0.04	0.03	0.02	0.01
Mg	1.02	1.25	0.39	1.20	1.77	1.10	1.70	1.08	1.41	1.68	1.14	1.00	0.56
∑ VI	4.55	4.84	4.19	4.89	5.13	4.68	5.03	4.77	5.08	5.03	4.79	4.60	4.29
Ca	0.00	0.00	0.00	0.00	0.01	0.00	0.00	0.00	0.00	0.01	0.01	0.00	0.00
Na	0.10	0.12	0.25	0.11	0.08	0.13	0.09	0.34	0.11	0.10	0.58	0.20	0.19
K	1.14	0.67	1.11	0.42	0.88	1.03	0.84	0.33	0.15	0.63	0.31	1.01	1.31
∑ X	1.24	0.79	1.36	0.54	0.96	1.16	0.93	0.67	0.26	0.74	0.90	1.20	1.50
∑ cations	13.79	13.63	13.55	13.43	14.09	13.85	13.97	13.44	13.34	13.77	13.69	13.80	13.80
X _{Mg}	0.62	0.60	0.57	0.58	0.57	0.58	0.62	0.60	0.59	0.66	0.56	0.58	0.78

Table I-25

sample phase core/rim* number text. pos.	Bw-29 i-type	Bw-29 i-type	Bw-29 i-type	Bw-29 i-type	Bw-29 i-type	Bw-29 i-type	Bw-29 i-type	Bw-29 i-type	Bw-29 i-type	Bw-29 i-type	Bw-29 i-type	Bw-29 i-type	Bw-29 i-type
	Bw29-431	Bw29-432	Bw29-429	Bw29-430	Bw29-7004	Bw29-705	Bw29-250	Bw29-289	Bw29-432	Bw29-433	Bw29-247	Bw29-222	Bw29-232
wt%													
SiO ₂	42.83	43.76	41.20	42.44	38.23	38.97	40.00	39.05	43.76	42.03	39.55	36.68	38.44
TiO ₂	0.01	0.00	0.00	0.00	0.00	0.00	0.00	0.01	0.00	0.00	0.00	0.00	0.01
Al ₂ O ₃	36.77	36.13	36.88	35.76	33.97	35.46	33.17	30.89	36.13	36.97	34.33	31.96	31.58
FeO**	5.91	5.14	6.23	5.41	5.36	5.02	6.62	6.78	5.14	6.29	6.82	6.06	6.12
MnO	0.12	0.01	0.16	0.05	0.08	0.09	0.13	0.10	0.01	0.05	0.09	0.14	0.12
MgO	1.39	1.32	1.56	1.56	1.44	1.40	1.64	1.74	1.32	1.55	1.40	1.45	1.58
CaO	0.84	0.98	0.73	1.33	1.09	1.52	0.95	1.08	0.98	1.08	0.70	0.85	0.87
Na ₂ O	0.36	0.29	0.41	0.38	0.14	0.22	0.12	0.17	0.29	0.38	0.07	0.09	0.07
K ₂ O	0.87	0.68	0.73	0.81	0.34	0.53	0.60	0.66	0.68	0.79	0.31	0.30	0.38
Total	89.10	88.32	87.93	87.75	80.64	83.25	83.25	80.50	88.32	89.16	83.28	77.53	79.16
cation basi							22 O						
Si	5.90	6.04	5.78	5.94	5.81	5.75	5.94	6.01	6.04	5.81	5.85	5.83	5.98
Al ^{IV}	2.10	1.96	2.22	2.06	2.19	2.25	2.06	1.99	1.96	2.19	2.15	2.17	2.02
∑ IV	8.00	8.00	8.00	8.00	8.00	8.00	8.00	8.00	8.00	8.00	8.00	8.00	8.00
Al ^{VI}	3.88	3.91	3.87	3.83	3.90	3.91	3.74	3.62	3.91	3.84	3.84	3.82	3.76
Ti	0.00	0.00	0.00	0.00	0.00	0.00	0.00	0.00	0.00	0.00	0.00	0.00	0.00
Fe*	0.68	0.59	0.73	0.63	0.68	0.62	0.82	0.87	0.59	0.73	0.84	0.81	0.80
Mn	0.01	0.00	0.02	0.01	0.01	0.01	0.02	0.01	0.00	0.01	0.01	0.02	0.02
Mg	0.29	0.27	0.33	0.32	0.33	0.31	0.36	0.40	0.27	0.32	0.31	0.34	0.37
∑ VI	4.86	4.78	4.95	4.79	4.91	4.85	4.94	4.91	4.78	4.89	5.00	4.99	4.94
Ca	0.12	0.15	0.11	0.20	0.18	0.24	0.15	0.18	0.15	0.16	0.11	0.14	0.14
Na	0.10	0.08	0.11	0.10	0.04	0.06	0.03	0.05	0.08	0.10	0.02	0.03	0.02
K	0.15	0.12	0.13	0.14	0.07	0.10	0.11	0.13	0.12	0.14	0.06	0.06	0.07
∑ X	0.37	0.34	0.35	0.45	0.28	0.40	0.30	0.36	0.34	0.40	0.19	0.23	0.24
∑ cations	13.23	13.12	13.30	13.24	13.20	13.25	13.24	13.27	13.12	13.29	13.19	13.22	13.18
X _{Mg}	0.30	0.31	0.31	0.34	0.32	0.33	0.31	0.31	0.31	0.30	0.27	0.30	0.32

Table I-26

sample phase core/rim* number text. pos.	Bw-8 i-type - Bw8-401	Bw-8 i-type - Bw8-402	Bw-8 i-type - Bw8-403	Bw-8 i-type - Bw8-404	Bw-8 i-type - Bw8-405	Bw-8 i-type - Bw8-406	Bw-8 i-type - Bw8-433	Bw-8 i-type - Bw8-434	Bw-8 i-type - Bw8-435	Bw-8 i-type - Bw8-436	Bw-8 i-type - Bw8-437	Bw-8 i-type - Bw8-702	Bw-8 i-type - Bw8-773
wt%													
SiO ₂	40.88	43.03	42.39	43.10	43.00	39.95	42.66	41.77	39.47	43.51	41.84	47.55	42.45
TiO ₂	0.00	0.02	0.00	0.00	0.01	0.00	0.02	0.01	0.01	0.03	0.00	0.00	0.00
Al ₂ O ₃	34.42	36.37	36.82	37.05	36.78	33.17	35.89	34.25	33.28	36.97	36.78	32.44	36.81
FeO**	3.59	3.44	3.86	3.42	3.95	3.40	3.87	4.03	4.07	3.26	4.29	10.23	4.67
MnO	0.09	0.04	0.09	0.11	0.15	0.11	0.16	0.09	0.15	0.07	0.09	0.25	0.16
MgO	1.88	1.84	2.15	1.82	2.23	1.53	2.09	1.97	2.05	1.85	2.36	6.73	2.31
CaO	1.46	1.89	1.48	1.37	1.24	3.43	1.44	1.56	1.29	1.05	1.26	0.01	1.16
Na ₂ O	0.19	0.27	0.36	0.37	0.38	0.16	0.17	0.21	0.16	0.44	0.36	0.18	0.41
K ₂ O	0.45	0.49	0.67	0.73	0.95	0.56	0.47	0.68	0.59	0.91	0.81	0.02	0.87
Total	82.98	87.39	87.86	87.98	88.69	82.33	86.83	84.59	81.06	88.09	87.79	97.41	88.88
cation basi							22 O						
Si	5.93	5.93	5.83	5.90	5.87	5.90	5.92	5.97	5.89	5.94	5.78	6.00	5.80
Al ^{IV}	2.07	2.07	2.17	2.10	2.13	2.10	2.08	2.03	2.11	2.06	2.22	2.00	2.20
∑ IV	8.00	8.00	8.00	8.00	8.00	8.00	8.00	8.00	8.00	8.00	8.00	8.00	8.00
Al ^{VI}	3.82	3.84	3.80	3.88	3.78	3.68	3.80	3.74	3.74	3.90	3.76	2.82	3.73
Ti	0.00	0.00	0.00	0.00	0.00	0.00	0.00	0.00	0.00	0.00	0.00	0.00	0.00
Fe*	0.39	0.36	0.40	0.35	0.41	0.38	0.40	0.43	0.46	0.33	0.45	0.97	0.48
Mn	0.01	0.00	0.01	0.01	0.02	0.01	0.02	0.01	0.02	0.01	0.01	0.03	0.02
Mg	0.41	0.38	0.44	0.37	0.45	0.34	0.43	0.42	0.46	0.38	0.49	1.26	0.47
∑ VI	4.63	4.58	4.66	4.62	4.66	4.40	4.66	4.60	4.67	4.62	4.70	5.08	4.70
Ca	0.23	0.28	0.22	0.20	0.18	0.54	0.21	0.24	0.21	0.15	0.19	0.00	0.17
Na	0.05	0.07	0.10	0.10	0.10	0.05	0.05	0.06	0.05	0.12	0.10	0.04	0.11
K	0.08	0.09	0.12	0.13	0.16	0.11	0.08	0.12	0.11	0.16	0.14	0.00	0.15
∑ X	0.36	0.44	0.43	0.43	0.45	0.69	0.34	0.42	0.36	0.43	0.43	0.05	0.43
∑ cations	12.99	13.01	13.09	13.05	13.11	13.10	13.00	13.02	13.03	13.05	13.13	13.13	13.13
X _{Mg}	0.51	0.51	0.52	0.51	0.53	0.47	0.52	0.49	0.50	0.53	0.52	0.57	0.50

Table I-27

sample phase core/rim* number text. pos.	Bw-8 i-type - Bw8-703	Ho-12 i-type - Ho12f1	Ho-12 i-type - Ho12f2	Ho-12 i-type - Ho12f3	Ho-12 i-type - Ho12f4	Ho-12 i-type - Ho12f5	Ho-12 i-type - Ho12f6	Ho-12 i-type - Ho12f7	Ho-12 i-type - Ho12f8	Ho-12 i-type - Ho12f9	Ho-12 i-type - Ho12f10	Ho-10 i-type - Ho10f1	Ho-10 i-type - Ho10f2
wt%													
SiO ₂	45.57	41.43	39.86	42.05	37.28	40.85	48.01	43.19	43.58	43.06	45.11	39.95	42.66
TiO ₂	0.00	0.01	0.01	0.02	0.00	0.01	0.02	0.00	0.00	0.00	0.00	0.00	0.00
Al ₂ O ₃	33.23	38.18	40.14	33.69	31.34	38.68	34.48	41.21	38.66	39.55	39.62	38.68	41.36
FeO**	4.33	0.80	0.72	2.35	1.38	1.43	2.07	1.08	1.22	1.21	0.90	0.55	0.47
MnO	0.12	0.00	0.04	0.05	0.07	0.04	0.03	0.08	0.04	0.02	0.01	0.00	0.02
MgO	2.77	0.33	0.23	0.54	0.23	0.39	0.73	0.41	0.38	0.29	0.24	0.40	0.36
CaO	1.48	0.91	1.03	1.06	1.12	1.06	2.24	1.02	0.99	1.05	0.98	1.65	1.33
Na ₂ O	0.40	0.07	0.13	0.12	0.20	0.14	0.07	0.28	0.24	0.23	0.21	0.07	0.14
K ₂ O	0.98	0.48	0.72	0.81	0.55	1.07	0.68	0.71	0.65	0.76	0.75	0.38	0.46
Total	88.88	82.20	82.88	80.68	72.17	83.66	88.33	87.97	85.76	86.17	87.81	81.68	86.79
cation basi							22 O						
Si	6.20	5.95	5.71	6.21	6.14	5.83	6.47	5.83	6.02	5.93	6.08	5.80	5.82
Al ^{IV}	1.80	2.05	2.29	1.79	1.86	2.17	1.53	2.17	1.98	2.07	1.92	2.20	2.18
∑ IV	8.00	8.00	8.00	8.00	8.00	8.00	8.00	8.00	8.00	8.00	8.00	8.00	8.00
Al ^{VI}	3.53	4.42	4.49	4.08	4.21	4.33	3.94	4.39	4.32	4.35	4.36	4.41	4.46
Ti	0.00	0.00	0.00	0.00	0.00	0.00	0.00	0.00	0.00	0.00	0.00	0.00	0.00
Fe*	0.44	0.09	0.08	0.26	0.17	0.15	0.21	0.11	0.13	0.13	0.09	0.06	0.05
Mn	0.01	0.00	0.01	0.01	0.01	0.00	0.00	0.01	0.00	0.00	0.00	0.00	0.00
Mg	0.56	0.07	0.05	0.12	0.06	0.08	0.15	0.08	0.08	0.06	0.05	0.09	0.07
∑ VI	4.55	4.58	4.62	4.46	4.45	4.57	4.30	4.59	4.53	4.54	4.50	4.56	4.58
Ca	0.22	0.14	0.16	0.17	0.20	0.16	0.32	0.15	0.15	0.15	0.14	0.26	0.19
Na	0.11	0.02	0.04	0.04	0.06	0.04	0.02	0.07	0.06	0.06	0.05	0.02	0.04
K	0.17	0.09	0.13	0.15	0.12	0.19	0.12	0.12	0.11	0.13	0.13	0.07	0.08
∑ X	0.49	0.25	0.33	0.36	0.38	0.39	0.46	0.34	0.33	0.35	0.33	0.35	0.31
∑ cations	13.05	12.82	12.95	12.82	12.83	12.96	12.76	12.93	12.85	12.89	12.83	12.91	12.89
X _{Mg}	0.56	0.45	0.39	0.31	0.25	0.35	0.41	0.43	0.38	0.32	0.34	0.59	0.60

Table I-28

sample phase	Ho-10 i-type	Ho-10 i-type	Ho-10 i-type	Ho-12 i-type	Ho-12 i-type	Ho-12 i-type	Ho-12 i-type	Ho-12 i-type	Ho-12 i-type	Ho-12 i-type	Ho-12 i-type	Ho-12 i-type	Ho-12 i-type
core/rim*	-	-	-	-	-	-	-	-	-	-	-	-	-
number	Ho10-f-4	Ho10-f-5	Ho10-f-6	Ho12-480	Ho12-f-1	Ho12-f-2	Ho12-f-3	Ho12-f-4	Ho12-f-5	Ho12-f-6	Ho12-f-7	Ho12-f-8	Ho12-f-9
text. pos.	-	-	-	-	-	-	-	-	-	-	-	-	-
wt%													
SiO ₂	46.52	42.89	42.80	38.97	41.43	39.86	42.05	37.28	40.85	48.01	43.19	43.58	43.06
TiO ₂	0.05	0.00	0.00	0.02	0.01	0.01	0.02	0.00	0.01	0.02	0.00	0.00	0.00
Al ₂ O ₃	34.09	38.54	38.55	29.60	38.18	40.14	33.69	31.34	38.68	34.48	41.21	38.66	39.55
FeO**	2.35	2.08	2.43	9.02	0.80	0.72	2.35	1.38	1.43	2.07	1.08	1.22	1.21
MnO	0.07	0.03	0.05	0.08	0.00	0.04	0.05	0.07	0.04	0.03	0.08	0.04	0.02
MgO	0.60	0.64	0.47	2.12	0.33	0.23	0.54	0.23	0.39	0.73	0.41	0.38	0.29
CaO	0.81	1.38	1.13	2.43	0.91	1.03	1.06	1.12	1.06	2.24	1.02	0.99	1.05
Na ₂ O	0.12	0.16	0.11	0.07	0.07	0.13	0.12	0.20	0.14	0.07	0.28	0.24	0.23
K ₂ O	2.07	0.46	0.33	0.51	0.48	0.72	0.81	0.55	1.07	0.68	0.71	0.65	0.76
Total	86.70	86.17	85.86	82.83	82.20	82.88	80.68	72.17	83.66	88.33	87.97	85.76	86.17
cation basis							22 O						
Si	6.42	5.93	5.93	5.84	5.95	5.71	6.21	6.14	5.83	6.47	5.83	6.02	5.93
Al ^{IV}	1.58	2.07	2.07	2.16	2.05	2.29	1.79	1.86	2.17	1.53	2.17	1.98	2.07
$\sum IV$	8.00	8.00	8.00	8.00	8.00	8.00	8.00	8.00	8.00	8.00	8.00	8.00	8.00
Al ^{VI}	3.97	4.21	4.23	3.08	4.42	4.49	4.08	4.21	4.33	3.94	4.39	4.32	4.35
Ti	0.01	0.00	0.00	0.00	0.00	0.00	0.00	0.00	0.00	0.00	0.00	0.00	0.00
Fe*	0.24	0.22	0.25	1.02	0.09	0.08	0.26	0.17	0.15	0.21	0.11	0.13	0.13
Mn	0.01	0.00	0.01	0.01	0.00	0.01	0.01	0.01	0.00	0.00	0.01	0.00	0.00
Mg	0.12	0.13	0.10	0.47	0.07	0.05	0.12	0.06	0.08	0.15	0.08	0.08	0.06
$\sum VI$	4.35	4.56	4.58	4.58	4.58	4.62	4.46	4.45	4.57	4.30	4.59	4.53	4.54
Ca	0.12	0.20	0.17	0.39	0.14	0.16	0.17	0.20	0.16	0.32	0.15	0.15	0.15
Na	0.03	0.04	0.03	0.02	0.02	0.04	0.04	0.06	0.04	0.02	0.07	0.06	0.06
K	0.36	0.08	0.06	0.10	0.09	0.13	0.15	0.12	0.19	0.12	0.12	0.11	0.13
$\sum X$	0.52	0.33	0.26	0.51	0.25	0.33	0.36	0.38	0.39	0.46	0.34	0.33	0.35
$\sum cations$	12.87	12.89	12.84	13.09	12.82	12.95	12.82	12.83	12.96	12.76	12.93	12.85	12.89
X _{Mg}	0.34	0.38	0.28	0.32	0.45	0.39	0.31	0.25	0.35	0.41	0.43	0.38	0.32

Table I-29

sample phase	Al-20 ms	Al-20 ms	Al-20 ms	Al-20 ms	Al-20 ms	Al-20 ms	Al-20 ms	Al-20 ms	Al-20 ms	Al-20 ms	Al-20 ms	Al-20 ms	Al-20 ms
core/rim*	-	-	-	-	-	-	-	-	-	-	-	-	-
number	Al20-2	Al20-3	Al20-4	Al20-8	Al20-9	Al20-22	Al20-42	Al20-43	Al20-48	Al20-62	Al20-65	Al20-102	Al20-103
text. pos.	chAl-ms pi.	chAl-ms pi.	chAl-ms pi.	chAl-ms pi.	chAl-ms pi.	chAl-ms pi.	chAl-ms pi.	chAl-ms pi.	chAl-ms pi.	chAl-ms pi.	chAl-ms pi.	chAl-ms pi.	chAl-ms pi.
wt%													
SiO ₂	44.95	45.99	45.80	43.67	43.17	44.67	43.98	46.53	42.29	48.04	44.08	45.53	45.91
TiO ₂	0.01	0.00	0.02	0.00	0.00	0.00	0.02	0.00	0.02	0.00	0.01	0.01	0.01
Al ₂ O ₃	31.98	31.79	33.23	31.72	30.17	32.35	30.46	32.24	31.42	30.57	27.63	30.66	34.08
FeO**	4.17	3.13	2.55	5.03	5.75	4.01	5.35	3.67	5.69	2.58	7.24	4.38	1.82
MnO	0.08	0.00	0.00	0.09	0.05	0.00	0.00	0.00	0.12	0.06	0.23	0.05	0.00
MgO	3.28	2.47	2.12	3.56	5.11	3.27	4.60	2.64	4.21	4.28	5.61	2.98	1.51
CaO	0.00	0.00	0.01	0.00	0.01	0.03	0.01	0.01	0.02	0.05	0.64	0.07	0.00
Na ₂ O	0.39	0.32	0.44	0.40	0.19	0.47	0.26	0.41	0.49	0.15	0.13	0.13	0.62
K ₂ O	9.96	10.16	9.89	9.27	10.02	9.92	8.47	9.91	8.70	9.57	4.60	9.59	9.78
Total	94.83	93.86	94.06	93.74	94.46	94.71	93.18	95.42	92.96	95.28	90.16	93.40	93.72
cation basi													
Si	6.12	6.27	6.20	6.03	5.98	6.08	6.09	6.25	5.91	6.41	6.24	6.27	6.21
Al ^{IV}	1.88	1.73	1.80	1.97	2.02	1.92	1.91	1.75	2.09	1.59	1.76	1.73	1.79
$\sum IV$	8.00	8.00	8.00	8.00	8.00	8.00	8.00	8.00	8.00	8.00	8.00	8.00	8.00
Al ^{VI}	3.25	3.39	3.51	3.19	2.91	3.27	3.06	3.35	3.09	3.21	2.85	3.25	3.64
Ti	0.00	0.00	0.00	0.00	0.00	0.00	0.00	0.00	0.00	0.00	0.00	0.00	0.00
Fe*	0.47	0.36	0.29	0.58	0.67	0.46	0.62	0.41	0.67	0.29	0.86	0.50	0.21
Mn	0.01	0.00	0.00	0.01	0.01	0.00	0.00	0.00	0.01	0.01	0.03	0.01	0.00
Mg	0.66	0.50	0.43	0.73	1.05	0.66	0.95	0.53	0.88	0.85	1.19	0.61	0.30
$\sum VI$	4.40	4.24	4.23	4.52	4.64	4.39	4.64	4.30	4.65	4.35	4.92	4.37	4.15
Ca	0.00	0.00	0.00	0.00	0.00	0.00	0.00	0.00	0.00	0.01	0.10	0.01	0.00
Na	0.10	0.09	0.11	0.11	0.05	0.12	0.07	0.11	0.13	0.04	0.03	0.03	0.16
K	1.73	1.77	1.71	1.63	1.77	1.72	1.50	1.70	1.55	1.63	0.83	1.69	1.69
$\sum X$	1.83	1.85	1.82	1.74	1.83	1.85	1.57	1.81	1.69	1.67	0.96	1.73	1.85
$\sum cations$	14.23	14.10	14.05	14.26	14.46	14.24	14.20	14.10	14.34	14.03	13.88	14.10	14.00
X _{Mg}	0.58	0.58	0.60	0.56	0.61	0.59	0.61	0.56	0.57	0.75	0.58	0.55	0.60

Table I-30

sample phase core/rim*	Bw-29 ms	Bw-29 ms	Bw-29 ms	Bw-29 ms	Bw-29 ms	Bw-29 ms	Bw-29 ms	Bw-29 ms	Bw-29 ms	Bw-29 ms	Bw-29 ms	Bw-29 ms	Bw-29 ms
number	Bw29-49	Bw29-50	Bw29-88	Bw29-89	Bw29-94	Bw29-102	Bw29-103	Bw29-111	Bw29-112	Bw29-113	Bw29-129	Bw29-149	Bw29-174
text. pos.	b-type	b-type	b-type	b-type	b-type	b-type	b-type	b-type	b-type	b-type	b-type	b-type	b-type
wt%													
SiO ₂	42.48	40.03	43.92	44.76	42.02	43.95	44.51	44.51	43.54	41.70	43.48	44.41	43.14
TiO ₂	0.03	0.00	0.03	0.40	0.03	0.04	0.00	0.38	0.71	0.03	0.05	0.04	0.04
Al ₂ O ₃	29.70	26.83	29.18	30.04	28.29	31.08	30.66	29.71	32.53	29.70	30.58	30.43	30.65
FeO**	8.19	12.99	8.57	6.79	11.20	7.30	7.22	6.50	6.47	10.15	8.39	7.88	8.95
MnO	0.09	0.02	0.05	0.01	0.08	0.06	0.02	0.00	0.00	0.08	0.01	0.04	0.02
MgO	2.92	4.79	3.43	2.38	3.74	2.87	2.88	2.42	0.96	3.18	3.07	2.74	3.30
CaO	0.00	0.00	0.00	0.02	0.04	0.00	0.01	0.03	0.04	0.03	0.00	0.01	0.00
Na ₂ O	0.37	0.29	0.42	0.47	0.43	0.48	0.44	0.47	0.53	0.51	0.45	0.35	0.34
K ₂ O	9.83	9.63	9.62	9.70	9.10	9.32	9.37	9.63	9.31	8.41	9.39	8.82	9.45
Total	93.60	94.58	95.24	94.62	94.91	95.09	95.12	93.64	94.17	93.79	95.43	94.71	95.88
cation basi													
Si	6.01	5.80	6.10	6.19	5.95	6.05	6.12	6.21	6.02	5.91	6.01	6.13	5.96
Al ^{IV}	1.99	2.20	1.90	1.81	2.05	1.95	1.88	1.79	1.98	2.09	1.99	1.87	2.04
∑ IV	8.00	8.00	8.00	8.00	8.00	8.00	8.00	8.00	8.00	8.00	8.00	8.00	8.00
Al ^{VI}	2.97	2.37	2.88	3.08	2.67	3.10	3.09	3.09	3.33	2.88	3.00	3.08	2.95
Ti	0.00	0.00	0.00	0.04	0.00	0.00	0.00	0.04	0.07	0.00	0.01	0.00	0.00
Fe*	0.97	1.57	1.00	0.78	1.33	0.84	0.83	0.76	0.75	1.20	0.97	0.91	1.03
Mn	0.01	0.00	0.01	0.00	0.01	0.01	0.00	0.00	0.00	0.01	0.00	0.00	0.00
Mg	0.62	1.03	0.71	0.49	0.79	0.59	0.59	0.50	0.20	0.67	0.63	0.56	0.68
∑ VI	4.57	4.98	4.60	4.40	4.80	4.54	4.51	4.39	4.35	4.77	4.60	4.56	4.67
Ca	0.00	0.00	0.00	0.00	0.01	0.00	0.00	0.00	0.01	0.00	0.00	0.00	0.00
Na	0.10	0.08	0.11	0.13	0.12	0.13	0.12	0.13	0.14	0.14	0.12	0.09	0.09
K	1.78	1.78	1.70	1.71	1.64	1.64	1.64	1.71	1.64	1.52	1.66	1.55	1.66
∑ X	1.88	1.86	1.82	1.84	1.77	1.76	1.76	1.84	1.79	1.67	1.77	1.65	1.75
∑ cations	14.44	14.84	14.41	14.24	14.57	14.30	14.28	14.23	14.14	14.43	14.38	14.21	14.42
X _{Mg}	0.39	0.40	0.42	0.38	0.37	0.41	0.42	0.40	0.21	0.36	0.39	0.38	0.40

Table I-31

sample phase core/rim*	Bw-3 ms	Bw-3 ms	Bw-3 ms	Bw-3 ms	Bw-3 ms	Bw-3 ms	Bw-3 ms	Bw-3 ms	Bw-3 ms	Bw-3 ms	Bw-3 ms	Bw-3 ms	Bw-3 ms
number	Bw3-16	Bw3-25	Bw3-27	Bw3-33	Bw3-34	Bw3-37	Bw3-41	Bw3-43	Bw3-46	Bw3-51	Bw3-52	Be31-54	Bw3-59
text. pos.	b-type	b-type	b-type	b-type	b-type	b-type	b-type	b-type	b-type	b-type	b-type	b-type	b-type
wt%													
SiO ₂	45.52	45.95	46.45	46.19	46.04	45.94	46.57	46.36	46.25	46.51	46.16	46.05	46.28
TiO ₂	0.10	0.00	0.03	0.01	0.05	0.04	0.01	0.06	0.09	0.17	0.09	0.06	0.02
Al ₂ O ₃	36.11	35.42	35.03	35.30	35.50	35.93	36.30	35.98	35.36	35.43	35.99	35.50	35.73
FeO**	1.13	1.25	1.23	1.06	1.00	0.98	1.29	0.87	1.15	1.01	1.06	1.16	0.99
MnO	0.06	0.00	0.00	0.01	0.00	0.04	0.00	0.03	0.01	0.00	0.00	0.09	0.00
MgO	0.59	0.66	0.82	0.73	0.71	0.55	0.65	0.51	0.75	0.62	0.61	0.64	0.65
CaO	0.00	0.00	0.00	0.00	0.01	0.00	0.01	0.00	0.00	0.02	0.00	0.00	0.00
Na ₂ O	0.67	0.69	0.64	0.66	0.60	0.63	0.70	0.69	0.74	0.72	0.64	0.64	0.70
K ₂ O	10.24	10.45	10.08	10.55	10.67	10.72	10.37	10.33	10.45	10.28	10.57	10.34	10.34
Total	94.43	94.46	94.34	94.51	94.57	94.85	95.96	94.85	94.79	94.79	95.11	94.47	94.79
cation basi													
Si	6.10	6.17	6.22	6.19	6.17	6.14	6.15	6.17	6.18	6.20	6.15	6.17	6.18
Al ^{IV}	1.90	1.83	1.78	1.81	1.83	1.86	1.85	1.83	1.82	1.80	1.85	1.83	1.82
∑ IV	8.00	8.00	8.00	8.00	8.00	8.00	8.00	8.00	8.00	8.00	8.00	8.00	8.00
Al ^{VI}	3.81	3.77	3.76	3.77	3.77	3.80	3.79	3.82	3.75	3.77	3.79	3.78	3.80
Ti	0.01	0.00	0.00	0.00	0.00	0.00	0.00	0.01	0.01	0.02	0.01	0.01	0.00
Fe*	0.13	0.14	0.14	0.12	0.11	0.11	0.14	0.10	0.13	0.11	0.12	0.13	0.11
Mn	0.01	0.00	0.00	0.00	0.00	0.00	0.00	0.00	0.00	0.00	0.00	0.01	0.00
Mg	0.12	0.13	0.16	0.15	0.14	0.11	0.13	0.10	0.15	0.12	0.12	0.13	0.13
∑ VI	4.07	4.05	4.06	4.03	4.03	4.03	4.07	4.03	4.04	4.02	4.04	4.05	4.04
Ca	0.00	0.00	0.00	0.00	0.00	0.00	0.00	0.00	0.00	0.00	0.00	0.00	0.00
Na	0.17	0.18	0.17	0.17	0.16	0.16	0.18	0.18	0.19	0.19	0.16	0.17	0.18
K	1.75	1.79	1.72	1.80	1.82	1.83	1.75	1.76	1.78	1.75	1.80	1.77	1.76
∑ X	1.93	1.97	1.89	1.98	1.98	1.99	1.93	1.93	1.97	1.94	1.96	1.93	1.94
∑ cations	14.00	14.01	13.95	14.01	14.01	14.02	13.99	13.96	14.01	13.96	14.00	13.99	13.98
X _{Mg}	0.48	0.48	0.54	0.55	0.56	0.50	0.47	0.51	0.54	0.52	0.51	0.49	0.54

Table I-32

sample phase core/rim*	Bw-8 ms	Bw-8 ms	Bw-8 ms	Bw-8 ms	Bw-8 ms	Bw-8 ms	Bw-8 ms	Bw-8 ms	Bw-8 ms	Bw-8 ms	Bw-8 ms	Bw-8 ms	Bw-8 ms
number text. pos.	Bw8-127 b-type	Bw8-95 b-type	Bw8-100 b-type	Bw8-87 b-type	Bw8-88 b-type	Bw8-89 b-type	Bw-80 b-type	Bw8-76 b-type	Bw8-77 b-type	Bw8-78 b-type	Bw8-58 b-type	Bw8-59 b-type	Bw8-60 b-type
wt%													
SiO ₂	47.40	47.48	47.42	48.23	47.29	47.40	48.90	46.82	47.18	46.14	46.60	46.88	46.22
TiO ₂	0.01	0.00	0.02	0.00	0.01	0.01	0.00	0.00	0.00	0.03	0.00	0.01	0.01
Al ₂ O ₃	34.39	35.30	35.01	35.24	35.89	36.32	37.38	35.86	35.72	36.01	35.50	34.61	36.28
FeO**	1.62	1.11	1.08	1.06	1.15	1.23	1.09	0.98	1.05	0.99	1.32	1.23	1.11
MnO	0.01	0.04	0.03	0.05	0.03	0.02	0.06	0.00	0.00	0.04	0.00	0.03	0.00
MgO	1.19	1.00	0.90	0.91	0.79	0.67	0.65	0.65	0.72	0.53	1.02	1.10	0.56
CaO	0.00	0.00	0.00	0.01	0.01	0.00	0.00	0.03	0.00	0.00	0.00	0.00	0.00
Na ₂ O	0.40	0.58	0.56	0.58	0.56	0.62	0.47	0.62	0.59	0.66	0.69	0.71	0.66
K ₂ O	10.30	10.39	10.18	10.27	10.37	10.11	9.13	10.33	10.12	9.97	9.79	9.67	10.22
Total	95.35	95.89	95.20	96.34	96.11	96.37	97.67	95.27	95.39	94.38	94.91	94.23	95.05
cation basi							22 O						
Si	6.29	6.25	6.28	6.31	6.22	6.20	6.25	6.20	6.23	6.17	6.19	6.27	6.14
Al ^{IV}	1.71	1.75	1.72	1.69	1.78	1.80	1.75	1.80	1.77	1.83	1.81	1.73	1.86
∑ IV	8.00	8.00	8.00	8.00	8.00	8.00	8.00	8.00	8.00	8.00	8.00	8.00	8.00
Al ^{VI}	3.67	3.74	3.75	3.74	3.78	3.80	3.88	3.80	3.80	3.84	3.76	3.72	3.83
Ti	0.00	0.00	0.00	0.00	0.00	0.00	0.00	0.00	0.00	0.00	0.00	0.00	0.00
Fe*	0.18	0.12	0.12	0.12	0.13	0.14	0.12	0.11	0.12	0.11	0.15	0.14	0.12
Mn	0.00	0.00	0.00	0.01	0.00	0.00	0.01	0.00	0.00	0.00	0.00	0.00	0.00
Mg	0.24	0.20	0.18	0.18	0.15	0.13	0.12	0.13	0.14	0.11	0.20	0.22	0.11
∑ VI	4.09	4.06	4.05	4.04	4.06	4.07	4.13	4.04	4.06	4.06	4.11	4.09	4.06
Ca	0.00	0.00	0.00	0.00	0.00	0.00	0.00	0.00	0.00	0.00	0.00	0.00	0.00
Na	0.10	0.15	0.14	0.15	0.14	0.16	0.12	0.16	0.15	0.17	0.18	0.18	0.17
K	1.74	1.75	1.72	1.71	1.74	1.69	1.49	1.75	1.71	1.70	1.66	1.65	1.73
∑ X	1.85	1.89	1.86	1.86	1.88	1.85	1.61	1.91	1.86	1.87	1.84	1.83	1.90
∑ cations	13.94	13.95	13.91	13.90	13.94	13.92	13.74	13.95	13.91	13.93	13.94	13.92	13.96
X _{Mg}	0.57	0.62	0.60	0.60	0.55	0.49	0.52	0.54	0.55	0.49	0.58	0.62	0.47

Table I-33

sample phase core/rim*	Ho-10 ms	Ho-10 ms	Ho-10 ms	Ho-10 ms	Ho-10 ms	Ho-10 ms	Ho-10 ms	Ho-10 ms	Ho-10 ms	Ho-10 ms	Ho-10 ms	Ho-10 ms	Ho-10 ms
number text. pos.	Ho10-48 b-type	Ho10-75 b-type	Ho10-76 b-type	Ho10-85 b-type	Ho10-100 b-type	Ho10-103 b-type	Ho10-105 b-type	Ho10-106 b-type	Ho10-109 b-type	Ho10-113 b-type	Ho10-114 b-type	Ho10-117 b-type	Ho10-120 b-type
wt%													
SiO ₂	47.51	47.73	44.98	46.83	45.69	45.64	46.58	46.40	46.06	46.11	45.36	47.85	50.21
TiO ₂	0.00	0.00	0.07	0.00	0.01	0.00	0.01	0.01	0.00	0.06	0.00	0.00	0.00
Al ₂ O ₃	29.80	34.15	34.28	34.90	36.12	33.81	35.16	35.08	34.29	36.18	34.68	31.79	32.55
FeO**	3.78	1.45	3.34	1.55	1.39	2.43	1.26	1.19	2.12	0.90	1.60	3.58	1.80
MnO	0.12	0.01	0.05	0.00	0.06	0.03	0.01	0.00	0.07	0.00	0.02	0.00	0.02
MgO	3.41	1.07	2.10	1.30	0.84	2.03	0.96	0.99	1.50	0.58	1.27	2.35	1.47
CaO	0.06	0.00	0.05	0.07	0.10	0.05	0.07	0.03	0.00	0.01	0.07	0.23	0.27
Na ₂ O	0.16	0.86	1.00	0.53	0.67	0.57	0.57	0.51	0.55	0.58	0.52	0.17	0.19
K ₂ O	9.06	9.78	8.67	10.16	10.14	10.02	10.04	10.05	10.04	10.10	10.15	8.23	8.40
Total	93.94	95.04	94.60	95.36	95.02	94.57	94.66	94.27	94.63	94.52	93.67	94.21	94.94
cation basi							22 O						
Si	6.45	6.34	6.06	6.22	6.09	6.16	6.22	6.22	6.19	6.15	6.15	6.42	6.59
Al ^{IV}	1.55	1.66	1.94	1.78	1.91	1.84	1.78	1.78	1.81	1.85	1.85	1.58	1.41
∑ IV	8.00	8.00	8.00	8.00	8.00	8.00	8.00	8.00	8.00	8.00	8.00	8.00	8.00
Al ^{VI}	3.22	3.68	3.51	3.68	3.77	3.53	3.75	3.75	3.62	3.84	3.69	3.44	3.63
Ti	0.00	0.00	0.01	0.00	0.00	0.00	0.00	0.00	0.00	0.01	0.00	0.00	0.00
Fe*	0.43	0.16	0.38	0.17	0.15	0.27	0.14	0.13	0.24	0.10	0.18	0.40	0.20
Mn	0.01	0.00	0.01	0.00	0.01	0.00	0.00	0.00	0.01	0.00	0.00	0.00	0.00
Mg	0.69	0.21	0.42	0.26	0.17	0.41	0.19	0.20	0.30	0.12	0.26	0.47	0.29
∑ VI	4.35	4.05	4.32	4.11	4.10	4.21	4.08	4.08	4.16	4.06	4.13	4.31	4.12
Ca	0.01	0.00	0.01	0.01	0.01	0.01	0.01	0.00	0.00	0.00	0.01	0.03	0.04
Na	0.04	0.22	0.26	0.14	0.17	0.15	0.15	0.13	0.14	0.15	0.14	0.05	0.05
K	1.57	1.66	1.49	1.72	1.73	1.72	1.71	1.72	1.72	1.72	1.75	1.41	1.41
∑ X	1.62	1.88	1.76	1.87	1.91	1.88	1.87	1.85	1.86	1.87	1.90	1.49	1.49
∑ cations	13.97	13.93	14.08	13.98	14.02	14.09	13.95	13.94	14.03	13.93	14.03	13.80	13.61
X _{Mg}	0.62	0.57	0.53	0.60	0.52	0.60	0.58	0.60	0.56	0.53	0.59	0.54	0.59

Table I-34

sample phase core/rim*	Ho-12 ms	Ho-12 ms	Ho-12 ms	Ho-12 ms	Ho-12 ms	Ho-12 ms	Ho-12 ms	Ho-12 ms	Ho-12 ms	Ho-12 ms	Ho-12 ms	Ho-12 ms	Ho-12 ms
number text. pos.	Ho12-205 b-type	Ho12-39 b-type	Ho12-86 b-type	Ho12-87 b-type	Ho12-95 b-type	Ho12-96 b-type	Ho12-182 b-type	Ho12-201 b-type	Ho12-202 b-type	Ho12-203 b-type	Ho12-204 b-type	Ho12-207 b-type	Ho12-175 b-type
wt%													
SiO ₂	46.95	46.91	47.60	46.04	46.91	46.08	48.21	47.30	47.03	46.69	47.48	47.18	50.51
TiO ₂	0.24	0.01	0.00	0.00	0.00	0.01	1.40	0.03	0.00	0.30	0.06	0.00	0.69
Al ₂ O ₃	34.54	35.21	35.65	36.75	34.43	33.31	30.02	38.24	38.02	34.48	37.88	37.99	27.61
FeO**	2.25	1.29	1.10	1.38	2.12	2.62	2.95	0.16	0.18	2.51	0.21	0.38	3.29
MnO	0.07	0.05	0.00	0.03	0.01	0.04	0.00	0.00	0.00	0.00	0.00	0.00	0.03
MgO	1.20	0.86	0.81	0.83	1.78	2.14	1.92	0.01	0.03	1.29	0.17	0.08	2.44
CaO	0.00	0.00	0.01	0.02	0.02	0.06	0.00	0.01	0.00	0.00	0.00	0.00	0.00
Na ₂ O	0.33	0.58	0.53	0.53	0.45	0.48	0.15	0.40	0.40	0.35	0.32	0.42	0.02
K ₂ O	10.24	9.78	9.84	9.19	9.93	9.66	9.57	10.36	10.11	10.09	10.51	10.16	9.46
Total	95.81	94.69	95.55	94.78	95.64	94.41	94.31	96.51	95.79	95.70	96.64	96.21	94.18
cation basi							22 O						
Si	6.23	6.24	6.27	6.11	6.22	6.21	6.50	6.14	6.15	6.20	6.16	6.15	6.80
Al ^{IV}	1.77	1.76	1.73	1.89	1.78	1.79	1.50	1.86	1.85	1.80	1.84	1.85	1.20
∑ IV	8.00	8.00	8.00	8.00	8.00	8.00	8.00	8.00	8.00	8.00	8.00	8.00	8.00
Al ^{VI}	3.63	3.77	3.79	3.85	3.60	3.51	3.27	4.00	4.01	3.60	3.96	3.98	3.19
Ti	0.02	0.00	0.00	0.00	0.00	0.00	0.14	0.00	0.00	0.03	0.01	0.00	0.07
Fe*	0.25	0.14	0.12	0.15	0.23	0.30	0.33	0.02	0.02	0.28	0.02	0.04	0.37
Mn	0.01	0.01	0.00	0.00	0.00	0.00	0.00	0.00	0.00	0.00	0.00	0.00	0.00
Mg	0.24	0.17	0.16	0.16	0.35	0.43	0.39	0.00	0.01	0.26	0.03	0.02	0.49
∑ VI	4.14	4.09	4.08	4.17	4.19	4.24	4.13	4.02	4.03	4.17	4.02	4.04	4.12
Ca	0.00	0.00	0.00	0.00	0.00	0.01	0.00	0.00	0.00	0.00	0.00	0.00	0.00
Na	0.08	0.15	0.14	0.14	0.12	0.13	0.04	0.10	0.10	0.09	0.08	0.10	0.01
K	1.73	1.66	1.65	1.55	1.68	1.66	1.65	1.72	1.69	1.71	1.74	1.69	1.62
∑ X	1.82	1.81	1.79	1.69	1.80	1.80	1.68	1.82	1.79	1.80	1.82	1.79	1.63
∑ cations	13.96	13.90	13.86	13.87	13.99	14.03	13.81	13.83	13.82	13.97	13.84	13.83	13.75
X _{Mg}	0.49	0.54	0.57	0.52	0.60	0.59	0.54	0.08	0.24	0.48	0.58	0.28	0.57

Table I-35

sample phase core/rim*	To-2 ms	To-2 ms	To-2 ms	To-2 ms	To-2 ms	To-2 ms	To-2 ms	To-2 ms	To-2 ms	To-2 ms	To-2 ms	To-2 ms	To-2 ms
number text. pos.	To2-168 ch-ms-pi	To2-169 ch-ms-pi	To2-175 ch-ms-pi	To2-140 ch-ms-pi	To2-92 ch-ms-pi	To2-64 ch-ms-pi	To2-58 ch-ms-pi	To2-61 ch-ms-pi	To2-449 ch-ms-pi	To2-491 ch-ms-pi	To2-497 ch-ms-pi	To2-500 ch-ms-pi	To2-527 ch-ms-pi
wt%													
SiO ₂	45.93	45.50	50.35	47.74	45.78	46.56	47.12	45.24	50.26	46.50	46.92	47.44	46.60
TiO ₂	0.02	0.00	0.00	0.00	0.02	0.02	0.00	0.00	0.03	0.01	0.03	0.00	0.02
Al ₂ O ₃	36.57	36.69	33.42	32.55	36.10	33.07	31.60	34.24	33.88	36.49	36.50	35.12	36.80
FeO**	1.39	1.45	1.30	1.83	1.19	1.89	2.40	2.25	1.58	1.84	1.22	1.69	1.25
MnO	0.02	0.00	0.04	0.11	0.00	0.03	0.05	0.01	0.00	0.04	0.00	0.02	0.02
MgO	0.69	0.85	1.28	1.50	0.70	1.70	2.19	1.82	1.54	1.39	0.73	1.57	0.84
CaO	0.00	0.01	0.17	0.08	0.02	0.01	0.01	0.02	0.04	0.03	0.00	0.00	0.00
Na ₂ O	0.59	0.62	0.21	0.24	0.57	0.45	0.63	0.65	0.34	0.74	0.52	0.47	0.41
K ₂ O	9.85	9.75	8.80	9.60	10.06	10.32	9.76	10.11	8.76	9.46	9.94	10.10	9.96
Total	95.05	94.87	95.55	93.67	94.43	94.05	93.77	94.35	96.46	96.49	95.84	96.40	95.92
cation basi							22 O						
Si	6.10	6.06	6.56	6.43	6.13	6.29	6.39	6.12	6.50	6.09	6.17	6.23	6.13
Al ^{IV}	1.90	1.94	1.44	1.57	1.87	1.71	1.61	1.88	1.50	1.91	1.83	1.77	1.87
∑ IV	8.00	8.00	8.00	8.00	8.00	8.00	8.00	8.00	8.00	8.00	8.00	8.00	8.00
Al ^{VI}	3.83	3.82	3.70	3.60	3.82	3.56	3.44	3.57	3.67	3.73	3.82	3.66	3.83
Ti	0.00	0.00	0.00	0.00	0.00	0.00	0.00	0.00	0.00	0.00	0.00	0.00	0.00
Fe*	0.15	0.16	0.14	0.21	0.13	0.21	0.27	0.25	0.17	0.20	0.13	0.19	0.14
Mn	0.00	0.00	0.00	0.01	0.00	0.00	0.01	0.00	0.00	0.00	0.00	0.00	0.00
Mg	0.14	0.17	0.25	0.30	0.14	0.34	0.44	0.37	0.30	0.27	0.14	0.31	0.16
∑ VI	4.12	4.15	4.09	4.12	4.09	4.12	4.16	4.20	4.14	4.20	4.10	4.15	4.13
Ca	0.00	0.00	0.02	0.01	0.00	0.00	0.00	0.01	0.01	0.00	0.00	0.00	0.00
Na	0.15	0.16	0.05	0.06	0.15	0.12	0.17	0.17	0.09	0.19	0.13	0.12	0.11
K	1.67	1.66	1.46	1.65	1.72	1.78	1.69	1.74	1.45	1.58	1.67	1.69	1.67
∑ X	1.82	1.82	1.54	1.72	1.87	1.90	1.85	1.92	1.54	1.77	1.80	1.81	1.78
∑ cations	13.94	13.97	13.63	13.84	13.96	14.02	14.01	14.11	13.68	13.98	13.90	13.96	13.91
X _{Mg}	0.47	0.51	0.64	0.59	0.51	0.62	0.62	0.59	0.64	0.57	0.52	0.62	0.54

Table I-36

sample phase core/rim*	Wa-4 ms	Wa-4 ms	Wa-4 ms	Wa-4 ms	Wa-4 ms	Wa-4 ms	Wa-4 ms	Wa-4 ms	Wa-4 ms	Wa-4 ms	Wa-4 ms	Wa-4 ms	Wa-4 ms
number	Wa4ms5-18	Wa45-182	Wa45-183	Wa45-184	Wa45-185	Wa45-186	Wa45-186	Wa4-50	Wa4-51	Wa4-56	Wa4-90	Wa4-93	Wa4-106
text. pos.	ch-ms-pi	ch-ms-pi	ch-ms-pi	ch-ms-pi	ch-ms-pi	ch-ms-pi	ch-ms-pi	ch-ms-pi	ch-ms-pi	ch-ms-pi	ch-ms-pi	ch-ms-pi	ch-ms-pi
wt%													
SiO ₂	47.66	45.58	47.21	46.94	46.71	47.22	47.22	45.43	46.01	47.73	47.54	47.33	46.04
TiO ₂	0.22	0.40	0.16	0.22	0.26	0.28	0.28	0.00	0.00	0.02	0.25	0.12	0.02
Al ₂ O ₃	34.22	33.74	35.24	35.94	35.91	35.19	35.19	34.53	35.72	35.27	35.19	35.84	34.78
FeO**	1.17	1.23	1.17	0.92	0.95	1.10	1.10	2.61	1.87	1.06	1.30	1.66	2.20
MnO	0.00	0.00	0.00	0.00	0.04	0.00	0.00	0.05	0.04	0.00	0.00	0.02	0.00
MgO	0.75	0.63	0.53	0.42	0.48	0.67	0.67	1.69	1.13	0.66	0.39	0.66	1.23
CaO	0.00	1.93	0.02	0.00	0.00	0.00	0.00	0.02	0.05	0.01	0.00	0.00	0.00
Na ₂ O	0.33	0.38	0.49	0.51	0.58	0.46	0.46	0.49	0.59	0.48	0.62	0.62	0.66
K ₂ O	10.16	9.60	9.87	9.90	9.63	9.95	9.95	9.89	9.97	9.77	9.91	10.06	9.95
Total	94.51	93.48	94.69	94.85	94.55	94.89	94.89	94.73	95.40	95.02	95.22	96.32	94.88
cation basi													
Si	6.35	6.19	6.28	6.22	6.21	6.27	6.27	6.11	6.12	6.31	6.29	6.21	6.17
Al ^{IV}	1.65	1.81	1.72	1.78	1.79	1.73	1.73	1.89	1.88	1.69	1.71	1.79	1.83
∑ IV	8.00	8.00	8.00	8.00	8.00	8.00	8.00	8.00	8.00	8.00	8.00	8.00	8.00
Al ^{VI}	3.73	3.60	3.80	3.84	3.83	3.77	3.77	3.59	3.72	3.80	3.78	3.76	3.66
Ti	0.02	0.04	0.02	0.02	0.03	0.03	0.03	0.00	0.00	0.00	0.03	0.01	0.00
Fe*	0.13	0.14	0.13	0.10	0.11	0.12	0.12	0.29	0.21	0.12	0.14	0.18	0.25
Mn	0.00	0.00	0.00	0.00	0.00	0.00	0.00	0.01	0.00	0.00	0.00	0.00	0.00
Mg	0.15	0.13	0.11	0.08	0.10	0.13	0.13	0.34	0.22	0.13	0.08	0.13	0.25
∑ VI	4.03	3.90	4.05	4.04	4.06	4.05	4.05	4.23	4.15	4.05	4.02	4.08	4.15
Ca	0.00	0.28	0.00	0.00	0.00	0.00	0.00	0.00	0.01	0.00	0.00	0.00	0.00
Na	0.09	0.10	0.13	0.13	0.15	0.12	0.12	0.13	0.15	0.12	0.16	0.16	0.17
K	1.73	1.66	1.67	1.67	1.63	1.68	1.68	1.70	1.69	1.65	1.67	1.68	1.70
∑ X	1.81	2.04	1.80	1.81	1.78	1.80	1.80	1.83	1.85	1.77	1.83	1.84	1.87
∑ cations	13.84	13.95	13.85	13.85	13.84	13.86	13.86	14.06	14.00	13.83	13.86	13.92	14.02
X _{Mg}	0.53	0.48	0.45	0.45	0.48	0.52	0.52	0.54	0.52	0.53	0.35	0.42	0.50

Table I-37

sample phase core/rim*	Wa-4 ms	We-9 ms	We-9 ms	We-9 ms	We-9 ms	We-9 ms	We-9 ms	We-9 ms	We-9 ms	We-9 ms	We-9 ms	We-9 ms	We-9 ms
number	Wa4-112	We9-76	We9-77	We9-80	We9-84	We9-89	We9-110	We9-118	We9-225	We9-235	We9-257	We9-259	We9-717
text. pos.	ch-ms-pi	chl-ms pi	chl-ms pi	chl-ms pi	chl-ms pi	chl-ms pi	chl-ms pi	chl-ms pi	chl-ms pi	chl-ms pi	chl-ms pi	chl-ms pi	chl-ms pi
wt%													
SiO ₂	45.82	46.51	47.54	46.44	47.16	46.59	52.83	46.88	49.53	47.55	48.36	48.47	45.49
TiO ₂	0.01	0.03	0.00	0.00	0.21	0.29	0.00	0.23	0.04	0.06	0.02	0.12	0.01
Al ₂ O ₃	34.80	35.62	35.59	37.03	35.60	36.05	33.53	36.08	35.57	35.14	34.96	35.16	36.71
FeO**	2.64	1.89	0.85	0.76	0.89	0.93	0.94	0.89	0.95	0.98	1.11	1.05	1.10
MnO	0.03	0.01	0.04	0.07	0.00	0.00	0.00	0.00	0.03	0.00	0.03	0.03	0.01
MgO	1.41	0.92	0.54	0.27	0.53	0.40	0.91	0.53	0.73	0.36	0.73	0.52	0.65
CaO	0.01	0.01	0.01	0.04	0.00	0.00	0.07	0.00	0.08	0.01	0.01	0.00	0.02
Na ₂ O	0.59	0.88	1.21	2.06	1.07	1.08	0.94	1.07	0.78	0.98	0.88	0.93	0.81
K ₂ O	10.13	9.73	8.83	8.31	9.56	9.41	7.24	9.37	8.44	9.07	8.95	8.92	8.81
Total	95.45	95.63	94.60	95.00	95.01	94.78	96.51	95.05	96.14	94.17	95.06	95.22	93.61
cation basi													
Si	6.13	6.16	6.29	6.13	6.24	6.18	6.73	6.20	6.41	6.32	6.36	6.36	6.09
Al ^{IV}	1.87	1.84	1.71	1.87	1.76	1.82	1.27	1.80	1.59	1.68	1.64	1.64	1.91
∑ IV	8.00	8.00	8.00	8.00	8.00	8.00	8.00	8.00	8.00	8.00	8.00	8.00	8.00
Al ^{VI}	3.61	3.72	3.83	3.88	3.79	3.82	3.77	3.82	3.83	3.83	3.79	3.80	3.89
Ti	0.00	0.00	0.00	0.00	0.02	0.03	0.00	0.02	0.00	0.01	0.00	0.01	0.00
Fe*	0.30	0.21	0.09	0.08	0.10	0.10	0.10	0.10	0.10	0.11	0.12	0.11	0.12
Mn	0.00	0.00	0.00	0.01	0.00	0.00	0.00	0.00	0.00	0.00	0.00	0.00	0.00
Mg	0.28	0.18	0.11	0.05	0.10	0.08	0.17	0.10	0.14	0.07	0.14	0.10	0.13
∑ VI	4.19	4.12	4.04	4.03	4.02	4.03	4.04	4.04	4.07	4.02	4.06	4.04	4.15
Ca	0.00	0.00	0.00	0.01	0.00	0.00	0.01	0.00	0.01	0.00	0.00	0.00	0.00
Na	0.15	0.23	0.31	0.53	0.27	0.28	0.23	0.28	0.20	0.25	0.23	0.24	0.21
K	1.73	1.64	1.49	1.40	1.61	1.59	1.18	1.58	1.39	1.54	1.50	1.49	1.51
∑ X	1.88	1.87	1.80	1.93	1.89	1.87	1.42	1.86	1.60	1.79	1.73	1.73	1.72
∑ cations	14.07	13.99	13.84	13.96	13.90	13.90	13.46	13.90	13.67	13.81	13.79	13.77	13.86
X _{Mg}	0.49	0.46	0.53	0.39	0.51	0.43	0.63	0.51	0.58	0.40	0.54	0.47	0.51

Table I-38

sample phase	Al-20 Na-mix.	Al-20 Na-mix.	Al-20 Na-mix.	Al-20 Na-mix.	Bw-8 Na-mix.	Bw-8 Na-mix.	Bw-8 Na-mix.	Bw-8 Na-mix.	Bw-8 Na-mix.	Bw-8 Na-mix.	Bw-8 Na-mix.	Bw-8 Na-mix.	Bw-8 Na-mix.
core/rim*	-	-	-	-	-	-	-	-	-	-	-	-	-
number	Al20-81	Al20-82	Al20120	Al20121	Bw8-724	Bw8-725	Bw8-726	Bw8-727	Bw8-728	Bw8-731	Bw8-732	Bw8-733	Bw8-738
text. pos.	-	-	-	-	-	-	-	-	-	-	-	-	-
wt%													
SiO ₂	50.61	51.87	51.35	51.39	51.68	47.70	47.97	55.31	55.85	48.48	49.94	49.35	48.31
TiO ₂	0.00	0.00	0.02	0.03	0.02	0.00	0.03	0.01	0.01	0.00	0.00	0.02	0.00
Al ₂ O ₃	32.97	34.03	34.74	30.57	37.87	39.63	38.58	36.15	34.47	36.11	38.00	39.83	37.18
FeO**	2.86	0.77	1.07	2.06	0.48	0.37	0.43	0.41	0.64	2.98	0.36	0.27	0.40
MnO	0.09	0.02	0.02	0.04	0.00	0.01	0.00	0.01	0.00	0.03	0.04	0.01	0.04
MgO	3.40	0.80	1.23	2.92	0.09	0.09	0.22	0.22	0.29	1.68	0.10	0.08	0.21
CaO	0.04	0.12	0.09	0.19	0.03	0.10	0.07	0.10	0.08	0.15	0.02	0.04	0.02
Na ₂ O	3.66	3.80	4.85	3.03	5.08	5.45	5.20	4.01	3.07	3.11	6.05	6.30	4.25
K ₂ O	1.17	2.43	1.60	3.48	0.46	0.65	0.99	0.28	0.26	0.54	0.70	0.47	3.87
Total	94.86	93.83	94.98	93.71	95.70	94.00	93.51	96.49	94.67	93.08	95.20	96.37	94.28
cation basis													
Si	6.50	6.67	6.54	6.72	6.46	6.11	6.19	6.78	6.95	6.30	6.32	6.17	6.27
Al ^{IV}	1.50	1.33	1.46	1.28	1.54	1.89	1.81	1.22	1.05	1.70	1.68	1.83	1.73
$\sum IV$	8.00	8.00	8.00	8.00	8.00	8.00	8.00	8.00	8.00	8.00	8.00	8.00	8.00
Al ^{VI}	3.48	3.83	3.76	3.43	4.03	4.10	4.05	4.01	4.00	3.83	3.99	4.04	3.95
Ti	0.00	0.00	0.00	0.00	0.00	0.00	0.00	0.00	0.00	0.00	0.00	0.00	0.00
Fe*	0.31	0.08	0.11	0.22	0.05	0.04	0.05	0.04	0.07	0.32	0.04	0.03	0.04
Mn	0.01	0.00	0.00	0.00	0.00	0.00	0.00	0.00	0.00	0.00	0.00	0.00	0.00
Mg	0.65	0.15	0.23	0.57	0.02	0.02	0.04	0.04	0.05	0.33	0.02	0.01	0.04
$\sum VI$	4.45	4.06	4.11	4.22	4.10	4.15	4.14	4.09	4.12	4.48	4.05	4.09	4.04
Ca	0.01	0.02	0.01	0.03	0.00	0.01	0.01	0.01	0.01	0.02	0.00	0.01	0.00
Na	0.91	0.95	1.20	0.77	1.23	1.35	1.30	0.95	0.74	0.78	1.48	1.53	1.07
K	0.19	0.40	0.26	0.58	0.07	0.11	0.16	0.04	0.04	0.09	0.11	0.08	0.64
$\sum X$	1.11	1.36	1.47	1.37	1.31	1.47	1.47	1.01	0.79	0.89	1.60	1.61	1.71
$\sum cations$	13.56	13.42	13.58	13.60	13.41	13.63	13.61	13.10	12.92	13.37	13.65	13.69	13.75
X _{Mg}	0.68	0.65	0.67	0.72	0.24	0.29	0.48	0.48	0.45	0.50	0.32	0.34	0.48

Table I-39

sample phase	Bw-8 Na-mix.	Bw-8 Na-mix.	Bw-8 Na-mix.	Bw-8 Na-mix.	Bw-8 Na-mix.	Bw-8 Na-mix.	Bw-8 Na-mix.	To-2 Na-mix.	To-2 Na-mix.	To-2 Na-mix.	To-2 Na-mix.	We-9 Na-mix.	We-9 Na-mix.
core/rim*	-	-	-	-	-	-	-	-	-	-	-	-	-
number	Bw8-741	Bw8-742	Bw8-778	Bw8-779	Bw8-781	Bw8-794	Bw8-796	To2-28	To2-29	To2-30	To2-40	We9-171	We9-243
text. pos.	-	-	-	-	-	-	-	-	-	-	-	-	-
wt%													
SiO ₂	49.98	47.22	51.65	53.79	48.64	56.86	57.61	49.60	44.01	50.22	48.90	42.33	50.19
TiO ₂	0.04	0.00	0.00	0.05	0.00	0.00	0.01	0.00	0.01	0.00	0.03	0.02	0.01
Al ₂ O ₃	36.18	36.81	35.79	33.56	38.53	33.40	33.74	36.47	32.24	34.42	33.93	29.03	35.06
FeO**	1.92	0.59	1.36	2.30	0.98	0.78	0.74	0.81	5.41	1.02	1.39	11.21	1.99
MnO	0.00	0.06	0.02	0.02	0.00	0.05	0.00	0.02	0.22	0.01	0.02	0.23	0.16
MgO	0.88	0.34	0.82	1.12	0.38	0.47	0.44	0.57	3.84	0.79	1.40	7.00	2.45
CaO	0.07	0.00	0.06	0.06	0.01	0.07	0.13	0.04	0.12	0.04	0.05	0.04	0.07
Na ₂ O	4.49	2.19	2.33	1.26	5.89	2.90	1.29	4.40	2.11	2.15	1.38	1.45	3.24
K ₂ O	1.41	7.74	0.23	0.11	0.34	0.30	0.27	3.14	3.76	5.93	7.69	3.73	2.07
Total	95.01	94.99	92.26	92.28	94.78	94.85	94.25	95.04	91.76	94.58	94.77	95.10	95.23
cation basi													
Si	6.38	6.20	6.63	6.88	6.20	7.06	7.13	6.36	6.05	6.53	6.43	5.83	6.41
Al ^{IV}	1.62	1.80	1.37	1.12	1.80	0.94	0.87	1.64	1.95	1.47	1.57	2.17	1.59
$\sum IV$	8.00	8.00	8.00	8.00	8.00	8.00	8.00	8.00	8.00	8.00	8.00	8.00	8.00
Al ^{VI}	3.83	3.89	4.04	3.94	3.98	3.94	4.05	3.88	3.27	3.80	3.68	2.53	3.68
Ti	0.00	0.00	0.00	0.00	0.00	0.00	0.00	0.00	0.00	0.00	0.00	0.00	0.00
Fe*	0.21	0.06	0.15	0.25	0.10	0.08	0.08	0.09	0.62	0.11	0.15	1.29	0.21
Mn	0.00	0.01	0.00	0.00	0.00	0.01	0.00	0.00	0.03	0.00	0.00	0.03	0.02
Mg	0.17	0.07	0.16	0.21	0.07	0.09	0.08	0.11	0.79	0.15	0.27	1.44	0.47
$\sum VI$	4.21	4.03	4.35	4.41	4.16	4.12	4.21	4.07	4.71	4.07	4.12	5.29	4.38
Ca	0.01	0.00	0.01	0.01	0.00	0.01	0.02	0.01	0.02	0.01	0.01	0.01	0.01
Na	1.11	0.56	0.58	0.31	1.45	0.70	0.31	1.09	0.56	0.54	0.35	0.39	0.80
K	0.23	1.30	0.04	0.02	0.06	0.05	0.04	0.51	0.66	0.98	1.29	0.66	0.34
$\sum X$	1.35	1.85	0.63	0.34	1.51	0.75	0.37	1.61	1.24	1.53	1.65	1.05	1.15
$\sum cations$	13.56	13.88	12.97	12.75	13.67	12.87	12.58	13.68	13.95	13.60	13.76	14.34	13.53
X _{Mg}	0.45	0.50	0.52	0.46	0.41	0.52	0.52	0.56	0.56	0.58	0.64	0.53	0.69

Table I-40

sample phase core/rim* number text. pos.	We-9 Na-mix. - We9-78	We-9 Na-mix. - We9-79	We-9 Na-mix. - We9116	We-9 Na-mix. - We9-99	We-9 Na-mix. - We9-100	We-9 Na-mix. - We9109	We-9 Na-mix. - We9-271	We-9 Na-mix. - We9-424	We-9 Na-mix. - We9-425	We-9 Na-mix. - We9-426	We-9 Na-mix. - We9-427	We-9 Na-mix. - We9-428	We-9 Na-mix. - We9-430
wt%													
SiO ₂	53.07	50.77	49.93	48.85	47.75	47.99	50.73	53.29	49.98	56.10	50.48	51.12	48.32
TiO ₂	0.00	0.00	0.02	0.05	0.02	0.06	0.03	0.00	0.00	0.00	0.05	0.00	0.00
Al ₂ O ₃	35.72	38.19	37.39	37.04	38.12	37.28	33.07	37.66	37.71	35.04	37.24	33.11	37.52
FeO**	0.74	0.52	0.55	0.72	0.49	0.65	3.85	0.52	0.44	0.63	0.54	1.87	0.75
MnO	0.00	0.03	0.03	0.01	0.00	0.02	0.09	0.04	0.00	0.00	0.01	0.02	0.04
MgO	0.20	0.08	0.26	0.21	0.11	0.44	2.41	0.26	0.15	0.45	0.22	1.51	0.25
CaO	0.02	0.09	0.03	0.09	0.17	0.06	0.03	0.13	0.03	0.11	0.05	0.05	0.09
Na ₂ O	4.91	5.85	4.88	4.18	5.31	3.03	3.71	3.23	5.72	2.30	5.48	0.88	3.51
K ₂ O	0.61	0.69	2.66	4.04	2.72	5.61	0.78	2.16	1.09	2.41	1.10	5.81	2.61
Total	95.27	96.23	95.77	95.20	94.70	95.21	94.70	97.28	95.12	97.04	95.18	94.36	93.13
cation basi							22 O						
Si	6.66	6.35	6.34	6.29	6.16	6.22	5.34	6.56	6.34	6.89	6.39	6.65	6.28
Al ^{IV}	1.34	1.65	1.66	1.71	1.84	1.78	0.66	1.44	1.66	1.11	1.61	1.35	1.72
∑ IV	8.00	8.00	8.00	8.00	8.00	8.00	6.00	8.00	8.00	8.00	8.00	8.00	8.00
Al ^{VI}	3.94	3.98	3.93	3.91	3.95	3.91	3.44	4.03	3.97	3.96	3.95	3.72	4.04
Ti	0.00	0.00	0.00	0.01	0.00	0.01	0.00	0.00	0.00	0.00	0.00	0.00	0.00
Fe*	0.08	0.05	0.06	0.08	0.05	0.07	0.34	0.05	0.05	0.06	0.06	0.20	0.08
Mn	0.00	0.00	0.00	0.00	0.00	0.00	0.01	0.00	0.00	0.00	0.00	0.00	0.00
Mg	0.04	0.01	0.05	0.04	0.02	0.09	0.38	0.05	0.03	0.08	0.04	0.29	0.05
∑ VI	4.05	4.06	4.04	4.03	4.03	4.08	0.73	4.13	4.05	4.10	4.06	4.22	4.17
Ca	0.00	0.01	0.00	0.01	0.02	0.01	0.00	0.02	0.00	0.01	0.01	0.01	0.01
Na	1.19	1.42	1.20	1.04	1.33	0.76	0.76	0.77	1.41	0.55	1.34	0.22	0.89
K	0.10	0.11	0.43	0.66	0.45	0.93	0.10	0.34	0.18	0.38	0.18	0.96	0.43
∑ X	1.29	1.54	1.64	1.72	1.80	1.70	0.86	1.13	1.59	0.94	1.53	1.19	1.33
∑ cations	13.35	13.60	13.68	13.75	13.83	13.77	11.04	13.26	13.63	13.04	13.59	13.41	13.50
X _{Mg}	0.33	0.22	0.46	0.35	0.28	0.55	0.53	0.47	0.37	0.56	0.42	0.59	0.37

Table I-41

sample phase core/rim* number text. pos.	Al-20 chl - Al20-28	Al-20 chl - Al20-37	Al-20 chl - Al20-190	Al-20 chl - Al20-101	Al-20 chl - Al20-107	Al-20 chl - Al20-109	Al-20 chl - Al20-114	Al-20 chl - Al20-117	Al-20 chl - Al20-134	Al-20 chl - Al20-137	Al-20 chl - Al20-30	Al-20 chl - Al20-31	Al-20 chl - Al20-174
wt%													
SiO ₂	32.69	25.85	26.89	25.40	25.78	25.60	25.71	25.68	27.77	25.94	37.31	36.80	31.87
TiO ₂	0.04	0.00	0.00	0.02	0.07	0.00	0.03	0.05	0.82	0.03	0.06	0.07	1.90
Al ₂ O ₃	22.87	22.44	21.45	22.60	22.55	22.18	21.97	22.56	21.10	21.95	22.88	21.68	20.45
FeO**	16.79	23.36	19.97	21.70	21.78	21.97	22.09	21.61	20.95	22.28	14.78	15.84	16.27
MnO	0.14	0.18	0.23	0.27	0.12	0.27	0.27	0.21	0.22	0.28	0.20	0.17	0.14
MgO	13.87	15.69	17.54	16.52	16.56	16.30	16.34	16.17	15.79	16.84	11.86	12.08	9.70
CaO	0.10	0.01	0.05	0.01	0.02	0.01	0.02	0.00	0.03	0.01	0.35	0.49	0.08
Na ₂ O	0.05	0.02	0.03	0.02	0.00	0.01	0.00	0.00	0.08	0.00	0.04	0.04	0.10
K ₂ O	2.83	0.13	0.13	0.03	0.07	0.02	0.02	0.15	2.01	0.01	3.03	1.55	6.16
Total	89.35	87.70	86.29	86.61	86.98	86.37	86.46	86.43	88.90	87.34	90.51	88.71	86.75
cation basi													
Si	6.42	5.38	5.58	5.31	5.36	5.38	5.40	5.38	5.69	5.39	7.07	7.11	6.61
Al ^{IV}	1.58	2.62	2.42	2.69	2.64	2.62	2.60	2.62	2.31	2.61	0.93	0.89	1.39
∑ IV	8.00	8.00	8.00	8.00	8.00	8.00	8.00	8.00	8.00	8.00	8.00	8.00	8.00
Al ^{VI}	3.71	2.88	2.83	2.89	2.89	2.86	2.83	2.94	2.78	2.77	4.18	4.04	3.60
Ti	0.01	0.00	0.00	0.00	0.01	0.00	0.00	0.01	0.13	0.00	0.01	0.01	0.30
Fe*	2.76	4.07	3.47	3.80	3.79	3.86	3.88	3.78	3.59	3.87	2.34	2.56	2.82
Mn	0.02	0.03	0.04	0.05	0.02	0.05	0.05	0.04	0.04	0.05	0.03	0.03	0.02
Mg	4.06	4.87	5.43	5.15	5.14	5.10	5.11	5.05	4.82	5.22	3.35	3.48	3.00
∑ VI	10.55	11.85	11.76	11.89	11.85	11.87	11.87	11.81	11.35	11.91	9.92	10.12	9.75
Ca	0.02	0.00	0.01	0.00	0.00	0.00	0.01	0.00	0.01	0.00	0.07	0.10	0.02
Na	0.02	0.01	0.01	0.01	0.00	0.01	0.00	0.00	0.03	0.00	0.02	0.01	0.04
K	0.71	0.03	0.03	0.01	0.02	0.00	0.00	0.04	0.52	0.00	0.73	0.38	1.63
∑ X	0.75	0.05	0.05	0.02	0.02	0.01	0.01	0.04	0.56	0.01	0.82	0.50	1.69
∑ cations	19.30	19.89	19.82	19.90	19.87	19.89	19.88	19.85	19.92	19.92	18.74	18.61	19.43
X _{Mg}	0.60	0.54	0.61	0.58	0.58	0.57	0.57	0.57	0.57	0.57	0.59	0.58	0.52

Table I-42

sample phase core/rim* number text. pos.	Bw-3 chl	Bw-3 chl	Bw-3 chl	Bw-8 chl	Bw-8 chl	Bw-8 chl	Bw-8 chl	Bw-8 chl	Bw-8 chl	Bw-8 chl	Bw-8 chl	Bw-8 chl	Bw-8 chl
	Bw3-349	Bw3-395	Bw3-396	Bw8-131	Bw-132	Bw8-133	Bw-136	Bw8-206	Bw8-220	Bw8-226	Bw8-228	Bw8-229	Bw8-230
wt%													
SiO ₂	29.53	29.52	27.75	26.49	25.42	24.80	25.33	27.07	26.85	24.95	25.26	25.57	26.26
TiO ₂	0.01	0.01	0.03	0.01	0.00	0.00	0.00	0.00	0.02	0.00	0.00	0.00	0.00
Al ₂ O ₃	20.88	21.79	30.73	20.95	21.67	22.72	21.50	21.32	23.01	22.10	22.17	21.90	21.38
FeO**	21.09	9.06	8.27	22.44	22.70	24.05	23.89	20.82	25.17	22.65	22.76	22.49	23.05
MnO	0.31	0.05	0.16	0.38	0.39	0.52	0.40	0.59	0.40	0.51	0.44	0.47	0.46
MgO	14.04	3.39	1.86	16.69	15.47	14.78	15.38	17.00	13.63	15.51	15.20	15.54	15.55
CaO	0.03	0.79	0.28	0.03	0.00	0.01	0.00	0.02	0.05	0.00	0.00	0.05	0.00
Na ₂ O	0.11	0.64	0.08	0.02	0.00	0.03	0.02	0.02	0.07	0.00	0.00	0.05	0.01
K ₂ O	1.49	0.85	3.35	0.01	0.02	0.03	0.01	0.02	0.03	0.01	0.01	0.02	0.01
Total	87.51	66.08	72.53	87.04	85.66	86.98	86.52	86.88	89.23	85.76	85.83	86.12	86.71
cation basi							28 O						
Si	6.08	7.36	6.36	5.53	5.41	5.24	5.38	5.61	5.52	5.31	5.37	5.41	5.52
Al ^{IV}	1.92	0.64	1.64	2.47	2.59	2.76	2.62	2.39	2.48	2.69	2.63	2.59	2.48
$\sum IV$	<i>8.00</i>	<i>8.00</i>	<i>8.00</i>	<i>8.00</i>	<i>8.00</i>	<i>8.00</i>	<i>8.00</i>	<i>8.00</i>	<i>8.00</i>	<i>8.00</i>	<i>8.00</i>	<i>8.00</i>	<i>8.00</i>
Al ^{VI}	3.15	5.77	6.66	2.69	2.85	2.91	2.75	2.82	3.09	2.86	2.92	2.87	2.82
Ti	0.00	0.00	0.01	0.00	0.00	0.00	0.00	0.00	0.00	0.00	0.00	0.00	0.00
Fe*	3.63	1.89	1.58	3.92	4.04	4.25	4.24	3.61	4.33	4.03	4.04	3.98	4.05
Mn	0.05	0.01	0.03	0.07	0.07	0.09	0.07	0.10	0.07	0.09	0.08	0.08	0.08
Mg	4.31	1.26	0.63	5.20	4.91	4.66	4.87	5.25	4.18	4.92	4.81	4.90	4.87
$\sum VI$	<i>11.15</i>	<i>8.93</i>	<i>8.91</i>	<i>11.88</i>	<i>11.87</i>	<i>11.91</i>	<i>11.93</i>	<i>11.78</i>	<i>11.66</i>	<i>11.91</i>	<i>11.86</i>	<i>11.84</i>	<i>11.83</i>
Ca	0.01	0.21	0.07	0.01	0.00	0.00	0.00	0.00	0.01	0.00	0.00	0.01	0.00
Na	0.04	0.31	0.04	0.01	0.00	0.01	0.01	0.01	0.03	0.00	0.00	0.02	0.01
K	0.39	0.27	0.98	0.00	0.00	0.01	0.00	0.01	0.01	0.00	0.00	0.01	0.00
$\sum X$	<i>0.44</i>	<i>0.79</i>	<i>1.08</i>	<i>0.02</i>	<i>0.00</i>	<i>0.02</i>	<i>0.01</i>	<i>0.02</i>	<i>0.05</i>	<i>0.00</i>	<i>0.00</i>	<i>0.04</i>	<i>0.01</i>
$\sum cations$	<i>19.60</i>	<i>17.72</i>	<i>18.00</i>	<i>19.89</i>	<i>19.87</i>	<i>19.93</i>	<i>19.94</i>	<i>19.80</i>	<i>19.71</i>	<i>19.91</i>	<i>19.86</i>	<i>19.87</i>	<i>19.83</i>
X _{Mg}	0.54	0.40	0.29	0.57	0.55	0.52	0.53	0.59	0.49	0.55	0.54	0.55	0.55

Table I-43

sample phase core/rim* number text. pos.	Ho-10 chl	Ho-10 chl	Ho-10 chl	Ho-10 chl	Ho-10 chl	Ho-10 chl	Ho-10 chl	Ho-10 chl	Ho-10 chl	Ho-10 chl	Ho-10 chl	Ho-10 chl	Ho-10 chl
	Ho10-72	Ho10-73	Ho10-98	Ho10-99	Ho10-104	Ho10-50	Ho10-63	Ho10-64	Ho10-137	Ho10-138	Ho10-139	Ho10-140	Ho10-158
wt%													
SiO ₂	26.13	25.14	28.74	26.85	25.79	36.07	30.10	30.26	25.17	24.66	24.86	24.85	26.09
TiO ₂	0.00	0.00	0.00	0.06	0.00	0.00	0.39	0.63	0.13	0.03	0.09	3.04	0.62
Al ₂ O ₃	21.51	22.32	19.54	18.30	19.96	26.63	20.95	20.80	20.66	21.29	20.43	19.13	20.52
FeO**	23.05	21.60	22.87	26.91	26.15	17.97	21.85	21.67	26.76	28.05	27.88	26.23	27.53
MnO	0.30	0.38	0.27	0.27	0.32	0.13	0.25	0.22	0.34	0.35	0.26	0.41	0.24
MgO	15.68	16.24	14.40	14.27	14.25	3.34	12.63	12.06	12.87	12.13	12.09	12.96	11.67
CaO	0.06	0.09	0.10	0.13	0.13	0.49	0.05	0.06	0.08	0.08	0.08	0.08	0.13
Na ₂ O	0.02	0.01	0.04	0.00	0.05	0.05	0.08	0.08	0.01	0.04	0.06	0.00	0.05
K ₂ O	0.04	0.02	1.87	0.06	0.04	2.23	3.68	4.39	0.04	0.04	0.00	0.05	0.47
Total	86.77	85.80	87.85	86.85	86.69	86.92	89.98	90.17	86.10	86.68	85.73	86.91	87.40
cation basi							28 O						
Si	5.49	5.32	6.00	5.77	5.54	7.15	6.12	6.16	5.46	5.35	5.45	5.36	5.60
Al ^{IV}	2.51	2.68	2.00	2.23	2.46	0.85	1.88	1.84	2.54	2.65	2.55	2.64	2.40
$\sum IV$	<i>8.00</i>	<i>8.00</i>	<i>8.00</i>	<i>8.00</i>	<i>8.00</i>	<i>8.00</i>	<i>8.00</i>	<i>8.00</i>	<i>8.00</i>	<i>8.00</i>	<i>8.00</i>	<i>8.00</i>	<i>8.00</i>
Al ^{VI}	2.82	2.88	2.80	2.40	2.58	5.36	3.15	3.16	2.75	2.80	2.73	2.22	2.79
Ti	0.00	0.00	0.00	0.01	0.00	0.00	0.06	0.10	0.02	0.00	0.01	0.49	0.10
Fe*	4.05	3.82	3.99	4.84	4.69	2.98	3.72	3.69	4.86	5.09	5.11	4.73	4.94
Mn	0.05	0.07	0.05	0.05	0.06	0.02	0.04	0.04	0.06	0.06	0.05	0.07	0.04
Mg	4.91	5.12	4.48	4.57	4.56	0.99	3.83	3.66	4.16	3.92	3.95	4.17	3.73
$\sum VI$	<i>11.83</i>	<i>11.88</i>	<i>11.32</i>	<i>11.87</i>	<i>11.89</i>	<i>9.35</i>	<i>10.80</i>	<i>10.64</i>	<i>11.85</i>	<i>11.89</i>	<i>11.86</i>	<i>11.69</i>	<i>11.60</i>
Ca	0.01	0.02	0.02	0.03	0.03	0.10	0.01	0.01	0.02	0.02	0.02	0.02	0.03
Na	0.01	0.01	0.02	0.00	0.02	0.02	0.03	0.03	0.00	0.02	0.02	0.00	0.02
K	0.01	0.01	0.50	0.02	0.01	0.56	0.95	1.14	0.01	0.01	0.00	0.01	0.13
$\sum X$	<i>0.03</i>	<i>0.03</i>	<i>0.54</i>	<i>0.05</i>	<i>0.06</i>	<i>0.69</i>	<i>1.00</i>	<i>1.18</i>	<i>0.03</i>	<i>0.05</i>	<i>0.04</i>	<i>0.03</i>	<i>0.18</i>
$\sum cations$	<i>19.86</i>	<i>19.91</i>	<i>19.86</i>	<i>19.91</i>	<i>19.96</i>	<i>18.04</i>	<i>19.80</i>	<i>19.83</i>	<i>19.88</i>	<i>19.93</i>	<i>19.90</i>	<i>19.72</i>	<i>19.78</i>
X _{Mg}	0.55	0.57	0.53	0.49	0.49	0.25	0.51	0.50	0.46	0.44	0.44	0.47	0.43

Table I-44

sample phase core/rim* number text. pos.	Ho-12 chl -	Ho-12 chl -	Ho-12 chl -	Ho-12 chl -	Ho-12 chl -	Ho-12 chl -	Ho-12 chl -	Ho-12 chl -	Ho-12 chl -	Ho-12 chl -	Ho-12 chl -	Ho-12 chl -	Ho-12 chl -
	Ho12-38 bt	Ho12-166 bt	Ho12-167 bt	Ho12-178 bt	Ho12-181 bt	Ho12-182 bt	Ho12-184 bt	Ho12-186 bt	Ho12-188 bt	Ho12-189 bt	Ho12-252 bt	Ho12-168 bt	Ho12-247 bt
wt%													
SiO ₂	25.95	27.71	25.43	26.70	24.10	23.64	27.05	25.79	25.33	24.14	30.62	29.54	25.91
TiO ₂	0.04	0.05	0.16	0.11	0.14	0.08	0.08	4.48	0.03	0.03	0.00	0.59	0.03
Al ₂ O ₃	21.22	18.38	20.08	19.89	21.91	22.41	22.36	19.41	22.68	21.92	23.51	16.31	20.71
FeO**	22.57	27.27	29.90	27.83	29.44	36.68	23.75	26.58	30.37	26.66	19.22	25.00	24.41
MnO	0.56	0.36	0.23	0.33	0.23	0.15	0.35	0.29	0.39	0.15	0.69	0.27	0.27
MgO	15.47	12.79	10.41	11.24	11.00	3.64	12.30	9.28	7.48	12.18	13.70	14.19	14.06
CaO	0.03	0.09	0.05	0.06	0.01	0.08	0.12	0.16	0.07	0.04	0.00	0.09	0.00
Na ₂ O	0.04	0.04	0.02	0.00	0.02	0.26	0.03	0.02	0.00	0.03	0.06	0.03	0.03
K ₂ O	0.05	0.02	0.00	0.04	0.03	0.01	0.08	0.85	0.02	0.01	1.31	0.87	0.02
Total	85.93	86.77	86.34	86.24	86.99	86.96	86.11	87.02	86.40	85.33	89.11	86.89	85.45
cation basi							28 O						
Si	5.51	5.95	5.59	5.79	5.26	5.36	5.72	5.57	5.55	5.29	6.09	6.28	5.58
Al ^{IV}	2.49	2.05	2.41	2.21	2.74	2.64	2.28	2.43	2.45	2.71	1.91	1.72	2.42
∑ IV	8.00	8.00	8.00	8.00	8.00	8.00	8.00	8.00	8.00	8.00	8.00	8.00	8.00
Al ^{VI}	2.81	2.61	2.79	2.87	2.89	3.34	3.29	2.51	3.41	2.95	3.60	2.36	2.83
Ti	0.01	0.01	0.03	0.02	0.02	0.01	0.01	0.73	0.00	0.01	0.00	0.09	0.01
Fe*	4.00	4.90	5.50	5.05	5.37	6.95	4.20	4.80	5.57	4.89	3.20	4.44	4.39
Mn	0.10	0.07	0.04	0.06	0.04	0.03	0.06	0.05	0.07	0.03	0.12	0.05	0.05
Mg	4.89	4.10	3.41	3.63	3.57	1.23	3.88	2.99	2.44	3.98	4.06	4.50	4.51
∑ VI	11.82	11.68	11.77	11.63	11.89	11.56	11.44	11.08	11.50	11.85	10.98	11.44	11.78
Ca	0.01	0.02	0.01	0.01	0.00	0.02	0.03	0.04	0.02	0.01	0.00	0.02	0.00
Na	0.02	0.02	0.01	0.00	0.01	0.11	0.01	0.01	0.00	0.01	0.02	0.01	0.01
K	0.01	0.01	0.00	0.01	0.01	0.00	0.02	0.23	0.01	0.00	0.33	0.23	0.01
∑ X	0.03	0.04	0.02	0.03	0.02	0.14	0.06	0.28	0.02	0.03	0.36	0.27	0.02
∑ cations	19.85	19.72	19.79	19.66	19.91	19.70	19.50	19.35	19.52	19.88	19.33	19.71	19.80
X _{Mg}	0.55	0.46	0.38	0.42	0.40	0.15	0.48	0.38	0.31	0.45	0.56	0.50	0.51

Table I-45

sample phase core/rim* number text. pos.	To-2 chl -	To-2 chl -	To-2 chl -	To-2 chl -	To-2 chl -	To-2 chl -	To-2 chl -	To-2 chl -	To-2 chl -	To-2 chl -	To-2 chl -	To-2 chl -	To-2 chl -
	To2-10	To2-17	To2-33	To2-57	To2-59	To2-65	To2-137	To2-141	To2-143	To2-159	To2-160	To2-446	To2-504
wt%													
SiO ₂	27.52	26.03	28.54	26.20	25.98	26.48	26.74	24.22	24.35	25.71	27.17	26.08	27.42
TiO ₂	0.03	0.00	0.01	0.01	0.00	0.00	0.00	0.00	0.00	0.01	0.00	0.00	0.00
Al ₂ O ₃	24.66	21.49	21.32	20.55	21.25	20.15	20.21	22.43	22.09	22.23	23.27	22.59	20.38
FeO**	20.26	22.45	20.54	22.07	22.47	23.12	23.37	24.23	23.86	22.56	21.31	20.88	21.27
MnO	0.62	0.81	0.75	0.87	0.78	0.70	0.86	0.61	0.41	0.86	0.65	0.82	1.11
MgO	14.11	15.75	14.36	15.22	15.96	15.67	15.31	14.81	14.68	15.80	15.31	15.33	17.14
CaO	0.19	0.03	0.07	0.03	0.04	0.03	0.08	0.01	0.01	0.02	0.04	0.02	0.02
Na ₂ O	0.16	0.00	0.00	0.04	0.00	0.00	0.00	0.01	0.03	0.01	0.10	0.02	0.00
K ₂ O	0.64	0.21	0.93	0.20	0.06	0.13	0.22	0.04	0.00	0.22	0.57	0.35	0.19
Total	88.22	86.79	86.51	85.19	86.58	86.31	86.78	86.36	85.45	87.44	88.40	86.08	87.52
cation basi							28 O						
Si	5.59	5.47	5.93	5.61	5.48	5.62	5.65	5.18	5.25	5.37	5.55	5.48	5.67
Al ^{IV}	2.41	2.53	2.07	2.39	2.52	2.38	2.35	2.82	2.75	2.63	2.45	2.52	2.33
∑ IV	8.00	8.00	8.00	8.00	8.00	8.00	8.00	8.00	8.00	8.00	8.00	8.00	8.00
Al ^{VI}	3.48	2.80	3.16	2.79	2.75	2.66	2.68	2.83	2.85	2.84	3.14	3.06	2.65
Ti	0.00	0.00	0.00	0.00	0.00	0.00	0.00	0.00	0.00	0.00	0.00	0.00	0.00
Fe*	3.44	3.95	3.57	3.95	3.96	4.10	4.13	4.33	4.30	3.94	3.64	3.67	3.68
Mn	0.11	0.14	0.13	0.16	0.14	0.13	0.15	0.11	0.07	0.15	0.11	0.15	0.19
Mg	4.27	4.94	4.45	4.86	5.01	4.96	4.82	4.72	4.72	4.92	4.66	4.80	5.29
∑ VI	11.30	11.83	11.31	11.76	11.87	11.84	11.79	11.99	11.94	11.86	11.55	11.67	11.81
Ca	0.04	0.01	0.02	0.01	0.01	0.01	0.02	0.00	0.00	0.00	0.01	0.00	0.00
Na	0.06	0.00	0.00	0.01	0.00	0.00	0.00	0.01	0.01	0.00	0.04	0.01	0.00
K	0.17	0.06	0.25	0.05	0.02	0.03	0.06	0.01	0.00	0.06	0.15	0.09	0.05
∑ X	0.27	0.06	0.26	0.07	0.02	0.04	0.08	0.02	0.01	0.07	0.20	0.11	0.05
∑ cations	19.58	19.89	19.58	19.83	19.89	19.88	19.86	20.01	19.96	19.92	19.75	19.78	19.86
X _{Mg}	0.55	0.56	0.55	0.55	0.56	0.55	0.54	0.52	0.52	0.56	0.56	0.57	0.59

Table I-46

sample phase core/rim* number text. pos.	To-2 chl	Wa-4 chl	Wa-4 chl	Wa-4 chl	Wa-4 chl	Wa-4 chl	Wa-4 chl	Wa-4 chl	Wa-4 chl	We-9 chl	We-9 chl	We-9 chl	We-9 chl	We-9 chl
	To2-536	Wa4-672 chl	Wa4-620 chl in Fsp	Wa4-621 chl in Fsp	Wa4-622 chl in Fsp	Wa4-623 chl in Fsp	Wa4-624 chl in Fsp	Wa4-666 chl in Fsp	Wa4-666 chl in Fsp	We9-55	We9-56	We9-63	We9-69	We9-70
wt%														
SiO ₂	26.97	32.16	26.74	26.80	27.24	27.40	31.12	25.86	29.63	26.00	25.30	25.25	24.71	
TiO ₂	0.00	3.69	0.07	0.00	0.04	0.00	0.00	0.01	0.00	0.00	0.05	0.01	0.01	
Al ₂ O ₃	20.27	19.30	19.50	19.56	18.72	19.41	19.22	20.32	23.26	21.16	22.14	22.95	22.48	
FeO**	24.15	21.62	25.94	25.62	25.17	25.02	22.59	25.68	19.20	23.81	24.20	24.69	24.77	
MnO	0.58	0.25	0.50	0.65	0.46	0.65	0.45	0.64	0.62	0.32	0.38	0.32	0.36	
MgO	14.34	8.48	14.19	13.77	14.60	14.36	12.17	13.03	13.34	15.48	14.40	13.80	13.81	
CaO	0.08	0.02	0.04	0.07	0.03	0.16	0.10	0.05	0.06	0.04	0.01	0.04	0.01	
Na ₂ O	0.03	0.06	0.00	0.00	0.01	0.11	0.40	0.00	0.08	0.02	0.06	0.09	0.01	
K ₂ O	0.52	6.19	0.07	0.09	0.10	0.09	1.01	0.08	0.44	0.05	0.05	0.20	0.04	
Total	86.94	91.87	87.05	86.60	86.37	87.20	87.05	85.68	86.62	86.88	86.62	87.34	86.19	
cation basi							28 O							
Si	5.71	6.48	5.70	5.74	5.83	5.80	6.47	5.61	6.04	5.48	5.37	5.32	5.29	
Al ^{IV}	2.29	1.52	2.30	2.26	2.17	2.20	1.53	2.39	1.96	2.52	2.63	2.68	2.71	
∑ IV	8.00	8.00	8.00	8.00	8.00	8.00	8.00	8.00	8.00	8.00	8.00	8.00	8.00	
Al ^{VI}	2.77	3.07	2.59	2.67	2.54	2.64	3.17	2.80	3.64	2.74	2.91	3.02	2.96	
Ti	0.00	0.56	0.01	0.00	0.01	0.00	0.00	0.00	0.00	0.00	0.01	0.00	0.00	
Fe*	4.27	3.64	4.62	4.59	4.50	4.43	3.92	4.65	3.28	4.20	4.30	4.35	4.43	
Mn	0.10	0.04	0.09	0.12	0.08	0.12	0.08	0.12	0.11	0.06	0.07	0.06	0.06	
Mg	4.52	2.55	4.51	4.39	4.66	4.53	3.77	4.21	4.06	4.87	4.56	4.34	4.41	
∑ VI	11.67	9.86	11.82	11.77	11.79	11.71	10.94	11.78	11.07	11.87	11.83	11.77	11.87	
Ca	0.02	0.00	0.01	0.02	0.01	0.04	0.02	0.01	0.01	0.01	0.00	0.01	0.00	
Na	0.01	0.02	0.00	0.00	0.00	0.05	0.16	0.00	0.03	0.01	0.02	0.04	0.00	
K	0.14	1.59	0.02	0.02	0.03	0.02	0.27	0.02	0.11	0.01	0.01	0.05	0.01	
∑ X	0.17	1.62	0.03	0.04	0.04	0.11	0.45	0.03	0.16	0.03	0.04	0.10	0.02	
∑ cations	19.84	19.47	19.85	19.81	19.83	19.82	19.39	19.81	19.23	19.90	19.87	19.87	19.88	
X _{Mg}	0.51	0.41	0.49	0.49	0.51	0.51	0.49	0.47	0.55	0.54	0.51	0.50	0.50	

Table I-47

sample phase core/rim* number text. pos.	We-9 chl	We-9 chl	We-9 chl	We-9 chl	We-9 chl	We-9 chl	We-9 chl	We-9 chl	We-9 chl	We-9 chl	We-9 chl	We-9 chl	We-9 chl
	We9-71	We9-72	We9-73	We9-74	We9-75	We9-85	We9-96	We9-97	We9-98	We9-107	We9-108	We9-117	We9-120
wt%													
SiO ₂	25.25	24.87	25.22	25.76	29.96	25.71	25.20	24.35	25.56	25.14	25.30	24.91	26.17
TiO ₂	0.00	0.01	0.04	0.00	0.02	0.01	0.00	0.02	0.00	0.24	0.00	0.00	0.00
Al ₂ O ₃	21.83	22.60	22.18	21.80	20.39	23.76	21.71	22.09	22.16	21.61	22.61	22.44	21.01
FeO**	24.07	22.95	24.22	21.98	20.29	24.36	23.64	24.38	22.92	24.27	22.13	24.63	23.70
MnO	0.26	0.48	0.44	0.43	0.54	0.54	0.35	0.32	0.36	0.34	0.54	0.27	0.33
MgO	14.49	14.62	14.63	16.14	16.04	13.23	14.90	13.83	14.53	14.14	15.74	13.91	15.42
CaO	0.02	0.02	0.00	0.02	0.02	0.00	0.04	0.05	0.04	0.02	0.02	0.02	0.02
Na ₂ O	0.01	0.03	0.02	0.03	0.08	0.06	0.05	0.02	0.08	0.04	0.01	0.03	0.04
K ₂ O	0.03	0.05	0.02	0.03	0.29	0.06	0.03	0.02	0.06	0.35	0.05	0.04	0.07
Total	85.96	85.65	86.75	86.22	87.63	87.73	85.92	85.09	85.71	86.16	86.45	86.26	86.75
cation basi							28 O						
Si	5.39	5.31	5.34	5.43	6.10	5.37	5.38	5.28	5.44	5.38	5.32	5.32	5.52
Al ^{IV}	2.61	2.69	2.66	2.57	1.90	2.63	2.62	2.72	2.56	2.62	2.68	2.68	2.48
∑ IV	8.00	8.00	8.00	8.00	8.00	8.00	8.00	8.00	8.00	8.00	8.00	8.00	8.00
Al ^{VI}	2.89	2.99	2.88	2.84	2.99	3.22	2.84	2.92	3.00	2.83	2.93	2.97	2.75
Ti	0.00	0.00	0.01	0.00	0.00	0.00	0.00	0.00	0.00	0.04	0.00	0.00	0.00
Fe*	4.30	4.10	4.29	3.87	3.45	4.25	4.22	4.42	4.08	4.34	3.89	4.40	4.18
Mn	0.05	0.09	0.08	0.08	0.09	0.09	0.06	0.06	0.06	0.06	0.10	0.05	0.06
Mg	4.62	4.65	4.62	5.07	4.87	4.12	4.74	4.47	4.61	4.51	4.94	4.43	4.85
∑ VI	11.85	11.83	11.88	11.85	11.40	11.69	11.87	11.88	11.75	11.79	11.86	11.84	11.84
Ca	0.00	0.00	0.00	0.00	0.00	0.00	0.01	0.01	0.01	0.00	0.01	0.00	0.00
Na	0.00	0.01	0.01	0.01	0.03	0.03	0.02	0.01	0.03	0.02	0.00	0.01	0.01
K	0.01	0.01	0.00	0.01	0.08	0.02	0.01	0.01	0.02	0.10	0.01	0.01	0.02
∑ X	0.01	0.03	0.01	0.02	0.11	0.04	0.04	0.02	0.06	0.12	0.02	0.03	0.04
∑ cations	19.86	19.86	19.89	19.88	19.51	19.73	19.90	19.90	19.81	19.91	19.88	19.87	19.88
X _{Mg}	0.52	0.53	0.52	0.57	0.59	0.49	0.53	0.50	0.53	0.51	0.56	0.50	0.54

Table I-48

sample phase	Bw-29 sec. bt	Bw-29 sec. bt	Bw-29 sec. bt	Bw-29 sec. bt	Bw-29 sec. bt	Bw-29 sec. bt	Bw-29 sec. bt	Bw-29 sec. bt	Bw-29 sec. bt	Bw-29 sec. bt	Bw-29 sec. bt	Bw-29 sec. bt	Bw-29 sec. bt
core/rim*	-	-	-	-	-	-	-	-	-	-	-	-	-
number	Bw29-150	Bw29-162	Bw29-163	Bw29-164	Bw29-167	Bw29-187	Bw29-330	Bw29-331	Bw29-332	Bw29-333	Bw29-334	Bw29-335	Bw29-336
text. pos.	b-type	b-type	b-type	b-type	b-type	b-type	b-type	b-type	b-type	b-type	b-type	b-type	b-type
wt%													
SiO ₂	36.28	34.63	34.74	35.11	34.66	35.60	35.30	34.49	34.97	34.61	34.91	34.91	34.76
TiO ₂	0.00	0.02	0.00	0.01	0.05	0.01	0.00	0.02	0.04	0.00	0.07	0.00	0.00
Al ₂ O ₃	21.77	21.81	21.01	21.76	20.56	20.88	19.85	20.22	20.55	19.72	19.82	19.81	21.69
FeO**	19.89	21.04	21.45	20.82	21.45	21.28	20.82	21.86	21.16	21.63	21.98	21.80	20.88
MnO	0.06	0.15	0.15	0.10	0.12	0.11	0.21	0.23	0.26	0.21	0.16	0.17	0.15
MgO	6.98	6.94	6.96	7.09	7.69	7.94	7.88	7.70	8.02	7.93	7.91	8.00	7.13
CaO	0.01	0.00	0.02	0.01	0.00	0.01	0.02	0.01	0.01	0.02	0.03	0.00	0.00
Na ₂ O	0.22	0.14	0.15	0.07	0.17	0.12	0.09	0.03	0.03	0.05	0.04	0.07	0.08
K ₂ O	9.00	8.96	9.24	8.45	8.88	9.08	9.40	9.02	9.01	8.85	9.22	9.21	9.28
Total	94.22	93.71	93.70	93.41	93.58	95.03	93.60	93.59	94.06	93.02	94.16	93.96	93.99
cation basis							22 O						
Si	5.54	5.37	5.42	5.43	5.41	5.45	5.50	5.40	5.42	5.44	5.44	5.44	5.38
Al ^{IV}	2.46	2.63	2.58	2.57	2.59	2.55	2.50	2.60	2.58	2.56	2.56	2.56	2.62
$\sum IV$	8.00	8.00	8.00	8.00	8.00	8.00	8.00	8.00	8.00	8.00	8.00	8.00	8.00
Al ^{VI}	1.46	1.36	1.28	1.40	1.18	1.21	1.15	1.13	1.17	1.10	1.08	1.08	1.34
Ti	0.00	0.00	0.00	0.00	0.01	0.00	0.00	0.00	0.00	0.00	0.01	0.00	0.00
Fe*	2.54	2.73	2.80	2.69	2.80	2.72	2.71	2.86	2.74	2.85	2.86	2.84	2.70
Mn	0.01	0.02	0.02	0.01	0.02	0.01	0.03	0.03	0.03	0.03	0.02	0.02	0.02
Mg	1.59	1.61	1.62	1.63	1.79	1.81	1.83	1.80	1.85	1.86	1.84	1.86	1.65
$\sum VI$	5.59	5.72	5.71	5.74	5.79	5.76	5.72	5.82	5.80	5.83	5.81	5.81	5.71
Ca	0.00	0.00	0.00	0.00	0.00	0.00	0.00	0.00	0.00	0.00	0.00	0.00	0.00
Na	0.07	0.04	0.04	0.02	0.05	0.03	0.03	0.01	0.01	0.02	0.01	0.02	0.02
K	1.75	1.77	1.84	1.67	1.77	1.77	1.87	1.80	1.78	1.78	1.83	1.83	1.83
$\sum X$	1.82	1.82	1.88	1.69	1.82	1.81	1.90	1.81	1.79	1.79	1.85	1.85	1.86
$\sum cations$	15.41	15.54	15.59	15.43	15.61	15.57	15.62	15.64	15.60	15.63	15.66	15.66	15.57
X _{Mg}	0.38	0.37	0.37	0.38	0.39	0.40	0.40	0.39	0.40	0.40	0.39	0.40	0.38

Table I-49

sample phase	Bw-3 sec. Bt	Bw-3 sec. Bt	Bw-3 sec. Bt	Bw-3 sec. Bt	Bw-3 sec. Bt	Bw-3 sec. Bt	Bw-3 sec. Bt	Bw-3 sec. Bt	Bw-3 sec. Bt	Bw-3 sec. Bt	Bw-3 sec. Bt	Bw-3 sec. Bt	Bw-3 sec. Bt
core/rim*	-	-	-	-	-	-	-	-	-	-	-	-	-
number	Bw3-320	Bw3-326	Bw3-328	Bw3-330	Bw3-419	Bw3-505	Bw3-506	Bw3-507	Bw3-508	Bw3-509	Bw3-510	Bw3-511	Bw3-512
text. pos.	b-type	b-type	b-type	b-type	b-type	b-type	b-type	b-type	b-type	b-type	b-type	b-type	b-type
wt%													
SiO ₂	35.30	33.71	34.81	36.17	35.42	34.74	35.26	34.49	34.42	34.90	34.66	35.14	35.50
TiO ₂	0.01	0.00	0.00	0.00	0.00	0.04	0.00	0.00	0.00	0.00	0.02	0.00	0.01
Al ₂ O ₃	21.26	21.72	21.11	22.70	20.81	21.65	21.03	21.68	21.33	21.13	21.12	20.92	20.85
FeO**	16.64	18.36	18.32	16.42	18.21	17.75	16.88	17.25	17.15	18.02	17.80	17.80	17.06
MnO	0.20	0.29	0.19	0.15	0.13	0.13	0.14	0.16	0.20	0.16	0.28	0.16	0.21
MgO	10.97	11.31	10.61	10.33	10.83	10.38	10.85	10.36	10.17	10.18	10.12	10.40	10.18
CaO	0.01	0.00	0.00	0.02	0.00	0.00	0.00	0.00	0.00	0.00	0.00	0.01	0.00
Na ₂ O	0.11	0.10	0.19	0.22	0.16	0.16	0.18	0.15	0.18	0.19	0.17	0.13	0.06
K ₂ O	9.01	8.28	8.65	9.27	9.03	9.33	9.11	9.55	9.33	9.22	9.43	9.26	9.61
Total	93.50	93.77	93.88	95.29	94.60	94.19	93.45	93.66	92.77	93.80	93.61	93.82	93.50
cation basi							22 O						
Si	5.37	5.16	5.32	5.38	5.37	5.29	5.38	5.29	5.32	5.35	5.33	5.37	5.44
Al ^{IV}	2.63	2.84	2.68	2.62	2.63	2.71	2.62	2.71	2.68	2.65	2.67	2.63	2.56
$\sum IV$	8.00	8.00	8.00	8.00	8.00	8.00	8.00	8.00	8.00	8.00	8.00	8.00	8.00
Al ^{VI}	1.19	1.08	1.12	1.36	1.09	1.18	1.17	1.20	1.20	1.16	1.16	1.15	1.20
Ti	0.00	0.00	0.00	0.00	0.00	0.00	0.00	0.00	0.00	0.00	0.00	0.00	0.00
Fe*	2.12	2.35	2.34	2.04	2.31	2.26	2.15	2.21	2.22	2.31	2.29	2.28	2.18
Mn	0.03	0.04	0.02	0.02	0.02	0.02	0.02	0.02	0.03	0.02	0.04	0.02	0.03
Mg	2.49	2.58	2.42	2.29	2.45	2.36	2.47	2.37	2.34	2.33	2.32	2.37	2.32
$\sum VI$	5.82	6.05	5.91	5.71	5.87	5.83	5.81	5.80	5.79	5.82	5.80	5.82	5.73
Ca	0.00	0.00	0.00	0.00	0.00	0.00	0.00	0.00	0.00	0.00	0.00	0.00	0.00
Na	0.03	0.03	0.05	0.06	0.05	0.05	0.05	0.04	0.05	0.06	0.05	0.04	0.02
K	1.75	1.62	1.69	1.76	1.75	1.81	1.77	1.87	1.84	1.80	1.85	1.81	1.88
$\sum X$	1.78	1.65	1.74	1.83	1.80	1.86	1.83	1.91	1.89	1.86	1.90	1.85	1.90
$\sum cations$	15.61	15.70	15.65	15.54	15.66	15.69	15.64	15.71	15.68	15.67	15.70	15.66	15.63
X _{Mg}	0.54	0.52	0.51	0.53	0.51	0.51	0.53	0.52	0.51	0.50	0.50	0.51	0.52

Table I-50

sample phase core/rim* number text. pos.	Bw-8 sec. Bt -	Bw-8 sec. Bt -	Bw-8 sec. Bt -	Bw-8 sec. Bt -	Bw-8 sec. Bt -	Bw-8 sec. Bt -	Bw-8 sec. Bt -	Bw-8 sec. Bt -	Bw-8 sec. Bt -	Bw-8 sec. Bt -	Bw-8 sec. Bt -	Bw-8 sec. Bt -	Bw-8 sec. Bt -
	Bw8-20 b-type	Bw8-83 b-type	Bw8-85 b-type	Bw8-86 b-type	Bw8-90 b-type	Bw8-91 b-type	Bw8-96 b-type	Bw8-101 b-type	Bw8-129 b-type	Bw8-134 b-type	Bw8-143 b-type	Bw8-20 b-type	Bw8-21 b-type
wt%													
SiO ₂	35.55	36.20	36.36	35.94	37.36	36.63	35.95	35.76	36.40	34.23	36.01	35.55	35.68
TiO ₂	0.07	0.00	0.00	0.00	0.00	0.00	0.00	0.02	0.01	1.23	0.06	0.07	0.02
Al ₂ O ₃	20.24	20.72	20.29	20.43	19.51	20.07	20.11	20.74	18.96	20.13	20.64	20.24	20.53
FeO**	18.25	16.95	17.22	17.27	17.03	17.39	18.07	17.20	17.49	20.03	17.78	18.25	18.33
MnO	0.27	0.27	0.26	0.31	0.24	0.24	0.26	0.41	0.25	0.14	0.21	0.27	0.31
MgO	11.00	10.73	10.81	11.34	11.15	11.11	10.80	10.95	11.40	9.57	10.64	11.00	11.19
CaO	0.00	0.02	0.01	0.00	0.01	0.00	0.01	0.00	0.01	0.00	0.00	0.00	0.00
Na ₂ O	0.15	0.12	0.16	0.15	0.16	0.14	0.10	0.14	0.09	0.24	0.23	0.15	0.19
K ₂ O	8.63	9.52	9.12	9.28	9.19	8.84	9.60	9.36	9.03	8.81	9.27	8.63	9.09
Total	94.16	94.54	94.23	94.72	94.64	94.42	94.92	94.58	93.66	94.40	94.84	94.16	95.33
cation basi							22 O						
Si	5.41	5.47	5.51	5.43	5.62	5.53	5.45	5.41	5.56	5.27	5.44	5.41	5.38
Al ^{IV}	2.59	2.53	2.49	2.57	2.38	2.47	2.55	2.59	2.44	2.73	2.56	2.59	2.62
$\sum IV$	8.00	8.00	8.00	8.00	8.00	8.00	8.00	8.00	8.00	8.00	8.00	8.00	8.00
Al ^{VI}	1.04	1.16	1.13	1.06	1.08	1.09	1.04	1.11	0.97	0.92	1.11	1.04	1.03
Ti	0.01	0.00	0.00	0.00	0.00	0.00	0.00	0.00	0.00	0.14	0.01	0.01	0.00
Fe*	2.32	2.14	2.18	2.18	2.14	2.19	2.29	2.18	2.23	2.58	2.25	2.32	2.31
Mn	0.03	0.03	0.03	0.04	0.03	0.03	0.03	0.05	0.03	0.02	0.03	0.03	0.04
Mg	2.50	2.42	2.44	2.55	2.50	2.50	2.44	2.47	2.60	2.20	2.40	2.50	2.51
$\sum VI$	5.90	5.75	5.78	5.84	5.75	5.82	5.81	5.81	5.84	5.86	5.79	5.90	5.89
Ca	0.00	0.00	0.00	0.00	0.00	0.00	0.00	0.00	0.00	0.00	0.00	0.00	0.00
Na	0.04	0.04	0.05	0.04	0.05	0.04	0.03	0.04	0.03	0.07	0.07	0.04	0.05
K	1.68	1.83	1.76	1.79	1.76	1.70	1.86	1.81	1.76	1.73	1.79	1.68	1.75
$\sum X$	1.72	1.87	1.81	1.83	1.81	1.74	1.89	1.85	1.79	1.80	1.85	1.72	1.80
$\sum cations$	15.63	15.62	15.59	15.67	15.56	15.56	15.70	15.66	15.63	15.66	15.64	15.63	15.70
X _{Mg}	0.52	0.53	0.53	0.54	0.54	0.53	0.52	0.53	0.54	0.46	0.52	0.52	0.52

Table I-51

sample phase core/rim* number text. pos.	Ho-10 sec. Bt -	Ho-10 sec. Bt -	Ho-10 sec. Bt -	Ho-12 sec. bt -	Ho-12 sec. bt -	Ho-12 sec. bt -	Ho-12 sec. bt -	Ho-12 sec. bt -	Ho-12 sec. bt -	Ho-12 sec. bt -	Ho-12 sec. bt -	Ho-12 sec. bt -	Ho-12 sec. bt -
	Ho10-84 b-type	Ho10-91 b-type	Ho10-119 b-type	Ho12C-42	Ho12C-47	Ho12C-81	Ho12C-83	Ho12C-84	Ho12C-85	Ho12-406	Ho12-407	Ho12-408	Ho12-409
wt%													
SiO ₂	35.17	37.08	38.56	35.53	34.66	36.96	37.26	37.56	37.20	36.42	34.95	36.17	37.70
TiO ₂	0.05	0.00	0.06	0.00	0.02	0.00	0.03	0.01	0.01	0.00	0.00	0.02	0.00
Al ₂ O ₃	19.39	19.28	21.76	19.79	20.98	18.75	19.64	19.14	20.63	18.43	20.28	18.61	21.83
FeO**	17.92	16.44	14.48	16.69	16.82	17.43	16.97	16.52	16.74	17.37	17.00	17.23	14.47
MnO	0.17	0.17	0.10	0.32	0.30	0.24	0.19	0.30	0.26	0.23	0.15	0.19	0.09
MgO	11.42	11.33	9.20	10.65	10.61	11.48	10.73	11.17	11.13	11.42	10.54	11.59	9.13
CaO	0.02	0.09	0.08	0.03	0.03	0.01	0.02	0.01	0.03	0.00	0.00	0.02	0.00
Na ₂ O	0.06	0.11	0.16	0.13	0.12	0.09	0.08	0.12	0.08	0.07	0.09	0.09	0.12
K ₂ O	8.31	8.86	9.43	8.73	8.63	8.93	8.17	9.02	8.91	9.12	9.06	8.64	9.32
Total	92.51	93.38	93.83	91.88	92.17	93.90	93.08	93.87	94.99	93.08	92.07	92.56	92.68
cation basi							22 O						
Si	5.44	5.63	5.74	5.51	5.36	5.62	5.66	5.68	5.55	5.60	5.43	5.58	5.69
Al ^{IV}	2.56	2.37	2.26	2.49	2.64	2.38	2.34	2.32	2.45	2.40	2.57	2.42	2.31
$\sum IV$	8.00	8.00	8.00	8.00	8.00	8.00	8.00	8.00	8.00	8.00	8.00	8.00	8.00
Al ^{VI}	0.97	1.08	1.55	1.13	1.19	0.98	1.17	1.09	1.17	0.94	1.14	0.96	1.57
Ti	0.01	0.00	0.01	0.00	0.00	0.00	0.00	0.00	0.00	0.00	0.00	0.00	0.00
Fe*	2.32	2.09	1.80	2.16	2.18	2.22	2.15	2.09	2.09	2.23	2.21	2.22	1.83
Mn	0.02	0.02	0.01	0.04	0.04	0.03	0.02	0.04	0.03	0.03	0.02	0.02	0.01
Mg	2.63	2.56	2.04	2.46	2.45	2.60	2.43	2.52	2.47	2.62	2.44	2.66	2.05
$\sum VI$	5.95	5.76	5.42	5.79	5.85	5.82	5.78	5.73	5.77	5.82	5.81	5.87	5.46
Ca	0.00	0.01	0.01	0.00	0.00	0.00	0.00	0.00	0.00	0.00	0.00	0.00	0.00
Na	0.02	0.03	0.05	0.04	0.04	0.03	0.02	0.03	0.02	0.02	0.03	0.03	0.03
K	1.64	1.72	1.79	1.73	1.70	1.73	1.58	1.74	1.70	1.79	1.80	1.70	1.79
$\sum X$	1.66	1.76	1.85	1.77	1.74	1.76	1.61	1.77	1.72	1.81	1.82	1.73	1.83
$\sum cations$	15.62	15.52	15.27	15.56	15.59	15.58	15.39	15.50	15.50	15.63	15.63	15.59	15.29
X _{Mg}	0.53	0.55	0.53	0.53	0.53	0.54	0.53	0.55	0.54	0.54	0.52	0.55	0.53

Table I-52

sample phase core/rim* number text. pos.	To-2 sec- bt -	To-2 sec- bt -	To-2 sec- bt -	To-2 sec- bt -	To-2 sec- bt -	To-2 sec- bt -	To-2 sec- bt -	To-2 sec- bt -	To-2 sec- bt -	To-2 sec- bt -	To-2 sec- bt -	Wa-4 sec. Bt -	Wa-4 sec. Bt -
	To2-45	To2-46	To2-47	To2-48	To2-53	To2-172	To2-487	To2-167	To2-157	To2-495	To2-531	Wa4cd3-49	Wa4cd3-53
wt%													
SiO ₂	37.01	35.31	36.82	36.02	35.38	34.27	35.14	34.66	36.15	36.22	36.36	36.46	33.93
TiO ₂	0.01	0.04	0.00	0.01	0.01	0.00	0.03	0.80	0.00	0.01	0.01	0.05	0.01
Al ₂ O ₃	19.09	20.30	19.01	19.24	20.30	22.20	20.49	21.09	19.90	20.87	20.80	19.55	20.79
FeO**	16.40	16.75	16.50	17.40	16.58	17.03	18.25	18.90	16.44	17.08	16.83	18.91	19.88
MnO	0.39	0.44	0.36	0.41	0.39	0.29	0.32	0.32	0.43	0.33	0.35	0.23	0.28
MgO	11.68	11.17	11.46	10.68	11.60	10.58	12.38	9.63	11.82	10.94	11.34	10.06	9.36
CaO	0.00	0.00	0.00	0.00	0.00	0.04	0.02	0.00	0.01	0.01	0.00	0.00	0.03
Na ₂ O	0.11	0.07	0.09	0.06	0.06	0.22	0.09	0.18	0.08	0.19	0.10	0.17	0.16
K ₂ O	9.31	8.82	9.28	9.00	8.33	8.12	7.69	8.69	8.41	8.95	9.28	8.86	7.69
Total	94.03	92.89	93.51	92.82	92.67	92.76	94.41	94.28	93.24	94.59	95.07	94.28	92.12
cation basi							22 O						
Si	5.60	5.42	5.61	5.55	5.42	5.26	5.31	5.30	5.50	5.45	5.45	5.56	5.31
Al ^{IV}	2.40	2.58	2.39	2.45	2.58	2.74	2.69	2.70	2.50	2.55	2.55	2.44	2.69
$\sum IV$	8.00	8.00	8.00	8.00	8.00	8.00	8.00	8.00	8.00	8.00	8.00	8.00	8.00
Al ^{VI}	1.01	1.09	1.02	1.05	1.09	1.27	0.96	1.09	1.06	1.16	1.12	1.07	1.15
Ti	0.00	0.00	0.00	0.00	0.00	0.00	0.00	0.09	0.00	0.00	0.00	0.01	0.00
Fe*	2.08	2.15	2.10	2.24	2.13	2.18	2.31	2.42	2.09	2.15	2.11	2.41	2.60
Mn	0.05	0.06	0.05	0.05	0.05	0.04	0.04	0.04	0.06	0.04	0.04	0.03	0.04
Mg	2.64	2.56	2.60	2.45	2.65	2.42	2.79	2.19	2.68	2.46	2.53	2.29	2.18
$\sum VI$	5.78	5.86	5.77	5.80	5.92	5.91	6.10	5.84	5.89	5.81	5.81	5.80	5.97
Ca	0.00	0.00	0.00	0.00	0.00	0.01	0.00	0.00	0.00	0.00	0.00	0.00	0.00
Na	0.03	0.02	0.03	0.02	0.02	0.07	0.03	0.05	0.02	0.06	0.03	0.05	0.05
K	1.80	1.73	1.80	1.77	1.63	1.59	1.48	1.69	1.63	1.72	1.77	1.72	1.54
$\sum X$	1.83	1.75	1.83	1.79	1.65	1.66	1.51	1.75	1.66	1.77	1.80	1.77	1.59
$\sum cations$	15.61	15.61	15.60	15.59	15.56	15.57	15.61	15.59	15.55	15.58	15.61	15.57	15.56
X _{Mg}	0.56	0.54	0.55	0.52	0.56	0.53	0.55	0.48	0.56	0.53	0.55	0.49	0.46

Table I-53

sample phase core/rim* number text. pos.	Wa-4 sec. Bt -	Wa-4 sec. Bt -	Wa-4 sec. Bt -	Wa-4 sec. Bt -	Wa-4 sec. Bt -	Wa-4 sec. Bt -	Wa-4 sec. Bt -	Wa-4 sec. Bt -	Wa-4 sec. Bt -	Wa-4 sec. Bt -	Wa-4 sec. Bt -	Wa-4 sec. Bt -	Wa-4 sec. Bt -
	Wa4-105	Wa4-103	Wa4-111	Wa4-153	Wa4-157	Wa4-163	Wa4-164	Wa-4479	Wa4-450	Wa4-446	Wa4-449	Wa4-239	Wa4-232
wt%													
SiO ₂	38.74	36.04	39.69	35.45	36.57	35.10	39.56	37.14	35.68	35.84	35.27	35.72	32.25
TiO ₂	0.00	0.04	0.00	0.00	0.06	1.77	0.02	0.03	0.00	0.00	0.06	0.07	0.00
Al ₂ O ₃	24.49	20.06	30.36	19.29	22.16	19.39	26.30	20.19	20.17	19.53	19.42	21.79	20.11
FeO**	16.57	19.65	11.86	21.00	18.03	21.00	12.16	17.58	18.64	18.41	19.39	18.44	21.59
MnO	0.17	0.16	0.19	0.13	0.15	0.17	0.09	0.19	0.18	0.20	0.15	0.17	0.20
MgO	7.28	9.46	4.67	9.58	7.87	8.23	3.93	9.78	10.01	9.63	9.53	10.06	10.03
CaO	0.01	0.00	0.05	0.00	0.00	0.00	0.25	0.01	0.02	0.03	0.00	0.01	0.03
Na ₂ O	0.28	0.14	0.35	0.17	0.17	0.16	0.15	0.09	0.12	0.11	0.11	0.11	0.09
K ₂ O	9.10	8.88	5.49	8.42	9.25	8.58	6.70	8.99	8.75	8.89	8.66	6.61	6.43
Total	96.65	94.43	92.65	94.06	94.30	94.38	89.17	94.01	93.58	92.65	92.58	92.99	90.72
cation basi							22 O						
Si	5.62	5.50	5.67	5.47	5.53	5.41	5.94	5.62	5.47	5.56	5.50	5.42	5.16
Al ^{IV}	2.38	2.50	2.33	2.53	2.47	2.59	2.06	2.38	2.53	2.44	2.50	2.58	2.84
$\sum IV$	8.00	8.00	8.00	8.00	8.00	8.00	8.00	8.00	8.00	8.00	8.00	8.00	8.00
Al ^{VI}	1.80	1.11	2.78	0.98	1.48	0.93	2.60	1.23	1.12	1.12	1.07	1.32	0.96
Ti	0.00	0.00	0.00	0.00	0.01	0.21	0.00	0.00	0.00	0.00	0.01	0.01	0.00
Fe*	2.01	2.51	1.42	2.71	2.28	2.71	1.53	2.23	2.39	2.39	2.53	2.34	2.89
Mn	0.02	0.02	0.02	0.02	0.02	0.02	0.01	0.02	0.02	0.03	0.02	0.02	0.03
Mg	1.57	2.15	0.99	2.21	1.78	1.89	0.88	2.21	2.29	2.23	2.21	2.28	2.39
$\sum VI$	5.41	5.80	5.22	5.92	5.57	5.76	5.02	5.69	5.83	5.76	5.83	5.96	6.27
Ca	0.00	0.00	0.01	0.00	0.00	0.00	0.04	0.00	0.00	0.00	0.00	0.00	0.00
Na	0.08	0.04	0.10	0.05	0.05	0.05	0.04	0.03	0.04	0.03	0.03	0.03	0.03
K	1.68	1.73	1.00	1.66	1.78	1.69	1.28	1.74	1.71	1.76	1.72	1.28	1.31
$\sum X$	1.76	1.77	1.10	1.71	1.83	1.73	1.37	1.76	1.75	1.80	1.75	1.31	1.35
$\sum cations$	15.17	15.57	14.32	15.63	15.40	15.49	14.39	15.45	15.58	15.56	15.59	15.28	15.61
X _{Mg}	0.44	0.46	0.41	0.45	0.44	0.41	0.37	0.50	0.49	0.48	0.47	0.49	0.45

Table I-54

sample phase core/rim* number text. pos.	Al-20 primary bt core	Al-20 primary bt core	Al-20 primary bt core	Al-20 primary bt core	Al-20 primary bt core	Al-20 primary bt core	Al-20 primary bt rim	Al-20 primary bt rim	Al-20 primary bt rim	Al-20 primary bt rim	Al-20 primary bt rim	Al-20 primary bt rim	Al-20 primary bt rim
	Al20-19 matrix	Al20-20 matrix	Al20-41 pi. cont.	Al20-88 pi. cont.	Al20-155 pi. cont.	Al20-167 pi. cont.	Al20-148 matrix	Al20-149 matrix	Al20-150 matrix	Al20-152 pi. cont.	Al20-152 pi. cont.	Al20-133 pi. cont.	Al20-133 pi. cont.
wt%													
SiO ₂	36.05	35.99	36.26	36.15	35.75	36.24	36.24	34.29	36.17	36.19	35.07	36.46	36.46
TiO ₂	4.00	3.10	3.16	4.33	3.35	3.71	3.34	3.16	3.12	3.29	3.27	2.77	2.77
Al ₂ O ₃	16.18	18.56	15.99	16.12	16.45	15.98	16.33	16.64	16.33	16.13	16.12	19.57	19.57
FeO**	19.05	17.64	17.96	18.34	18.18	18.74	18.04	17.88	18.30	18.23	17.91	16.33	16.33
MnO	0.09	0.09	0.13	0.05	0.00	0.10	0.05	0.08	0.11	0.08	0.04	0.12	0.12
MgO	11.24	10.43	11.98	11.67	11.88	11.62	11.85	11.35	12.10	11.87	11.70	10.05	10.05
CaO	0.00	0.01	0.01	0.01	0.01	0.00	0.02	0.03	0.01	0.00	0.05	0.03	0.03
Na ₂ O	0.29	0.11	0.13	0.29	0.28	0.30	0.27	0.34	0.35	0.29	0.33	0.20	0.20
K ₂ O	8.70	8.83	8.79	8.67	8.24	8.54	8.45	8.20	8.47	8.53	7.99	8.11	8.11
Total	95.83	94.98	94.69	95.71	94.22	95.37	94.67	92.02	95.04	94.77	92.56	93.80	93.80
cation basi							22 O						
Si	5.46	5.44	5.53	5.45	5.46	5.49	5.50	5.38	5.48	5.51	5.45	5.50	5.50
Al ^{IV}	2.54	2.56	2.47	2.55	2.54	2.51	2.50	2.62	2.52	2.49	2.55	2.50	2.50
$\sum IV$	8.00	8.00	8.00	8.00	8.00	8.00	8.00	8.00	8.00	8.00	8.00	8.00	8.00
Al ^{VI}	0.34	0.74	0.40	0.32	0.42	0.35	0.43	0.45	0.40	0.40	0.41	0.98	0.98
Ti	0.46	0.35	0.36	0.49	0.38	0.42	0.38	0.37	0.36	0.38	0.38	0.31	0.31
Fe*	2.41	2.23	2.29	2.31	2.32	2.38	2.29	2.34	2.32	2.32	2.33	2.06	2.06
Mn	0.01	0.01	0.02	0.01	0.00	0.01	0.01	0.01	0.01	0.01	0.01	0.02	0.02
Mg	2.54	2.35	2.72	2.62	2.70	2.63	2.68	2.65	2.73	2.69	2.71	2.26	2.26
$\sum VI$	5.76	5.69	5.80	5.75	5.83	5.79	5.79	5.84	5.83	5.80	5.84	5.63	5.63
Ca	0.00	0.00	0.00	0.00	0.00	0.00	0.00	0.00	0.00	0.00	0.01	0.00	0.00
Na	0.08	0.03	0.04	0.08	0.08	0.09	0.08	0.10	0.10	0.09	0.10	0.06	0.06
K	1.68	1.70	1.71	1.67	1.60	1.65	1.64	1.64	1.64	1.65	1.58	1.56	1.56
$\sum X$	1.77	1.74	1.75	1.67	1.69	1.74	1.72	1.75	1.74	1.74	1.69	1.62	1.62
$\sum cations$	15.53	15.42	15.54	15.50	15.52	15.52	15.51	15.58	15.57	15.54	15.53	15.25	15.25
X _{Mg}	0.51	0.51	0.54	0.53	0.52	0.53	0.54	0.53	0.54	0.54	0.54	0.52	0.52

Table I-55

sample phase core/rim* number text. pos.	Bw-29 primary bt core	Bw-29 primary bt core	Bw-29 primary bt rim	Bw-29 primary bt rim	Bw-29 primary bt rim	Bw-29 primary bt core	Bw-29 primary bt core	Bw-29 primary bt core	Bw-29 primary bt core	Bw-29 primary bt core	Bw-29 primary bt rim	Bw-29 primary bt rim	Bw-29 primary bt rim
	Bw29-60 matrix	Bw29-61 matrix	Bw29-62 matrix	Bw29-63 matrix	Bw29-196 matrix	Bw29-171 pi. cont.	Bw29-176 pi. cont.	Bw29-177 pi. cont.	Bw29-217 pi. cont.	Bw29-136 pi. cont.	Bw29-189 pi. cont.	Bw29-101 pi. cont.	Bw29-90 pi. cont.
wt%													
SiO ₂	34.13	33.98	34.12	33.87	34.61	34.42	34.42	34.97	34.29	34.52	33.56	34.04	34.15
TiO ₂	3.14	2.86	2.70	3.19	2.97	3.08	2.97	2.93	3.76	0.06	0.10	0.11	0.67
Al ₂ O ₃	18.36	18.17	18.62	18.16	18.59	18.66	19.14	18.97	18.33	21.02	21.84	20.86	19.64
FeO**	23.43	23.93	24.00	24.15	23.28	22.66	23.12	21.99	24.13	20.93	21.57	22.09	23.30
MnO	0.09	0.07	0.06	0.02	0.06	0.05	0.09	0.13	0.06	0.09	0.14	0.03	0.10
MgO	5.97	6.00	6.09	5.91	5.97	5.84	6.33	5.88	5.53	8.05	6.83	7.76	6.91
CaO	0.00	0.00	0.00	0.00	0.01	0.00	0.00	0.00	0.01	0.00	0.00	0.00	0.02
Na ₂ O	0.22	0.27	0.22	0.19	0.28	0.16	0.14	0.21	0.22	0.17	0.17	0.19	0.20
K ₂ O	8.98	8.79	8.76	8.99	8.81	8.99	8.99	9.13	8.97	8.47	9.12	8.17	8.42
Total	94.54	94.31	94.69	94.69	94.75	93.94	95.33	94.34	95.45	93.31	93.33	93.24	93.39
cation basi							22 O						
Si	5.37	5.37	5.35	5.34	5.40	5.41	5.34	5.45	5.35	5.37	5.27	5.33	5.39
Al ^{IV}	2.63	2.63	2.65	2.66	2.60	2.59	2.66	2.55	2.65	2.63	2.73	2.67	2.61
$\sum IV$	8.00	8.00	8.00	8.00	8.00	8.00	8.00	8.00	8.00	8.00	8.00	8.00	8.00
Al ^{VI}	0.77	0.75	0.80	0.71	0.83	0.86	0.84	0.93	0.72	1.22	1.31	1.18	1.04
Ti	0.37	0.34	0.32	0.38	0.35	0.36	0.35	0.34	0.44	0.01	0.01	0.01	0.08
Fe*	3.08	3.16	3.15	3.18	3.04	2.98	3.00	2.87	3.15	2.72	2.83	2.89	3.07
Mn	0.01	0.01	0.01	0.00	0.01	0.01	0.01	0.02	0.01	0.01	0.02	0.00	0.01
Mg	1.40	1.41	1.42	1.39	1.39	1.37	1.46	1.37	1.29	1.87	1.60	1.81	1.62
$\sum VI$	5.63	5.67	5.70	5.66	5.61	5.58	5.66	5.53	5.60	5.83	5.76	5.89	5.83
Ca	0.00	0.00	0.00	0.00	0.00	0.00	0.00	0.00	0.00	0.00	0.00	0.00	0.00
Na	0.07	0.08	0.07	0.06	0.08	0.05	0.04	0.06	0.07	0.05	0.05	0.06	0.06
K	1.80	1.77	1.75	1.81	1.75	1.80	1.78	1.82	1.79	1.68	1.82	1.63	1.69
$\sum X$	1.87	1.85	1.82	1.87	1.84	1.85	1.82	1.88	1.85	1.73	1.88	1.69	1.76
$\sum cations$	15.50	15.53	15.52	15.53	15.45	15.43	15.48	15.40	15.45	15.56	15.64	15.58	15.59
X _{Mg}	0.31	0.31	0.31	0.30	0.31	0.31	0.33	0.32	0.29	0.41	0.36	0.38	0.35

Table I-56

sample phase core/rim* number text. pos.	Bw-3 primary bt core	Bw-3 primary bt core	Bw-3 primary bt core	Bw-3 primary bt rim	Bw-3 primary bt rim	Bw-3 primary bt rim	Bw-3 primary bt core	Bw-3 primary bt core	Bw-3 primary bt core	Bw-3 primary bt core	Bw-3 primary bt rim	Bw-3 primary bt rim	Bw-3 primary bt rim
	Bw3-192 matrix	Bw3-193 matrix	Bw3-194 matrix	Bw3-209 matrix	Bw3-212 matrix	Bw3-221 matrix	Bw3-7 pi. cont.	Bw3-85 pi. cont.	Bw3-86 pi. cont.	Bw3-87 pi. cont.	Bw3-36 pi. cont.	Bw3-39 pi. cont.	Bw3-42 pi. cont.
wt%													
SiO ₂	35.14	35.04	34.31	34.55	34.71	35.00	35.09	35.01	34.84	34.63	34.77	35.21	35.50
TiO ₂	4.01	4.21	4.29	3.28	3.15	3.45	3.81	3.24	2.73	3.00	0.03	0.26	0.43
Al ₂ O ₃	18.57	18.30	18.43	17.95	19.26	18.33	18.43	18.58	19.36	18.34	20.28	20.86	20.34
FeO**	21.05	20.45	20.88	21.61	19.21	20.76	20.20	19.70	19.36	19.86	19.02	18.63	17.95
MnO	0.12	0.08	0.09	0.07	0.10	0.16	0.07	0.13	0.13	0.12	0.29	0.11	0.16
MgO	7.53	7.80	7.27	8.05	8.29	7.71	8.20	8.45	8.58	8.81	10.92	10.28	10.09
CaO	0.01	0.00	0.00	0.00	0.01	0.00	0.00	0.00	0.00	0.00	0.00	0.01	0.00
Na ₂ O	0.19	0.19	0.12	0.15	0.16	0.13	0.17	0.17	0.20	0.20	0.19	0.19	0.19
K ₂ O	9.40	9.30	8.90	9.29	8.73	9.19	9.36	9.43	9.54	9.12	8.19	9.21	9.03
Total	96.11	95.44	94.35	94.98	93.72	94.81	95.34	94.80	94.82	94.13	93.71	94.76	93.68
cation basi							22 O						
Si	5.36	5.37	5.32	5.35	5.36	5.40	5.37	5.38	5.35	5.36	5.34	5.35	5.43
Al ^{IV}	2.64	2.63	2.68	2.65	2.64	2.60	2.63	2.62	2.65	2.64	2.66	2.65	2.57
∑ IV	8.00	8.00	8.00	8.00	8.00	8.00	8.00	8.00	8.00	8.00	8.00	8.00	8.00
Al ^{VI}	0.70	0.67	0.69	0.63	0.87	0.73	0.69	0.75	0.85	0.71	1.01	1.09	1.10
Ti	0.46	0.48	0.50	0.38	0.37	0.40	0.44	0.38	0.32	0.35	0.00	0.03	0.05
Fe*	2.68	2.62	2.71	2.80	2.48	2.68	2.58	2.53	2.48	2.57	2.44	2.37	2.30
Mn	0.02	0.01	0.01	0.01	0.01	0.02	0.01	0.02	0.02	0.02	0.04	0.01	0.02
Mg	1.71	1.78	1.68	1.86	1.91	1.77	1.87	1.94	1.96	2.03	2.50	2.33	2.30
∑ VI	5.57	5.56	5.59	5.68	5.63	5.61	5.59	5.61	5.63	5.68	5.99	5.83	5.77
Ca	0.00	0.00	0.00	0.00	0.00	0.00	0.00	0.00	0.00	0.00	0.00	0.00	0.00
Na	0.06	0.06	0.03	0.04	0.05	0.04	0.05	0.05	0.06	0.06	0.06	0.05	0.06
K	1.83	1.82	1.76	1.84	1.72	1.81	1.83	1.85	1.87	1.80	1.60	1.79	1.76
∑ X	1.89	1.87	1.80	1.88	1.77	1.85	1.88	1.90	1.93	1.86	1.66	1.84	1.82
∑ cations	15.46	15.44	15.39	15.57	15.41	15.46	15.47	15.51	15.55	15.54	15.65	15.67	15.59
X _{Mg}	0.39	0.40	0.38	0.40	0.43	0.40	0.42	0.43	0.44	0.44	0.51	0.50	0.50

Table I-57

sample phase core/rim* number text. pos.	Bw-3 primary bt rim	Bw-8 primary bt core	Bw-8 primary bt core	Bw-8 primary bt core	Bw-8 primary bt rim	Bw-8 primary bt rim	Bw-8 primary bt rim	Bw-8 primary bt rim	Bw-8 primary bt core	Bw-8 primary bt core	Bw-8 primary bt core	Bw-8 primary bt rim	Bw-8 primary bt rim
	Bw3-44 pi. cont.	Bw8-474 matrix	Bw8-477 matrix	Bw8-478 matrix	Bw8-491 matrix	Bw8-492 matrix	Bw8-493 matrix	Bw8-3 pi. cont.	Bw8-13 pi. cont.	Bw8-15 pi. cont.	Bw8-560 pi. cont.	Bw8-566 pi. cont.	Bw8-567 pi. cont.
wt%													
SiO ₂	34.82	33.33	33.75	33.50	32.36	33.55	36.57	34.59	34.73	34.66	34.27	34.75	34.70
TiO ₂	0.27	4.90	4.46	4.77	1.76	3.68	2.05	4.05	4.03	3.58	2.43	0.43	0.55
Al ₂ O ₃	20.60	18.53	18.47	18.35	20.50	18.40	18.68	18.78	18.78	18.51	19.69	20.33	21.41
FeO**	18.26	21.08	21.26	20.50	20.99	20.27	19.46	20.72	20.03	20.71	19.56	18.92	18.27
MnO	0.23	0.15	0.11	0.09	0.18	0.13	0.23	0.23	0.23	0.24	0.29	0.16	0.17
MgO	10.09	6.94	7.04	6.85	9.12	7.80	8.26	7.44	7.57	7.90	8.53	10.15	9.62
CaO	0.00	0.00	0.00	0.01	0.00	0.03	0.01	0.00	0.00	0.00	0.00	0.00	0.00
Na ₂ O	0.18	0.14	0.10	0.15	0.10	0.24	0.05	0.23	0.18	0.19	0.14	0.10	0.22
K ₂ O	9.23	9.35	9.20	9.23	7.16	9.17	8.89	9.23	9.26	9.31	9.20	8.55	9.20
Total	93.70	94.53	94.40	93.59	92.17	93.34	94.20	95.34	94.89	95.14	94.20	93.42	94.18
cation basi							22 O						
Si	5.36	5.20	5.26	5.26	5.10	5.27	5.60	5.31	5.34	5.34	5.30	5.36	5.30
Al ^{IV}	2.64	2.80	2.74	2.74	2.90	2.73	2.40	2.69	2.66	2.66	2.70	2.64	2.70
∑ IV	8.00	8.00	8.00	8.00	8.00	8.00	8.00	8.00	8.00	8.00	8.00	8.00	8.00
Al ^{VI}	1.09	0.61	0.65	0.66	0.91	0.68	0.97	0.71	0.75	0.70	0.88	1.05	1.16
Ti	0.03	0.57	0.52	0.56	0.21	0.43	0.24	0.47	0.47	0.42	0.28	0.05	0.06
Fe*	2.35	2.75	2.77	2.69	2.77	2.66	2.49	2.66	2.58	2.67	2.53	2.44	2.34
Mn	0.03	0.02	0.01	0.01	0.02	0.02	0.03	0.03	0.03	0.03	0.04	0.02	0.02
Mg	2.31	1.61	1.64	1.60	2.14	1.83	1.89	1.70	1.74	1.81	1.97	2.33	2.19
∑ VI	5.81	5.57	5.59	5.53	6.05	5.63	5.61	5.58	5.55	5.63	5.70	5.89	5.77
Ca	0.00	0.00	0.00	0.00	0.00	0.00	0.00	0.00	0.00	0.00	0.00	0.00	0.00
Na	0.05	0.04	0.03	0.05	0.03	0.07	0.01	0.07	0.05	0.06	0.04	0.03	0.06
K	1.81	1.86	1.83	1.85	1.44	1.84	1.73	1.81	1.82	1.83	1.81	1.68	1.79
∑ X	1.86	1.90	1.86	1.90	1.47	1.92	1.75	1.88	1.87	1.88	1.86	1.71	1.86
∑ cations	15.68	15.47	15.45	15.42	15.52	15.54	15.36	15.46	15.42	15.51	15.56	15.60	15.63
X _{Mg}	0.50	0.37	0.37	0.37	0.44	0.41	0.43	0.39	0.40	0.40	0.44	0.49	0.48

Table I-58

sample phase core/rim* number text. pos	Ho-10 primary bt matrix	Ho-10 primary bt matrix	Ho-10 primary bt matrix	Ho-10 primary bt matrix	Ho-10 primary bt matrix	Ho-10 primary bt matrix	Ho-10 primary bt matrix	Ho-10 primary bt matrix	Ho-10 primary bt matrix	Ho-10 primary bt matrix	Ho-10 primary bt matrix	Ho-10 primary bt matrix	Ho-10 primary bt matrix
wt%													
SiO ₂	34.40	34.49	33.88	34.13	34.58	34.90	34.87	34.45	34.27	34.44	34.18	34.82	34.70
TiO ₂	4.13	4.14	4.70	1.74	3.43	3.94	4.07	3.98	3.14	3.52	3.35	4.13	4.50
Al ₂ O ₃	17.86	17.65	18.44	19.20	18.69	18.06	17.47	17.48	18.55	17.99	18.13	17.76	18.03
FeO**	20.11	20.17	18.86	18.63	18.88	20.07	20.61	20.43	19.78	19.89	19.27	20.67	20.45
MnO	0.04	0.21	0.19	0.15	0.16	0.17	0.11	0.17	0.19	0.15	0.15	0.07	0.14
MgO	8.06	7.83	7.07	9.79	7.86	8.24	8.17	8.24	8.69	8.46	8.45	8.27	7.56
CaO	0.00	0.03	0.00	0.00	0.03	0.01	0.07	0.02	0.05	0.01	0.01	0.07	0.10
Na ₂ O	0.19	0.19	0.16	0.17	0.20	0.19	0.17	0.22	0.18	0.17	0.16	0.18	0.24
K ₂ O	9.28	9.18	8.93	8.32	8.61	9.20	8.89	9.17	8.87	9.07	8.83	9.09	9.04
Total	94.15	93.94	92.37	92.16	92.47	94.85	94.57	94.23	93.76	93.77	92.59	95.14	94.90
cation basis							22 O						
Si	5.35	5.37	5.33	5.34	5.41	5.37	5.40	5.36	5.32	5.36	5.37	5.36	5.35
Al ^{IV}	2.65	2.63	2.67	2.66	2.59	2.63	2.60	2.64	2.68	2.64	2.63	2.64	2.65
∑ IV	8.00	8.00	8.00	8.00	8.00	8.00	8.00	8.00	8.00	8.00	8.00	8.00	8.00
Al ^{VI}	0.62	0.62	0.75	0.88	0.85	0.65	0.58	0.57	0.72	0.66	0.72	0.58	0.63
Ti	0.48	0.49	0.56	0.20	0.40	0.46	0.47	0.47	0.37	0.41	0.40	0.48	0.52
Fe*	2.61	2.63	2.48	2.44	2.47	2.58	2.67	2.66	2.57	2.59	2.53	2.66	2.64
Mn	0.01	0.03	0.02	0.02	0.02	0.02	0.01	0.02	0.02	0.02	0.02	0.01	0.02
Mg	1.87	1.82	1.66	2.28	1.83	1.89	1.89	1.91	2.01	1.96	1.98	1.90	1.74
∑ VI	5.59	5.57	5.48	5.83	5.57	5.60	5.62	5.62	5.69	5.65	5.65	5.62	5.55
Ca	0.00	0.00	0.00	0.00	0.01	0.00	0.01	0.00	0.01	0.00	0.00	0.01	0.02
Na	0.06	0.06	0.05	0.05	0.06	0.06	0.05	0.07	0.05	0.05	0.05	0.05	0.07
K	1.84	1.82	1.79	1.66	1.72	1.81	1.75	1.82	1.76	1.80	1.77	1.78	1.78
∑ X	1.90	1.89	1.84	1.71	1.78	1.86	1.82	1.89	1.82	1.86	1.82	1.85	1.87
∑ cations	15.48	15.46	15.32	15.54	15.36	15.46	15.44	15.52	15.52	15.50	15.47	15.47	15.41
X _{Mg}	0.42	0.41	0.40	0.48	0.43	0.42	0.41	0.42	0.44	0.43	0.44	0.42	0.40

Table I-59

sample phase core/rim* number text. pos	Ho-12 primary bt matrix	Ho-12 primary bt matrix	Ho-12 primary bt matrix	Ho-12 primary bt matrix	Ho-12 primary bt matrix	Ho-12 primary bt matrix	Ho-12 primary bt matrix	Ho-12 primary bt matrix	Ho-12 primary bt matrix	Ho-12 primary bt matrix	Ho-12 primary bt matrix	Ho-12 primary bt matrix	Ho-12 primary bt matrix
wt%													
SiO ₂	34.95	35.22	35.29	34.94	35.14	34.76	34.59	34.65	34.83	34.95	35.10	35.42	34.83
TiO ₂	4.15	4.72	4.43	4.21	4.38	4.90	3.87	4.14	3.50	4.96	2.43	4.14	4.18
Al ₂ O ₃	17.85	18.00	17.87	17.48	19.00	17.54	18.14	17.75	18.61	17.62	19.06	17.59	17.19
FeO**	20.06	20.25	19.53	18.94	19.46	20.16	20.13	19.75	19.83	19.28	17.79	19.46	20.10
MnO	0.15	0.13	0.11	0.20	0.14	0.19	0.18	0.17	0.21	0.08	0.17	0.19	0.10
MgO	7.96	7.77	7.71	7.79	7.29	7.36	7.99	7.69	7.97	7.42	8.92	8.08	7.92
CaO	0.00	0.00	0.00	0.00	0.00	0.00	0.00	0.00	0.01	0.00	0.00	0.00	0.00
Na ₂ O	0.21	0.25	0.22	0.19	0.21	0.12	0.22	0.17	0.12	0.13	0.12	0.17	0.22
K ₂ O	8.96	8.83	9.25	9.18	8.91	8.96	9.07	9.06	9.14	9.40	9.30	9.21	9.33
Total	94.36	95.25	94.51	93.04	94.62	94.19	94.34	93.48	94.31	93.89	92.92	94.38	93.96
cation basi							22 O						
Si	5.40	5.39	5.44	5.46	5.38	5.40	5.36	5.41	5.38	5.42	5.44	5.46	5.43
Al ^{IV}	2.60	2.61	2.56	2.54	2.62	2.60	2.64	2.59	2.62	2.58	2.56	2.54	2.57
∑ IV	8.00	8.00	8.00	8.00	8.00	8.00	8.00	8.00	8.00	8.00	8.00	8.00	8.00
Al ^{VI}	0.65	0.63	0.68	0.68	0.81	0.60	0.67	0.67	0.77	0.64	0.92	0.66	0.58
Ti	0.48	0.54	0.51	0.49	0.50	0.57	0.45	0.49	0.41	0.58	0.28	0.48	0.49
Fe*	2.59	2.59	2.51	2.48	2.49	2.62	2.61	2.58	2.56	2.50	2.31	2.51	2.62
Mn	0.02	0.02	0.01	0.03	0.02	0.03	0.02	0.02	0.03	0.01	0.02	0.02	0.01
Mg	1.83	1.77	1.77	1.82	1.67	1.70	1.85	1.79	1.83	1.71	2.06	1.86	1.84
∑ VI	5.58	5.55	5.49	5.49	5.50	5.52	5.60	5.55	5.60	5.44	5.60	5.53	5.54
Ca	0.00	0.00	0.00	0.00	0.00	0.00	0.00	0.00	0.00	0.00	0.00	0.00	0.00
Na	0.06	0.07	0.06	0.06	0.06	0.04	0.06	0.05	0.04	0.04	0.03	0.05	0.07
K	1.77	1.72	1.82	1.83	1.74	1.77	1.79	1.80	1.80	1.86	1.84	1.81	1.85
∑ X	1.83	1.80	1.88	1.89	1.80	1.81	1.86	1.86	1.84	1.90	1.87	1.86	1.92
∑ cations	15.41	15.35	15.37	15.38	15.30	15.33	15.46	15.40	15.44	15.34	15.47	15.39	15.46
X _{Mg}	0.41	0.41	0.41	0.42	0.40	0.39	0.41	0.41	0.42	0.41	0.47	0.43	0.41

Table I-60

sample phase core/rim* number text. pos	To-2 primary bt core	To-2 primary bt core	To-2 primary bt core	To-2 primary bt core	To-2 primary bt core	To-2 primary bt core	To-2 primary bt core	To-2 primary bt core	To-2 primary bt core	To-2 primary bt core	To-2 primary bt core	To-2 primary bt core	To-2 primary bt core
	To2-70 matrix	To2-71 matrix	To2-78 matrix	To2-79 matrix	To2-121 matrix	To2-122 matrix	To2-125 matrix	To2-126 matrix	To2-431 matrix	To2-435 matrix	To2-436 matrix	To2-480 matrix	To2-425 matrix
wt%													
SiO ₂	34.75	34.53	35.09	34.69	34.48	34.59	34.47	34.64	34.62	34.51	34.59	34.54	34.39
TiO ₂	3.29	3.17	3.22	3.09	2.80	3.11	3.07	2.87	2.48	1.71	3.23	2.83	2.80
Al ₂ O ₃	18.39	18.97	18.40	18.73	18.96	18.93	19.21	19.22	19.47	20.82	19.39	19.59	19.18
FeO**	19.68	20.04	20.04	19.75	20.56	19.98	19.93	19.25	19.72	19.39	19.48	19.63	19.57
MnO	0.17	0.23	0.23	0.28	0.24	0.27	0.28	0.18	0.29	0.22	0.24	0.27	0.32
MgO	8.36	8.30	8.30	8.15	8.19	8.24	8.27	8.55	8.37	8.64	8.08	8.39	8.29
CaO	0.00	0.01	0.00	0.01	0.00	0.00	0.01	0.00	0.00	0.01	0.00	0.00	0.03
Na ₂ O	0.21	0.21	0.18	0.18	0.21	0.20	0.24	0.23	0.24	0.29	0.28	0.23	0.26
K ₂ O	9.11	9.12	9.34	9.16	9.20	9.10	8.88	9.13	9.15	8.89	9.32	8.94	9.10
Total	94.01	94.63	94.81	94.11	94.71	94.42	94.42	94.07	94.38	94.49	94.66	94.43	93.97
cation basi													
Si	5.38	5.32	5.40	5.37	5.33	5.34	5.32	5.34	5.34	5.29	5.32	5.31	5.33
Al ^{IV}	2.62	2.68	2.60	2.63	2.67	2.66	2.68	2.66	2.66	2.71	2.68	2.69	2.67
∑ IV	8.00	8.00	8.00	8.00	8.00	8.00	8.00	8.00	8.00	8.00	8.00	8.00	8.00
Al ^{VI}	0.74	0.77	0.73	0.79	0.78	0.78	0.81	0.84	0.88	1.04	0.83	0.86	0.83
Ti	0.38	0.37	0.37	0.36	0.33	0.36	0.36	0.33	0.29	0.20	0.37	0.33	0.33
Fe*	2.55	2.58	2.58	2.56	2.66	2.58	2.57	2.48	2.54	2.48	2.50	2.52	2.54
Mn	0.02	0.03	0.03	0.04	0.03	0.03	0.04	0.02	0.04	0.03	0.03	0.04	0.04
Mg	1.93	1.91	1.90	1.88	1.89	1.90	1.90	1.97	1.92	1.97	1.85	1.92	1.92
∑ VI	5.62	5.66	5.62	5.63	5.68	5.65	5.67	5.64	5.67	5.73	5.59	5.67	5.65
Ca	0.00	0.00	0.00	0.00	0.00	0.00	0.00	0.00	0.00	0.00	0.00	0.00	0.00
Na	0.06	0.06	0.05	0.05	0.06	0.06	0.07	0.07	0.07	0.09	0.08	0.07	0.08
K	1.80	1.79	1.83	1.81	1.81	1.79	1.75	1.80	1.80	1.74	1.83	1.75	1.80
∑ X	1.86	1.86	1.89	1.87	1.88	1.85	1.82	1.87	1.87	1.82	1.91	1.82	1.88
∑ cations	15.49	15.51	15.50	15.49	15.56	15.50	15.49	15.51	15.54	15.55	15.51	15.50	15.53
X _{Mg}	0.43	0.42	0.42	0.42	0.42	0.42	0.43	0.44	0.43	0.44	0.43	0.43	0.43

Table I-61

sample phase core/rim* number text. pos	Wa-4 primary bt core	Wa-4 primary bt core	Wa-4 primary bt core	Wa-4 primary bt core	Wa-4 primary bt core	Wa-4 primary bt core	Wa-4 primary bt core	Wa-4 primary bt core	Wa-4 primary bt core	Wa-4 primary bt core	Wa-4 primary bt core	Wa-4 primary bt core	Wa-4 primary bt core
	Wa4-7 matrix	Wa4-8 matrix	Wa4-60 matrix	Wa4-61 matrix	Wa4-62 matrix	Wa4-63 matrix	Wa4-64 matrix	Wa4-65 matrix	Wa4-66 matrix	Wa4-67 matrix	Wa4-70 matrix	Wa4-71 matrix	Wa4-72 matrix
wt%													
SiO ₂	34.39	34.23	33.39	33.60	34.04	34.13	34.19	33.56	33.55	34.05	34.15	34.52	34.28
TiO ₂	4.32	4.44	4.75	4.64	4.37	4.26	3.83	4.15	3.69	3.66	4.04	3.67	3.86
Al ₂ O ₃	18.69	18.56	18.08	18.54	18.00	18.92	18.58	18.63	19.28	18.89	18.21	18.23	18.06
FeO**	21.99	22.23	22.38	22.34	22.42	20.94	22.31	22.49	22.17	22.19	22.50	22.93	22.06
MnO	0.11	0.10	0.08	0.13	0.12	0.06	0.11	0.14	0.10	0.13	0.06	0.13	0.19
MgO	5.99	5.81	6.03	5.94	6.07	6.46	6.73	6.15	6.30	6.58	6.34	6.36	6.70
CaO	0.01	0.01	0.01	0.04	0.04	0.00	0.00	0.13	0.00	0.01	0.00	0.00	0.00
Na ₂ O	0.12	0.12	0.19	0.24	0.26	0.21	0.23	0.15	0.13	0.13	0.11	0.12	0.16
K ₂ O	9.39	9.30	9.12	9.18	8.83	9.09	9.11	8.97	9.19	9.16	9.19	9.12	9.28
Total	95.31	95.13	94.14	94.72	94.20	94.15	95.13	94.41	94.49	94.87	94.70	95.14	94.67
cation basi													
Si	5.33	5.33	5.26	5.25	5.34	5.31	5.31	5.26	5.24	5.30	5.33	5.37	5.35
Al ^{IV}	2.67	2.67	2.74	2.75	2.66	2.69	2.69	2.74	2.76	2.70	2.67	2.63	2.65
∑ IV	8.00	8.00	8.00	8.00	8.00	8.00	8.00	8.00	8.00	8.00	8.00	8.00	8.00
Al ^{VI}	0.75	0.73	0.62	0.67	0.66	0.79	0.70	0.70	0.80	0.76	0.69	0.71	0.67
Ti	0.50	0.52	0.56	0.55	0.52	0.50	0.45	0.49	0.43	0.43	0.47	0.43	0.45
Fe*	2.85	2.89	2.95	2.92	2.94	2.73	2.89	2.95	2.90	2.89	2.94	2.98	2.88
Mn	0.01	0.01	0.01	0.02	0.02	0.01	0.01	0.02	0.01	0.02	0.01	0.02	0.03
Mg	1.38	1.35	1.42	1.38	1.42	1.50	1.56	1.44	1.47	1.53	1.48	1.48	1.56
∑ VI	5.51	5.51	5.55	5.53	5.55	5.52	5.61	5.59	5.61	5.62	5.58	5.61	5.59
Ca	0.00	0.00	0.00	0.01	0.01	0.00	0.00	0.02	0.00	0.00	0.00	0.00	0.00
Na	0.04	0.04	0.06	0.07	0.08	0.06	0.07	0.05	0.04	0.04	0.03	0.04	0.05
K	1.86	1.85	1.83	1.83	1.77	1.81	1.80	1.79	1.83	1.82	1.83	1.81	1.85
∑ X	1.90	1.88	1.89	1.91	1.85	1.87	1.87	1.86	1.87	1.86	1.86	1.84	1.90
∑ cations	15.40	15.39	15.44	15.45	15.41	15.38	15.48	15.45	15.48	15.47	15.45	15.46	15.48
X _{Mg}	0.33	0.32	0.32	0.32	0.33	0.35	0.35	0.33	0.34	0.35	0.33	0.33	0.35

Table I-62

sample phase core/rim* number text. pos	We-9 primary bt core We9-121 matrix	We-9 primary bt core We9-122 matrix	We-9 primary bt core We9-123 matrix	We-9 primary bt core We9-124 matrix	We-9 primary bt core We9-125 matrix	We-9 primary bt core We9-126 matrix	We-9 primary bt core We9-127 matrix	We-9 primary bt core We9-129 matrix	We-9 primary bt core We9-130 matrix	We-9 primary bt core We9-131 matrix	We-9 primary bt core We9-132 matrix	We-9 primary bt core We9-133 matrix	We-9 primary bt core We9-134 matrix
wt%													
SiO ₂	34.45	34.67	34.38	33.97	33.61	34.20	34.37	34.40	34.68	34.57	34.49	34.70	33.94
TiO ₂	4.70	4.60	4.10	4.34	3.82	3.47	3.79	4.55	3.87	3.44	4.26	5.97	3.88
Al ₂ O ₃	17.95	17.76	17.62	17.38	17.24	18.49	18.31	17.42	17.86	18.02	17.93	16.46	17.68
FeO**	19.70	20.52	20.90	20.57	20.88	21.42	19.90	20.34	21.01	20.79	20.54	21.25	21.03
MnO	0.12	0.18	0.15	0.15	0.20	0.16	0.10	0.11	0.16	0.14	0.09	0.19	0.20
MgO	7.53	7.49	7.62	7.49	8.65	8.12	8.06	7.71	7.92	8.02	7.72	6.97	7.75
CaO	0.00	0.01	0.00	0.01	0.00	0.00	0.01	0.01	0.00	0.00	0.01	0.10	0.06
Na ₂ O	0.24	0.22	0.19	0.19	0.14	0.16	0.24	0.22	0.22	0.24	0.19	0.16	0.16
K ₂ O	9.13	8.97	9.06	8.93	8.03	9.04	9.28	9.02	9.21	8.97	9.15	8.91	8.80
Total	93.81	94.49	94.09	93.06	92.65	95.10	94.11	93.84	94.99	94.20	94.43	94.85	93.57
cation basi													
Si	5.35	5.37	5.36	5.35	5.31	5.28	5.34	5.37	5.36	5.37	5.35	5.39	5.33
Al ^{IV}	2.65	2.63	2.64	2.65	2.69	2.72	2.66	2.63	2.64	2.63	2.65	2.61	2.67
∑ IV	8.00	8.00	8.00	8.00	8.00	8.00	8.00	8.00	8.00	8.00	8.00	8.00	8.00
Al ^{VI}	0.64	0.61	0.60	0.58	0.52	0.65	0.69	0.57	0.61	0.67	0.62	0.40	0.60
Ti	0.55	0.54	0.48	0.51	0.45	0.40	0.44	0.53	0.45	0.40	0.50	0.70	0.46
Fe*	2.56	2.66	2.73	2.71	2.76	2.77	2.58	2.65	2.72	2.70	2.66	2.76	2.76
Mn	0.02	0.02	0.02	0.02	0.03	0.02	0.01	0.01	0.02	0.02	0.01	0.02	0.03
Mg	1.74	1.73	1.77	1.76	2.04	1.87	1.87	1.79	1.82	1.86	1.78	1.61	1.81
∑ VI	5.51	5.56	5.60	5.59	5.80	5.71	5.59	5.57	5.62	5.65	5.58	5.49	5.66
Ca	0.00	0.00	0.00	0.00	0.00	0.00	0.00	0.00	0.00	0.00	0.00	0.02	0.01
Na	0.07	0.07	0.06	0.06	0.04	0.05	0.07	0.07	0.07	0.07	0.06	0.05	0.05
K	1.81	1.77	1.80	1.80	1.62	1.78	1.84	1.79	1.82	1.78	1.81	1.76	1.76
∑ X	1.88	1.84	1.86	1.86	1.66	1.83	1.91	1.86	1.88	1.85	1.87	1.83	1.82
∑ cations	15.39	15.39	15.46	15.44	15.46	15.54	15.50	15.43	15.50	15.50	15.45	15.32	15.48
X _{Mg}	0.41	0.39	0.39	0.39	0.42	0.40	0.42	0.40	0.40	0.41	0.40	0.37	0.40

Table I-63

sample phase core/rim* number text. pos	Al-20 chl-ms ch-120-46 ch-ms pi.	Al-20 chl-ms ch-120-47 ch-ms pi.	Al-20 chl-ms ch-120-54 ch-ms pi.	Al-20 chl-ms ch-120-57 ch-ms pi.	Al-20 chl-ms ch-120-58 ch-ms pi.	Al-20 chl-ms ch-120-60 ch-ms pi.	Al-20 chl-ms ch-120-60 ch-ms pi.	Al-20 chl-ms ch-120-64 ch-ms pi.	Al-20 chl-ms ch-120-66 ch-ms pi.	Al-20 chl-ms ch-120-68 ch-ms pi.	Al-20 chl-ms ch-120-73 ch-ms pi.	Al-20 chl-ms ch-120-77 ch-ms pi.	Al-20 chl-ms ch-120-78 ch-ms pi.
wt%													
SiO ₂	45.72	43.74	45.44	45.35	43.28	48.65	46.10	43.59	45.18	39.95	40.48	47.40	47.01
TiO ₂	0.03	0.00	0.00	0.01	0.02	0.04	0.04	0.00	0.00	0.02	0.01	0.04	0.00
Al ₂ O ₃	25.56	26.11	28.15	28.60	25.99	28.55	29.11	29.00	28.68	29.94	29.02	28.60	29.77
FeO**	7.32	9.99	6.67	7.25	5.37	4.06	6.20	5.14	6.66	4.16	7.42	6.40	5.74
MnO	0.05	0.14	0.21	0.15	0.12	0.13	0.22	0.11	0.26	0.17	0.12	0.15	0.10
MgO	6.69	8.05	5.92	5.92	4.75	5.09	5.30	6.86	5.87	3.94	6.46	5.36	4.91
CaO	0.30	0.32	0.63	0.63	0.61	0.65	0.67	0.04	0.56	0.45	0.16	0.73	0.68
Na ₂ O	0.08	0.07	0.05	0.05	0.08	0.10	0.09	0.11	0.04	0.09	0.10	0.08	0.11
K ₂ O	6.53	5.48	4.40	4.49	4.27	5.03	4.70	7.76	4.59	3.45	7.09	4.84	4.82
Total	92.29	93.90	91.50	92.44	84.50	92.29	92.41	92.60	91.84	82.17	90.87	93.60	93.14
cation basi													
Si	6.39	6.09	6.30	6.24	6.45	6.57	6.31	6.06	6.24	6.06	5.82	6.40	6.35
Al ^{IV}	1.61	1.91	1.70	1.76	1.55	1.43	1.69	1.94	1.76	1.94	2.18	1.60	1.65
∑ IV	8.00	8.00	8.00	8.00	8.00	8.00	8.00	8.00	8.00	8.00	8.00	8.00	8.00
Al ^{VI}	2.60	2.37	2.89	2.88	3.01	3.11	3.00	2.82	2.92	3.41	2.74	2.96	3.10
Ti	0.00	0.00	0.00	0.00	0.00	0.00	0.00	0.00	0.00	0.00	0.00	0.00	0.00
Fe*	0.86	1.16	0.77	0.83	0.67	0.46	0.71	0.60	0.77	0.53	0.89	0.72	0.65
Mn	0.01	0.02	0.02	0.02	0.02	0.01	0.03	0.01	0.03	0.02	0.01	0.02	0.01
Mg	1.39	1.67	1.22	1.21	1.06	1.03	1.08	1.42	1.21	0.89	1.39	1.08	0.99
∑ VI	4.86	5.22	4.92	4.95	4.75	4.62	4.82	4.85	4.93	4.85	5.03	4.78	4.75
Ca	0.05	0.05	0.09	0.09	0.10	0.09	0.10	0.01	0.08	0.07	0.03	0.11	0.10
Na	0.02	0.02	0.01	0.01	0.02	0.03	0.02	0.03	0.01	0.03	0.03	0.02	0.03
K	1.16	0.97	0.78	0.79	0.81	0.87	0.82	1.38	0.81	0.67	1.30	0.83	0.83
∑ X	1.23	1.04	0.89	0.89	0.93	0.99	0.94	1.41	0.90	0.77	1.35	0.96	0.96
∑ cations	14.09	14.26	13.80	13.84	13.69	13.60	13.76	14.26	13.83	13.61	14.38	13.74	13.70
X _{Mg}	0.62	0.59	0.61	0.59	0.61	0.69	0.60	0.70	0.61	0.63	0.61	0.60	0.60

Table I-64

sample phase core/rim* number text. pos	Bw-29 ms-bt -	Bw-29 ms-bt -	Bw-29 ms-bt -	Bw-29 ms-bt -	Bw-29 ms-bt -	Bw-29 ms-bt -	Bw-29 ms-bt -	Bw-29 ms-bt -	Bw-29 ms-bt -	Bw-29 ms-bt -	Bw-29 ms-bt -	Bw-29 ms-bt -	Bw-29 ms-bt -
	Bw29-49 b-type	Bw29-50 b-type	Bw29-88 b-type	Bw29-89 b-type	Bw29-94 b-type	Bw29-102 b-type	Bw29-103 b-type	Bw29-111 b-type	Bw29-112 b-type	Bw29-113 b-type	Bw29-129 b-type	Bw29-149 b-type	Bw29-174 b-type
wt%													
SiO ₂	42.48	40.03	43.92	44.76	42.02	43.95	44.51	44.51	43.54	41.70	43.48	44.41	43.14
TiO ₂	0.03	0.00	0.03	0.40	0.03	0.04	0.00	0.38	0.71	0.03	0.05	0.04	0.04
Al ₂ O ₃	29.70	26.83	29.18	30.04	28.29	31.08	30.66	29.71	32.53	29.70	30.58	30.43	30.65
FeO**	8.19	12.99	8.57	6.79	11.20	7.30	7.22	6.50	6.47	10.15	8.39	7.88	8.95
MnO	0.09	0.02	0.05	0.01	0.08	0.06	0.02	0.00	0.00	0.08	0.01	0.04	0.02
MgO	2.92	4.79	3.43	2.38	3.74	2.87	2.88	2.42	0.96	3.18	3.07	2.74	3.30
CaO	0.00	0.00	0.00	0.02	0.04	0.00	0.01	0.03	0.04	0.03	0.00	0.01	0.00
Na ₂ O	0.37	0.29	0.42	0.47	0.43	0.48	0.44	0.47	0.53	0.51	0.45	0.35	0.34
K ₂ O	9.83	9.63	9.62	9.70	9.10	9.32	9.37	9.63	9.31	8.41	9.39	8.82	9.45
Total	93.60	94.58	95.24	94.62	94.91	95.09	95.12	93.64	94.17	93.79	95.43	94.71	95.88
cation basi							22 O						
Si	6.01	5.80	6.10	6.19	5.95	6.05	6.12	6.21	6.02	5.91	6.01	6.13	5.96
Al ^{IV}	1.99	2.20	1.90	1.81	2.05	1.95	1.88	1.79	1.98	2.09	1.99	1.87	2.04
$\sum IV$	8.00	8.00	8.00	8.00	8.00	8.00	8.00	8.00	8.00	8.00	8.00	8.00	8.00
Al ^{VI}	2.97	2.37	2.88	3.08	2.67	3.10	3.09	3.09	3.33	2.88	3.00	3.08	2.95
Ti	0.00	0.00	0.00	0.04	0.00	0.00	0.00	0.04	0.07	0.00	0.01	0.00	0.00
Fe*	0.97	1.57	1.00	0.78	1.33	0.84	0.83	0.76	0.75	1.20	0.97	0.91	1.03
Mn	0.01	0.00	0.01	0.00	0.01	0.01	0.00	0.00	0.00	0.01	0.00	0.00	0.00
Mg	0.62	1.03	0.71	0.49	0.79	0.59	0.59	0.50	0.20	0.67	0.63	0.56	0.68
$\sum VI$	4.57	4.98	4.60	4.40	4.80	4.54	4.51	4.39	4.35	4.77	4.60	4.56	4.67
Ca	0.00	0.00	0.00	0.00	0.01	0.00	0.00	0.00	0.01	0.00	0.00	0.00	0.00
Na	0.10	0.08	0.11	0.13	0.12	0.13	0.12	0.13	0.14	0.14	0.12	0.09	0.09
K	1.78	1.78	1.70	1.71	1.64	1.64	1.64	1.71	1.64	1.52	1.66	1.55	1.66
$\sum X$	1.88	1.86	1.82	1.84	1.77	1.76	1.76	1.84	1.79	1.67	1.77	1.65	1.75
$\sum cations$	14.44	14.84	14.41	14.24	14.57	14.30	14.28	14.23	14.14	14.43	14.38	14.21	14.42
X _{Mg}	0.39	0.40	0.42	0.38	0.37	0.41	0.42	0.40	0.21	0.36	0.39	0.38	0.40

Table I-65

sample phase core/rim* number text. pos	Bw-3 chl-ms -	Bw-3 chl-ms -	Bw-3 chl-ms -	Bw-3 chl-ms -	Bw-3 chl-ms -	Bw-3 chl-ms -	Bw-3 chl-ms -	Bw-3 chl-ms -	Bw-3 chl-ms -	Bw-3 chl-ms -	Bw-3 chl-ms -	Bw-3 chl-ms -	Bw-3 chl-ms -
	Bw3-111	Bw3-23	Bw3-22	Bw3-280	Bw3-285	Bw3-323	Bw3-292	Bw3-335	Bw3-410	Bw3-273	Bw3-294	Bw3-311	Bw3-398
wt%													
SiO ₂	44.11	42.38	43.86	43.98	39.45	44.89	44.02	44.73	42.14	48.40	44.38	41.02	44.77
TiO ₂	0.03	0.00	0.00	0.01	0.01	0.00	0.03	0.02	0.00	0.12	0.39	0.02	0.05
Al ₂ O ₃	30.70	30.32	29.99	31.36	29.43	34.43	30.93	32.81	31.04	34.66	34.79	27.59	34.50
FeO**	6.17	6.89	7.31	7.01	9.77	3.17	6.53	6.11	7.09	2.88	3.32	10.39	3.48
MnO	0.10	0.13	0.23	0.09	0.14	0.09	0.09	0.08	0.07	0.05	0.03	0.10	0.04
MgO	3.84	4.24	5.67	4.42	6.94	2.26	4.33	3.75	4.11	2.31	1.59	6.48	2.15
CaO	0.33	0.40	0.48	0.45	0.49	0.00	0.39	0.58	0.30	0.52	0.08	0.07	0.11
Na ₂ O	0.07	0.06	0.24	0.10	0.06	0.58	0.11	0.17	0.10	0.44	0.04	0.28	0.36
K ₂ O	5.48	4.51	2.67	4.18	2.00	9.94	4.50	4.68	4.02	6.86	1.52	7.99	7.65
Total	90.82	88.94	90.46	91.60	88.33	95.37	90.92	92.93	88.87	96.24	86.16	93.93	93.09
cation basi							22 O						
Si	6.17	6.06	6.11	6.08	5.73	6.04	6.12	6.07	6.01	6.28	6.21	5.83	6.08
Al ^{IV}	1.83	1.94	1.89	1.92	2.27	1.96	1.88	1.93	1.99	1.72	1.79	2.17	1.92
$\sum IV$	8.00	8.00	8.00	8.00	8.00	8.00	8.00	8.00	8.00	8.00	8.00	8.00	8.00
Al ^{VI}	3.22	3.17	3.03	3.19	2.77	3.49	3.20	3.32	3.23	3.58	3.96	2.46	3.59
Ti	0.00	0.00	0.00	0.00	0.00	0.00	0.00	0.00	0.00	0.01	0.04	0.00	0.01
Fe*	0.72	0.82	0.85	0.81	1.19	0.36	0.76	0.69	0.84	0.31	0.39	1.24	0.39
Mn	0.01	0.02	0.03	0.01	0.02	0.01	0.01	0.01	0.01	0.01	0.00	0.01	0.00
Mg	0.80	0.90	1.18	0.91	1.50	0.45	0.90	0.76	0.87	0.45	0.33	1.37	0.44
$\sum VI$	4.76	4.91	5.09	4.92	5.48	4.31	4.87	4.79	4.96	4.36	4.72	5.08	4.43
Ca	0.05	0.06	0.07	0.07	0.08	0.00	0.06	0.08	0.05	0.07	0.01	0.01	0.02
Na	0.02	0.02	0.06	0.03	0.02	0.15	0.03	0.05	0.03	0.11	0.01	0.08	0.09
K	0.98	0.82	0.47	0.74	0.37	1.71	0.80	0.81	0.73	1.14	0.27	1.45	1.32
$\sum X$	1.05	0.90	0.61	0.83	0.46	1.86	0.89	0.94	0.80	1.32	0.29	1.54	1.43
$\sum cations$	13.80	13.81	13.70	13.75	13.94	14.17	13.75	13.73	13.76	13.68	13.02	14.61	13.87
X _{Mg}	0.53	0.52	0.58	0.53	0.56	0.56	0.54	0.52	0.51	0.59	0.46	0.53	0.52

Table I-66

sample phase core/rim* number text. pos	To-2 ms-bt	To-2 ms-bt	To-2 ms-bt	To-2 ms-bt	To-2 ms-bt	To-2 ms-bt	To-2 ms-bt	To-2 ms-bt	To-2 ms-bt	To-2 ms-bt	To-2 ms-bt	To-2 ms-bt	To-2 ms-bt
	To2-412	To2-413	To2-421	To2-422	To2-433	To2-441	To2-442	To2-443	To2-445	To2-447	To2-448	To2-411	To2-444
wt%													
SiO ₂	43.28	42.21	47.75	41.47	45.82	45.01	43.42	42.85	46.18	41.22	42.17	38.10	44.16
TiO ₂	0.01	0.00	0.03	0.00	0.05	0.04	0.02	0.00	0.00	0.00	0.01	0.01	0.01
Al ₂ O ₃	29.18	29.02	29.15	28.23	29.92	29.45	29.25	29.24	31.13	32.32	28.72	25.06	29.69
FeO**	7.17	8.76	6.00	8.80	5.43	7.54	9.34	8.76	3.71	6.41	7.71	14.33	6.57
MnO	0.11	0.20	0.09	0.22	0.11	0.18	0.19	0.24	0.03	0.26	0.17	0.31	0.18
MgO	4.48	5.55	3.38	5.96	4.25	4.59	5.59	5.28	3.04	4.61	5.94	9.10	4.67
CaO	0.06	0.05	0.35	0.02	0.05	0.49	0.46	0.57	0.02	0.00	0.00	0.05	0.02
Na ₂ O	0.15	0.13	0.09	0.11	0.12	0.10	0.05	0.10	0.16	0.48	0.19	0.09	0.12
K ₂ O	9.66	9.36	7.79	9.51	10.01	5.59	4.66	4.81	9.70	6.25	10.02	6.67	9.63
Total	94.12	95.32	94.65	94.33	95.80	92.99	92.97	91.86	93.99	91.58	94.94	93.74	95.04
cation basi													
Si	6.05	5.89	6.46	5.87	6.22	6.20	6.03	6.02	6.29	5.80	5.90	5.56	6.08
Al ^{IV}	1.95	2.11	1.54	2.13	1.78	1.80	1.97	1.98	1.71	2.20	2.10	2.44	1.92
∑ IV	8.00	8.00	8.00	8.00	8.00	8.00	8.00	8.00	8.00	8.00	8.00	8.00	8.00
Al ^{VI}	2.86	2.66	3.11	2.58	3.00	2.99	2.82	2.86	3.30	3.15	2.64	1.87	2.90
Ti	0.00	0.00	0.00	0.00	0.01	0.00	0.00	0.00	0.00	0.00	0.00	0.00	0.00
Fe*	0.84	1.02	0.68	1.04	0.62	0.87	1.08	1.03	0.42	0.75	0.90	1.75	0.76
Mn	0.01	0.02	0.01	0.03	0.01	0.02	0.02	0.03	0.00	0.03	0.02	0.04	0.02
Mg	0.93	1.16	0.68	1.26	0.86	0.94	1.16	1.11	0.62	0.97	1.24	1.98	0.96
∑ VI	4.65	4.86	4.48	4.90	4.50	4.82	5.08	5.03	4.34	4.90	4.81	5.64	4.64
Ca	0.01	0.01	0.05	0.00	0.01	0.07	0.07	0.09	0.00	0.00	0.00	0.01	0.00
Na	0.04	0.03	0.02	0.03	0.03	0.03	0.01	0.03	0.04	0.13	0.05	0.03	0.03
K	1.72	1.67	1.34	1.72	1.73	0.98	0.83	0.86	1.69	1.12	1.79	1.24	1.69
∑ X	1.77	1.71	1.42	1.75	1.77	1.08	0.91	0.98	1.73	1.25	1.84	1.28	1.73
∑ cations	14.42	14.57	13.90	14.65	14.27	13.91	13.99	14.00	14.07	14.15	14.65	14.92	14.37
X _{Mg}	0.53	0.53	0.50	0.55	0.58	0.52	0.52	0.52	0.59	0.56	0.58	0.53	0.56

Table I-67

sample phase core/rim* number text. pos	We-9 chl-ms	We-9 chl-ms	We-9 chl-ms	We-9 chl-ms	We-9 chl-ms	We-9 chl-ms	We-9	We-9	We-9	We-9	We-9	We-9	We-9
	We9-171 chl-ms pi	We9-172 chl-ms pi	We9-173 chl-ms pi	We9-174 chl-ms pi	We9-260 chl-ms pi	We9-265 chl-ms pi	We9-54	We9-101	We9-87	We9-54	We9-101	We9-87	We9-54
wt%													
SiO ₂	42.33	46.48	45.00	46.40	47.85	43.61	32.83	29.52	28.44	32.83	29.52	28.44	32.83
TiO ₂	0.02	0.01	0.03	0.00	0.11	0.07	0.01	0.00	0.01	0.01	0.00	0.01	0.01
Al ₂ O ₃	29.03	31.55	30.52	31.57	34.67	29.64	24.21	23.23	21.64	24.21	23.23	21.64	24.21
FeO**	11.21	4.83	8.18	4.93	1.45	6.87	18.10	20.67	20.79	18.10	20.67	20.79	18.10
MnO	0.23	0.10	0.17	0.13	0.06	0.17	0.42	0.52	0.57	0.42	0.52	0.57	0.42
MgO	7.00	2.84	5.05	2.81	0.71	4.57	11.44	12.69	14.94	11.44	12.69	14.94	11.44
CaO	0.04	0.09	0.07	0.11	0.01	0.03	0.12	0.06	0.00	0.12	0.06	0.00	0.12
Na ₂ O	1.45	0.12	1.72	0.15	0.41	0.20	0.31	0.09	0.06	0.31	0.09	0.06	0.31
K ₂ O	3.73	6.84	2.15	7.28	4.26	7.50	1.02	1.25	1.08	1.02	1.25	1.08	1.02
Total	95.10	92.89	92.89	93.40	89.55	92.66	88.46	88.04	87.58	88.46	88.04	87.58	88.46
cation basi													
Si	5.83	6.32	6.13	6.30	6.47	6.09	5.08	4.72	4.60	5.08	4.72	4.60	5.08
Al ^{IV}	2.17	1.68	1.87	1.70	1.53	1.91	2.92	3.28	3.40	2.92	3.28	3.40	2.92
∑ IV	8.00	8.00	8.00	8.00	8.00	8.00	8.00	8.00	8.00	8.00	8.00	8.00	8.00
Al ^{VI}	2.53	3.38	3.02	3.36	4.00	2.98	1.50	1.09	0.72	1.50	1.09	0.72	1.50
Ti	0.00	0.00	0.00	0.00	0.01	0.01	0.00	0.00	0.00	0.00	0.00	0.00	0.00
Fe*	1.29	0.55	0.93	0.56	0.16	0.80	2.34	2.76	2.81	2.34	2.76	2.81	2.34
Mn	0.03	0.01	0.02	0.02	0.01	0.02	0.05	0.07	0.08	0.05	0.07	0.08	0.05
Mg	1.44	0.58	1.02	0.57	0.14	0.95	2.64	3.02	3.60	2.64	3.02	3.60	2.64
∑ VI	5.29	4.52	5.00	4.50	4.33	4.76	6.54	6.95	7.22	6.54	6.95	7.22	6.54
Ca	0.01	0.01	0.01	0.02	0.00	0.01	0.02	0.01	0.00	0.02	0.01	0.00	0.02
Na	0.39	0.03	0.45	0.04	0.11	0.05	0.09	0.03	0.02	0.09	0.03	0.02	0.09
K	0.66	1.19	0.37	1.26	0.74	1.34	0.20	0.25	0.22	0.20	0.25	0.22	0.20
∑ X	1.05	1.23	0.84	1.32	0.85	1.40	0.31	0.29	0.24	0.31	0.29	0.24	0.31
∑ cations	14.34	13.75	13.84	13.82	13.17	14.15	14.85	15.24	15.46	14.85	15.24	15.46	14.85
X _{Mg}	0.53	0.51	0.52	0.50	0.47	0.54	0.53	0.52	0.56	0.53	0.52	0.56	0.53

Table I-68

sample phase core/rim* number text. pos	Bw-29 crd core Bw29-10	Bw-29 crd core Bw29-13	Bw-29 crd core Bw29-21	Bw-29 crd core Bw29-22	Bw-29 crd rim Bw29-34	Bw-29 crd rim Bw29-41	Bw-3 crd rim Bw3a1-7	Bw-3 crd core Bw3a1-8	Bw-3 crd core Bw3a1-11	Bw-3 crd core Bw3a1-12	Bw-3 crd rim Bw3a1-19	Bw-3 crd rim Bw3a1-30	Bw-3 crd rim Bw3a1-76
wt.% oxides													
SiO ₂	47.06	47.09	47.06	47.01	47.04	47.30	47.80	47.85	47.71	48.00	47.51	48.18	47.68
TiO ₂	b. d.	b. d.	b. d.	b. d.	b. d.	b. d.	b. d.	b. d.	b. d.	b. d.	b. d.	b. d.	b. d.
Al ₂ O ₃	31.77	31.51	31.67	31.58	31.42	31.78	31.76	32.23	31.62	32.17	31.97	32.16	32.11
FeO**	13.45	12.99	13.04	13.32	13.04	12.45	9.49	9.84	9.63	9.87	9.84	9.66	9.54
MnO	0.21	0.33	0.35	0.34	0.23	0.43	0.39	0.26	0.24	0.25	0.28	0.22	0.54
MgO	5.19	5.26	5.39	5.37	5.50	5.59	7.23	7.12	7.18	7.06	7.10	7.28	7.28
CaO	b. d.	b. d.	b. d.	b. d.	b. d.	b. d.	b. d.	b. d.	b. d.	b. d.	b. d.	b. d.	b. d.
Na ₂ O	0.13	0.15	0.13	0.14	0.16	0.10	0.35	0.36	0.33	0.31	0.37	0.34	0.38
K ₂ O	0.00	0.03	0.02	0.02	0.00	0.05	0.03	0.01	0.01	0.02	0.02	0.02	0.35
Total	97.89	97.36	97.68	97.80	97.41	97.76	97.05	97.70	96.73	97.69	97.12	97.94	97.94
cation basis							18 O						
Si	4.99	5.01	5.00	4.99	5.01	5.01	5.03	5.00	5.03	5.02	5.00	5.02	4.99
Al ^{IV}	3.97	3.95	3.96	3.95	3.94	3.96	3.94	3.97	3.93	3.96	3.97	3.95	3.96
∑ IV	8.97	8.97	8.96	8.95	8.95	8.97	8.96	8.98	8.97	8.98	8.97	8.97	8.95
Al ^{VI}	-	-	-	-	-	-	-	-	-	-	-	-	-
Fe*	1.19	1.16	1.16	1.18	1.16	1.10	0.83	0.86	0.85	0.86	0.87	0.84	0.83
Mn	0.02	0.03	0.03	0.03	0.02	0.04	0.03	0.02	0.02	0.02	0.02	0.02	0.05
Mg	0.82	0.84	0.85	0.85	0.87	0.88	1.13	1.11	1.13	1.10	1.11	1.13	1.14
∑ VI	2.04	2.02	2.04	2.06	2.05	2.02	2.00	1.99	2.00	1.98	2.01	1.99	2.02
Ca	-	-	-	-	-	-	-	-	-	-	-	-	-
Na	0.03	0.03	0.03	0.03	0.03	0.02	0.07	0.07	0.07	0.06	0.07	0.07	0.08
K	0.00	0.00	0.00	0.00	0.00	0.01	0.00	0.00	0.00	0.00	0.00	0.00	0.05
∑ X	0.03	0.04	0.03	0.03	0.03	0.03	0.08	0.07	0.07	0.07	0.08	0.07	0.12
∑ cations	11.03	11.03	11.03	11.05	11.04	11.02	11.04	11.05	11.03	11.03	11.05	11.04	11.09
X _{Mg}	0.41	0.42	0.42	0.42	0.43	0.44	0.58	0.56	0.57	0.56	0.56	0.57	0.58

Table I-69

sample phase core/rim* number text. pos	Bw-8 crd core Bw8-4	Bw-8 crd core Bw8-5	Bw-8 crd core Bw8-6	Bw-8 crd rim Bw8-7	Bw-8 crd rim Bw8-8	Bw-8 crd rim Bw8-9	Ho-10 crd core Ho10-5	Ho-10 crd core Ho10-8	Ho-10 crd core Ho10-9	Ho-10 crd rim Ho10-10	Ho-10 crd rim Ho10-13	Ho-10 crd rim Ho10-14	Ho-10 crd rim Ho10-15
wt.% oxide													
SiO ₂	47.84	47.69	47.41	47.45	48.23	48.28	47.55	47.36	47.97	47.72	47.88	47.76	47.29
TiO ₂	b. d.	b. d.	b. d.	b. d.	b. d.	b. d.	0.00	0.01	0.02	0.00	0.02	0.00	0.00
Al ₂ O ₃	32.11	31.89	31.80	31.92	32.25	32.16	32.06	32.29	31.58	31.46	31.78	31.85	32.10
FeO**	10.09	10.41	10.60	10.41	10.12	10.43	9.58	9.49	9.50	9.32	9.61	9.19	9.54
MnO	0.33	0.31	0.25	0.25	0.28	0.28	0.35	0.31	0.22	0.30	0.25	0.39	0.29
MgO	7.11	7.20	7.02	6.82	7.06	7.09	7.71	7.58	7.77	7.76	7.70	7.68	7.70
CaO	b. d.	b. d.	b. d.	b. d.	b. d.	b. d.	0.02	0.02	0.02	0.01	0.00	0.03	0.03
Na ₂ O	0.23	0.19	0.19	0.23	0.18	0.19	0.25	0.25	0.25	0.25	0.28	0.29	0.29
K ₂ O	0.01	0.01	0.02	0.00	0.01	0.02	0.01	0.00	0.03	0.00	0.03	0.00	0.00
Total	97.74	97.73	97.29	97.14	98.16	98.45	97.52	97.31	97.37	96.82	97.54	97.18	97.24
							2.48	2.69	2.63	3.18	2.46	2.82	2.76
cation basi							18 O						
Si	5.01	5.00	5.00	5.00	5.02	5.02	4.98	4.97	5.03	5.03	5.01	5.01	4.97
Al ^{IV}	3.96	3.94	3.95	3.97	3.96	3.94	3.96	3.99	3.90	3.90	3.92	3.94	3.97
∑ IV	8.97	8.94	8.95	8.97	8.98	8.96	8.94	8.96	8.93	8.93	8.93	8.95	8.94
Al ^{VI}	-	-	-	-	-	-	-	-	-	-	-	-	-
Fe*	0.88	0.91	0.93	0.92	0.88	0.91	0.84	0.83	0.83	0.82	0.84	0.81	0.84
Mn	0.03	0.03	0.02	0.02	0.02	0.02	0.03	0.03	0.02	0.03	0.02	0.03	0.03
Mg	1.11	1.13	1.10	1.07	1.10	1.10	1.20	1.19	1.21	1.22	1.20	1.20	1.21
∑ VI	2.02	2.07	2.06	2.01	2.00	2.03	2.07	2.05	2.07	2.07	2.07	2.04	2.07
Ca	-	-	-	-	-	-	-	-	-	-	-	-	-
Na	0.05	0.04	0.04	0.05	0.04	0.04	0.05	0.05	0.05	0.05	0.06	0.06	0.06
K	0.00	0.00	0.00	0.00	0.00	0.00	0.00	0.00	0.00	0.00	0.00	0.00	0.00
∑ X	0.05	0.04	0.04	0.05	0.04	0.04	0.05	0.05	0.05	0.05	0.06	0.06	0.06
∑ cations	11.04	11.05	11.05	11.03	11.02	11.03	11.07	11.06	11.05	11.05	11.06	11.05	11.07
X _{Mg}	0.56	0.55	0.54	0.54	0.55	0.55	0.59	0.59	0.59	0.60	0.59	0.60	0.59

Table I-70

sample phase core/rim*	Ho-12 crd	Ho-12 crd	Ho-12 crd	Ho-12 crd	Ho-12 crd	Ho-12 crd	Ho-12 crd	Ho-12 crd	Wa-4 crd	Wa-4 crd	Wa-4 crd	Wa-4 crd	Wa-4 crd	Wa-4 crd
number	Ho12C1-1	Ho12C1-2	Ho12C-10	Ho12C-11	Ho12C-25	Ho12C-34	Ho12-215	Ho12-215	Wa4crd3-9	Wa4cd3-10	Wa4cd3-11	Wa4cd3-38	Wa4cd3-39	Wa4bt4-69
text. pos	-	-	-	-	-	-	-	-	-	-	-	-	-	-
wt.% oxide														
SiO ₂	47.70	47.51	46.98	47.87	48.18	47.61	47.79	47.79	48.26	48.17	47.72	47.36	47.80	47.87
TiO ₂	0.02	0.00	0.00	0.00	0.01	0.01	0.03	0.03	b. d.	b. d.	b. d.	b. d.	b. d.	b. d.
Al ₂ O ₃	32.57	32.13	32.62	31.98	32.36	32.62	31.88	32.07	32.11	31.84	31.55	31.54	31.54	31.86
FeO**	10.05	10.51	10.23	10.14	10.36	10.03	10.27	10.95	10.94	11.03	11.01	11.23	11.23	11.29
MnO	0.38	0.36	0.45	0.41	0.44	0.40	0.36	0.36	0.30	0.33	0.39	0.37	0.37	0.37
MgO	7.04	6.89	6.65	7.19	7.16	7.14	6.86	6.47	6.71	6.60	6.37	6.51	6.51	6.53
CaO	0.01	0.02	0.06	0.02	0.00	0.02	0.00	b. d.	b. d.	b. d.	b. d.	b. d.	b. d.	b. d.
Na ₂ O	0.11	0.20	0.21	0.36	0.20	0.21	0.28	0.13	0.14	0.14	0.15	0.15	0.15	0.15
K ₂ O	0.02	0.06	0.14	0.11	0.00	0.02	0.01	0.02	0.06	0.03	0.05	0.05	0.05	0.05
Total	97.93	97.68	97.33	98.11	98.70	98.08	97.48	98.32	98.47	97.71	96.90	97.69	97.69	98.14
cation basi														
Si	4.98	4.99	4.95	5.00	5.00	4.97	5.02	5.04	5.02	5.02	5.02	5.03	5.03	5.02
Al ^{IV}	4.01	3.98	4.05	3.94	3.96	4.01	3.95	3.94	3.94	3.94	3.94	3.94	3.91	3.94
∑ IV	8.99	8.96	9.00	8.94	8.96	8.98	8.97	8.98	8.96	8.96	8.96	8.97	8.94	8.95
Al ^{VI}	-	-	-	-	-	-	-	-	-	-	-	-	-	-
Fe*	0.88	0.92	0.90	0.89	0.90	0.88	0.90	0.96	0.95	0.97	0.98	0.99	0.99	0.99
Mn	0.03	0.03	0.04	0.04	0.04	0.04	0.03	0.03	0.03	0.03	0.03	0.03	0.03	0.03
Mg	1.10	1.08	1.04	1.12	1.11	1.11	1.07	1.01	1.04	1.03	1.01	1.02	1.02	1.02
∑ VI	2.01	2.03	1.99	2.04	2.05	2.02	2.01	1.99	2.02	2.03	2.02	2.04	2.04	2.04
Ca	-	-	-	-	-	-	-	-	-	-	-	-	-	-
Na	0.02	0.04	0.04	0.07	0.04	0.04	0.06	0.03	0.03	0.03	0.03	0.03	0.03	0.03
K	0.00	0.01	0.02	0.01	0.00	0.00	0.00	0.00	0.01	0.00	0.01	0.01	0.01	0.01
∑ X	0.03	0.05	0.07	0.09	0.04	0.05	0.06	0.03	0.04	0.04	0.04	0.04	0.04	0.04
∑ cations	11.03	11.05	11.05	11.07	11.04	11.05	11.03	11.01	11.03	11.03	11.03	11.02	11.03	11.03
X _{Mg}	0.56	0.54	0.54	0.56	0.55	0.56	0.54	0.51	0.52	0.52	0.51	0.51	0.51	0.51

Table I-71

sample phase core/rim*	Wa-4 crd	We-9 crd	We-9 crd	We-9 crd	We-9 crd	We-9 crd	We-9 crd	We-9 crd
number	Wa4cd8-81	We9cd1-2	We9cd1-3	We9cd1-4	We9cd1-18	We9cd1-22	We9cd1-23	We9cd1-28
text. pos	-	-	-	-	-	-	-	-
wt.% oxide								
SiO ₂	47.99	47.72	48.23	47.88	49.30	47.98	47.50	47.81
TiO ₂	b. d.	b. d.	b. d.	b. d.	b. d.	b. d.	b. d.	b. d.
Al ₂ O ₃	32.25	32.29	32.31	32.40	31.63	31.88	32.30	32.19
FeO**	11.79	9.80	10.09	9.46	10.05	9.83	10.14	10.08
MnO	0.32	0.40	0.35	0.32	0.34	0.31	0.38	0.37
MgO	6.33	7.10	7.17	7.19	6.89	7.25	7.18	7.38
CaO	b. d.	0.05	0.01	0.03	0.05	0.04	0.04	0.04
Na ₂ O	0.12	0.13	0.08	0.16	0.15	0.16	0.18	0.17
K ₂ O	0.01	0.01	0.00	0.00	0.06	0.01	0.03	0.00
Total	98.83	97.53	98.29	97.45	98.49	97.47	97.77	98.04
cation basi								
Si	5.00	5.00	5.01	5.01	5.11	5.03	4.97	4.99
Al ^{IV}	3.96	3.99	3.96	3.99	3.86	3.94	3.99	3.96
∑ IV	8.96	8.98	8.97	9.00	8.97	8.96	8.96	8.95
Al ^{VI}	-	-	-	-	-	-	-	-
Fe*	1.03	0.86	0.88	0.83	0.87	0.86	0.89	0.88
Mn	0.03	0.04	0.03	0.03	0.03	0.03	0.03	0.03
Mg	0.98	1.11	1.11	1.12	1.06	1.13	1.12	1.15
∑ VI	2.04	2.01	2.02	1.98	1.97	2.02	2.05	2.06
Ca	-	0.01	0.00	0.00	0.01	0.00	0.00	0.00
Na	0.02	0.03	0.02	0.03	0.03	0.03	0.04	0.03
K	0.00	0.00	0.00	0.00	0.01	0.00	0.00	0.00
∑ X	0.03	0.03	0.02	0.04	0.04	0.04	0.04	0.04
∑ cations	11.03	11.02	11.01	11.01	10.98	11.02	11.05	11.05
X _{Mg}	0.49	0.56	0.56	0.58	0.55	0.57	0.56	0.57

Table II-1

number phase text. pos.	E862 illite m-type dioc.	E875 illite m-type di.-trioc.	F114 illite m-type dioc.	F117 smectite m-type di.-trioc.	F125 smectite m-type di.-trioc.	F131 illite m-type dioc.	F135 smectite m-type di.-trioc.	F137 illite m-type di.-trioc.	F359 smectite m-type di.-trioc.	F062 illite m-type dioc.	H12asse smectite m-type dioc.	Ho12afp6 illite m-type di.-trioc.
wt%												
SiO ₂	50.03	47.23	50.80	43.76	40.29	50.60	42.80	50.60	47.90	51.47	54.75	47.33
TiO ₂	0.00	0.00	0.00	0.00	0.00	0.00	0.00	0.00	0.00	0.00	0.00	0.00
Al ₂ O ₃	32.48	29.21	35.09	30.84	26.22	34.31	26.12	31.42	28.24	32.29	31.81	28.92
FeO**	4.79	8.22	1.90	9.67	13.56	2.80	12.74	3.98	10.57	3.52	4.52	9.04
MnO	0.00	0.00	0.00	0.00	0.00	0.00	0.00	0.00	0.00	0.00	0.00	0.00
MgO	2.39	4.68	0.50	9.37	12.65	0.30	10.86	3.29	6.68	1.69	2.69	4.28
CaO	0.00	0.20	0.10	0.10	0.20	0.00	0.40	0.00	0.20	0.20	0.00	0.50
Na ₂ O	0.40	0.70	4.30	1.00	2.20	4.60	1.00	0.80	0.40	0.60	0.30	0.70
K ₂ O	6.30	6.00	4.00	1.50	0.90	3.90	2.10	6.30	2.00	6.80	2.30	5.40
Total	96.39	96.24	96.68	96.24	96.02	96.52	96.02	96.39	96.00	96.58	96.36	96.16
cation base							22 O					
Si	6.44	6.22	6.45	5.70	5.40	6.46	5.70	6.51	6.22	6.60	6.82	6.23
Al ^{IV}	1.56	1.78	1.55	2.30	2.60	1.54	2.30	1.49	1.78	1.40	1.18	1.77
∑ IV	8.00	8.00	8.00	8.00	8.00	8.00	8.00	8.00	8.00	8.00	8.00	8.00
Al ^{VI}	3.37	2.75	3.70	2.43	1.55	3.62	1.81	3.28	2.54	3.47	3.49	2.72
Fe*	0.46	0.81	0.18	0.95	1.37	0.27	1.28	0.39	1.03	0.34	0.42	0.90
Mn	-	-	-	-	-	-	-	-	-	-	-	-
Mg	0.46	0.92	0.09	1.82	2.53	0.06	2.16	0.63	1.29	0.32	0.50	0.84
∑ VI	4.29	4.49	3.97	5.20	5.45	3.94	5.24	4.29	4.86	4.14	4.41	4.46
Ca	0.00	0.03	0.01	0.01	0.03	0.00	0.06	0.00	0.03	0.03	0.00	0.07
Na	0.10	0.18	1.06	0.25	0.57	1.14	0.26	0.20	0.10	0.15	0.07	0.18
K	1.03	1.01	0.65	0.25	0.15	0.63	0.36	1.03	0.33	1.11	0.37	0.91
∑ X	1.13	1.21	1.72	0.52	0.75	1.77	0.67	1.23	0.46	1.29	0.44	1.16
∑ cations	13.43	13.70	13.69	13.71	14.20	13.72	13.91	13.53	13.32	13.43	12.85	13.62
X _{Mg}	0.50	0.53	0.34	0.66	0.65	0.17	0.63	0.62	0.56	0.49	0.54	0.48

Table II-1

number phase text. pos.	Ho12ass2 smectite m-type di.-trioc.	Ho12bss1 smectite m-type di.-trioc.	Hp12bss4 smectite m-type di.-trioc.	Ho12bun2 illite m-type di.-trioc.	Ho12bss6 smectite m-type di.-trioc.	Ho12bss7 smectite m-type di.-trioc.	Ho12bss9 smectite m-type di.-trioc.	Ho12bss3 illite m-type di.-trioc.	Ho12bs12 illite m-type dioc.	Ho12bs13 smectite m-type dioc.	Ho12bs14 smectite m-type dioc.	Ho12bs15 illite m-type dioc.
wt%												
SiO ₂	49.74	50.51	45.40	41.64	45.88	44.72	42.22	45.78	46.84	49.74	54.65	49.64
TiO ₂	0.00	0.00	0.00	0.00	0.00	0.00	0.00	0.00	0.00	0.00	0.00	0.00
Al ₂ O ₃	31.81	28.92	28.43	26.12	27.37	31.52	25.06	29.40	27.95	31.13	32.68	28.53
FeO**	6.96	7.59	10.85	15.64	10.94	9.31	16.00	10.75	9.31	6.60	3.07	8.41
MnO	0.00	0.00	0.00	0.00	0.00	0.00	0.00	0.00	0.00	0.00	0.00	0.00
MgO	2.69	5.68	7.37	5.48	7.67	7.87	7.77	4.18	4.88	3.59	2.79	4.28
CaO	0.30	0.10	0.30	0.40	0.20	0.00	0.50	0.20	0.30	0.10	0.10	0.30
Na ₂ O	0.20	3.10	0.60	0.50	0.60	1.10	0.60	0.50	0.60	0.40	0.10	0.40
K ₂ O	4.60	0.30	3.20	6.00	3.40	1.60	3.60	5.30	6.30	4.10	3.00	4.70
Total	96.29	96.19	96.15	95.78	96.06	96.12	95.75	96.12	96.19	95.65	96.39	96.26
cation base								22 O				
Si	6.40	6.44	5.97	5.73	6.05	5.81	5.74	6.07	6.22	6.42	6.80	6.45
Al ^{IV}	1.60	1.56	2.03	2.27	1.95	2.19	2.26	1.93	1.78	1.58	1.20	1.55
∑ IV	8.00	8.00	8.00	8.00	8.00	8.00	8.00	8.00	8.00	8.00	8.00	8.00
Al ^{VI}	3.22	2.79	2.38	1.96	2.30	2.63	1.76	2.66	2.59	3.16	3.59	2.82
Fe*	0.67	0.73	1.07	1.62	1.08	0.91	1.64	1.07	0.93	0.64	0.29	0.82
Mn	-	-	-	-	-	-	-	-	-	-	-	-
Mg	0.52	1.08	1.45	1.12	1.51	1.52	1.58	0.83	0.97	0.69	0.52	0.83
∑ VI	4.41	4.60	4.90	4.70	4.89	5.06	4.97	4.56	4.48	4.49	4.40	4.47
Ca	0.04	0.01	0.04	0.06	0.03	0.00	0.07	0.03	0.04	0.01	0.01	0.04
Na	0.05	0.77	0.15	0.13	0.15	0.28	0.16	0.13	0.15	0.10	0.02	0.10
K	0.75	0.05	0.54	1.05	0.57	0.26	0.62	0.90	1.07	0.68	0.48	0.78
∑ X	0.85	0.83	0.73	1.24	0.75	0.54	0.86	1.05	1.26	0.79	0.51	0.92
∑ cations	13.26	13.43	13.63	13.94	13.65	13.60	13.82	13.61	13.74	13.28	12.91	13.39
X _{Mg}	0.43	0.60	0.57	0.41	0.58	0.63	0.49	0.44	0.51	0.52	0.64	0.50

Table II-1

number	Ho12bs17	Ho12bs18
phase	smectite	smectite
text. pos.	m-type diact.	m-type di.-trioct.
wt%		
SiO ₂	51.95	53.01
TiO ₂	0.00	0.00
Al ₂ O ₃	28.53	31.81
FeO**	8.95	5.96
MnO	0.00	0.00
MgO	3.29	2.99
CaO	0.20	0.00
Na ₂ O	0.40	0.20
K ₂ O	2.70	2.20
Total	96.02	96.17
cation base		
Si	6.66	6.66
Al ^{IV}	1.34	1.34
∑ IV	8.00	8.00
Al ^{VI}	2.97	3.37
Fe*	0.86	0.56
Mn	-	-
Mg	0.63	0.56
∑ VI	4.46	4.50
Ca	0.03	0.00
Na	0.10	0.05
K	0.44	0.35
∑ X	0.57	0.40
∑ cations	13.03	12.90
X _{Mg}	0.42	0.50

Table II-2

number	E889	E857	F110	F064	F074	F080	Ho12aamr	Ho12afa2	Ho12afp3	Ho12afp4	Ho12afp5	Ho12afp7
phase	mixture	mixture	mixture	mixture	mixture	mixture	mixture	mixture	mixture	mixture	mixture	mixture
text. pos.	f-type bulk anal.	f-type bulk anal.	f-type bulk anal.	f-type bulk anal.	f-type bulk anal.	f-type bulk anal.	f-type bulk anal.	f-type bulk anal.	f-type bulk anal.	f-type bulk anal.	f-type bulk anal.	f-type bulk anal.
wt%												
SiO ₂	44.43	47.13	37.69	50.12	50.22	46.17	49.25	45.69	49.16	49.64	50.41	44.82
TiO ₂	0.00	0.00	0.00	0.00	0.00	0.00	0.00	0.00	0.00	0.00	0.00	0.00
Al ₂ O ₃	30.99	38.32	29.11	37.06	37.06	36.12	32.77	36.43	34.86	35.60	36.02	35.07
FeO**	10.85	7.95	20.33	5.51	4.43	9.40	8.41	10.39	7.86	7.50	6.15	12.11
MnO	0.00	0.00	0.00	0.00	0.00	0.00	0.00	0.00	0.00	0.00	0.00	0.00
MgO	9.37	2.79	8.07	1.79	2.09	2.79	2.39	3.19	2.09	3.69	2.19	3.19
CaO	0.20	0.60	0.40	0.30	0.20	0.70	1.10	1.30	1.20	0.80	1.10	1.10
Na ₂ O	0.70	0.20	0.70	0.60	0.30	0.30	0.40	0.50	0.50	0.70	0.80	0.40
K ₂ O	2.20	2.10	1.40	3.90	5.10	3.40	4.40	1.30	3.30	1.00	2.50	1.70
Total	98.74	99.10	97.70	99.29	99.40	98.88	98.72	98.80	98.98	98.92	99.16	98.39
cation base							22 O					
Si	5.68	5.85	5.06	6.19	6.21	5.83	6.23	5.74	6.15	6.12	6.22	5.71
Al ^{IV}	2.32	2.15	2.94	1.81	1.79	2.17	1.77	2.26	1.85	1.88	1.78	2.29
∑ IV	8.00	8.00	8.00	8.00	8.00	8.00	8.00	8.00	8.00	8.00	8.00	8.00
Al ^{VI}	2.35	3.45	1.67	3.59	3.62	3.21	3.12	3.14	3.29	3.30	3.46	2.97
Fe*	1.04	0.74	2.05	0.51	0.41	0.89	0.80	0.98	0.74	0.70	0.57	1.16
Mn	-	-	-	-	-	-	-	-	-	-	-	-
Mg	1.78	0.52	1.62	0.33	0.39	0.53	0.45	0.60	0.39	0.68	0.40	0.61
∑ VI	5.17	4.71	5.34	4.43	4.41	4.63	4.37	4.72	4.42	4.67	4.44	4.74
Ca	0.03	0.08	0.06	0.04	0.03	0.09	0.15	0.18	0.16	0.11	0.15	0.15
Na	0.17	0.05	0.18	0.14	0.07	0.07	0.10	0.12	0.12	0.17	0.19	0.10
K	0.36	0.33	0.24	0.61	0.80	0.55	0.71	0.21	0.53	0.16	0.39	0.28
∑ X	0.56	0.46	0.48	0.80	0.90	0.72	0.96	0.51	0.81	0.43	0.73	0.53
∑ cations	13.73	13.17	13.82	13.23	13.32	13.34	13.33	13.23	13.23	13.10	13.17	13.27
X _{Mg}	0.63	0.41	0.44	0.39	0.48	0.37	0.36	0.38	0.35	0.49	0.41	0.34

Table II-2

number phase text. pos.	Ho12ass1 mixture f-type bulk anal.	Ho12api1 mixture f-type bulk anal.	Ho12bpi2 mixture f-type bulk anal.	Ho12bpi3 mixture f-type bulk anal.	ho12sfp6 mixture f-type bulk anal.	ho12sfp7 mixture f-type bulk anal.	Ho12bun1 mixture f-type bulk anal.	Ho12bpi7 mixture f-type bulk anal.	1-22101 mixture f-type bulk anal.
wt%									
SiO ₂	45.49	48.77	44.72	43.86	50.51	45.69	46.17	43.18	45.40
TiO ₂	0.00	0.00	0.00	0.00	0.00	0.00	0.00	0.00	0.00
Al ₂ O ₃	32.77	35.18	32.35	31.20	36.02	36.85	30.26	28.48	35.70
FeO**	12.47	7.41	9.94	11.75	5.96	10.66	12.47	13.83	10.57
MnO	0.00	0.00	0.00	0.00	0.00	0.00	0.00	0.00	0.00
MgO	6.28	2.39	7.77	7.77	2.49	3.19	5.08	7.97	3.59
CaO	0.40	1.20	0.50	0.60	1.10	1.00	0.00	2.40	1.00
Na ₂ O	0.50	0.80	0.80	0.80	0.70	0.20	0.00	0.70	0.50
K ₂ O	0.70	3.30	2.50	2.50	2.20	1.20	4.20	1.70	1.90
Total	98.61	99.05	98.59	98.48	98.98	98.79	98.18	98.26	98.66
cation base								22 O	
Si	5.76	6.10	5.71	5.65	6.23	5.73	5.97	5.64	5.74
Al ^{IV}	2.24	1.90	2.29	2.35	1.77	2.27	2.03	2.36	2.26
∑ IV	8.00	8.00	8.00	8.00	8.00	8.00	8.00	8.00	8.00
Al ^{VI}	2.65	3.29	2.58	2.39	3.46	3.18	2.58	2.02	3.06
Fe*	1.19	0.70	0.95	1.14	0.55	1.01	1.21	1.36	1.01
Mn	-	-	-	-	-	-	-	-	-
Mg	1.19	0.45	1.48	1.49	0.46	0.60	0.98	1.55	0.68
∑ VI	5.03	4.43	5.01	5.02	4.47	4.78	4.77	4.93	4.74
Ca	0.05	0.16	0.07	0.08	0.15	0.13	0.00	0.34	0.14
Na	0.12	0.19	0.20	0.20	0.17	0.05	0.00	0.18	0.12
K	0.11	0.53	0.41	0.41	0.35	0.19	0.69	0.28	0.31
∑ X	0.29	0.88	0.67	0.69	0.66	0.38	0.69	0.80	0.56
∑ cations	13.32	13.32	13.68	13.72	13.13	13.16	13.47	13.72	13.31
X _{Mg}	0.50	0.39	0.61	0.57	0.45	0.37	0.45	0.53	0.40

Table II-3

number phase text. pos.	E888 chl	F121 chl	F127 chl	E888 chl	F121 chl	F127 chl
wt%						
SiO ₂	29.80	33.90	32.10	28.72	32.68	30.94
TiO ₂	0.00	0.00	0.00	0.00	0.00	0.00
Al ₂ O ₃	23.90	24.50	23.70	25.02	25.65	24.81
FeO**	23.50	22.60	21.90	21.24	20.43	19.79
MnO	0.00	0.00	0.00	0.00	0.00	0.00
MgO	22.20	18.00	21.00	22.12	17.93	20.92
CaO	0.10	0.10	0.10	0.10	0.10	0.10
Na ₂ O	0.40	0.60	0.80	0.40	0.40	0.40
K ₂ O	0.20	0.30	0.40	0.20	0.20	0.20
Total	100.10	100.00	100.00	97.80	97.39	97.17
cation base				28 O		
Si	6.02	5.73	7.82	5.90	5.62	5.62
Al ^{IV}	1.98	2.27	0.18	2.10	2.38	2.38
∑ IV	8.00	8.00	8.00	8.00	8.00	8.00
Al ^{VI}	3.54	3.35	3.27	3.25	3.08	3.01
Fe*	3.14	2.72	6.21	3.35	2.93	2.93
Mn	0.00	0.00	0.00	0.00	0.00	0.00
Mg	5.97	4.76	5.59	6.03	4.83	5.67
∑ VI	11.97	11.26	11.57	11.93	11.26	11.61
Ca	0.02	0.02	0.02	0.02	0.02	0.02
Na	0.14	0.21	0.28	0.14	0.14	0.14
K	0.05	0.07	0.09	0.05	0.05	0.05
∑ X	0.21	0.29	0.39	0.21	0.21	0.21
∑ cations	20.18	19.56	19.96	20.14	19.47	19.82
X _{Mg}	0.63	0.59	0.63	0.65	0.61	0.65

Table II-4

number phase text. pos.	Ho12acd1 crd	Ho12acd2 crd	Ho12acd3 crd	Ho12acof crd	Ho12acd1 crd	Ho12acd2 crd	Ho12acd3 crd	Ho12acof crd
wt%								
SiO ₂	49.10	49.90	48.80	50.20	47.33	48.10	47.04	48.39
TiO ₂	0.00	0.00	0.00	0.00	0.00	0.00	0.00	0.00
Al ₂ O ₃	29.50	30.70	30.40	32.70	30.89	32.14	31.83	34.24
FeO ⁺⁺	10.90	12.20	12.50	9.70	9.85	11.03	11.30	8.77
MnO	0.40	0.50	0.60	0.50	0.32	0.40	0.48	0.40
MgO	7.80	6.80	7.70	5.70	7.77	6.78	7.67	5.68
CaO	0.00	0.00	0.00	0.00	0.00	0.00	0.00	0.00
Na ₂ O	0.00	0.00	0.00	0.50	0.00	0.00	0.00	0.50
K ₂ O	0.00	0.00	0.00	0.30	0.00	0.00	0.00	0.30
Total	97.70	100.10	100.00	99.60	96.15	98.44	98.31	98.26
cation base					18 O			
Si	5.16	5.14	5.05	5.14	5.03	5.01	4.93	5.00
Al ^{IV}	3.65	3.72	3.71	3.86	3.87	3.95	3.93	4.00
Σ IV	<i>8.81</i>	<i>8.86</i>	<i>8.77</i>	<i>9.00</i>	<i>8.90</i>	<i>8.96</i>	<i>8.87</i>	<i>9.00</i>
Al ^{VI}	-	-	-	-	-	-	-	-
Fe ⁺	0.96	1.05	1.08	0.83	0.88	0.96	0.99	0.76
Mn	0.04	0.04	0.05	0.04	0.03	0.04	0.04	0.03
Mg	1.22	1.04	1.19	0.87	1.23	1.05	1.20	0.88
Σ VI	<i>2.21</i>	<i>2.14</i>	<i>2.32</i>	<i>1.74</i>	<i>2.14</i>	<i>2.05</i>	<i>2.23</i>	<i>1.67</i>
Ca	0.00	0.00	0.00	0.00	0.00	0.00	0.00	0.00
Na	0.00	0.00	0.00	0.10	0.00	0.00	0.00	0.10
K	0.00	0.00	0.00	0.04	0.00	0.00	0.00	0.04
Σ X	<i>0.00</i>	<i>0.00</i>	<i>0.00</i>	<i>0.14</i>	<i>0.00</i>	<i>0.00</i>	<i>0.00</i>	<i>0.14</i>
Σ cations	<i>11.02</i>	<i>11.00</i>	<i>11.09</i>	<i>11.02</i>	<i>11.04</i>	<i>11.01</i>	<i>11.10</i>	<i>10.95</i>
X _{Mg}	0.56	0.50	0.52	0.51	0.58	0.52	0.55	0.54

Cordierite intra-grain spectra - Bw-3

Table III-1a

Number	CO ₂	CO ₂	H ₂ O I	H ₂ O I	H ₂ O II	H ₂ O II	CO ₂	H ₂ O I	H ₂ O II	CO ₂	H ₂ O I	H ₂ O II	H ₂ O _{tot.}
	p.height A*	p.height B*	p.height A	p.height B	p.height A	p.height B	mean	mean	mean	wt% mean	wt% mean	wt% mean	wt% mean
Bw3a-3-3a	0.45	0.37	0.65	0.67	0.73	0.76	0.41	0.66	0.75	0.05	0.22	0.28	0.50
Bw3a-3-3c	0.44	0.42	0.62	0.70	0.69	0.63	0.43	0.66	0.66	0.06	0.22	0.28	0.50
Bw3a-3-3f	0.33	0.45	0.66	0.69	0.73	0.76	0.39	0.68	0.75	0.05	0.24	0.29	0.52
Bw3a-3-3g	0.42	0.44	0.65	0.65	0.63	0.72	0.43	0.65	0.68	0.06	0.23	0.28	0.51
Bw3a-3-3j	0.28	0.45	0.65	0.65	0.72	0.65	0.37	0.65	0.69	0.05	0.23	0.28	0.51
Bw3a-3-3k	0.41	0.30	0.65	0.68	0.64	0.74	0.36	0.67	0.69	0.05	0.20	0.28	0.48
Bw3a-3-3l	0.28	0.47	0.69	0.67	0.75	0.67	0.38	0.68	0.71	0.05	0.25	0.29	0.53
Bw3a-3-3m	0.49	0.31	0.70	0.64	0.67	0.73	0.40	0.67	0.70	0.05	0.21	0.28	0.50
Bw3a-3-3n	0.45	0.42	0.63	0.61	0.61	0.69	0.44	0.62	0.65	0.06	0.22	0.26	0.49
Bw3a-3-3p	0.40	0.38	0.69	0.64	0.64	0.71	0.39	0.67	0.68	0.05	0.23	0.28	0.51
Bw3a-3-3s	0.38	0.41	0.70	0.67	0.71	0.72	0.40	0.69	0.72	0.05	0.24	0.29	0.53
Bw3a-9-1a	0.40	0.31	0.67	0.67	0.64	0.62	0.36	0.67	0.63	0.05	0.21	0.28	0.49
Bw3a-9-1d	0.42	0.47	0.66	0.79	0.66	0.64	0.45	0.73	0.65	0.06	0.24	0.31	0.55

Cordierite rim spectra - Bw-3

Table III-1b

Number	CO ₂	CO ₂	H ₂ O I	H ₂ O I	H ₂ O II	H ₂ O II	CO ₂	H ₂ O I	H ₂ O II	CO ₂	H ₂ O I	H ₂ O II	H ₂ O _{tot.}
	p.height A*	p.height B*	p.height A	p.height B	p.height A	p.height B	mean	mean	mean	wt% mean	wt% mean	wt% mean	wt% mean
Bw3a-3-3e	0.40	0.27	0.72	0.66	0.81	0.81	0.34	0.69	0.81	0.04	0.21	0.29	0.50
Bw3a-3-3i	0.35	0.42	0.97	0.83	1.02	1.05	0.39	0.90	1.04	0.05	0.30	0.38	0.68
Bw3a-3-3h	0.36	0.33	0.72	0.76	0.88	0.77	0.35	0.74	0.83	0.05	0.22	0.31	0.54
Bw3a-3-3o	0.40	0.37	0.78	0.77	0.92	1.08	0.39	0.78	1.00	0.05	0.24	0.33	0.57
Bw3a-3-3q	0.34	0.31	0.72	0.73	0.77	0.83	0.33	0.73	0.80	0.04	0.22	0.31	0.53
Bw3a-3-3r	0.34	0.41	0.67	0.70	0.79	0.71	0.38	0.69	0.75	0.05	0.23	0.29	0.52
Bw3a-9-1b	0.40	0.28	0.70	0.90	0.74	0.83	0.34	0.80	0.79	0.04	0.21	0.34	0.55
Bw3a-9-1c	0.41	0.31	0.72	0.83	0.74	0.63	0.36	0.78	0.69	0.05	0.22	0.33	0.55

*A and B refer to two FTIR measurements obtained in situ with a rotation of 90° of the sample between analysis A and B.

Cordierite intra-grain spectra - Ho12

Table III-2a

Number	CO ₂	CO ₂	H ₂ O I	H ₂ O I	H ₂ O II	H ₂ O II	CO ₂	H ₂ O I	H ₂ O II	CO ₂	H ₂ O I	H ₂ O II	H ₂ O _{tot.}
	p.height A*	p.height B*	p.height A	p.height B	p.height A	p.height B	mean	mean	mean	wt% mean	wt% mean	wt% mean	wt% mean
Ho12-a-4-2o	0.27	0.23	0.77	0.78	0.51	0.50	0.25	0.78	0.51	0.03	0.21	0.33	0.54
Ho12-a-4-2k	0.24	0.30	0.72	0.84	0.49	0.47	0.27	0.78	0.48	0.04	0.22	0.33	0.55
Ho12-a-4-2j	0.27	0.29	0.75	0.82	0.48	0.48	0.28	0.79	0.48	0.04	0.22	0.33	0.55
Ho12-a-4-2hb	0.22	0.29	0.91	0.91	0.80	0.84	0.26	0.91	0.82	0.03	0.25	0.39	0.64
Ho12-a-4-2b	0.27	0.22	0.78	0.72	0.48	0.56	0.25	0.75	0.52	0.03	0.21	0.32	0.53
Ho12-a-4-2a	0.23	0.29	0.72	0.77	0.52	0.46	0.26	0.75	0.49	0.03	0.21	0.32	0.53
Ho12-a-4-2c	0.30	0.64	0.78	0.69	0.49	0.60	0.47	0.74	0.55	0.06	0.30	0.31	0.61
Ho12-a-4-2f	0.26	0.21	0.75	0.73	0.55	0.65	0.24	0.74	0.60	0.03	0.20	0.31	0.52
Ho12-a-4-2h	0.24	0.30	0.73	0.79	0.53	0.52	0.27	0.76	0.53	0.04	0.22	0.32	0.54
Ho12-a-5-1m	0.22	0.13	0.70	0.84	0.55	0.52	0.18	0.77	0.54	0.02	0.18	0.33	0.50
Ho12-a-5-1k	0.22	0.12	0.68	0.81	0.52	0.45	0.17	0.75	0.49	0.02	0.17	0.32	0.49
Ho12-a-5-f	0.07	0.16	0.77	0.68	0.42	0.57	0.12	0.73	0.50	0.02	0.20	0.31	0.51
Ho12-a-5-e	0.16	0.07	0.75	0.86	0.64	0.54	0.12	0.81	0.59	0.02	0.17	0.34	0.52
Ho12-a-5-d	0.07	0.16	1.00	0.74	0.59	0.42	0.12	0.87	0.51	0.02	0.25	0.37	0.62
Ho12-a-5-c	0.16	0.07	0.61	0.78	0.51	0.38	0.12	0.70	0.45	0.02	0.14	0.30	0.44
Ho12-a-5-a	0.17		0.67		0.49		0.09	0.34	0.25	0.01	0.14	0.14	0.28
Ho12-a-1-2j	0.32	0.13	0.43	0.61	0.39	0.41	0.23	0.52	0.40	0.03	0.12	0.22	0.34
Ho12-a-1-2i	0.16	0.30	0.52	0.42	0.33	0.41	0.23	0.47	0.37	0.03	0.17	0.20	0.37
Ho12-a-2-2h	0.32	0.14	0.43	0.52	0.38	0.41	0.23	0.48	0.40	0.03	0.12	0.20	0.32
Ho12-a-1-2b	0.14	0.33	0.64	0.51	0.44	0.44	0.24	0.58	0.44	0.03	0.21	0.24	0.45
Ho12-a-1-2	0.21	0.37	0.55	0.44	0.34	0.37	0.29	0.50	0.36	0.04	0.20	0.21	0.41
Ho12-a-2-2b	0.12	0.35	0.55	0.43	0.40	0.43	0.24	0.49	0.42	0.03	0.19	0.21	0.40
Ho12-a-1-1n	0.09	0.09	0.81	0.83	0.43	0.59	0.09	0.82	0.51	0.01	0.19	0.35	0.54
Ho12-a-1-1m	0.07	0.07	0.64	0.75	0.49	0.38	0.07	0.70	0.44	0.01	0.15	0.30	0.45
Ho12-a-1-j	0.09	0.09	0.62	0.77	0.52	0.38	0.09	0.70	0.45	0.01	0.15	0.30	0.45
Ho12-a-1-1i	0.10	0.06	0.77	0.70	0.41	0.54	0.08	0.74	0.48	0.01	0.18	0.31	0.49
Ho12-a-1-1h	0.10	0.33	0.59	0.52	0.41	0.54	0.22	0.56	0.48	0.03	0.20	0.24	0.43
Ho12-a-1-1d	0.09	0.07	0.75	0.80	0.56	0.41	0.08	0.78	0.49	0.01	0.17	0.33	0.50
Ho12-a-1-b	0.13	0.10	0.77	0.67	0.39	0.49	0.12	0.72	0.44	0.02	0.18	0.31	0.49
Ho12-a-1-a	0.09	0.09	0.64	0.74	0.46	0.38	0.09	0.69	0.42	0.01	0.15	0.29	0.45

*A and B refer to two FTIR measurements obtained in situ with a rotation of 90° of the sample between analysis A and B.

Cordierite rim spectra - Ho12

Table III-2b

Number	CO ₂	CO ₂	H ₂ O I	H ₂ O I	H ₂ O II	H ₂ O II	CO ₂	H ₂ O I	H ₂ O II	CO ₂	H ₂ O I	H ₂ O II	H ₂ O _{tot.}
	p.height A*	p.height B*	p.height A	p.height B	p.height A	p.height B	mean	mean	mean	wt% mean	wt% mean	wt% mean	wt% mean
Ho12-a-4-2n	0.22		2.08				0.11	1.04	0.00	0.01	0.44	0.44	0.88
Ho12-a-4-2i	0.27	0.27	0.78	0.83	0.74	0.71	0.27	0.81	0.73	0.04	0.22	0.34	0.56
Ho12-a-4-2g	0.22		1.10		0.98		0.11	0.55	0.49	0.01	0.23	0.23	0.47
Ho12-a-4-2e	0.24	0.28	0.74	0.74	0.49	0.49	0.26	0.74	0.49	0.03	0.22	0.31	0.53
Ho12-a-4-2m	0.24	0.24	0.74	0.76	0.54	0.53	0.24	0.75	0.54	0.03	0.21	0.32	0.53
Ho12-a-4-2l	0.24	0.26	0.74	0.71	0.48	0.51	0.25	0.73	0.50	0.03	0.21	0.31	0.52
Ho12-a-5-1o	0.22	0.15	0.78	0.85	0.74	0.63	0.19	0.82	0.69	0.02	0.20	0.35	0.54
Ho12-5-a-1l	0.19	0.16	0.86	0.90	0.62	0.67	0.18	0.88	0.65	0.02	0.22	0.37	0.59
Ho12-5-a-1j	0.13	0.23	1.00	0.90	0.65	0.84	0.18	0.95	0.75	0.02	0.26	0.40	0.66
Ho12-a-5-b	0.10	0.14	0.78	0.74	0.42	0.65	0.12	0.76	0.54	0.02	0.20	0.32	0.52
Ho12-a-5-1g	0.19	0.12	0.80	0.86	0.62	0.49	0.16	0.83	0.56	0.02	0.20	0.35	0.55
Ho12-a-5-h	0.12	0.17	0.72	0.67	0.37	0.51	0.15	0.70	0.44	0.02	0.19	0.30	0.48
Ho12-a-5-1n	0.14	0.20	0.78	0.72	0.47	0.69	0.17	0.75	0.58	0.02	0.21	0.32	0.53
Ho12-a-5-i	0.22	0.10	0.70	0.77	0.51	0.38	0.16	0.74	0.45	0.02	0.17	0.31	0.48
Ho12-a-1-2e		0.28	2.21				0.14	1.11	0.00	0.02	0.53	0.47	1.00
Ho12-a-1-2f	0.22		1.87				0.11	0.94	0.00	0.01	0.44	0.40	0.84
Ho12-a-1-2d	0.33	0.15	0.70	0.74	0.76	0.73	0.24	0.72	0.75	0.03	0.18	0.31	0.49
Ho12-a-1-2c	0.35	0.15			1.23	0.39	0.25	0.00		0.03	0.03	0.00	0.03
Ho12-a-1-2g	0.13	0.31	0.56	0.62	0.38	0.60	0.22	0.59	0.49	0.03	0.18	0.25	0.44
Ho12-a-1-2k	0.12	0.33	0.59	0.57	0.42	0.57	0.23	0.58	0.50	0.03	0.20	0.25	0.44
Ho12-a-1-2l	0.13		0.83				0.07	0.42	0.00	0.01	0.18	0.18	0.35
Ho12-a-2-d	0.39		1.23				0.20	0.62	0.00	0.03	0.26	0.26	0.52
Ho12-a-1-1l	0.09	0.03	0.81	0.77	0.50	0.62	0.06	0.79	0.56	0.01	0.18	0.34	0.51
Ho12-a-1-k	0.03		1.30		1.13		0.02	0.65	0.57	0.00	0.28	0.28	0.55
Ho12-a-1-1fg	0.09	0.06	0.97	1.06	0.77	0.84	0.08	1.02	0.81	0.01	0.22	0.43	0.65
Ho12-a-1-c	0.10	0.09	0.80	0.70	0.46	0.54	0.10	0.75	0.50	0.01	0.19	0.32	0.51
Ho12-a-1-1e	0.09	0.29	0.65	0.52	0.55	0.57	0.19	0.59	0.56	0.02	0.20	0.25	0.45
Ho12-a-1-1f	0.32	0.04	0.48	0.57	0.45	0.41	0.18	0.53	0.43	0.02	0.11	0.22	0.33
Ho12-a-1-1lb	0.16	0.12	0.91	0.88	0.59	0.78	0.14	0.90	0.69	0.02	0.22	0.38	0.60

*A and B refer to two FTIR measurements obtained *in situ* with a rotation of 90° of the sample between analysis A and B.

Cordierite intra-grain spectra - Wa-4

Table III-3a

Number	CO ₂	CO ₂	H ₂ O I	H ₂ O I	H ₂ O II	H ₂ O II	CO ₂	H ₂ O I	H ₂ O II	CO ₂	H ₂ O I	H ₂ O II	H ₂ O _{tot.}
	p.height A*	p.height B*	p.height A	p.height B	p.height A	p.height B	mean	mean	mean	wt% mean	wt% mean	wt% mean	wt% mean
Wa4-2-2a	0.29	0.32	0.57	0.66	0.60	0.57	0.31	0.62	0.59	0.04	0.19	0.26	0.45
Wa4-2-2c	0.29	0.31	0.70	0.67	0.62	0.65	0.30	0.69	0.64	0.04	0.21	0.29	0.51
Wa4-2-2c	0.38	0.27	0.49	0.49	0.64	0.72	0.33	0.49	0.68	0.04	0.16	0.21	0.37
Wa4-2-2b	0.27	0.40	0.56	0.57	0.69	0.64	0.34	0.57	0.67	0.04	0.20	0.24	0.44
Wa4-8-2a	0.31	0.30	0.63	0.63	0.65	0.59	0.31	0.63	0.62	0.04	0.20	0.27	0.46
Wa4-8-2d	0.30	0.33	0.65	0.70	0.62	0.58	0.32	0.68	0.60	0.04	0.21	0.29	0.49
Wa4-8-2f	0.34	0.34	0.64	0.67	0.59	0.56	0.34	0.66	0.58	0.04	0.21	0.28	0.49
Wa4-8-2i	0.46	0.32	0.74	0.70	0.66	0.68	0.39	0.72	0.67	0.05	0.22	0.31	0.53
Wa4-8-2k	0.34	0.30	0.66	0.71	0.58	0.59	0.32	0.69	0.59	0.04	0.20	0.29	0.49
Wa4-8-2l	0.35	0.34	0.72	0.67	0.60	0.62	0.35	0.70	0.61	0.05	0.22	0.30	0.52
Wa4-8-2m	0.37	0.34	0.72	0.67	0.62	0.62	0.36	0.70	0.62	0.05	0.22	0.30	0.52
Wa4-8-2n	0.30	0.33	0.73	0.67	0.61	0.62	0.32	0.70	0.62	0.04	0.22	0.30	0.52
Wa4-8-2o	0.33	0.34	0.68	0.73	0.66	0.67	0.34	0.71	0.67	0.04	0.22	0.30	0.52
Wa4-8-2r	0.27	0.34	0.72	0.67	0.60	0.64	0.31	0.70	0.62	0.04	0.22	0.30	0.52
Wa4-8-2q	0.38	0.35	0.68	0.73	0.59	0.60	0.37	0.71	0.60	0.05	0.22	0.30	0.52
Wa4-1-1o	0.24	0.37	0.66	0.59	0.65	0.61	0.31	0.63	0.63	0.04	0.22	0.27	0.48
Wa4-1-1n	0.35	0.34	0.67	0.70	0.69	0.72	0.35	0.69	0.71	0.05	0.21	0.29	0.51
Wa4-1-1i	0.22	0.40	0.69	0.58	0.66	0.80	0.31	0.64	0.73	0.04	0.23	0.27	0.50
Wa4-1-1e	0.22	0.40	0.69	0.64	0.67	0.67	0.31	0.67	0.67	0.04	0.23	0.28	0.51
Wa4-1-1d	0.42	0.22	0.67	0.66	0.67	0.63	0.32	0.67	0.65	0.04	0.19	0.28	0.47
Wa4-1-1b	0.27	0.44	0.64	0.57	0.62	0.59	0.36	0.61	0.61	0.05	0.23	0.26	0.49
Wa4-1-1a	0.36	0.22	0.60	0.63	0.55	0.58	0.29	0.62	0.57	0.04	0.17	0.26	0.44
Wa4-1-1j	0.23	0.40	0.66	0.66	0.66	0.66	0.32	0.66	0.66	0.04	0.22	0.28	0.51
Wa4-9-2l	0.52	0.50	0.62	0.60	0.80	0.76	0.51	0.61	0.78	0.07	0.24	0.26	0.50
Wa4-9-2k	0.41	0.26	0.62	0.65	0.72	0.79	0.34	0.64	0.76	0.04	0.19	0.27	0.46
Wa4-9-2i	0.69	0.55	0.57	0.59	0.73	0.80	0.62	0.58	0.77	0.08	0.24	0.25	0.48
Wa4-9-2h	0.52	0.62	0.59	0.55	0.71	0.67	0.57	0.57	0.69	0.07	0.26	0.24	0.50
Wa4-9-2g	0.55	0.71	0.60	0.57	0.79	0.74	0.63	0.59	0.77	0.08	0.28	0.25	0.53
Wa4-9-2f	0.43	0.53	0.63	0.58	0.76	0.72	0.48	0.61	0.74	0.06	0.25	0.26	0.50
Wa4-8-2b	0.47	0.63	0.62	0.58	0.89	0.84	0.55	0.60	0.87	0.07	0.27	0.25	0.52
Wa4-9-2a	0.63	0.55	0.59	0.59	0.82	0.83	0.59	0.59	0.83	0.08	0.24	0.25	0.49

*A and B refer to two FTIR measurements obtained *in situ* with a rotation of 90° of the sample between analysis A and B.

Cordierite rim spectra - Wa-4

Table III-3b

Number	CO ₂		H ₂ O I		H ₂ O II		CO ₂ p.height	H ₂ O I p.height	H ₂ O II p.height	CO ₂ wt% mean	H ₂ O I wt% mean	H ₂ O II wt% mean	H ₂ O _{int.} wt% mean
	A*	B*	A	B	A	B							
Wa4-2-2e	0.29		0.64		0.97		0.29	0.64	0.97	0.02	0.14	0.14	0.27
Wa4-2-2d	0.30				1.19		0.30	-	1.19	0.02	0.00	0.00	0.00
Wa4-2-2a	0.24				1.13		0.24	-	1.13	0.02	0.00	0.00	0.00
Wa4-8-2b*	0.30		0.75		0.71		0.30	0.75	0.71	0.02	0.16	0.16	0.32
Wa4-8-2c	0.30	0.32	0.74	0.71	0.65	0.68	0.31	0.73	0.67	0.04	0.22	0.31	0.53
Wa4-8-2p	0.32	0.38	0.74	0.72	0.77	0.77	0.35	0.73	0.77	0.05	0.24	0.31	0.55
Wa4-8-2h	0.43	0.21	0.78	0.66	0.58	0.67	0.32	0.72	0.63	0.04	0.21	0.31	0.52
Wa4-8-2e	0.41	0.42	0.72	0.66	0.59	0.60	0.42	0.69	0.60	0.05	0.24	0.29	0.53
Wa4-8-2g	0.33	0.30	0.69	0.64	0.57	0.59	0.32	0.67	0.58	0.04	0.21	0.28	0.49
Wa4-8-2j	0.32	0.33	0.70	0.65	0.59	0.59	0.33	0.68	0.59	0.04	0.22	0.29	0.51
Wa4-1-1n	0.35	0.19	0.59	0.63	0.62	0.67	0.27	0.61	0.65	0.04	0.17	0.26	0.42
Wa4-1-1m*	0.16		1.52				0.16	1.52	-	0.01	0.32	0.32	0.65
Wa4-1-1l	0.21	0.40	0.74	0.66	0.80	0.79	0.31	0.70	0.80	0.04	0.24	0.30	0.54
Wa4-1-1k	0.35	0.21	0.66	0.76	0.72	0.83	0.28	0.71	0.78	0.04	0.18	0.30	0.49
Wa4-1-1h	0.22	0.38	0.76	0.70	0.84	0.79	0.30	0.73	0.82	0.04	0.24	0.31	0.55
Wa4-1-1f	0.40	0.22	0.66	0.70	0.79	0.79	0.31	0.68	0.79	0.04	0.19	0.29	0.48
Wa4-1-1c	0.20	0.40	0.73	0.66	0.79	0.65	0.30	0.70	0.72	0.04	0.24	0.30	0.53
Wa4-1-1g	0.22	0.40	0.66	0.67	0.67	0.63	0.31	0.67	0.65	0.04	0.22	0.28	0.51
Wa4-9--2o	0.51	0.52	0.64	0.60	0.83	0.91	0.52	0.62	0.87	0.07	0.25	0.26	0.51
Wa4-9-2n	0.29	0.23	0.74	0.65	0.87	0.83	0.26	0.70	0.85	0.03	0.21	0.30	0.50
Wa4-9-2m*	0.49		1.12				0.49	1.12	-	0.03	0.24	0.24	0.48
Wa4-9-2j	0.49	0.67	0.66	0.62	0.91	0.90	0.58	0.64	0.91	0.08	0.28	0.27	0.55
Wa4-4-2x*	0.62		0.67		1.02		0.62	0.67	1.02	0.04	0.14	0.14	0.28
Wa-4-9-2e	0.40	0.33	0.65	0.69	0.74	0.78	0.37	0.67	0.76	0.05	0.21	0.28	0.49
Wa4-9-2d	0.49	0.73	0.62	0.59	0.88	0.87	0.61	0.61	0.88	0.08	0.29	0.26	0.54
Wa4-9-2bc	0.35	0.24	0.72	0.77	0.87	0.99	0.30	0.75	0.93	0.04	0.20	0.32	0.52

*A and B refer to two FTIR measurements obtained *in situ* with a rotation of 90° of the sample between analysis A and B.

Danksagung

Mein Dank gilt sämtlichen Mitarbeitern des Mineralogischen Institutes der Universität Heidelberg.

Mein besonderer Dank gilt meinem Doktorvater Frau Prof. Dr. Angelika Kalt, die mir auch aus der Ferne stets mit Rat und Tat zur Seite stand.

Herrn Prof. Dr. Rainer Altherr sei Dank für die Erstellung des Zweitgutachtens und auch für die sonstige Unterstützung, die er mir hat zukommen lassen.

Bei Herrn Prof. Dr. W.F. Müller möchte ich mich dafür bedanken, dass er mir die Arbeiten am Transelektronenmikroskop des Mineralogischen Instituts der TU Darmstadt ermöglicht hat. Herrn Dr. Peter von Aken, Eric Barnert und Hauke Gorzawski sei Dank für die Hilfe bei der Handhabung des Gerätes.

Bei Herrn Dr. Harald Behrens bedanke ich mich für das Ermöglichen der FTIR-Messungen.

Bei Herrn Dr. Laurence Warr, Heiko Hofmann und Anja Schleicher bedanke ich mich für die Hilfe bei den XRD-Mesungen

Dr. Hans-Peter Meyer danke ich für die Hilfe bei den Mikrosonden- und Rasterelektronenmikroskopuntersuchungen.

Ilona Fin danke ich für die Präparation von Dick- und Dünnschliffen und insbesondere die Herstellung der TEM relevanten Schliffe.

Bei Ilse Glas bedanke ich mich für die prompte Hilfe bei den DTA-Tests, der Handhabung des REM und der Besorgung diverser Chemikalien.

Besonders möchte ich mich bei meinen 'Leidensgenossen' bedanken, nämlich Nicole Steppan, Stefan Hepp, Bettina Olker, Melanie Kaliwoda, Horst Marschall, Mario Koch, Stefan Prowatke und ganz besonders bei Jens Paquin. Es ist gut zu wissen, dass man nicht alleine ist. Ebenso bedanke ich mich bei Georg Partzsch, Thomas Zack und Stephan Klemme, die stets für einen Plausch, wissenschaftlich oder nicht-wissenschaftlich, zu haben waren.

Mein inniger Dank gilt meinen Eltern ohne deren Unterstützung dies alles nicht möglich gewesen wäre. Auch finanziell haben Sie uns immer wieder aufgefangen und Schlimmeres verhindert.

Mein tiefster Dank gilt meiner Lebensgefährtin Claudia, die mich oft entbehren musste und die unsere Familie so oft allein auf ihren Schultern trug. Danke Claudia, Du bist die beste Partnerin, die ich mir wünschen kann. Danke auch an meine Töchter, Paulina und Amelie, dafür dass Ihr mir immer wieder ein Chance gebt. Claudia, Du wirst sehen, auch wenn im Moment vieles im Argen ist, eines Tages werden wir darüber lachen können.

Erklärung

Hiermit erkläre ich, Jörn C, Ogiermann, geboren am 30.08.1971 in Offenbach/Main, an Eides statt, dass ich die vorgelegte Dissertation selbst verfaßt und mich dabei keiner anderen als der von mir ausdrücklich bezeichneten Quellen und Hilfen bedient habe.

Ich, Jörn C, Ogiermann, geboren am 30.08.1971 in Offenbach/Main, erkläre zudem an Eides statt, dass ich an keiner anderen Stelle ein Prüfungsverfahren beantragt habe, dass ich die Dissertation nicht in dieser oder anderer Form bereits anderweitig als Prüfungsarbeit verwendet habe und dass ich sie an keiner anderen Fakultät als Dissertation vorgelegt hat.

Heidelberg, den 28.10.2002

